

Research on

Engineering

Structures

Materials

M

R

E

S

P-ISSN: 2148-9807 E-ISSN: 2149-4088

www.jresm.org

Volume
8

Issue
4

December
2022

The International Journal of **Research on Engineering Structures and Materials (RESM)** is a peer-reviewed open access journal (p-ISSN: 2148-9807; o-ISSN: 2149-4088) published by MIM Research Group. It is published in February, June, September, and December.

The main objective of RESM is to provide an International academic platform for researchers to share scientific results related to all aspects of mechanical, civil, and material engineering areas.

RESM aims the publication of original research articles, reviews, short communications technical reports, and letters to the editor on the latest developments in the related fields.

All expenditures for the publication of the manuscripts are most kindly reimbursed by *MIM Research Group*. Thus, authors do not need to pay for publishing their studies in the journal.

The scope of the journal covers (but not limited to) behavior of structures, machines and mechanical systems, vibration, impact loadings and structural dynamics, mechanics of materials (elasticity, plasticity, fracture mechanics), material science (structure and properties of concrete, metals, ceramics, composites, plastics, wood, etc.), nano-materials performances of new and existing buildings and other structural systems, design of buildings and other structural systems, seismic behavior of buildings and other structural systems, repair and strengthening of structural systems, case studies and failure of structural systems, safety and reliability in structural and material engineering, use of new and innovative materials and techniques in energy systems and mechanical aspects of biological systems (biomechanics and biomimetics).

The topics covered in JRESM include:

- Structural Engineering
- Mechanical Engineering
- Material Engineering
- Earthquake Engineering
- Nano-technology
- Energy Systems (Focus on Renewable)
- Biomechanics and Biomimetics
- Environment (Material and Engineering System Related Issues)
- Computer Engineering and Data Science (Material and Engineering System-Related Issues)

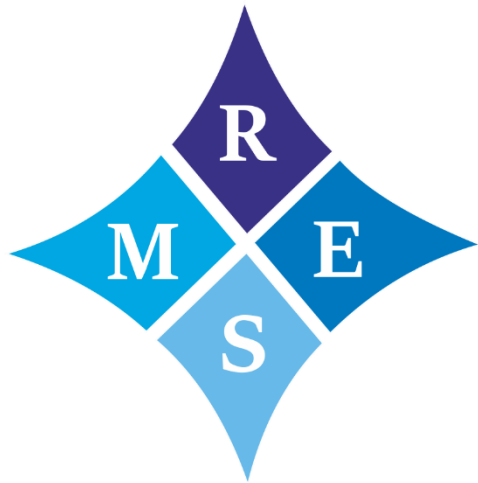
Abstracting and Indexing

Please visit <http://www.jresm.org> for more information.

Graphics and Design

Yunus Demirtaş

ydemirtas@jresm.net



**RESEARCH on
ENGINEERING STRUCTURES &
MATERIALS**

RESEARCH on ENGINEERING STRUCTURES & MATERIALS

Editorial Board

Editor in Chief		
Hayri Baytan Özmen	Usak University	Turkey

Editor (Energy, Thermodynamics)		
Canan Kandilli	Usak University	Turkey

Editor (Physics, Fluid Dynamics)		
Antonio F. Miguel	University of Evora	Portugal

Editor (Earthquake Eng., Structural Eng.)		
Michele Barbato	University of California Davis	USA

Editor (Mechanics, Biosystems, Meta-materials)		
Alp Karakoç	Aalto University	Finland

Editor (Applied Mechanics, Manufacturing, Design)		
Faris Tarlochan	Qatar University	Qatar

Editor (Civil Engineering)		
Mehmet Palancı	Arel University	Turkey

Editor (Earthquake Engineering)		
Raudhah Ahmadi	University Malaysia Sarawak	Malaysia

Editor (Civil, Construction-Architectural and Environmental Engineering)		
Francesco D'Annibale	University of L'Aquila	Italy

Editorial Office

Publishing Assistant		
Yunus Demirtaş	Eskişehir Technical University	Turkey
Yusuf Öztürk	MIM Resarch Group	Turkey

Language Editors		
Gaye Kuru	Usak University	Turkey
Mete Çal	Niğde Ömer Halisdemir University	Turkey

Editorial Board Members

Farid Abed-Meraim	Arts et Metiers ParisTech	France
P. Anbazhagan	Indian Institute of Science	India
Raffaele Barretta	University of Naples Federico II	Italy
R.S. Beniwal	Council of Scientific and Industrial Research	India
Antonio Caggiano	University of Buenos Aires	Argentina
Noel Challamel	University of South Brittany	France
Abdulkadir Çevik	Gaziantep University	Turkey
J. Paulo Davim	University of Aveiro	Portugal
Hom Nath Dhakal	University of Portsmouth	UK
Ali Faghidian	Islamic Azad University	Iran
S. Amir M. Ghannadpour	Shahid Beheshti University	Iran
Ali Goodarzi	Harvard University	USA
Jian Jiang	National Institute of Standards and Technology	USA
Ramazan Karakuzu	Dokuz Eylül University	Turkey
Arkadiusz Kwiecien	Cracow University of Technology	Poland
Stefano Lenci	Universita Politecnica delle Marche	Italy
Silva Lozančić	University of Osijek	Croatia
Fabio Mazza	University of Calabria	Italia
Yuan Meini	North University of China	China
Stergios A. Mitoulis	University of Surrey	UK
Vinayagam Mohanavel	Anna University	India
Ehsan Noroozinejad Farsangi	Kerman Graduate University of Technology	Iran
Alaa M. Rashad	Shaqra University	Saudi Arabia
Mohammad Mehdi Rashidi	University of Tongji	China
Pier Paolo Rossi	University of Catania	Italy
Neritan Shkodrani	Polythecnic University of Tirana	Albania
Y.B. Yang	National Taiwan University	Taiwan

Advisory Board Members

Yaser Açıkbaş	Usak University	Turkey
Mehmet Ada	Usak University	Turkey
Mohammad Afrazi	Tarbiat Modares University	Iran
Ayşe Bilge Aksoy	Celal Bayar University	Turkey
Ali Özhan Akyüz	Burdur Mehmet Akif Ersoy University	Turkey
Mohammad Al Biajawi	Universiti Malaysia Pahang	Malaysia
Gabriel Arce	Louisiana State University	USA
E. Arunraj	Karunya Institute of Technology and Sciences	India
K. Ashwini	Jawaharlal Nehru Technological University Hyderabad	India
Olumoyewa Atoyebi	Landmark University	Nigeria
Samuel Awe	Automotive Components Floby AB	Sweden
Ameer Baiee	University of Babylon	Iraq
Ajay Sudhir Bale	CMR University	India
Megha Bhatt	SV National Institute of Technology	India
Tanik Bayram Cayci	Pamukkale University	Turkey
Noé Cheung	Universidade Estadual de Campinas	Brazil
Chella Gifta Christopher	National Engineering College	India
Hüseyin Coşkun	Usak University	Turkey
Daniel Cruze	Hindustan Institute of Technology and Science	India
Ali İhsan Çelik	Kayseri University	Turkey
Ahmet Demir	Bolu University	Turkey
Cengiz Görkem Dengiz	Ondokuz Mayıs University	Turkey
Marwan Effendy	Universitas Muhammadiyah Surakarta	Indonesia
Halil Murat Enginsoy	Çanakkale Onsekiz Mart University	Turkey
Ali Erçetin	Bingöl University	Turkey
S. Ali Faghidian	Islamic Azad University	Iran

Advisory Board Members

Christopher Fapohunda	Federal University Oye-Ekiti	Nigeria
Abdullah Fettahoglu	Usak University	Turkey
Mehmet Cemal Genes	Eastern Mediterranean University	North Cyprus
Vahidreza Gharehbaghi	University of Southern Queensland	Australia
Anjeza Gjini	Polytechnic University of Tirana	Albania
Layachi Guelmine	University Of Bordj Bou Arreridj	Algeria
Kadir Günaydın	GE Aviation	Turkey
Orhan Gülcan	General Electric Aviation	USA
Marijana Hadzima-Nyarko	University of Osijek	Croatia
Dulce Franco Henriques	Instituto Politécnico de Lisboa	Portugal
Qing Hong	Midwestern University	USA
Ercan Isik	Bitlis Eren University	Turkey
Khairul Nizar Ismail	Universiti Malaysia Perlis	Malaysia
Berrin Ikizler	Ege University	Turkey
Saifulnizan Jamian	Universiti Tun Hussein Onn Malaysia	Malaysia
Joel Shelton Joseph	RGM College of Engineering and Technology	India
Arunkumar K.	-	India
Nikhil R. Kadam	Birla Institute of Technology and Science	India
Abdulhalim Karasin	Dicle University	Turkey
Hemant B. Kaushik	Indian Institute of Technology Guwahati	India
Mehmet Kaya	Yozgat Bozok University	Turkey
Zafer Kaya	Dumlupınar University	Turkey
Sedat Kömürcü	Istanbul Technical University	Turkey
B. Radha Krishnan	College of Engineering and Technology	India
Karthik Krishnasamy	Vel Tech Rangarajan Dr Sagunthala R&D Institute of Science and Technology	India
Nitin Kumar	University of California Davis	USA
Manjunatha Kuruba	B.M.S College of Engineering	India

Advisory Board Members

Ravichandran M.	K.Ramakrishnan College of Engineering	India
Lomesh Mahajan	Dr. Babasaheb Ambedkar Technological University	India
Waqas Ahmed Mahar	University of Liege	Belgium
Emrah Meral	Osmaniye Korkut Ata University	Turkey
Sedat Metlek	Mehmet Akif Ersoy University	Turkey
Masoomeh Mirrashid	Semnan University	Iran
Mustafa K. A. Mohammed	Dijlah University College	Iraq
Berker Nacak	Usak University	Turkey
Samson Olalekan Odeyemi	Kwara State University	Nigeria
Mehmet Orhan	Pamukkale University	Turkey
Alp Özdemir	Eskişehir Technical University	Turkey
Yasin Onuralp Özkılıç	Necmettin Erbakan University	Turkey
Partheeban Pachaivannan	Chennai Institute of Technology	India
Moslem Paidar	Islamic Azad University	Iran
Chitaranjan Pany	Vikram Sarabhi Space Center	India
Vikas Patel	National Council for Cement and Building Materials	India
Lalit Pawar	Veermata Jijabai Technological Institute	India
Amin Moslemi Petrudi	Tehran University	Iran
Josphat Phiri	Aalto University	Finland
B.Prabakaran	Hindustan Institute of Technology and Science	India
K. Venkatesh Raja	Sona College of Technology	India
Badrinarayan Rath	Wollega University	Ethiopia
Pier Paola Rossi	University of Catania	Italy
Francesca Russo	Instituto per la Tecnologia delle Membrane CNR-ITM	Italy
Abbasali Sadeghi	Islamic Azad University	Iran
S. Reza Salimbahrami	Semnan University	Iran

Advisory Board Members

M.Helen Santhi	Vellore Institute of Technology	India
Sudesh Singh	Sharda University	India
Rianti Dewi Sulamet-Ariobimo	Universitas Trisakti	Indonesia
Hamide Tekeli	Suleyman Demirel University	Turkey
Serdar Tez	Pamukkale University	Turkey
Tugce Tezel	Akdeniz University	Turkey
Subash Thanappan	Ambo University	Ethiopia
Fatma Coskun Topuz	Yuzuncu Yil University	Turkey
Prem Kumar V.	-	India
Suiwen Wu	University of Nevada	USA
Jhair Yacila	Pontifical Catholic University of Peru	Peru
Omid Aminoroayai Yamani	K. N. Toosi University of Technology	USA

In This Issue

Research Article

643 **Lemiye Atabek Savaş**

Synthesis of β -strontium hydrogen phosphate nanosheets and its effect on thermal and tribo-mechanical properties of polypropylene composites

Research Article

659 **Özgür Demircan, Fatma Burcu Uzunoğlu, Naser Rezaei Ansaroudi**

Influence of multi-walled carbon nanotubes on tensile and flexural properties of polyamide 66/short glass fiber composites

Technical Note

675 **Nasir Mohammed Tahir, Adamu Umar Alhaji, Ibrahim Abdullahi**

Performance evaluation of unmanned aerial vehicle wing made from sterculiasetigeradelile fiber and pterocarpuserinaceus wood dust epoxy composite using finite element method Abaqus and structural testing

Research Article

695 **Nikolay Dolgov, Maris Hauka, Leonids Vinogradovs**

Adhesion strength evaluation for plasma-sprayed coatings based on intensity of singular stress

Research Article

707 **Prem Kumar V., Vasugi V.**

Experimental investigation on bamboo fibre reinforced mortar using artificial neural network – a comparative study

Research Article

721 **Mehmet Topuz**

Effect of ZrO₂ on morphological and adhesion properties of hydroxyapatite reinforced poly- (lactic) acid matrix hybrid coatings on Mg substrates

Research Article

735 **Olatunji Oladimeji Ojo, Gbadebo Samuel John**

Weldability of interlocked-end friction stir welding of aluminum alloy: single and double-sided welding

Research Article

751 **Mehmet Hakan Demir**

Numerical investigation of the combined effects of coating layer properties and specific heat capacities of materials on the heat transfer mechanism in solidification of pure metals

Research Article

773 **Tanvi Saxena, V.K. Chawla**

Evaluation of mechanical properties for banana-carbon fiber reinforced nano-clay epoxy composite using analytical modeling and simulation

Technical Note

799 **Bora Şener, Toros Arda Akşen, Emre Esener, Mehmet Fırat**

On the effect of numerical parameters in finite element through thickness modeling for springback prediction

Research Article

811 **Altin Bidaj, Huseyin Bilgin, Marjo Hysenlliu, Irakli Premti, Rrapo Ormeni**

Performance of URM structures under earthquake shakings: Validation using a template building structure by the 2019 Albanian earthquakes

Research Article

835 **Birendra Kumar Bohara, Prasenjit Saha**

Nonlinear behaviour of reinforced concrete moment resisting frame with steel brace

Technical Note

853 **Om V. Vaidya, Kapil Malviya, Yuvaraj L. Bhirud**

The strength characteristics of concrete using recycled concrete aggregates

Technical Note

861 **Lalit B. Pawar, Keshav K. Sangle, Yuvaraj L. Bhirud**

Experimental investigation of spalling effect of elevated temperature on concrete containing waste plastic aggregates

Research Article

885 **Mahesh V. Raut**

Leverage of high-volume fly ash along with glass fiber for sustainable concrete

Free access to tables of content, abstracts and full text of papers for web visitors.

Copyright © 2022

Research on Engineering Structures & Materials

MIM Research Group Publications

P-ISSN: 2148-9807

E-ISSN: 2149-4088

<http://www.jresm.org>



ABSTRACTING / INDEXING

The international journal of Research on Engineering Structures and Materials (RESM) is currently Abstracted/Indexed by Asos Indeks, CiteFactor, Cosmos, CrossRef, Directory of Research Journal Indexing, Engineering Journals (ProQuest), EZB Electronic Journal Library, Global Impact Factor, Google Scholar, International Institute of Organized Research (I2OR), International Scientific Indexing (ISI), Materials Science & Engineering Database (ProQuest), Open Academic Journals Index, Publication Forum, Research Bible/Scientific Indexing Service, Root Indexing, Scopus, Ulakbim TR Index (Tubitak), Universal Impact Factor and under evaluation by many other respected indexes.

Check web site for current indexing info, www.jresm.org

Scopus®



Publication
Forum



Research Article

Synthesis of β -strontium hydrogen phosphate nanosheets and its effect on thermal and tribo-mechanical properties of polypropylene composites

Lemiye Atabek Savaş^{*,a}

Department of Materials Science and Engineering, Erciyes University, Kayseri, Turkey

Article Info

Abstract

Article history:

Received 22 Feb 2022

Revised 9 May 2022

Accepted 5 June 2022

Keywords:

Strontium hydrogen phosphate;
Nanosheet;
Polypropylene;
Mechanical properties;
Wear

β -strontium hydrogen phosphate nanosheets (SHPs) with a thickness range of 35-50 nm were synthesized by hydrothermal method using strontium nitrate ($\text{Sr}(\text{NO}_3)_2$) and diammonium hydrogen phosphate ($(\text{NH}_4)_2\text{HPO}_4$) as reagents. Polypropylene (PP)/SHP nanocomposites were prepared using melt blending technique with different filler concentrations ranging from 1 wt.% to 7 wt.%. Composites were characterized primarily by tensile test, flexural test, thermogravimetric analyses and ball-on-disc sliding wear test. Experimental results revealed that the inclusion of nanosheets into PP improved the thermal stability of the composites. In addition, the tensile and flexural properties of the composites improved with SHP loading. A maximum increment of 6.0 % in tensile strength compared to pure PP was observed at 7 wt.% SHP concentration, and flexural strength of the composites was found to be higher than that of the pure polymer at each filler concentration. However, an increase was observed in the friction coefficient and wear rates of the composites due to increased hardness and rigidity of the matrix with the addition of SHP, which produced micro-cutting and micro-plowing actions that caused increased abrasive wear of the composites.

© 2022 MIM Research Group. All rights reserved

1. Introduction

In today's industry where specific strength is important along with advanced material properties, polymer composites have drawn significant attention with their high strength, light weight, good corrosion and chemical resistance properties compared to traditional engineering materials. In order to endow polymer composites with mechanical and functional properties, many kinds of micro- and nano-fillers can be added into the polymers [1, 2]. The micro-fillers usually require high volume fractions to have a significant influence on the properties of the composites [3]. However, high filler loadings may cause processing difficulties due to increased viscosity of the matrix material [1]. On the other hand, the incorporation of nano-fillers in very small amounts give the same or more contribution to the composites due to enhanced surface area and thus complex physical interactions between the reinforcement and the polymer matrix [1, 4, 5]. Furthermore, apart from mechanical improvements, thermal and functional characteristics obtained with nano-fillers make polymer nanocomposites unique candidates for specific industrial applications [6-8].

Nano-fillers can be classified according to their dimensional morphology as one dimensional (1D), two dimensional (2D), and three dimensional (3D), which all have their own advantages, disadvantages, and exclusive properties [1, 4]. The morphology of the nano-fillers plays an important role in the final nanocomposite performance [9]. It is well

*Corresponding author: atabekl@erciyes.edu.tr

^a orcid.org/0000-0002-6504-5846

DOI: <http://dx.doi.org/10.17515/resm2022.404ma0810>

Res. Eng. Struct. Mat. Vol. 8 Iss. 4 (2022) 643-658

known that the use of two dimensional (2D) nanofillers (sheets, platelets, or flakes) with high aspect ratio, significantly improves the thermal stability, mechanical and tribological properties of the composites [10, 11]. Since 2D nanofillers offer more contact area with polymer chains than 1D nanofillers, they show higher performance and are therefore more preferred in nanocomposites [12]. The previous studies revealed that good improvements in tensile strength, wear resistance and thermal stability of different polymers were obtained using 2D nanofillers in the structure such as graphene [12, 13], layered silicates [4, 14], layered double hydroxide [3, 15], hexagonal boron nitride [16], molybdenum disulfide [17, 18], α -zirconium phosphate [19, 20], and layered metal carbides [11, 21]. Feng et al. [22] have reported that the addition of 1.6 wt.% molybdenum disulfide (MoS_2) led to remarkably improved thermal stability of PP. In another work, Lonkar et al. [15] have demonstrated that organomodified layered double hydroxide (LDH) is highly effective at enhancing the elastic modulus and tensile strength of PP. They found that tensile strength and modulus of PP/LDH composite with 7 wt.% filler concentration was about 27% and 26% higher than pure PP, respectively. Sun et al. [19] have successfully synthesized α -zirconium phosphate (ZrP) nanoplatelets through a hydrothermal method and then used it to improve the mechanical and tribological performance of polyamide 66 (PA66). Compared to pure PA66, they achieved 10% improvement in tensile modulus and 14% increase in tensile strength in the nanocomposite with 1.0 wt.% ZrP nanoplatelet content. At this concentration, 43% reduction in the coefficient of friction and 59% reduction in the wear rate of the composites was observed. In the light of these studies, it has been well recognized that different nanoplatelet additives may have positive results on the mechanical and tribological properties of polymer nanocomposites because of their high aspect ratio, high specific surface area and thin laminated structure. As with other synthetic 2D nanofillers, SHP nanosheets are also likely to have positive effects on the thermal, mechanical and wear resistance properties of PP.

In this study, considering the above mentioned advantageous nanosheet structure, the possible contribution of SHP on the tribo-mechanical and thermal properties of PP composites were investigated. When the literature is searched, it is realized that there are a limited number of studies on SHPs. These studies cover X-ray diffraction (XRD) analysis of different strontium phosphate compound powders including α - and β - type for their value in the identification of phosphate materials [23], synthesis of β -type strontium hydrogen phosphate (β - SrHPO_4) nanosheets for using immobilization of lead ions from acidic aqueous solution [24], preparation of α - and β - SrHPO_4 nanoparticles via a polyol-mediated synthesis and their characterization using XRD and Fourier transform infrared spectroscopy (FTIR) [25], and lastly the synthesis of β - SrHPO_4 and determining the range of incorporation of calcium into the structure for biomedical applications [26]. Apart from above mentioned works, no study has been found in which SHPs are combined with a polymer matrix and their structural and mechanical properties are examined.

PP matrix was selected in current study because of its advantageous properties such as being suitable for melt-based production methods, chemical and dimensional stability, affordable cost, high wear resistance, and its recent applications with several nanofillers such as graphene, montmorillonite, layered double hydroxide, and carbon nanotubes [27, 28]. Firstly, SHPs were successfully synthesized by a hydrothermal process and then blended with PP using melt blending via a twin screw extruder. Maleic anhydride-grafted polypropylene (MAPP) was used as compatibilizer to enhance interfacial adhesion of the constituents one step further. The characterization of SHPs has been carried out through XRD, field emission scanning electron microscopy (FE-SEM), FTIR, and thermogravimetric analysis (TGA). The effect of SHPs on the mechanical properties of PP was determined using tensile, flexural and Shore D hardness tests. The thermal and tribological properties of the composites were evaluated by using TGA and ball-on disc wear test, respectively.

After all, failure modes and wear mechanisms of the samples were analyzed and explicated. This work puts forth an opinion, for the first time, about the thermal, mechanical and wear performance contribution of SHP within a polymeric matrix. Throughout the study, the main advantages and limitations of the composites have been highlighted with the hope that this will pave the way for further works on different properties of SHP reinforced composites.

2. Materials and Methods

2.1. Materials

Diammonium hydrogen phosphate ((NH₄)₂HPO₄) and cetyltrimethylammonium bromide (CTAB) was purchased from Sigma-Aldrich (USA). Strontium nitrate (Sr(NO₃)₂) was supplied from Tekkim (Turkey). All chemical reagents were used as received without further purification. Polypropylene (PP) - Ecolen HZ40P in pellet form was obtained from Hellenic Petroleum (Greece). It has a density and melt flow index of 0.90 g/cm³ (ASTM D792) and 12 g/10 min (2.16 kg, 230 °C, ASTM D1238), respectively. Maleic anhydride-grafted polypropylene (MAPP) in pellet form was provided from Sigma-Aldrich (USA) with a maleic anhydride content of 8-10 wt.%, a density of 0.93 g/cm³ and a melting point of 156 °C. Before using, PP and MAPP pellets were cut into granules with a size of about millimeter level using a chopper with milling blades to enhance the mixing efficiency during melt blending process. High-purity deionized water with a resistivity of 18.2 MΩ.cm (at 25 °C) was used in all procedures.

2.2. Synthesis of SHPs

Sr(NO₃)₂ and (NH₄)₂HPO₄ were used as starting materials for hydrothermal synthesis of SHPs. Firstly, 63 g of Sr(NO₃)₂ and 0.36 g of CTAB were dissolved in 400 ml deionized water under mechanical stirring for 20 min (solution A). Secondly, 33 g of (NH₄)₂HPO₄ was dissolved in 200 ml deionized water (solution B). Then A and B solutions were added to each other and stirred at room temperature (800 rpm for 20 min). The resulting suspension was kept in a pressure vessel at 90 °C for 6 h, and then left at room temperature for 12 h. The resulting white precipitate was filtered and washed with deionized water and ethanol several times. The obtained filter cake was dried in a static oven at 100 °C for 12 h, then ground, and sieved using a 45 μm sieve. β-SrHPO₄ platelets obtained were then stored in airtight plastic bags without applying any treatment, until they were dried for melt blending process. The above-mentioned process is the same as the protocol proposed by Zhuang et al. [24], but the quantities have been scaled up tenfold considering the amount of SHP required to produce the composites.

2.3. Production of PP/SHP Nanocomposites

Prior to the mixing step, PP, MAPP and SHPs were dried at 100 °C for 12 h to eliminate residual moisture. Four different SHPs content (1-3-5-7 wt.%) was used to produce PP/SHP nanocomposites. MAPP was added to the composites in the amount of 30% of the filler concentrations, as stated in Table 1. The copolymer/filler ratio is a suggested method to determine the amount of the required compatibilizer, and 30% ratio is taken from the literature [29]. The melt blending process was performed by using a laboratory type co-rotating twin screw extruder with a screw diameter of 12 mm, and a screw length (*L*) to diameter (*D*) ratio of 24 (Gulnar, Turkey). The barrel temperature profile of the extruder was set at 35-180-185-190-190-180 °C from the feeding zone to the die exit. The screw speed was fixed at 75 rpm. The rod-shaped composite product extruded from the die tip was hardened immediately by using a fan and chopped by an in-situ pelletizing unit. The obtained nanocomposite pellets were dried at a temperature of 100 °C for overnight to

remove the moisture content. The dried pellets then molded into the shape of test samples by an injection-molding machine (Xplore IM12, The Netherlands) with a barrel temperature of 200 °C. The mold temperature and injection pressure were 20 °C and 8 bars, respectively. For using as a control sample, pure PP was treated under the same conditions.

Table 1. The composition of the samples used in this study

Sample code	PP (wt.%)	MAPP (wt.%)	SHP (wt.%)
PP	100	0	0
PP/ 1SHP	98.7	0.3	1
PP/ 3SHP	96.1	0.9	3
PP/ 5SHP	93.5	1.5	5
PP/ 7SHP	90.9	2.1	7

2.4. Structural Characterization

XRD patterns of SHPs were measured by using Bruker AXS-D8 Advanced (Germany) diffractometer using CuK α radiation ($\lambda=1.5405$ Å) and 0.02° angle step. TGA measurements were carried out using Hitachi High-Tech STA7300 (Japan) under nitrogen atmosphere from ambient temperature up to 800 °C at a linear heating rate of 10 °C/min. PerkinElmer Spotlight 400 FTIR (USA) spectrometer was used to examine the functional groups vibrations of the SHPs at an optical resolution of 4 cm⁻¹. Morphology of the samples was investigated using Zeiss Gemini 500 FE-SEM (Germany) at 3.0 kV after sputter coated with gold for conductivity.

2.5. Mechanical Characterization

The tensile tests were performed using a tensile-compression test machine with 5 kN loading capacity (Devotrans GP/R/DNN/CKS-III, Turkey) according to ASTM D638. Tensile tests were carried out at 5 mm/min test speed using dog-bone shaped (type-V) samples. The flexural tests were carried out on the same machine according to ASTM D790 using a 2.54 mm/min cross-head speed. The dimension of the flexural samples was 125 mm in length, 12.7 mm in width and 3.2 mm in thickness, and a span of 55 mm was used in three-point bending mode. Shore D hardness measurements were also done according to ASTM D2240. At least four measurements were made for all tests and their averages and standard deviations were presented.

2.6. Wear Tests

Wear tests were performed on the cylindrical samples of 8 mm in thickness and 30 mm in diameter using a custom build ball-on-disc wear tester at dry sliding friction (ASTM G99). Tribo-tests were conducted at ambient temperature of 25 ± 2 °C and the humidity of 25%. In tests, the ball was loaded horizontally to the ground against a vertically rotating composite disc to reduce the wear debris and third-body abrasive wear effect, as shown in Fig. 1. Similar studies on different materials that used similar test configurations can be found in the literature [30-32]. This type of configuration reduces the debris in the wear track and therefore contributes to keep the wear mechanism unchanged [33]. The samples were polished one side up to R_a≈0.20 μm. ø5 mm Si₃N₄ balls were used as counterparts due to its high hardness and no chemical affinity for the materials tested. Before each test, the surface of the samples and balls were cleaned by using alcohol and dried carefully. The normal load was selected as 5 N, and the disc speed was selected as 1100 rpm which corresponds to 0.7 m/s sliding speed in the center of the wear track. Wear tests were ended

at 420 m sliding distance which corresponds to a 10 min test duration. The volume loss V (mm^3) and the wear rate K ($\text{mm}^3 \text{N}^{-1} \text{m}^{-1}$) of the samples were obtained from the Eq. 1 and Eq. 2, respectively [34]. Here, b and d are the track width and diameter (mm), respectively, r is the radius of the Si_3N_4 ball (mm), F is the vertical load (N), and S is the ball sliding distance (m). Wear track diameter was fixed at 12 mm in all the tests. The average wear track widths were calculated using the “trapezoidal area model” described elsewhere [35]. The steady-state coefficient of friction (CoF) values of the samples were also obtained from a load cell sensor and compared according to SHP concentration. After the test, worn surfaces of the samples were investigated with optical microscopy and their wear mechanisms were compared.

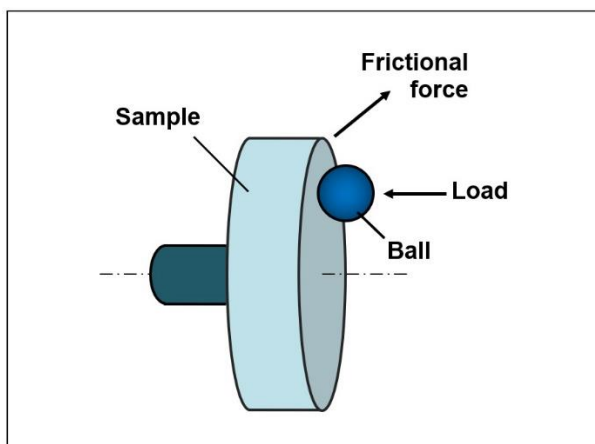


Fig. 1 Ball-on-disc test configuration

$$V = \left[\frac{\pi r^2}{180} \arcsin\left(\frac{b}{2r}\right) - \frac{b}{2} \sqrt{r^2 - \frac{b^2}{4}} \right] \pi d \quad (1)$$

$$K = \frac{V}{FS} \quad (2)$$

3. Results and Discussion

3.1. SHP Morphology and Structure

The XRD results revealed that SHPs successfully synthesized at high purity as seen in Fig. 2a. All the diffraction peaks of SHP were indexed according to the reported crystal structure of β - SrHPO_4 (JCPDS 12-0368) with hexagonal crystal structure and no foreign peak was detected. This result is in good agreement with the observations reported by Zhuang et al. [24]. The morphology of SHPs observed by SEM is composed of regular nanosheets as seen in Fig. 2b. The thickness of SHPs was in the range of 35-50 nm. FTIR spectra was used to confirm the presence of characteristic absorption bands of SHPs. The weak bands at 2998 cm^{-1} and 1785 cm^{-1} in Fig. 2c arise from the vibration of hydrogen bridge bonds. The peaks between 1300 cm^{-1} and 500 cm^{-1} are ascribed to $\nu(\text{PO}_4)$, $\delta(\text{PO}_4)$ and $\delta(\text{O-H})$ vibrations [25]. TGA is a tool to assess the thermal stability of a material by monitoring the mass loss during heating of a sample at controlled heating rate. The TGA and corresponding DTG curves of SHPs are shown in Fig. 2d. It is obvious that SHP

degrades mainly in two steps with maximum rates at 376 °C and 587 °C, according to following reactions [23]:



In the first degradation step, SHPs decompose into hydrated strontium pyrophosphate and water (Eq. 3). In the second step, dehydrated strontium pyrophosphate continues to decompose into β -strontium pyrophosphate and water (Eq. 4). According to the results, total weight loss till 800 °C is only 5.2% which indicates that SHP has a high thermal stability.

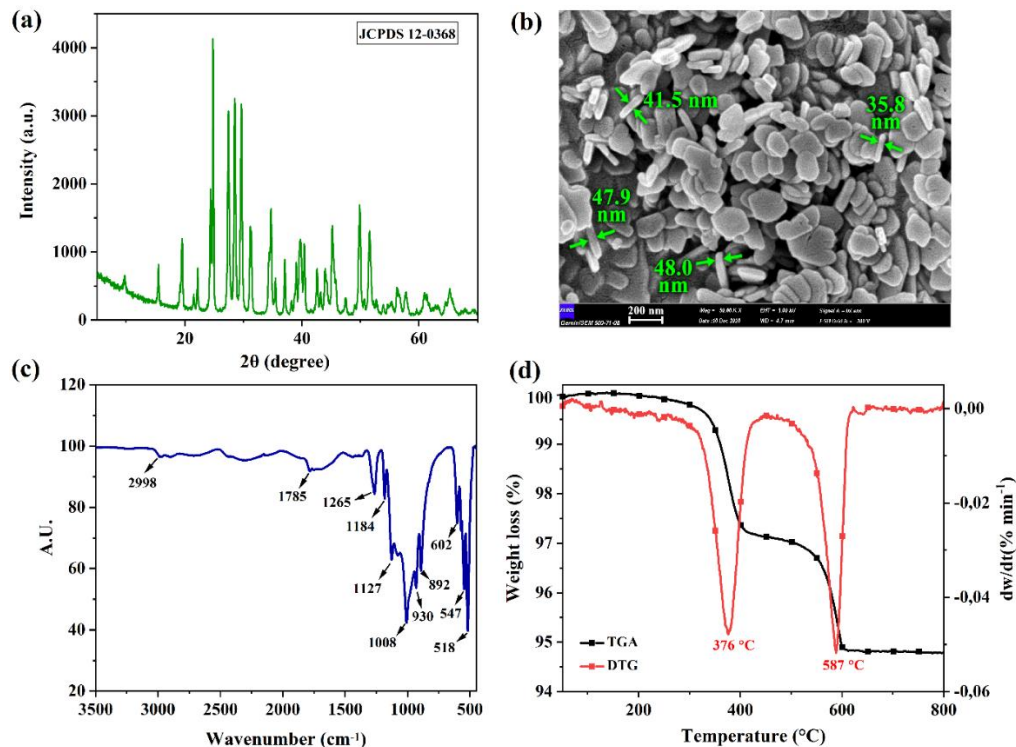


Fig. 2 (a) XRD pattern, (b) SEM image, (c) FTIR spectra, (d) TGA and DTG graphs of SHPs

3.2. Thermal Properties of PP/SHP Nanocomposites

One of the important features for the detection of the multifunctionality of polymer composites is thermal stability. TGA and dTGA curves of pure PP and PP/SHP nanocomposites are shown in Fig. 3a and Fig. 3b, respectively, and related data about residues and temperatures corresponding to 5% ($T_{5\%}$) and maximum degradation rates (T_{max}), which are used to evaluate the decomposition of the samples are summarized in Table 2. The pure PP only exhibits one step stage (at 457 °C) which is attributed to the decomposition of macromolecule chains [36]. The addition of SHPs was also found to have no effect on the thermal degradation profiles of the composites, and they showed one step mass loss stage with maximum rates at between 458 °C and 464 °C. However, the incorporation of SHPs leads to a slight shift toward higher $T_{5\%}$ and T_{max} values in comparison with that of pure PP. This behavior indicates that the addition of SHPs leads to

an improvement in thermal stability of PP/SHP nanocomposites. This is attributed to the barrier effect of the sheet structure of SHPs which reduces the heat conduction in the PP and inhibits the diffusion of the volatile degradation products from the polymer onto the gas phase [12, 13]. The char yield of PP/SHP nanocomposites was increased with identical filler content. As summarized in Table 2, PP showed a char residue of 3.07% at 800 °C, but PP/SHP nanocomposites showed an improvement in the char yield in the range of 43.9-73.8% compared to that of pure PP, possibly due to the catalytic carbonization effect of SHPs.

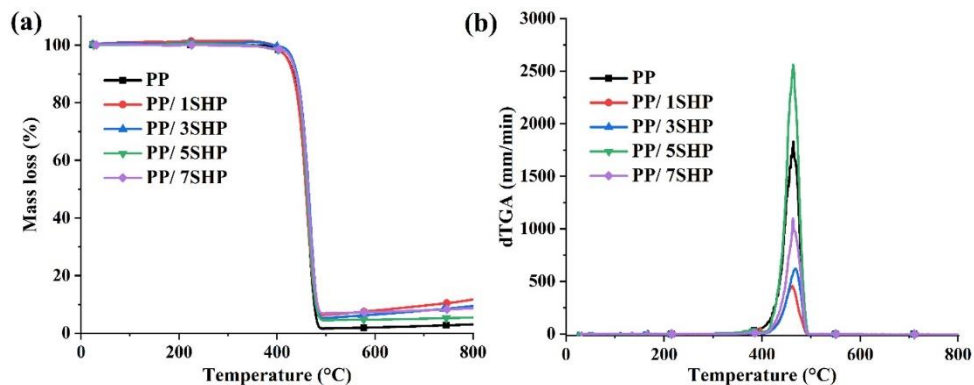


Fig. 3 (a) TGA and (b) dTGA curves of PP and PP/SHP nanocomposites

Table 2. TGA results of the samples

Sample code	$T_{5\%}$ (°C)	T_{max} (°C)	Char yield (%)
PP	418	457	3.07
PP/ 1SHP	421	458	11.73
PP/ 3SHP	429	464	9.57
PP/ 5SHP	428	460	5.48
PP/ 7SHP	428	463	8.72

3.3. Tensile and Flexural Properties of PP/SHP Nanocomposites

The morphological analysis of the fracture surface of PP/SHP nanocomposites with different SHP content is presented in Fig. 4. When SEM micrographs are examined, it is understood that there are different regions where SHPs are uniformly distributed and also coagulated in PP matrix. It was determined that the number of coagulated particles increased with the increase in SHP concentration in the composites. While the coagulated particles are few as seen in Fig. 4a-I, there can be tens of them as indicated by the purple arrows in Fig. 4b with the increase in SHP concentration. Despite the compatibilizer used, SHPs were tended to self-aggregate with the increase in concentration and form nano/micron sized particulates. This is a situation that may adversely affect the mechanical properties of PP/SHP nanocomposites. However, it is noteworthy that there is also a linear increase in the number of homogeneously distributed individual particles. Looking closely at micrographs, it is possible to see homogeneously dispersed particles in PP matrix for all concentrations as seen in Fig. 4b-II and as indicated by yellow arrows in Fig. 4d. Similar phenomena have been previously reported in studies using non-polar polymers [13]. Although various factors may be effective in the low mixing efficiency in polymer nanocomposites, the insufficient shear stresses in laboratory type twin screw extruders and screw configuration is considered one of the main reasons. Despite the partially poor dispersion of SHPs observed in all composites, it is understood that the use

of compatibilizer increases the adhesion efficiency of even coagulated particles with PP matrix by forming polymer branches adhering to particulates as seen in the detailed view in Fig. 4d-III.

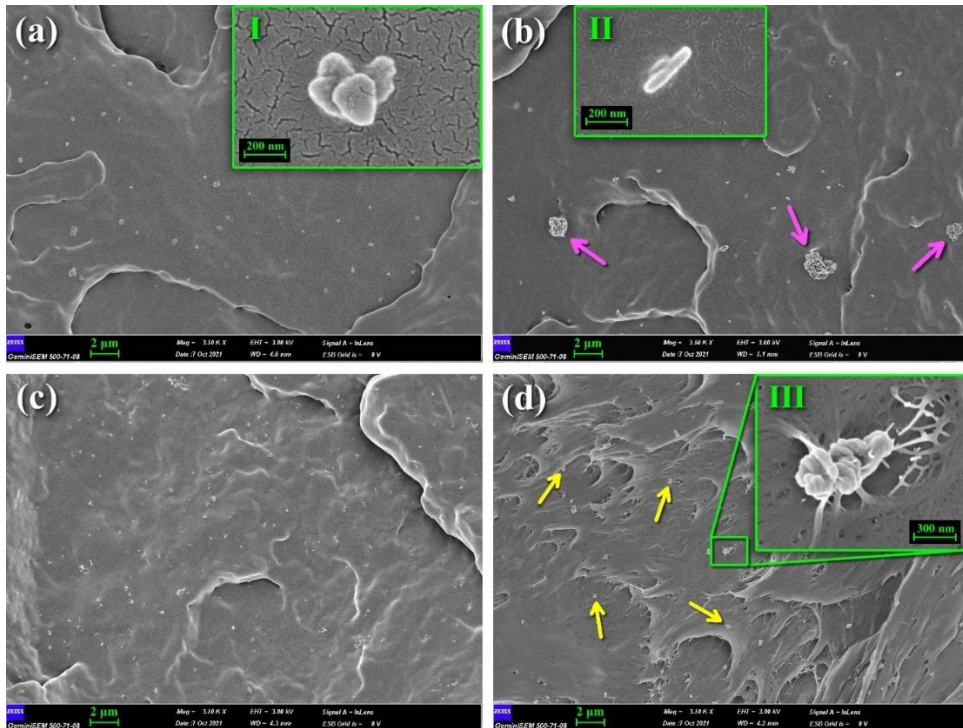


Fig. 4 SEM micrographs of the fracture surfaces of the nanocomposites: (a) PP/ 1SHP, (b) PP/ 3SHP, (c) PP/ 5SHP, and (d) PP/ 7SHP

Hardness is known as an important indicator of mechanical and wear behaviors of polymer composites. Shore D hardness values of pure PP and PP/SHP nanocomposites is given in Fig. 5. It was found that the hardness values of the nanocomposites were higher than that of pure PP for each filler content. It is already known that the addition of hard particles into a relatively soft structure will result in an increase in hardness and stiffness [37]. Although a linear increase was observed at low concentrations, no significant change was found after 3 wt.% SHP concentration. At 7 wt.% SHP content, the hardness of 73.1 Shore D was achieved. Considering the indentation depth and contact area of the Shore D tip used in the hardness measurement, it is understood that the particles are distributed homogeneously enough to affect the general rigidity of the structure, even if there is some agglomeration in the composite structure.

The tensile and flexural test graphs of the samples are given in Fig. 6, and related test data are summarized in Table 3. PP exhibited a tensile strength of 44.8 MPa, and a tensile modulus of 582.2 MPa. The incorporation of SHP into the structure caused an increase in tensile strength of the composites. The highest tensile strength value of 47.5 MPa was observed at 7 wt.% SHP content. At this concentration, the increase in tensile strength compared to the pristine polymer is about 6.0%. It is well known that relatively rigid structure of nanoparticles in a soft polymer matrix causes effects such as absorption of energy and prevention of crack formation, which has positive results on mechanical properties of the composites if the particle distribution is homogeneous and the adhesion

among the constituents is strong enough [21]. Moreover, large surface-active centers of SHPs cause more physical and chemical interactions with the matrix material [38].

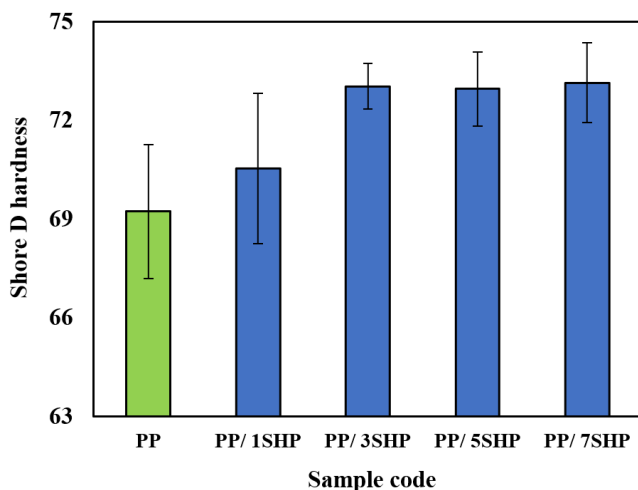


Fig. 5 Shore D hardness values of PP and PP/SHP nanocomposites

The increment in elastic modulus appeared in different magnitudes at various SHP concentration. It is thought that the reduction in exfoliation level and increase in rigid filler content compensate each other. The highest elastic modulus of 698.5 MPa was found at the composite with 1 wt.% SHP concentration. It is well known that the increment in elastic modulus is attributed to the high aspect ratio of nanofillers used in polymer nanocomposites. This behavior has been described in a similar study and explained by the two-dimensional geometry of nanosheets. Achaby and Qaiss [12] observed the same effect for graphene nanosheets in polyethylene matrix. Although there is no linear change according to the amount of reinforcement, it was determined that the elongation at break values decreased with the increase in stiffness in the composites compared to pure PP. Although the tensile strength increased, this caused the transition from ductile to brittle fracture. Conversely, ductile PP showed very high elongation value with the alignment of polymer chains along the longitudinal axis of the tensile test sample. The elongation at break of PP reduced from 615% to about 22% at 7 wt.% SHP concentration. Although no meaningful change was observed depending on the filler concentration, SHPs were seen to act as physical crosslinking points in polymer matrix and restrict the movement of PP chains, leading PP/SHP nanocomposites deformed in a brittle manner. A similar behavior was reported by Roserh et al. [39] where the percentage of elongation at break decreases with increasing graphite nanosheets content in PP matrix.

Table 3. Mechanical properties of the samples

Sample code	Tensile properties			Flexural properties		
	Tensile strength (MPa)	Tensile modulus (MPa)	Elongation at break (%)	Flexural strength (MPa)	Flexural modulus (MPa)	Elongation at break (%)
PP	44.8 ± 0.9	582.2 ± 26.4	614.9 ± 91.9	46.3 ± 1.4	1330.5 ± 105.0	-
PP/ 1SHP	46.4 ± 1.1	698.5 ± 43.6	20.5 ± 6.7	46.2 ± 1.0	1386.8 ± 58.8	-
PP/ 3SHP	45.8 ± 0.3	641.7 ± 41.6	23.0 ± 1.3	47.5 ± 0.4	1465.0 ± 113.4	-
PP/ 5SHP	45.5 ± 1.1	615.8 ± 112.2	20.0 ± 1.6	49.1 ± 1.2	1465.5 ± 142.1	-
PP/ 7SHP	47.5 ± 1.7	686.6 ± 123.4	22.4 ± 2.6	46.8 ± 2.7	1477.2 ± 76.2	-

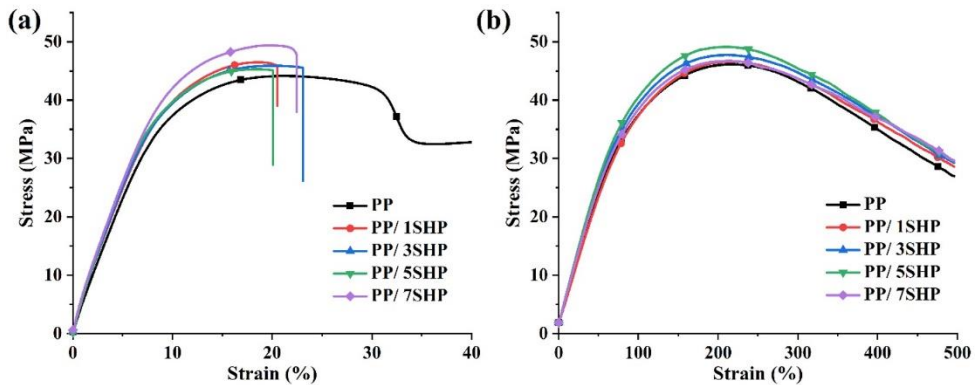


Fig. 6 (a) Tensile and (b) flexural stress-strain curves of PP and PP/SHP nanocomposites

Apart from the tensile test, flexural tests also give a good outlook on the mechanical properties of materials under the combination of tensile and compression loads. As seen in Fig. 6b, all samples reach a maximum loading capacity up to a certain strain value, and then the stress gradually decreases. The flexural strength and modulus values of PP are 46.3 MPa and 1330.5 MPa, respectively. No significant change was observed in the flexural strength of the composite with the addition of 1 wt.% SHP. After this concentration, flexural strength of the composites increased to a maximum value of 49.1 MPa for 5 wt.% SHP concentration. It is noteworthy that the flexural strength decreased again after this concentration. Although nano- and micro-agglomerations were evident from the SEM micrographs of the composites, SHPs were thought to show reinforcing effect and enhance the flexural strength of PP with the contribution of individual particulates homogeneously dispersed in the structure. In polymer composites, stress is transmitted from the matrix to the filler via interface; hence, good adhesion between the fillers and matrix allows for more efficient transfer of energy and leads to enhanced mechanical properties. The increase in flexural strength indicates that the efficient load transfer from the matrix to individual SHP particulates is occurred under the stress applied in the test. However, relatively dense characteristic of SHP due to the presence of metallic atoms in the structure adversely influences the final mechanical properties of the composites, thus an inhomogeneous stress distribution occurs within PP. This behavior was described by Zahibi and co-workers for 2D bauxite nanosheets in an epoxy matrix [5]. Flexural modulus of the composites were found to increase with filler concentration, and the highest modulus of about 1477 MPa was achieved at 7 wt.% SHP content. The composite elastic modulus is mainly dependent on the volumetric fraction of the filler in the composite, together with the intrinsic stiffness of the matrix and filler. The increment in the modulus is expected due to the high stiffness of the SHPs compared to pure PP. At the end of the flexural tests, none of the samples were broken within a 25 mm strain limit. During flexural test where the material is exposed to compression and shear forces in addition to tensile forces, the cracks do not exert such a key role as in the case of tensile test. As said before, decrease in the elongation at break values of PP/SHP nanocomposites arise from the fact that SHPs restrict the mobility of PP chains. In the light of these findings, the improvement both in the tensile and flexural strength of the composites can mainly attributed to the rigid 2D sheet nature of the filler. These observations are consistent with the conclusions found in previous studies [5, 10, 12, 17, 38]. It is also thought that the level of homogeneous distribution of individual particulates in the composite structure is responsible for the improvements observed at different SHP concentrations. However, along with the results obtained, there are other factors to be considered such as production method, surface treatment and concentration of the nanosheets. Although these issues still need to be explored, in

summary, tensile and flexural test results seem to be promising about the reinforcing potentiality of SHPs.

3.4. Wear Properties of PP/SHP Nanocomposites

CoF versus sliding time curves of the nanocomposites are shown in Fig. 7a. Average CoF values and wear rates of the samples with different SHPs concentrations are given in Fig. 7b and Fig. 7c, respectively. Fig. 7a indicates that all the CoFs reach nearly a steady state condition after about 200 s sliding time, which is corresponding to 140 m sliding distance. The characteristic structures of the CoF curves of the samples throughout the sliding distance were generally similar to each other, and no distinctive difference was observed. However, a slight fluctuation in the CoF curve of the sample containing 5 wt.% SHP is noticeable, and the highest CoF of 0.47 was reached at this concentration.

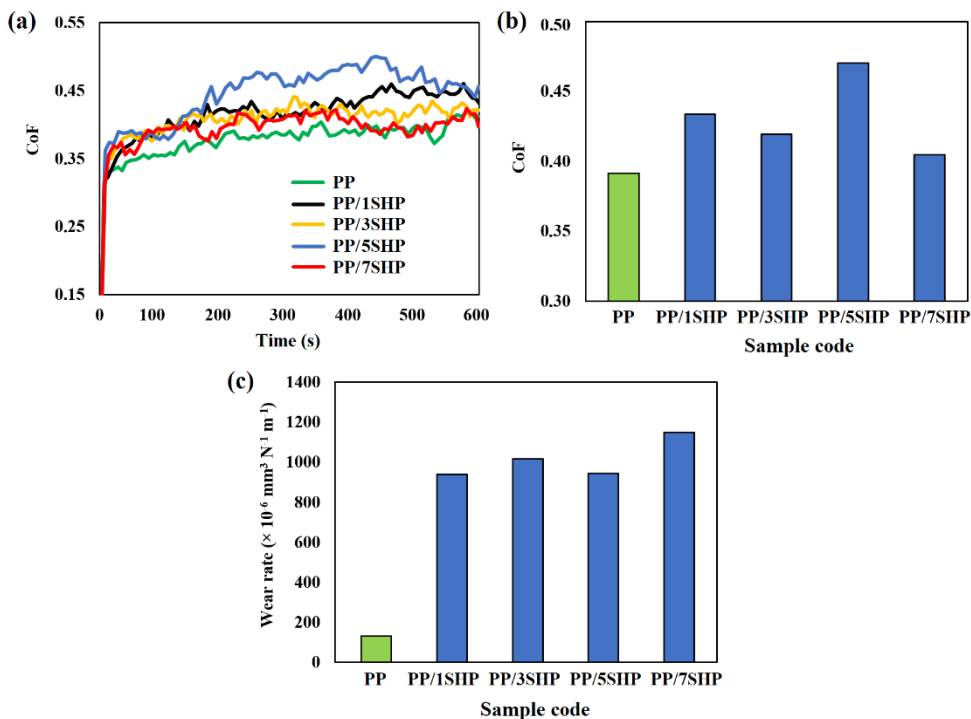


Fig. 7 (a) CoF versus sliding time curves, (b) average CoF, and (c) wear rate values of PP and PP/SHP nanocomposites

It is clearly seen in Fig. 7b and c that CoFs and wear rates of the nanocomposites are both higher than those of the pure PP. PP/ 7SHP showed the lowest CoF value of 0.40, but highest wear rate of $K = 1151 \times 10^{-6} \text{ mm}^3 \text{ N}^{-1} \text{ m}^{-1}$ among the composites tested. However, no meaningful change was observed in CoF and wear rates depending on the SHP concentration. There is generally a close relationship between mechanical properties and sliding wear resistance of polymer composites. If the strength and modulus of polymers are increased with reinforcements, improvement in wear resistance should also be expected [40]. However, the literature regarding the wear mechanisms of nanoplatelet reinforced composites has been quite scarce. While the wear resistance of particulate reinforced polymer composites improves with good interfacial bonding between filler and matrix, it can vary with the volume fraction of fillers depending on the filler and matrix type.

In addition, polymers have different wear characteristics from metals and ceramics due to their viscoelastic nature and their ability to transfer material easily to the counterparts [41]. In polymer composites, fillers are also included in this phenomenon and may show abrasive effect depending on sliding conditions as stated before. This explains why the wear rates of the composites are higher compared to that of pure PP.

Worn surfaces of the samples are shown in Fig. 8. Some color adjustments were made on the images to expose the wear tracks clearly. It is seen that the worn area in contact with the ball is much rougher than the unworn sample surface, due to micro-plowing and micro-cutting actions formed by abrasion. It was also found that micro and macro size scratches were observed in the sliding direction of the ball in all samples because of the same abrasive wear mechanism. In addition, the stuck wear debris was found on the wear tracks of the samples despite the vertical configuration of the test rig. Although the wear tracks of the samples had similar longitudinal scratches, signs of plastic deformation and adhesive wear were also observed. However, when the SHP concentration is taken into consideration, it is seen that there are certain changes in the wear characteristics of the nanocomposites. It is obvious from Fig. 8d and Fig. 8e that adhesive wear and plastic deformation observed especially at the edges of the wear tracks at higher SHP concentrations (5 and 7 wt.%). In polymer composites, beside adhesive and abrasive wear mechanisms, the fatigue wave or crack formation is another wear phenomenon. Such findings are often seen due to fatigue wear caused by repeated cycles of an asperity of the counter material on the worn surface. Fatigue wear also increases with increasing stress or defect concentration on the sample [42].

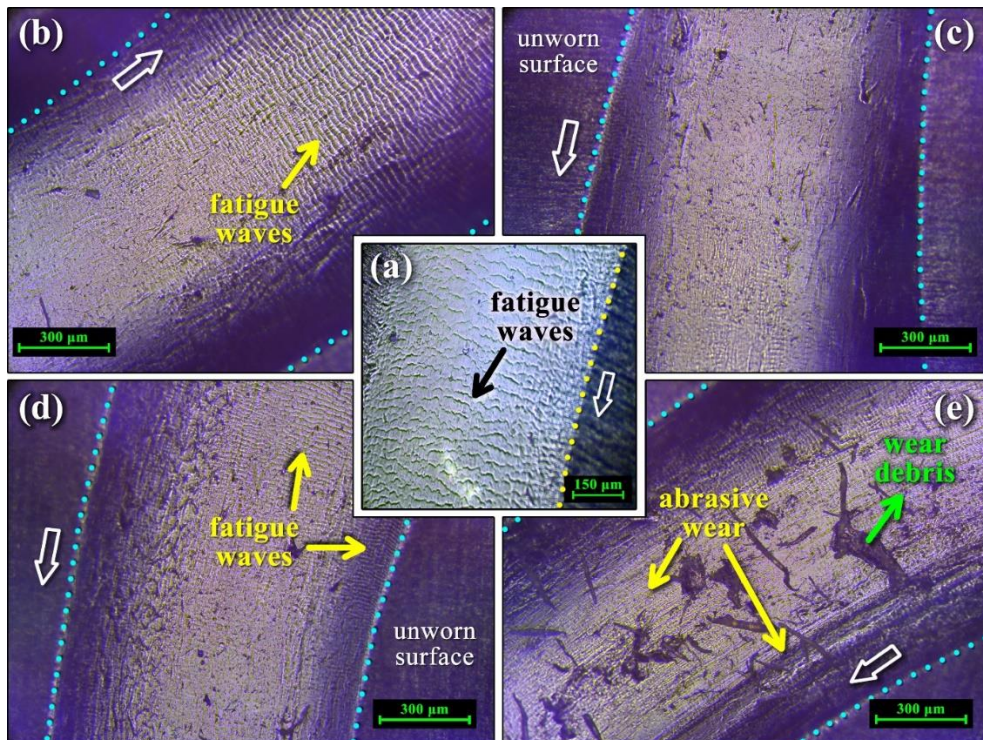


Fig. 8 Optic microscope images of the worn surface of pure PP and the nanocomposite samples: (a) PP, (b) PP/ 1SHP, (c) PP/ 3SHP, (d) PP/ 5SHP, and (e) PP/ 7SHP (the blank arrows indicate the sliding direction of the ball)

Looking closely at Fig. 8a, Fig. 8b and Fig. 8c, while many fatigue waves are observed in PP, PP/ 1SHP and PP/ 3SHP samples, it is seen that they decrease in higher SHP concentrations. In addition, segments where the transition from fatigue wear to abrasive wear occurred in different parts of the wear track were determined in all samples. On the other hand, it has been found that abrasive wear and micro-scratches are dominant due to the relatively higher rigidity of the nanocomposites at higher filler concentrations originating from SHP. As stated before, it is clear that rigid SHP as the third-body element in the wear system increases the wear rate due to the abrasive wear effect with micro-cutting and micro-plowing actions.

4. Conclusions

After SHPs were synthesized by hydrothermal method, PP/SHP composites were successfully produced via melt blending technique for the first time. The effects of filler concentration on the thermal, mechanical and tribological properties of the composites have led to the following conclusions:

- SHPs are conducive to improving the thermal stability of PP/SHP composites. With the loading of 3 wt.% SHPs, $T_{5\%}$ and T_{max} values of the composites were increased by 11 °C and 7 °C, respectively, compared to pure PP. In addition, introduction of SHPs clearly enhanced the residue formation of PP/SHP composites.
- SHPs in PP also showed a noticeable difference in mechanical properties of the samples, even if coagulated particulates are seen in the structure. The highest tensile and flexural strengths of 47.5 and 49.1 MPa was achieved at the composites with 7 and 5 wt.% SHP concentration, respectively.
- In addition, an increase was observed in elastic modulus of the composites compared to pure PP. The improvement in mechanical properties is thought to be due to the rigid 2D structure of SHPs which leads to more contact area with polymer chains and leads to higher resistance especially against compression load, even at high agglomeration rates.
- From the wear test results, the transition from fatigue wear to abrasive wear was observed after 3 wt.% SHP concentration due to the increase in composite hardness. The high rigidity of SHP compared to the pure polymer increased the micro-plowing phenomenon in contact with the counter material. Therefore, an increase was observed in the CoF and wear rates of the composites, independent of the SHP concentration. However, it is thought that the high resistance to fatigue wear obtained at high SHP concentrations may be advantageous for different applications.

Acknowledgement

This work is supported by Erciyes University Scientific Research Unit under grant no BAP-FKB-2020-9952.

References

- [1] Bhattachary M. Polymer nanocomposites-A comparison between carbon nanotubes, graphene, and clay as nanofillers. *Materials*, 2016; 9(4): 262. <https://doi.org/10.3390/ma9040262>
- [2] Brevnov PN, Kirsankina GR, Zabolotnov AS, Krashennnikov VG, Grinev VG, Berezkina NG, Sinevich EA, Shcherbina MA, Novokshonova LA. Synthesis and properties of nanocomposite materials based on ultra-high-molecular-weight polyethylene and

- graphite nanoplates. *Polymer Science, Series C*, 2016; 58: 38-49. <https://doi.org/10.1134/S1811238216010021>
- [3] Mochane MJ, Magagula SI, Sefadi JS, Sadiku ER, Mokhena TC. Morphology, Thermal Stability, and Flammability Properties of Polymer-Layered Double Hydroxide (LDH) Nanocomposites: A Review. *Crystals*, 2020; 10(7): 612. <https://doi.org/10.3390/cryst10070612>
- [4] Rathod V, Kumar JS, Jain A. Polymer and ceramic nanocomposites for aerospace applications. *Applied Nanoscience*, 2017; 7: 519-548. <https://doi.org/10.1007/s13204-017-0592-9>
- [5] Zabihi O, Ahmadi M, Ferdowsi MRG, Li Q, Fakhrhoseini SM, Mahmoodi R, Ellis AV Naebe M. Natural bauxite nanosheets: A multifunctional and sustainable 2D nano-reinforcement for high performance polymer nanocomposites. *Composites Science and Technology* 2019; 184: 107868. <https://doi.org/10.1016/j.compscitech.2019.107868>
- [6] Saxena N. Thermal and mechanical behavior of polymer nano-composite. *Journal of Polymer Engineering*, 2010; 30: 575-586. <https://doi.org/10.1515/POLYENG.2010.30.9.575>
- [7] Gharabaghi H, Rafizadeh M, Taromi FA. Synthesis of exfoliated PA66 nanocomposites via interfacial polycondensation: effect of layered silicate and silica nanoparticles. *Bulletin of Materials Science*, 2016; 39: 935-941. <https://doi.org/10.1007/s12034-016-1228-5>
- [8] Yetkin SH. Tribological properties of compatibilizer and graphene oxide-filled polypropylene nanocomposites. *Bulletin of Materials Science*, 2020; 43: 89. <https://doi.org/10.1007/s12034-020-2061-4>
- [9] Jordan J, Jacob KI, Tannenbaum R, Sharaf MA, Jasiuk I. Experimental trends in polymer nanocomposites-a review. *Materials Science and Engineering A*, 2005; 393: 1-11. <https://doi.org/10.1016/j.msea.2004.09.044>
- [10] Varghese AM, Singh S, Rangaraj VM Mittal V. Two-dimensional mullite nanostructure: Synthesis and reinforcement effect on polypropylene/maleic anhydride graft ethylene vinyl acetate matrix. *Journal of Applied Polymer Science*, 2019; 136: 48233. <https://doi.org/10.1002/app.48233>
- [11] Xu Z, Shen X, Wang T, Yang Y, Yi J, Cao M, Shen J, Xiao Y, Guan J, Jiang X, Tang B, Li H. Investigation on tribological and thermo-mechanical properties of Ti3C2 nanosheets/epoxy nanocomposites *ACS Omega*, 2021; 43: 29184-29191. <https://doi.org/10.1021/acsomega.1c04620>
- [12] Achaby ME, Qasis A. Processing and properties of polyethylene reinforced by graphene nanosheets and carbon nanotubes. *Materials and Design*, 2013; 44: 81-89. <https://doi.org/10.1016/j.matdes.2012.07.065>
- [13] Li CQ, Zha JW, Long HQ, Wang SJ, Zhang DL, Dang ZM. Mechanical and dielectric properties of graphene incorporated polypropylene nanocomposites using polypropylene-graft-maleic anhydride as a compatibilizer. *Composites Science and Technology*, 2017; 153: 111-118. <https://doi.org/10.1016/j.compscitech.2017.10.015>
- [14] Burmistr MV, Sukhyy KM, Shilov VV, Pissis P, Spanoudaki A, Sukha IV, Tomilo VI, Gomza YP. Synthesis, structure, thermal and mechanical properties of nanocomposites based on linear polymers and layered silicates modified by polymeric quaternary ammonium salts (ionenes). *Polymer*, 2005; 46: 12226-12232. <https://doi.org/10.1016/j.polymer.2005.10.094>
- [15] Lonkar SP, Therias S, Leroux F, Gardette JL, Singh RP. Thermal, mechanical, and rheological characterization of polypropylene/layered double hydroxide nanocomposites. *Polymer Engineering and Science*, 2012; 52: 2006-2014. <https://doi.org/10.1002/pen.23147>
- [16] Chen L, Chen B, Li J, Tong X, Zhao H, Wang L. Enhancement of mechanical and wear resistance performance in hexagonal boron nitride-reinforced epoxy nanocomposites. *Polymer International*, 2017; 66: 659-664. <https://doi.org/10.1002/pi.5296>

- [17] Feng X, Xing W, Liu J, Qiu S, Hu Y, Liew KM. Reinforcement of organo-modified molybdenum disulfide nanosheets on the mechanical and thermal properties of polyurethane acrylate films. *Composites Science and Technology*, 2016; 137: 188-195. <https://doi.org/10.1016/j.compscitech.2016.11.002>
- [18] Wadi VS, Jena KK, Haliq K, Alhassan SM. Enhanced mechanical toughness of isotactic polypropylene using bulk molybdenum disulfide. *ACS Omega*, 2020; 5: 11394-11401. <https://doi.org/10.1021/acsomega.0c00419>
- [19] Sun H, Fang Z, Li T, Lei F, Jiang F, Li D, Zhou Y, Sun D. Enhanced mechanical and tribological performance of PA66 nanocomposites containing 2D layered α -zirconium phosphate nanoplatelets with different sizes. *Advanced Composites and Hybrid Materials*, 2019; 2: 407-422. <https://doi.org/10.1007/s42114-019-00100-z>
- [20] Zhang R, Hu Y, Li B, Chen Z, Fan W. Studies on the preparation and structure of polyacrylamide/ α -zirconium phosphate nanocomposites. *Journal of Materials Science*, 2007; 42: 5641-5646. <https://doi.org/10.1007/s10853-006-0629-z>
- [21] Zhang H, Wang L, Chen Q, Li P, Zhou A, Cao X, Hu Q. Preparation, mechanical and anti-friction performance of MXene/polymer composites. *Materials and Design*, 2016; 92: 682-689. <https://doi.org/10.1016/j.matdes.2015.12.084>
- [22] Feng X, Wang B, Wang X, Wen P, Cai W, Hu Y, Liew KM. Molybdenum disulfide nanosheets as barrier enhancing nanofillers in thermal decomposition of polypropylene composites. *Chemical Engineering Journal*, 2016; 295: 278-287. <https://doi.org/10.1016/j.cej.2016.03.059>
- [23] Ropp RC, Aia A, Hoffman CWW, Veleker TJ, Mooney RW. X-Ray powder diffraction patterns of strontium phosphates. *Analytical Chemistry*, 1959; 31: 1163-1166. <https://doi.org/10.1021/ac60151a026>
- [24] Zhuang FQ, Tan RQ, Shen WF, Zhang XP, Xu W, Song WJ. Synthesis of β -type strontium hydrogen phosphate nanosheets and its immobilization of Pb^{2+} in acidic aqueous solution. *Acta Metallurgica Sinica*, 2015; 28(4): 438-443. <https://doi.org/10.1007/s40195-015-0214-z>
- [25] Roming M, Feldmann C. Selective synthesis of α - and β -SrHPO₄ nanoparticles. *Journal of Materials Science*, 2008; 43: 5504-5507. <https://doi.org/10.1007/s10853-008-2830-8>
- [26] Boanini E, Gazzano M, Rubini K, Mazzeo PP, Bigi A. Structural interplay between strontium and calcium in α -CaHPO₄ and β -SrHPO₄. *Ceramics International*, 2021; 47: 24412-24420. <https://doi.org/10.1016/j.ceramint.2021.05.156>
- [27] Shi Y, Liu C, Liu L, Fu L, Yu B, Lv Y, Yang F, Song P. Strengthening, toughening and thermally stable ultra-thin MXene nanosheets/ polypropylene nanocomposites via nanoconfinement. *Chemical Engineering Journal*, 2019; 378: 122267. <https://doi.org/10.1016/j.cej.2019.122267>
- [28] Shubhra QTH, Alam AKMN, Quaiyyum MA. Mechanical properties of polypropylene composites: A review. *Journal of Thermoplastic Composite Materials*, 2011; 26: 362-391. <https://doi.org/10.1177/0892705711428659>
- [29] El-Sabbagh A. Effect of coupling agent on natural fibre in natural fibre/polypropylene composites on mechanical and thermal behaviour. *Compos Part B - Engineering*, 2014; 57: 126-135. <https://doi.org/10.1016/j.compositesb.2013.09.047>
- [30] Liu T, Wood W, Li B, Lively B, Zhong W-H. Effect of reinforcement on wear debris of carbon nanofiber/high density polyethylene composites: Morphological study and quantitative analysis. *Wear*, 2012; 294-295: 326-335. <https://doi.org/10.1016/j.wear.2012.07.010>
- [31] Prasad BK. Sliding wear behaviour of bronzes under varying material composition, microstructure and test conditions. *Wear*, 2004; 257: 110-123. <https://doi.org/10.1016/j.wear.2003.10.021>

- [32] Zhang LC, Zarudi I, Xiao KQ. Novel behaviour of friction and wear of epoxy composites reinforced by carbon nanotubes. *Wear*, 2006; 261: 806-811. <https://doi.org/10.1016/j.wear.2006.01.033>
- [33] Devaraju A, Perumal AE, Alphonsa J, Kailas SV, Venugopal S. Sliding wear behavior of plasma nitrided austenitic stainless steel type AISI 316LN in the temperature range from 25 to 400 °C at 10⁻⁴ bar. *Wear*, 2012; 288: 17-26. <https://doi.org/10.1016/j.wear.2012.03.002>
- [34] Taktak S, Akbulut H. Dry wear and friction behaviour of plasma nitrided Ti-6AL-4 V alloy after explosive shock treatment. *Tribology International*, 2007; 40: 423-432. <https://doi.org/10.1016/j.triboint.2006.02.060>
- [35]avaş S, Al-Obaidi A. Influence of PP-g-MA compatibilization on the mechanical and wear properties of polypropylene/thermoplastic polyurethane blends. *Tribology Transaction*, 2018; 61: 754-764. <https://doi.org/10.1080/10402004.2017.1406173>
- [36] Yuan B, Hu Y, Chen X, Shi Y, Niu Y, Zhang Y, He S, Dai H. Dual modification of graphene by polymeric flame retardant and Ni (OH)₂ nanosheets for improving flame retardancy of polypropylene. *Composites Part A*, 2017; 100: 106-117. <https://doi.org/10.1016/j.compositesa.2017.04.012>
- [37] Fu SY, Feng XQ, Lauke B, Mai YW. Effects of particle size, particle/matrix interface adhesion and particle loading on mechanical properties of particulate-polymer composites. *Composites Part B: Engineering*, 2008; 39: 933-961. <https://doi.org/10.1016/j.compositesb.2008.01.002>
- [38] Wang Y, Gao J, Ma Y, Agarwal US. Study on mechanical properties, thermal stability and crystallization behavior of PET/MMT nanocomposites. *Composites Part B*, 2006; 37: 399-407. <https://doi.org/10.1016/j.compositesb.2006.02.014>
- [39] Roserh D, Gribbe GA, Luinstra GA. Graphite nanosheets-polypropylene composites from in toluene delaminated graphite using atactic polypropylene as dispersant. *Composites Science Technology*, 2018; 156: 28-38. <https://doi.org/10.1016/j.compscitech.2017.12.023>
- [40] Morioka Y, Tsuchiya Y, Shioya M. Correlations between the abrasive wear, fatigue, and tensile properties of filler-dispersed polyamide 6. *Wear*, 2015; 338: 297-306. <https://doi.org/10.1016/j.wear.2015.07.003>
- [41] Österle W, Dmitrev AI, Wetzel B, Zhang G, Häusler I, Jim BC. The role of carbon fibers and silica nanoparticles on friction and wear reduction of an advanced polymer matrix composite. *Materials Design*, 2016; 93: 474-484. <https://doi.org/10.1016/j.matdes.2015.12.175>
- [42] Myshkin NK, Petrokovets MI and Kovalev AV. Tribology of polymers: Adhesion, friction, wear, and mass-transfer. *Tribology International*, 2005; 38: 910-921. <https://doi.org/10.1016/j.triboint.2005.07.016>



Research Article

Influence of multi-walled carbon nanotubes on tensile and flexural properties of polyamide 66/short glass fiber composites

Özgür Demircan*^{1,2,a}, Fatma Burcu Uzunoğlu^{2,b}, Naser Rezaei Ansaroudi^{1,c}

¹Department of Metallurgical and Material Engineering, Ondokuz Mayıs University, Samsun, Turkey

²Department of Nanoscience and Nanotechnology, Ondokuz Mayıs University, Samsun, Turkey

Article Info

Article history:

Received 07 Jun 2022

Revised 27 Jul 2022

Accepted 10 Aug 2022

Keywords:

Composite material;
Thermoplastics;
Polymer
Nanocomposite;
Polyamide 66; Glass
fiber; Carbon nanotube;
Plastic injection
moulding

Abstract

In this study, influence of multi-walled carbon nanotubes (MWCNTs) on tensile and flexural behaviour of 15% short glass fiber (SGF) reinforced Polyamide 66 (PA 66/15SGF) and 30% short glass fiber reinforced Polyamide 66 (PA 66/30SGF) is investigated. Test specimens composed of neat PA 66, PA 66/15SGF, PA 66/30SGF and PA 66/30SGF/MWCNTs are produced using plastic injection moulding machine; and their tensile and flexural properties are characterized. The effects of MWCNTs contents on the micro-structure and morphology of the composites were investigated by using a scanning electron microscope (SEM), fourier transform infrared spectroscopy analysis (FTIR) and optical microscopy (OM). Mechanical analyses reveal that neat PA 66 exhibits the lowest elastic modulus, 2.11 GPa, and tensile strength, 60.61 MPa, while the highest tensile modulus, 4.69 GPa, and strength, 87.05 MPa, are exhibited by PA 66/30SGF/MWCNT and PA 66/30SGF, respectively. In other words, with the addition of MWCNT, tensile strength of PA 66/30SGF decreases by 13.4 % whereas the elastic modulus increases by nearly 4.7 %. In addition, flexural test results shows that the integration of MWCNTs improves the flexural strength and flexural modulus of PA 66/30SGF by 1% and 12%, respectively.

© 2022 MIM Research Group. All rights reserved.

1. Introduction

Thermoplastics are commonly used in both commodity and industrial applications covering many industrial fields such as automobile, aeronautic and aviation, defence, sports industry and so forth [1, 2]. Some thermoplastics are considered to be suitable substitutes for metallic materials in industrial applications [3]. However, in spite of their advantages, thermoplastic materials may become deformed during the use or production [4]. In order to avoid these deformations and to increase their mechanical performance, thermoplastics can be filled with microscale or nanoscale reinforcing materials such as carbon fibers (CF), glass fibers (GF), carbon nanotubes (CNTs), nanoclays and so on [5, 6].

Being a thermoplastic, Polyamide 66 (PA 66) is one of the most outstanding materials used as engineering resin owing to its good mechanical, chemical and thermal performance [7, 8]. Apart from neat PA 66, there are various types of polyamides reinforced with materials such as glass fibers. The addition of glass fibers is known to increase the mechanical properties of polyamide-matrix composites [9-17]. The main factors determining the tensile properties of PA 66/GF composites are fiber fracture, diameter, length, orientation and interfacial strength [18-21]. In addition, production parameters such as mold temperature, injection pressure and speed may affect the mechanical properties of the polymer matrix composite materials [22, 23]. Recently, nanomaterials too have been used as reinforcement; and one of the most prominent of them are carbon nanotubes [24-26]. In terms of their forms, CNTs are categorized as single-walled carbon nanotubes (SWCNTs)

*Corresponding author: ozgur.demircan@omu.edu.tr

^a orcid.org/0000-0001-8235-3966 ; ^b orcid.org/0000-0002-4197-785X; ^c orcid.org/0000-0001-9933-9706
DOI: <http://dx.doi.org/10.17515/resm2022.443ma0607>

[27] and multi-walled carbon nanotubes (MWCNTs) [28]. The use of MWCNTs as nanofillers is due to their superior mechanical properties such as very high tensile strength varying between 11-63 GPa [29] and Young's modulus, which is approximately 1 TPa [29, 30]. However, polymer matrices have drawn more attention in industrial applications owing to their light weight, easy machinability and production costs [31-34].

A number of theoretical and experimental studies have been carried out to date regarding CNTs/polymer composites [35-48]. Majority of these studies indicate that CNTs are able to improve the mechanical properties of polymer matrix composite systems. Coleman et al. [25], Miyagawa et al. [49] and F.S.A. Khan et al. [48] provided comprehensive reviews on the mechanical reinforcement of polymers by the use CNTs. It is suggested that well-dispersion of nano materials is an important parameter controlling the efficiency of load transfer and hence determining some of the mechanical properties [50]. Therefore, CNT-polymer matrix interaction and crack behaviour of CNTs/polymer composites have been the subjects of several studies [51-56]. Ajayan et al. [57] examined morphology of fractured epoxy/SWCNTs composites by SEM and observed SWCNTs stretching across a crack opening in the epoxy resin. Liu et al. [58] investigated the morphology and mechanical properties of MWCNTs-reinforced Polyamide 6 (PA 6) composites. The authors reported a 26% reduction in tensile strength, which was explained by the brittleness of polymer matrix after the addition MWCNTs. Ferreira et al. [59] explored that addition of CNTs significantly improves the tensile strength and elastic modulus of PA 6/CNTs composites. Chopra et al. [60] studied PA 6/MWCNTs nanocomposites and reported that the presence of MWCNTs increases the tensile strength of Polyamide 6 by nearly 12%. Similarly, Kartel et al. [61] studied the tensile properties of PA 6/CNTs composites and reported that the tensile strength of the composite exhibits non-linear dependence behaviour by the addition of CNTs up to 0.5 wt.%. The mechanical tests performed by them showed that the PA 6 matrix composites incorporating 0.25 wt. % CNTs exhibit the highest tensile strength.

Although a great number of studies on CNTs/polymer composites are available in literature, there are not sufficient amount of studies focusing on the composites reinforced with the combination of short fibers and nanofillers [62, 63]. Therefore, the full potential of nanofillers and the properties of their combinations with other reinforcement materials, such as glass fibers, have not fully become known yet. This paper aims to introduce the tensile and flexural properties of MWCNTs-integrated Polyamide 66/short glass fiber nanocomposites so that the results obtained from this study can be used in designing new thermoplastic composites with MWCNTs.

2. Experimental

2.1. Composite Constituents

Neat PA 66, 15 wt. % short fiber glass reinforced PA 66 (PA 66/15SGF) and 30 wt. % short fiber reinforced PA 66 (PA 66/30SGF) granules (Mat Polymer, Istanbul/Turkey) were used as polymer materials in composite. MWCNTs, which were obtained from the manufacturer, (Ege Nanotek Kimya Sanayi, Izmir/Turkey) were used as nano reinforcements in composites (Table 1).

2.2. Fabrication Method

Figure 1 (a) to (h) shows the preparation process of the PA 66/30SGF/MWCNTs composite. The plastic injection machine was used to produce the test specimens. The granules were fed to the machine via a hopper and then pushed towards the nozzle by a rotating screw in the hot resistances. The temperature in the resistances which was nearly 285°C and the rotary motion of the screw facilitated PA 66/SGF granules to melt and

adequately mix with MWCNTs. Once this melted mixture reached the nozzle, it was injected into the moulds being hold between two clamps and took its final shape.

Table 1. Properties of MWCNTs

Parameter	Value
Purity (%)	>95 % (CNT) >97 % (C)
Outer diameter (nm)	10-20
Interior diameter (nm)	5-10
Length (μm)	10-30
Surface area (m^2/g)	>200
Colour	Black
Ash	Mass < % 1.5
Electrical conductivity (S/cm)	>100
Density (tap) (g/cm^3)	0.22
Density (true) (g/cm^3)	2.1



Fig. 1 Preparation process of PA 66/30SGF/MWCNT composite specimens

2.3. Characterization

Four types of specimens in accordance with ISO 527-2 type-1A and ISO 178 standards were produced by plastic injection moulding machine. A JSM-7001 F machine was used to characterize scanning electron microscope (SEM) (Japan) properties. Tensile and flexural properties of the specimens were examined using Instron 5982 100 KN (USA) test machine at room temperature with a crosshead speed of 5mm/min. Mechanical tests and specimens are shown in Figure 2 (a) to (d).



Fig. 2 Mechanical tests and specimens: (a) tensile test; (b) tensile test specimens in accordance with ISO 527-2 type-1A standard; (c) 3-point flexural test; (d) flexural test specimens in accordance with ISO 178 standard

3. Results and Discussion

3.1. Chemical Analysis

The aim of analyzing the molecular configuration of PA 66 by means of Fourier transform infrared (FTIR) spectroscopy is to correlate the structures to the performance properties of the final product. With sufficient knowledge about the chemical structure, polymerization reaction can be controlled and hence good performance properties can be achieved. Upon this purpose, FTIR spectra of neat PA66, PA 66/15SGF, PA 66/30SGF and PA 66/30SGF/MWCNT composites were measured and are shown in Figure 3. Due to very small weight fraction of MWCNTs in the composite and the affinity in chemical compositions of PA 66 and MWCNTs, the signature region did not exhibit a notable

difference. In neat PA 66, the absorption band at 3267 cm^{-1} is attributed to the stretching vibrations of N-H group. The absorption bands at 2912 cm^{-1} , 2843 cm^{-1} and 1192 cm^{-1} result from the symmetric and asymmetric C-H stretch vibrations and C-H twisting. The data obtained from FTIR analysis confirmed the chemical structure of PA 66 and PA 66/GF. Similar results were obtained by several researchers [64-66].

In this study, FTIR spectra of the composite specimens showed no significant change with regard to chemical composition of the constituent, which means that there are only physical interactions between the constituents. However, owing to the high-temperature (nearly 285°C) and the rotary motion of the screw in the hot resistances of plastic injection machine, chemical interactions between the constituents might occur as well [67].

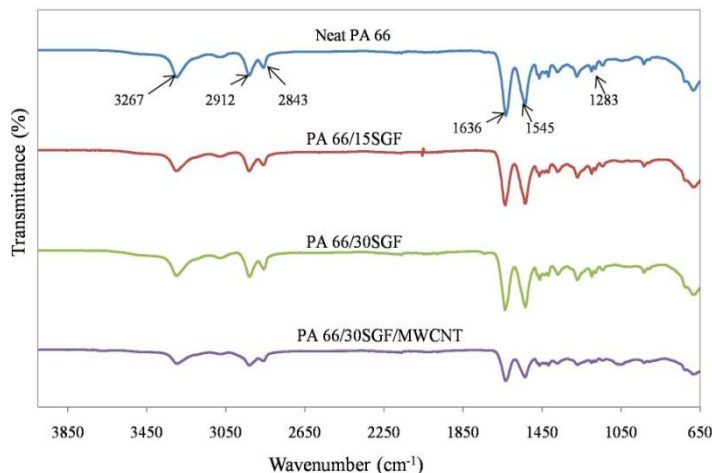


Fig. 3 FTIR spectra of the composite specimens

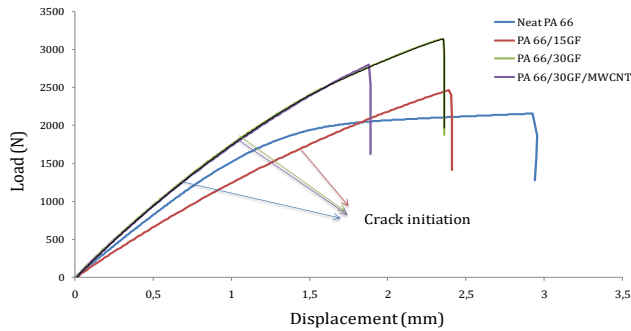
3.2 Tensile Test Results

Figure 4 (a) to (c) represent the load-displacement curves, stress-strain curves during tensile tests and the tensile test results of the composites, respectively. PA 66/30SGF exhibits the highest tensile strength (87.05 MPa) whereas PA 66/30SGF/MWCNT exhibits the highest elastic modulus (4.69 GPa). It can be inferred from the graph that the addition of glass fibers improves the tensile strength and elastic modulus of PA 66. This improvement could be explained by the good mechanical performance of glass fibers [10, 13, 68].

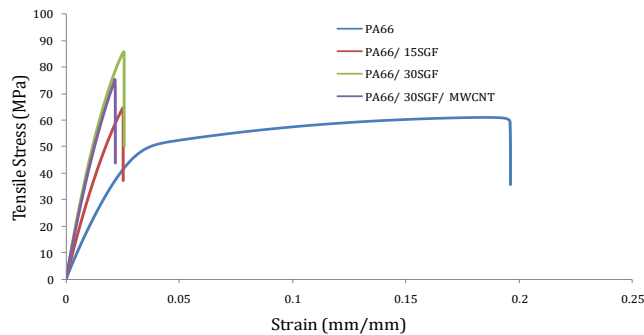
In the present study, we note that the addition of 0.4 wt. % MWCNTs leads to a decline by 14% in tensile strength. This negative effect can be attributed to the poor dispersion and random orientation of the MWCNTs as well as their tendency to form agglomerates in the matrix. Moreover, it is obvious that the presence of MWCNTs increases the elastic modulus of PA 66/30SGF by 4.7 %. Therefore, it could be suggested that MWCNTs contributes to the mechanical performance of PA 66/GF by sharing the external stress as well as bridging along the cracks. Moreover, they strengthen the composite system by improving the surface of glass fibers. As a result of even load distribution along the matrix, mechanical properties of the specimens increases. The obtained data also show that MWCNTs are compatible with glass fibers, which is very promising for the development of hybrid-filler composite systems.

Similar to this study, Jin et al. [69] noted a slight increase in the elastic modulus of PA 66/GF composite with the incorporation of CNTs and MWCNTs, which was attributed to the

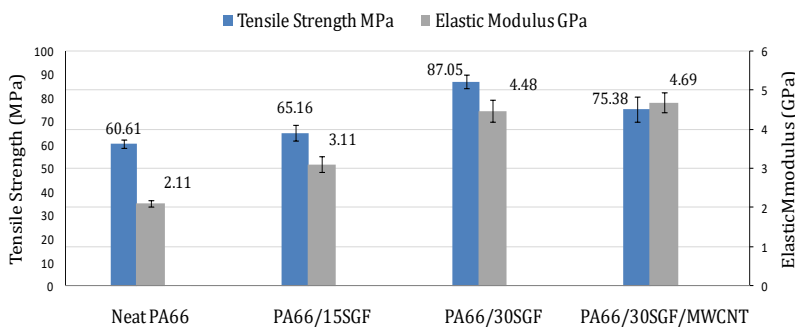
interconnecting effect between the glass fibers and the PA 66 as a result of MWCNT coating. Qiu et al. [65] reported that the addition of 1.0 wt.% MWCNTs improves the elastic modulus of PA 66 by 3.14%. Furthermore, the authors observed that the SCF reinforced Polyamide 6/MWCNT composites incorporating low MWCNT content behave like polymer composites containing two different types of fillers whereas those incorporating high MWCNT content behave like short fiber reinforced nanocomposites.



(a)



(b)

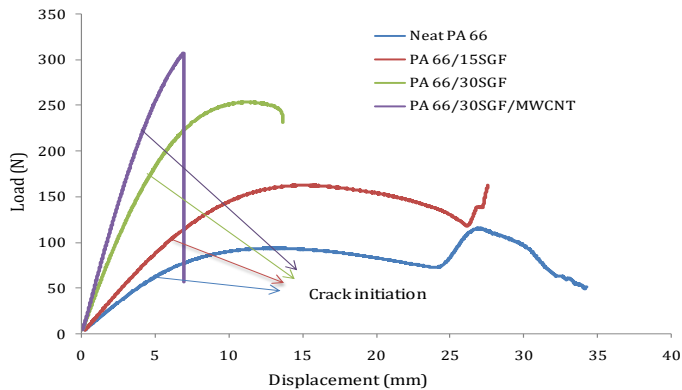


(c)

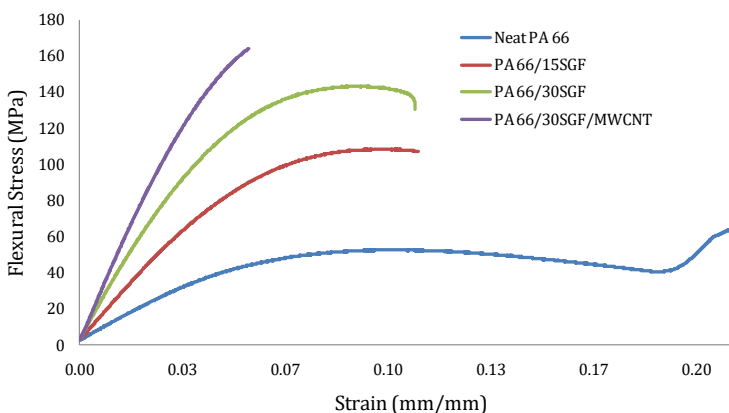
Fig.4 (a) Load-displacement curves of the specimens after the tensile tests; (b) Stress-strain curves of the specimens; (c) Tensile properties of the specimens

3.3 Flexural Test Results

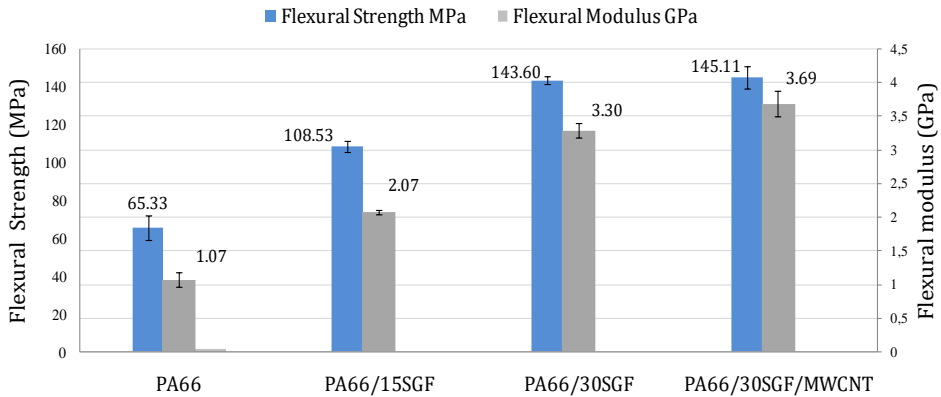
Fig 5 (a) to (c) demonstrate the load-displacement curves and stress-strain curves of the specimens during 3-point flexural tests and the flexural test results of the specimens, respectively PA 66/30SGF/MWCNTs composite exhibits the highest flexural strength (145.11 MPa) and flexural modulus (3.69 GPa) while neat PA 66 exhibits the lowest strength (65.33 MPa) and elastic modulus (1.07 GPa). Flexural strength and flexural modulus of the specimens significantly increase with increasing SGF content, which can be explained by the good mechanical properties of glass fibers as well as their well dispersion and homogeneous distribution in the matrix. Besides, an increase in flexural strength (by 1%) and flexural modulus (by 12%) after MWCNTs integration was observed, which can be attributed to the good surface interaction between the nanotubes and the PA 66 matrix as well as the surface improvement of glass fibers as a result of the MWCNTs coating. These results are compatible with a number of studies in literature. Autay et al. [9] studied the flexural properties of SGF reinforced PA 66 and reported that reinforcement resulted in an enhancement in the maximum flexural stress by nearly 36.3% for PA 66/10GF and 47.2% for PA 66/30GF in comparison to neat PA 66. Koilraj et al. [70] investigated the flexural properties of injection moulded PA 66/MWCNT and reported that the incorporation of 0.5 wt.% CNT content increases the flexural modulus by 5.8%.



(a)



(b)



(c)

Fig. 5 (a) Load-displacement curves of the specimens after three-point flexural tests; (b) Stress-strain curves of the specimens; (c) Flexural properties of the specimens

Figure 6 (a) and (b) represents the optical micrographs of the tensile fractured specimens after 3-point flexural tests. Failure modes of the composite specimens are dominantly matrix cracks along the direction of loading. Compared to the composite specimens with MWCNTs, longer cracks are observed in fractured PA 66/SGF.

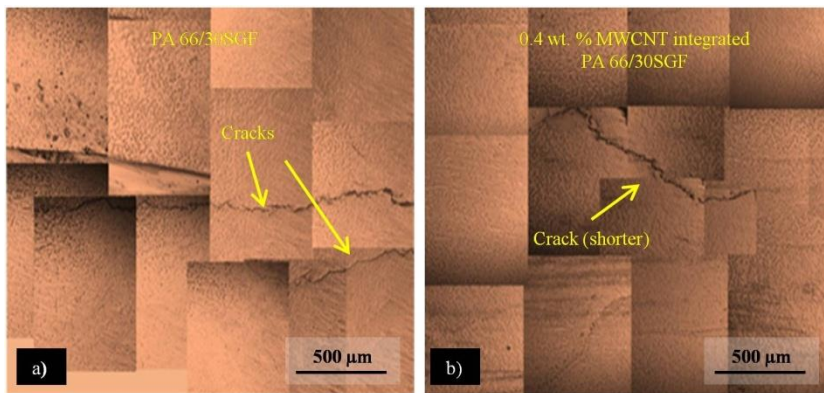


Fig. 6 Optical micrographs of fractured (a) PA 66/30SGF and (b) 0.4 wt.% MWCNT integrated PA 66/30SGF specimens monitored after 3-point flexural tests

3.4. Fracture Aspects of the Composite Specimens

SEM images of fracture surface morphologies of PA 66/30SGF/MWCNT composite are shown in Figure 7 (a) to (c). Figure 7 (a) indicates the SEM image of an individual glass fiber coated with MWCNTs. Higher magnification SEM images of the individual MWCNT coated glass fiber are shown in Figure 7 (b) and (c).

Uniform distribution of the fillers and their facial interaction with the matrix are key parameters for an effective reinforcement mechanism. To obtain good mechanical properties, fillers should evenly share the external stress applied to the matrix material. Regarding the CNT-polymer composites, CNTs are expected to bridge across the cracks formed inside the matrix during the fracture. This behaviour of CNTs prevents the crack

opening and propagation and hence improves the mechanical performance of the composite. Furthermore, if incorporated together with fibers, CNTs can function as effective interface modifiers improving the surface area of fibers and facilitate the adhesion between fiber and matrix.

The monitored SEM images in Figure 7 (a) to (c) demonstrate that some individual MWCNTs function as bridges between the surface of glass fiber and the PA 66 matrix. This bridging phenomenon contributes to toughness improvement by allowing the release of stress and absorbing the fracture energy. Similar observations were made in a number of studies. Qian et al. [71] observed nanotubes bridging across the cracks in polystyrene matrix by means of a TEM and noted that the elastic modulus of the composite increases by nearly 25% with the inclusion of 1 wt.% CNT. Punch et al. [72] examined the fractured surface morphology of PA 6/SCF/MWCNT composites by SEM and obtained clear images of nanotubes interconnecting lumps of the PA 6-matrix. Jin et al. [69] too obtained clear SEM images of CNTs and MWCNTs bridging across the cracks formed inside the PA 66/GF composites. The authors also revealed that MWCNTs coating glass fibers can significantly improve the interaction between the glass fiber and the matrix.

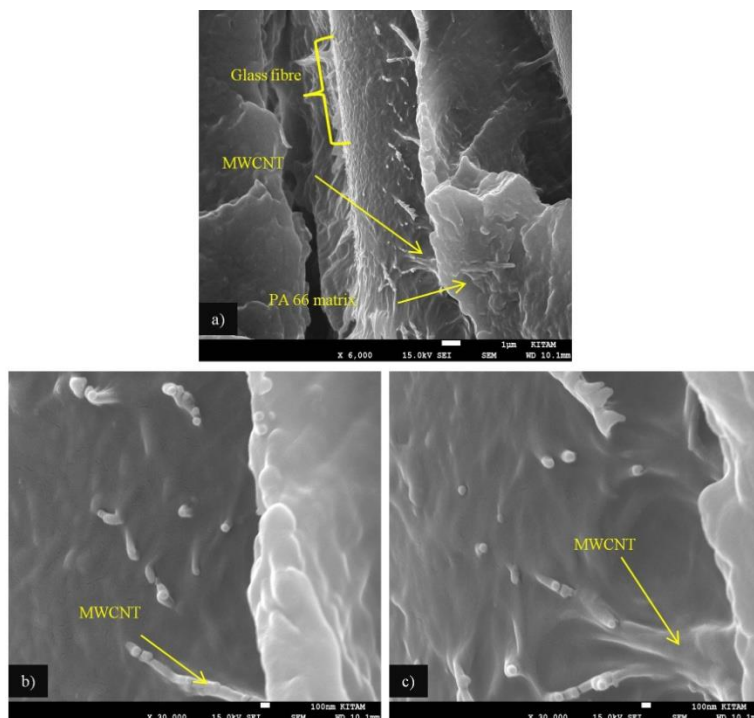


Fig. 7 SEM images of fractured MWCNTs-integrated PA 66/30SGF specimen

Figure 8 (a) and (b) show MWCNT pull-out, which probably occurred due to the fracture and poor interfacial interaction. While a crack is opening, nanotube is stretched absorbing the fracture energy transferred from the matrix. When the fracture ends, the crack somewhat closes and nanotube loosens getting a curved form as shown in Figure 8 (a) and (b).

Figure 9 (a) and (b) show the MWCNTs embedded within polymer matrix, which indicates good interfacial interaction. However, entangled MWCNT agglomerates were also observed as shown in Figure 9 (c), which restricts the dispersion and adversely affects the

mechanical properties. MWCNTs are prone to agglomerate. Earlier, agglomeration tendency of CNTs was attributed to the Van der Waals forces alone; however, the long length and high polarizability of the CNTs could also be determining factors that enhance the energy required to disperse a nanotube within the matrix [73].

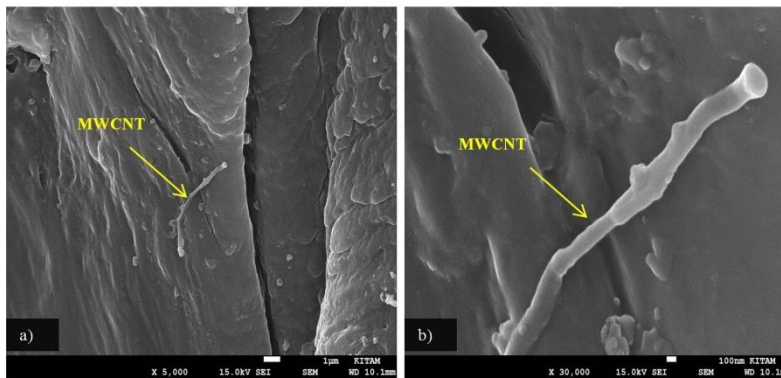


Fig. 8 SEM images of an individual MWCNT pull-out in a fractured PA 66/30SGF matrix

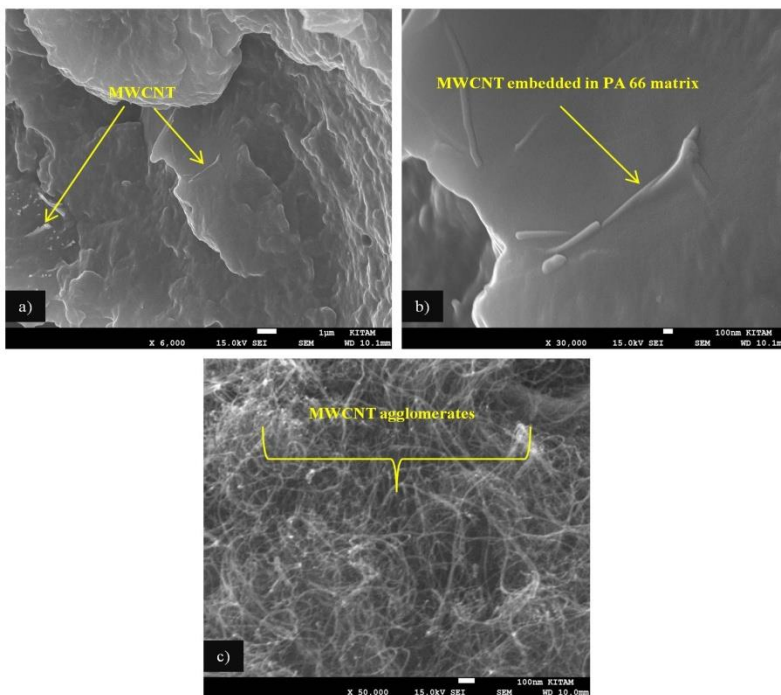


Fig. 9 SEM images of (a) MWCNTs embedded in PA 66/30SGF; (b) (higher-magnification) MWCNT embedded in PA 66/30SGF; (c) agglomerated MWCNTs

4. Conclusions

In this study mechanical properties of neat PA 66, PA 66/15SGF, PA 66/30SGF and 0.4 wt.% MWCNT integrated PA 66/30SGF were investigated. Furthermore, the effects of MWCNTs contents on the micro-structure and morphology of the composites were

investigated by using a scanning electron microscope (SEM), fourier transform infrared spectroscopy analysis (FTIR) and optical microscopy (OM). The conclusions based on the findings are summarized as follow:

- FTIR spectra revealed no chemical interaction between PA 66, SGF and MWCNTs, which means that there are only physical interactions between the constituents.
- The mechanical tests shows that PA 66/15GF and PA 66/30GF composites exhibit improved tensile and flexural properties compared with neat PA 66, which is due to the good mechanical properties of the glass fibers and the sufficient distribution of the external stress throughout the matrix.
- Regarding PA 66/30SGF/MWCNT composites, the presence of MWCNTs results in improvement in elastic modulus by 4.7%, flexural strength by 1% and flexural modulus by 12%.
- The improvement in the mechanical properties with the addition of MWCNTs is explained by i) high mechanical properties of MWCNTs, ii) the bridging phenomenon of MWCNTs, which prevents crack opening and propagation during the fracture of the composite
- Despite the improvement in elastic modulus and flexural properties, a decrease in the tensile strength was observed. This failure is due to the presence of MWCNT agglomerates acting as defects or stress concentration sites in PA 66/30SGF composite system.
- From the SEM images of MWCNT coated glass fibers, we can deduce that MWCNTs modify the surface area of fibers and some individual MWCNTs function as bridges between the surface of glass fiber and the PA 66 matrix.
- Considering the improvement in elastic modulus, flexural modulus and flexural strength, it can be concluded that even a small mass fraction of MWCNT is capable of enhancing the mechanical performance of glass fiber filled PA 66. This achievement proves that MWCNTs are quite promising for designing new thermoplastic composites.

Our future study will be investigating the tensile, bending and Charpy impact properties of hemp fiber reinforced thermoplastic composite materials.

Acknowledgement

The authors acknowledge that the fund of this study has been provided by Research fund of Ondokuz Mayıs University Project No: PYO.MUH.1901.18.008.

References

- [1] Hv D. Processing Techniques of polymer matrix composites-A review. International Journal Of Engineering Research and General Science. 2016;Volume 4.
- [2] Yern Chee C, Chuah CH, Ching KY, Luqman Chuah A, Rahman A. Applications of thermoplastic-based blends. 2017. p. 111-29. <https://doi.org/10.1016/B978-0-08-100408-1.00005-4>
- [3] Gilbert M. Chapter 1 - Plastics Materials: Introduction and Historical Development. In: Gilbert M, editor. Brydson's Plastics Materials (Eighth Edition): Butterworth-Heinemann; 2017. p. 1-18.
- [4] Awaja F, Zhang S, Tripathi M, Nikiforov A, Pugno N. Cracks, microcracks and fracture in polymer structures: Formation, detection, autonomic repair. Progress in Materials Science. 2016;83:536-73. <https://doi.org/10.1016/j.pmatsci.2016.07.007>
- [5] Rajak DK, Pagar DD, Kumar R, Pruncu CI. Recent progress of reinforcement materials: a comprehensive overview of composite materials. Journal of Materials Research and Technology. 2019;8:6354-74. <https://doi.org/10.1016/j.jmrt.2019.09.068>

- [6] Xanthos M. Polymers and Polymer Composites. Functional Fillers for Plastics 2005. p. 1-16. <https://doi.org/10.1002/3527605096.ch1>
- [7] Chow WS, Mohd Ishak ZA. Polyamide blend-based nanocomposites: A review. Express Polymer Letters. 2015;9:211-32. <https://doi.org/10.3144/expresspolymlett.2015.22>
- [8] Vagholkar P. Nylon (Chemistry, Properties and Uses). International Journal of Scientific Research. 2016;5:349-51.
- [9] Autay R, Missaoui S, Mars J, Dammak F. Mechanical and tribological study of short glass fiber-reinforced PA 66. Polymers and Polymer Composites. 2019;27:587-96. <https://doi.org/10.1177/0967391119853956>
- [10] Çuvalcı H, Erbay K, İpek H. Investigation of the Effect of Glass Fiber Content on the Mechanical Properties of Cast Polyamide. Arabian Journal for Science and Engineering. 2014;39:9049-56. <https://doi.org/10.1007/s13369-014-1409-8>
- [11] Ho Ming H, Hwang Jiun R, Wang Pin N, Kuo Shun C. Study on Tensile Properties of Nylon 66 Reinforced Composites. Proceedings of the 2016 International Conference on Education, Management, Computer and Society: Atlantis Press; 2016. p. 1660-3.
- [12] Javangula S, Ghorashi B, Draucker CC. Mixing of glass fibers with nylon 6,6. Journal of Materials Science. 1999;34:5143-51. <https://doi.org/10.1023/A:1004777520458>
- [13] Kim J-W, Kim H-S, Lee D-G. Tensile Strength of Glass Fiber-Reinforced Plastic by Fiber Orientation and Fiber Content Variations. International Journal of Modern Physics: Conference Series. 2012;06:640-5. <https://doi.org/10.1142/S201019451200390X>
- [14] Lingesh BV, Rudresh BM, Ravikumar BN. Effect of Short Glass Fibers on Mechanical Properties of Polyamide66 and Polypropylene (PA66/PP) Thermoplastic Blend Composites. Procedia Materials Science. 2014;5:1231-40. <https://doi.org/10.1016/j.mspro.2014.07.434>
- [15] Nuruzzaman DM, Iqbal AKMA, Oumer AN, Ismail NM, Basri S. Experimental investigation on the mechanical properties of glass fiber reinforced nylon. IOP Conference Series: Materials Science and Engineering. 2016;114. <https://doi.org/10.1088/1757-899X/114/1/012118>
- [16] Srivastava VK, Lal S. Mechanical properties of E-glass fibre reinforced nylon 6/6 resin composites. Journal of Materials Science. 1991;26:6693-8. <https://doi.org/10.1007/BF02402662>
- [17] Ünal H, Ermiş K. Determination of mechanical performance of glass fiber reinforced and elastomer filled polyamide 6 composites. International Advanced Researches and Engineering Journal. 2021;5:405-11. <https://doi.org/10.35860/iarej.934740>
- [18] Bernasconi A, Cosmi F. Analysis of the dependence of the tensile behaviour of a short fibre reinforced polyamide upon fibre volume fraction, length and orientation. Procedia Engineering. 2011;10:2129-34. <https://doi.org/10.1016/j.proeng.2011.04.352>
- [19] Sato N, Kurauchi T, Sato S, Kamigaito O. Reinforcing Mechanism by Small Diameter Fiber in Short Fiber Composite. Journal of Composite Materials. 1988;22:850-73. <https://doi.org/10.1177/002199838802200905>
- [20] Thomason JL. Structure-property relationships in glass reinforced polyamide, part 2: The effects of average fiber diameter and diameter distribution. Polymer Composites. 2007;28:331-43. <https://doi.org/10.1002/pc.20260>
- [21] Thomason JL. Structure-property relationships in glass-reinforced polyamide, part 1: The effects of fiber content. Polymer Composites. 2006;27:552-62. <https://doi.org/10.1002/pc.20226>
- [22] Güllü A, Özdemir A, Özdemir E. Experimental investigation of the effect of glass fibres on the mechanical properties of polypropylene (PP) and polyamide 6 (PA6) plastics. Materials & Design. 2006;27:316-23. <https://doi.org/10.1016/j.matdes.2004.10.013>
- [23] Zainudin ES, Sapuan S, Imihezri SSS. A Review of the Effect of Moulding Parameters on the Performance of Polymeric Composite Injection Moulding. Turkish Journal of Engineering and Environmental Sciences. 2006;30:23-34.

- [24] Baughman R, Zakhidov A, Heer W. Carbon Nanotubes-The Route Toward Applications. Science (New York, NY). 2002;297:787-92. <https://doi.org/10.1126/science.1060928>
- [25] Coleman JN, Khan U, Gun'ko YK. Mechanical Reinforcement of Polymers Using Carbon Nanotubes. Advanced Materials. 2006;18:689-706. <https://doi.org/10.1002/adma.200501851>
- [26] Zhang C, Wu L, de Perrot M, Zhao X. Carbon Nanotubes: A Summary of Beneficial and Dangerous Aspects of an Increasingly Popular Group of Nanomaterials. Frontiers in Oncology. 2021;11. <https://doi.org/10.3389/fonc.2021.693814>
- [27] Iijima S, Ichihashi T. Single-shell carbon nanotubes of 1-nm diameter. Nature. 1993;363:603-5. <https://doi.org/10.1038/363603a0>
- [28] Iijima S. Helical microtubules of graphitic carbon. Nature. 1991;354:56-8. <https://doi.org/10.1038/354056a0>
- [29] Yu M-F, Lourie O, Dyer M, Moloni K, Kelly T, Ruoff R. Strength and Breaking Mechanism of Multiwall Carbon Nanotubes Under Tensile Load. Science. 2000;287:637-40. <https://doi.org/10.1126/science.287.5453.637>
- [30] Salvetat J-P, Briggs GAD, Bonard J-M, Bacsá RR, Kulik AJ, Stöckli T, et al. Elastic and Shear Moduli of Single-Walled Carbon Nanotube Ropes. Physical Review Letters. 1999;82:944-7. <https://doi.org/10.1103/PhysRevLett.82.944>
- [31] Du JH. The present status and key problems of carbon nanotube based polymer composites. Express Polymer Letters - EXPRESS POLYM LETT. 2007;1:253-73. <https://doi.org/10.3144/expresspolymlett.2007.39>
- [32] Sahoo N, Rana S, Cho J, Li L, Chan SH. Polymer Nanocomposites Based on Functionalized Carbon Nanotubes. Progress in Polymer Science. 2010;35:837-67. <https://doi.org/10.1016/j.progpolymsci.2010.03.002>
- [33] Shankar S, Rhim J-W. Polymer Nanocomposites for Food Packaging Applications. 2016. p. 29-55. <https://doi.org/10.1002/9781118542316.ch3>
- [34] Song K, Zhang Y, Meng J, Green EC, Tajaddod N, Li H, et al. Structural Polymer-Based Carbon Nanotube Composite Fibers: Understanding the Processing-Structure-Performance Relationship. Materials. 2013;6:2543-77. <https://doi.org/10.3390/ma6062543>
- [35] Du JH, Bai J, Cheng HM. The present status and key problems of carbon nanotube based polymer composites. Express Polymer Letters. 2007;1:253-73. <https://doi.org/10.3144/expresspolymlett.2007.39>
- [36] Arash B, Wang Q, Varadan VK. Mechanical properties of carbon nanotube/polymer composites. Sci Rep. 2014;4:6479. <https://doi.org/10.1038/srep06479>
- [37] Chen T, Liu H, Wang X, Zhang H, Zhang X. Properties and Fabrication of PA66/Surface-Modified Multi-Walled Nanotubes Composite Fibers by Ball Milling and Melt-Spinning. Polymers (Basel). 2018;10. <https://doi.org/10.3390/polym10050547>
- [38] Coleman JN, Khan U, Blau WJ, Gun'ko YK. Small but strong: A review of the mechanical properties of carbon nanotube-polymer composites. Carbon. 2006;44:1624-52. <https://doi.org/10.1016/j.carbon.2006.02.038>
- [39] Hassani J A, Ishak Z, Mohamed A. Preparation and characterization of polyamide 6 nanocomposites using MWCNTs based on bimetallic Co-Mo/MgO catalyst. Express Polymer Letters. 2013;8:177-86. <https://doi.org/10.3144/expresspolymlett.2014.21>
- [40] Jin F-L, Park S-J. A review of the preparation and properties of carbon nanotubes-reinforced polymer composites. Carbon letters. 2011;12:57-69. <https://doi.org/10.5714/CL.2011.12.2.057>
- [41] Khan W, Sharma R, Saini P. Carbon Nanotube-Based Polymer Composites: Synthesis, Properties and Applications. Carbon Nanotubes - Current Progress of their Polymer Composites 2016. <https://doi.org/10.5772/62497>
- [42] Moniruzzaman M, Chattopadhyay J, Billups WE, Winey KI. Tuning the mechanical properties of SWNT/nylon 6,10 composites with flexible spacers at the interface. Nano Lett. 2007;7:1178-85. <https://doi.org/10.1021/nl062868e>

- [43] Spitalsky Z, Tasis D, Papagelis K, Galiotis C. Carbon nanotube-polymer composites: Chemistry, processing, mechanical and electrical properties. *Progress in Polymer Science*. 2010;35:357-401. <https://doi.org/10.1016/j.progpolymsci.2009.09.003>
- [44] Tarfaoui M, Lafdi K, El Moumen A. Mechanical properties of carbon nanotubes based polymer composites. *Composites Part B: Engineering*. 2016;103:113-21. <https://doi.org/10.1016/j.compositesb.2016.08.016>
- [45] Zabegaeva ON, Sapozhnikov DA, Buzin MI, Krestinin AV, Kotelnikov VA, Baiminov BA, et al. Nylon-6 and single-walled carbon nanotubes polyamide composites. *High Performance Polymers*. 2016;29:411-21. <https://doi.org/10.1177/0954008316645848>
- [46] Zhang J, Gao X, Zhang X, Liu H, Zhang H, Zhang X. Polyamide 66 and amino-functionalized multi-walled carbon nanotube composites and their melt-spun fibers. *Journal of Materials Science*. 2019;54:11056-68. <https://doi.org/10.1007/s10853-019-03619-0>
- [47] Su X, Wang R, Li X, Araby S, Kuan H-C, Naeem M, et al. A comparative study of polymer nanocomposites containing multi-walled carbon nanotubes and graphene nanoplatelets. *Nano Materials Science*. 2021. <https://doi.org/10.1016/j.nanoms.2021.08.003>
- [48] Khan FSA, Mubarak NM, Khalid M, Khan MM, Tan YH, Walvekar R, et al. Comprehensive review on carbon nanotubes embedded in different metal and polymer matrix: fabrications and applications. *Critical Reviews in Solid State and Materials Sciences*. 2021:1-28. <https://doi.org/10.1080/10408436.2021.1935713>
- [49] Miyagawa H, Misra M, Mohanty AK. Mechanical properties of carbon nanotubes and their polymer nanocomposites. *J Nanosci Nanotechnol*. 2005;5:1593-615. <https://doi.org/10.1166/jnn.2005.181>
- [50] Hiremath A, Murthy AA, Thipperudrappa S, K N B. Nanoparticles Filled Polymer Nanocomposites: A Technological Review. *Cogent Engineering*. 2021;8:1991229. <https://doi.org/10.1080/23311916.2021.1991229>
- [51] Gorga RE, Lau KKS, Gleason KK, Cohen RE. The importance of interfacial design at the carbon nanotube/polymer composite interface. *Journal of Applied Polymer Science*. 2006;102:1413-8. <https://doi.org/10.1002/app.24272>
- [52] Gupta AK, Harsha SP. Effect of crack and determination of fracture energy of carbon nanotube-reinforced polymer composites. *Proceedings of the Institution of Mechanical Engineers, Part N: Journal of Nanoengineering and Nanosystems*. 2014;229:110-6. <https://doi.org/10.1177/1740349914531758>
- [53] Kuronuma Y, Shindo Y, Takeda T, Narita F. Fracture behaviour of cracked carbon nanotube-based polymer composites: Experiments and finite element simulations. *Fatigue & Fracture of Engineering Materials & Structures*. 2010;33:87-93. <https://doi.org/10.1111/j.1460-2695.2009.01419.x>
- [54] Kuronuma Y, Shindo Y, Takeda T, Narita F. Crack growth characteristics of carbon nanotube-based polymer composites subjected to cyclic loading. *Engineering Fracture Mechanics*. 2011;78:3102-10. <https://doi.org/10.1016/j.engfracmech.2011.09.006>
- [55] Shindo Y, Kuronuma Y, Takeda T, Narita F, Fu S-Y. Electrical resistance change and crack behavior in carbon nanotube/polymer composites under tensile loading. *Composites Part B: Engineering*. 2012;43:39-43. <https://doi.org/10.1016/j.compositesb.2011.04.028>
- [56] Takeda T, Shindo Y, Naraoka F, Kuronuma Y, Narita F. Crack and Electrical Resistance Behaviors of Carbon Nanotube-Based Polymer Composites under Mixed-Mode I/II Loading. *Materials Transactions*. 2013;54:1105-9. <https://doi.org/10.2320/matertrans.M2013080>
- [57] Ajayan PM, Schadler LS, Giannaris C, Rubio A. Single-Walled Carbon Nanotube-Polymer Composites: Strength and Weakness. *Advanced Materials*. 2000;12:750-3.

- [https://doi.org/10.1002/\(SICI\)1521-4095\(200005\)12:10<750::AID-ADMA750>3.0.CO;2-6](https://doi.org/10.1002/(SICI)1521-4095(200005)12:10<750::AID-ADMA750>3.0.CO;2-6)
- [58] Liu, Phang IY, Shen L, Chow SY, Zhang W-D. Morphology and Mechanical Properties of Multiwalled Carbon Nanotubes Reinforced Nylon-6 Composites. *Macromolecules*. 2004;37:7214-22. <https://doi.org/10.1021/ma049132t>
- [59] Ferreira T, Paiva MC, Pontes AJ. Dispersion of carbon nanotubes in polyamide 6 for microinjection moulding. *Journal of Polymer Research*. 2013;20. <https://doi.org/10.1007/s10965-013-0301-7>
- [60] Chopra S, Deshmukh KA, Deshmukh AD, Peshwe DR. Functionalization and Melt-compounding of MWCNTs in PA-6 for Tribological Applications. *IOP Conference Series: Materials Science and Engineering*. 2018;346. <https://doi.org/10.1088/1757-899X/346/1/012005>
- [61] Kartel M, Sementsov Y, Mahno S, Trachevskiy V, Bo W. Polymer Composites Filled with Multiwall Carbon Nanotubes. *Universal Journal of Materials Science*. 2016;4:23-31. <https://doi.org/10.13189/ujms.2016.040202>
- [62] Mahato KK, Rathore DK, Prusty RK, Dutta K, Ray BC. Tensile behavior of MWCNT enhanced glass fiber reinforced polymeric composites at various crosshead speeds. *IOP Conference Series: Materials Science and Engineering*. 2017;178. <https://doi.org/10.1088/1757-899X/178/1/012006>
- [63] Nguyen-Tran HD, Hoang VT, Do VT, Chun DM, Yum YJ. Effect of Multiwalled Carbon Nanotubes on the Mechanical Properties of Carbon Fiber-Reinforced Polyamide-6/Polypropylene Composites for Lightweight Automotive Parts. *Materials (Basel)*. 2018;11. <https://doi.org/10.3390/ma11030429>
- [64] Lakkur Munirajappa M, Harijan Basavaraju R. Microstructural characterization of short glass fiber and PAN based carbon fiber reinforced nylon 6 polymer composites. *Polymer Engineering & Science*. 2018;58:1428-37. <https://doi.org/10.1002/pen.24737>
- [65] Qiu L, Chen Y, Yang Y, Xu L, Liu X. A Study of Surface Modifications of Carbon Nanotubes on the Properties of Polyamide 66/Multiwalled Carbon Nanotube Composites. *Journal of Nanomaterials*. 2013;2013. <https://doi.org/10.1155/2013/252417>
- [66] Navarro-Pardo F, Martínez-Hernández AL, Castaño VM, Rivera-Armenta JL, Medellín-Rodríguez FJ, Martínez-Barrera G, et al. Influence of 1D and 2D Carbon Fillers and Their Functionalisation on Crystallisation and Thermomechanical Properties of Injection Moulded Nylon 6,6 Nanocomposites. *Journal of Nanomaterials*. 2014;2014:1-13. <https://doi.org/10.1155/2014/670261>
- [67] Demircan O, Al-darkazali A, İnanç İ, Eskizeybek V. Investigation of the effect of CNTs on the mechanical properties of LPET/glass fiber thermoplastic composites. *Journal of Thermoplastic Composite Materials*. 2020;33:1652-73. <https://doi.org/10.1177/0892705719833105>
- [68] Hsiung HM, Ren HJ, Ning WP, Chi KS. Study on Tensile Properties of Nylon 66 Reinforced Composites. *Atlantis Press*; 2016. p. 1660-3. <https://doi.org/10.2991/emcs-16.2016.415>
- [69] Jin J, Zhang L, Chen W, Li C-Z. Synthesis of glass fiber-multiwall carbon nanotube hybrid structures for high-performance conductive composites. *Polymer Composites*. 2013;34:1313-20. <https://doi.org/10.1002/pc.22544>
- [70] Koilraj TT, Kalaichelvan K. Experimental Study on Mechanical Properties of PA66 Blended with MWNTs. *Applied Mechanics and Materials*. 2015;766-767:383-8. <https://doi.org/10.4028/www.scientific.net/AMM.766-767.383>
- [71] Qian D, Dickey EC, Andrews R, Rantell T. Load transfer and deformation mechanisms in carbon nanotube-polystyrene composites. *Applied Physics Letters*. 2000;76:2868. <https://doi.org/10.1063/1.126500>

- [72] Puch F, Hopmann C. Morphology and tensile properties of unreinforced and short carbon fibre reinforced Nylon 6/multiwalled carbon nanotube-composites. *Polymer*. 2014;55:3015-25. <https://doi.org/10.1016/j.polymer.2014.04.052>
- [73] Banerjee J, Dutta K. Melt-mixed carbon nanotubes/polymer nanocomposites. *Polymer Composites*. 2019;40:4473-88. <https://doi.org/10.1002/pc.25334>



Technical Note

Performance evaluation of unmanned aerial vehicle wing made from *sterculiasetigeradelile* fiber and *pterocarpuserinaceus* wood dust epoxy composite using finite element method Abaqus and structural testing

Nasir Mohammed Tahir^{*1,a}, Adamu Umar Alhaji^{2,b}, Ibrahim Abdullahi^{2,c}

¹National Space Research and Development Agency

²Department of Mechanical Engineering, Bayero University, Kano

Article Info

Abstract

Article history:

Received 02 Jan 2022

Revised 06 Jul 2022

Accepted 18 Jul 2022

Keywords:

Unmanned Aerial Vehicle Wing (UAV);
Finite Element Method;
Abaqus Software;
Schrenk Method;
Sterculiasetigeradelile fiber (SSD);
Pterocarpuserinaceus (PTE) wood dust;
Structural Testing.

Finite Element Method such as Abaqus software is increasingly used to analyze structures such as the Unmanned Aerial Vehicle Wing. Unmanned Aerial Vehicle is usually fabricated using synthetic materials such as Glass fibers, Carbon fibers and Kevlar. The problems with the synthetic fibers are environmental pollution during processing, energy consumption during processing and cost of production. Natural fibres can be used as replacement for synthetic fibers due to their comparable physical and mechanical properties. The research involves the simulation of an Unmanned Aerial Vehicle wing made from 5% Cold Alkaline treated 5% *Sterculiasetigeradelile* fiber (SSD) at 0-degree orientation and 7.5% *Pterocarpuserinaceus* (PTE) Wood dust Epoxy composite using Abaqus software. The wing was subjected to aerodynamic wing loading from 167.57N to 895N (3kg to 16kg). The result showed that the wing produced using the Novel material could withstand the most critical flight load distribution in conformation with Federal Aviation Regulation (FAR) part 23 Airworthiness standards with an ultimate design load of 5.7. At the point of failure, the wing could withstand an Ultimate load factor of 20.26. Structural physical testing was performed for a wing loading of 167.75N to 335.50N (3kg to 6kg). The wing successfully resisted the critical in-flight loading confirming the simulation result. The Novel material of lower density (1.093g/cm³) could withstand the wing loading requirement making it suitable for the UAV wing application.

© 2022 MIM Research Group. All rights reserved.

1. Introduction

Unmanned Aerial Vehicles (UAVs) have been used with great success for military intelligence providing an alternative to manned craft due to their small size, reduced risk of life and reduced cost. The Vehicles have many civil applications which include search and rescue missions, exploration, surveying of oil pipelines, forest fires and agricultural applications [1]. Unmanned Aerial Vehicle wings are in airfoil shape and are designed to develop lift when they are moved through the air. Unmanned Aerial Vehicles are commonly produced using synthetic fibres such as Carbon fiber and Glass fiber. The problems with synthetic fibers include high energy consumption during processing, environmental pollution and high cost. Natural fibres such as the *Sterculiasetigeradelile* fibre have not been explored for Unmanned Aerial Vehicles but have the mechanical and physical properties that could withstand the aerodynamic loading requirements. In 1940, spitfire fuselage was designed and built using flax fibres reinforced in phenolic resin. The material was stacked together at different orientations and then hot pressed. The material was known by the name Aerolite. The material was used for the main spar of the Bristol Breinheim bomber [2].

*Corresponding author: n-tahir@hotmail.co.uk

^a orcid.org/0000-0003-0553-3968; ^b orcid.org/0000-0002-0738-4129; ^c orcid.org/0000-0002-9555-3630;
DOI: <http://dx.doi.org/10.17515/resm2022.378ma0102tn>

The finite element method (FEM) is the numerical method used to solve the boundary value problem. The finite element method involves the representation of a given domain as a collection of discrete parts. The essence of the finite element method is to divide the original continuum of the complicated geometry with infinite numbers of the degree of freedom (DOF) into several subdivisions of the continuum with specific geometry termed elements. The elements are interconnected at specific points on the sides of the elements. These are called nodes in the discretized model. Element equations are derived for each of the elements in the discretized model based on appropriate physical theories and principles [3].

Numerical analysis was conducted in predicting the response of structures to given load. i.e the lift distributed along the wing span following the Schrenk method lift distribution calculation. The numerical method was conducted for half wing span in order to reduce the computation time due to symmetry of the UAV wing. The desired output was to find whether the UAV wing could withstand the given load [4]. The model of the UAV wing was developed using ABAQUS/CAE Version 6.11 FE analysis commercial software.

An optimized composite material from 5% Cold Alkaline treated 5% SterculiaSetigeraDelile fibre (SSD) at 0-degree orientation and 7.5% PterocarpusErinaceus (PTE) Wood dust Epoxy have been produced for the potential application. This research involves the simulation of an Unmanned Aerial Vehicle wing using wood fiber and wood dust reinforcements using Abaqus software and Structural testing was used to validate the model.

Synthetic fibres such as Carbon fibre, Glass fibre and Epoxy Matrix are commonly used for the production of Aerospace structures but the production of the fibres has negative impact on the environment. The work is novel in the fact that a new material was made from wood fibre, wood dust and epoxy matrix was used in the production of the Unmanned Aerial Vehicle wing. The wing produced can withstand the critical flight load distribution in conformation with Federal Aviation Regulation. The Novel material could be used as a potential replacement for Carbon fibres in some aerospace applications.

Sullivan, Hwang, Rais-Rohani and Lacy (2009) investigated the strength and stiffness characteristics of a carbon composite wing of an ultralight unmanned Aerial Vehicle. The wing consisted of a foam-core sandwich skin and multiple spars with varying laminate ply pattern and wall thickness dimension. A three-tier whiffle tree was designed for the structural testing of the UAV wing and was used to subject the wing to load in a manner that was consistent with a pull-over-maneuver condition. The wing was loaded incrementally beyond the limit load and the design ultimate load to the point of structural failure. Abaqus software was used to develop the finite element model of the wing; boundary conditions were applied. The static response under simulated wing loading condition was obtained. The strain and deflection prediction from the finite element method were found to be in good agreement with the experimental observation. Despite the Carbon fibre being light, the UAV wing was found to be strong with strength to weight ratio of at least 40 at failure. The Ultralight UAV structural components were designed using Federal Aviation Regulation (FAR) Part 23(normal category) airworthiness standard. The forces applied at each loading condition for the limit load condition of 3.8g and an Ultimate load condition of 5.7g. At the point of failure, the strength to weight ratio was 40 times greater. The result obtained at the point of failure was 17% higher than the Ultimate design load factor [5].

Rumayshah, Prayoga and Moelyadi (2018) designed High Altitude long endurance UAV. Structural testing of composite wing was performed using Finite Element Method. ABAQUS/CAE was used to predict the stress and the deformation of the wing when subjected to loading. The UAV was initially produced using Balsa wood and failed during

flight test as a result of extreme side wind leading to extreme bending. A second generation UAV was designed using composite materials for the wing structure. For the second generation HALE UAV ITB, the UAV had a wing span of 16m, with a chord length of 0.4m. The CAD model was first generated using CATIA V5 in 3D. The part was translated into ABAQUS/CAE. The material used for the UAV was Woven Carbon Epoxy at different fibre orientation and stacking sequence. Non-linear Prandtl Lifting Line Theory (NLLT) was used to estimate the lift distribution on the UAV wing. The weight of the UAV wing was automatically processed considering the material density input in the Abaqus preprocessing. ENCASTE boundary condition was applied to the wing root rib to prevent translation and rotations in all directions. The wing tip was free from all constraints. The overall load and boundary condition are applied to the UAV wing. The global seed was generated for the whole model with a size of approximately 5mm. The total displacement was 3.265m. The new structural configuration had a Tsai-Wu failure criterion is at a value of 0.865[4].

Kanesun, Mansor and Abdul-latif (2014) performed structural and finite element analysis on UAV wing. The geometrical modeling of the wing structural components was conducted in Solidworks and imported into Abaqus/CAE. Only half of the wing was modeled to reduce the total number of elements used in the analysis. The wing skin was made from Carbon fibre fabric, Kevlar Veil and Honey comb cores. The experiment was conducted on the UAV full wing provided by Unmanned System Technology Sdn Bhd. Sandbags weighing 1kg was used to represent the aerodynamic loads on the wing. The deflection values between the bending values and finite element analysis using Abaqus was between ranges 0.35% to 16.4%. The span length(b) 5.1257m, chord length, 0.5886m, mass 45.5kg, number of spar 2 and number of ribs 12[6].

Hutagalung, Latif and Israr (2016) performed structural analysis on a composite UAV wing using Abaqus FEM simulation software. The semi-monoque structure consists of one main mono-spar, 4 major ribs, carbon tubes and a flap. The CAMAR UAV wing was designed using solidwork 2014. The internal components consisted of monospar, 5 leading edge ribs, 5 trailing edge ribs, carbon tubes, carbon support and the wing skin. The geometrical modeling of the wing structural component was designed using Solidworks 2014 and the 3-dimensional model was imported to Abaqus software for numerical simulations. The wing was assumed to be symmetrical, therefore only half of the wing span model was used in the numerical analysis and lead to reduction in computation time. The materials used for the UAV wing was the Carbon fibre fabric (with Epoxy) and the Carbon fibre braided (with Epoxy) with various stacking sequence with the skin of the wing having a sequence of [0₂, 45, -45, 0_{1/2}]_s with 9 layers. The total thickness of the components would be 0.002286m. All of the components use the mesh generation which are Quad-Dominated and automatic structured meshing. The boundary condition 'Encaste' was applied at the fuselage-wing interface and the wing was subjected to wing loading of 8140.35N/m². The maximum deflection recorded was 1.780mm, which occurs at the wing tip. A high deflection means that it would disturb flight performance, thus reducing the battery management system of UAV ending with shorter range and endurance. The UAV wing has a Tsai-Hill value 0.1806 and Tsai-Wu value 0.1734. Both failure index showed that the UAV wing is much capable of handling the load acted upon it as both are less than 1 which brings meaning that they do not fail. In summary, researchers have used finite element analysis software Abaqus for structural analysis of UAV wing using carbon fibre of different fibre orientations and stacking sequence. The results were confirmed by experimental analysis. Abaqus software was used in this research for the structural analysis of an Unmanned Aerial Vehicle wing made from SterculiaSetigeraDelile fibre, PterocarpusErinacues Epoxy composite and structural analysis was used for the confirmation of the results [7].

2. Material and Method

2.1. Modeling of the UAV

The UAV wing parameters initially used in this simulation consist of 1 spars, 2 ribs, and 2 wing skin.

Table 1. Important parameters for the UAV wing

Parameters	Value
Span length, b (mm)	924
Chord length, c, (mm)	147
Aspect Ratio (A.R)	6.28
UAV weight(kg)	3
Number of spars	1
Number of ribs	2
Number of Wing Skin	2
Spar Height(mm)	15.40
Spar Thickness(mm)	2.5
Wing Skin Thickness(mm)	2
Spar thickness(mm)	2.5

The geometric modeling of the UAV wing was done using ABAQUS/CAE. The process involves airfoil selection in which high lift airfoil was selected. The airfoil selected was the Wortmann FX 63-137 (fx 63137-il) human power aircraft airfoil due to its high lift to drag ratio and high stall angle [8]. Only half span of the wing was modeled to reduce the number of elements and to reduce the computation time.

Finite Element Method was used to predict the structural response which becomes overly complex with calculations. The static structural analysis was performed using Finite Element Software ABAQUS /CAE. ABAQUS was chosen since it has pre-processing features that makes composite material property definition easier [4].

The UAV Wing was modeled as follows:

Part module- Abacus Software was used to model the components of the wing for simulation. The coordinates of the Airfoil were imported from the Airfoiltol website which was used in creating the Wing skin, Spars and wing ribs.

Material module- The mechanical properties were specified in the module, specifying the angle of orientation and the specified thickness. The software has a composite layup manager which allows the stacking of composites at specified angles of orientation and with varying thickness.

Assembly module- Assembly of the UAV wing.

Load module- ENCASTRE boundary condition was applied to the Root Rib connection to the fuselage which would prevent translation and rotation in all directions [4,7, 9]. The load distribution calculated using the Schrenk method was applied on the wing. The wing was divided into four sections and the pressure was applied to each section.

Meshing - The global seed mesh was generated for the whole model with an approximate size of 0.5mm. Quad-dominated shape element and structured mesh technique were used for the whole wing except for the ribs with many curved edges. The mesh technique used for the ribs was free mesh [4,9]. Tsai Hill and Tsai Wu’s failure Criterion was to analyze the failure of the wing.

Job- The Job process was initiated and after completion, the failure was analyzed using the Tsai-Hill, Tsai-Wu failure criterion.

Table 2. Mechanical properties of composite materials used for the simulations [4, 10]

Mechanical Properties of optimum composite	Cold SSD 5% WD=7.5%	Woven Carbon fibre Epoxy
Tensile Strength Longitudinal(MPa)	26.90	600
Tensile Strength Transverse(MPa)	6.63	600
Flexural Strength (MPa)	77.38	-
Compression Strength Longitudinal direction(MPa)	53.25	570
Compression Strength Transverse Direction(MPa)	31.52	570
Poisson ratio, ν_{12}	0.41	0.1
Poisson ratio, ν_{23}	0.37	0.1
Elastic Modulus E_1 (GPa)	1.16	70
Elastic Modulus E_2 (GPa)	0.9	70
Shear Strength(MPa)	4.16	90
Shear Modulus, G_{12} (GPa)	0.411	5
Shear Modulus, G_{13} (GPa)	0.411	5
Shear Modulus, G_{23} (GPa)	0.33	5

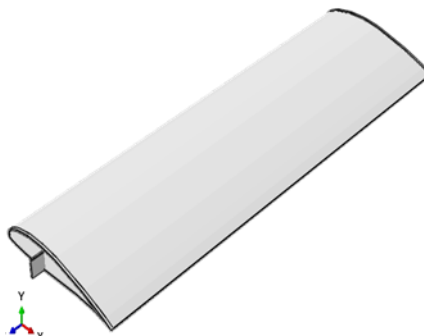


Fig. 1 Modeled unmanned aerial vehicle wing using Abaqus software

The wing was subjected to various loadings under the regulations of Federal Aviation Regulation (FAR) part 23: Airworthiness Standard. The maximum load factor that was used was 3.8 which is the maximum wing loading that would be experienced during flight and a safety factor of 1.5 making it an ultimate load factor of 5.7 [11]. For a 3kg UAV, the ultimate load is calculated as follows:

$$L = nW \tag{1}$$

$$UL = 3 \times 9.81 \times 3.8 \times 1.5 = 167.75 N .$$

2.2. Calculation of Lift Distribution Using Schrenk Method

The Schrenk method is simple approximation methods of finding spanwise lift distribution which has been proposed by Dr. Ing Oster Schrenk and has been accepted by the Civil

Aeronautics Administration (CAA) as a satisfactory method for civil aircraft. Schrenk method uses the average between the planform lift and elliptical lift distribution. The mathematical model for the Schrenk method is shown [12]:

$$L'_{elliptical} = \frac{4L}{\pi b} \sqrt{1 - \left(\frac{2y}{b}\right)^2} \tag{2}$$

$$L'_{planform} = \frac{2L}{(1 + \lambda)b} \left(1 + \frac{2y}{b} (\lambda - 1)\right) \tag{3}$$

$$L'_{schrenk} = \frac{L'_{elliptical} + L'_{planform}}{2} \tag{4}$$

where L : total lift force (N), L' : lift distribution (N/m), λ : Taper ratio, b = wingspan (m) , y : spanwise distance of section(m) [12]. The formula is used in the calculation of the lift distribution on the wing.

The Schrenk method assumes that the lift distribution along the wingspan is the average lift based on the trapezoidal and the lift based on the elliptical wing. To determine the aircraft lift distribution, the wing was divided into 40 sections each having a span of 11.55mm.

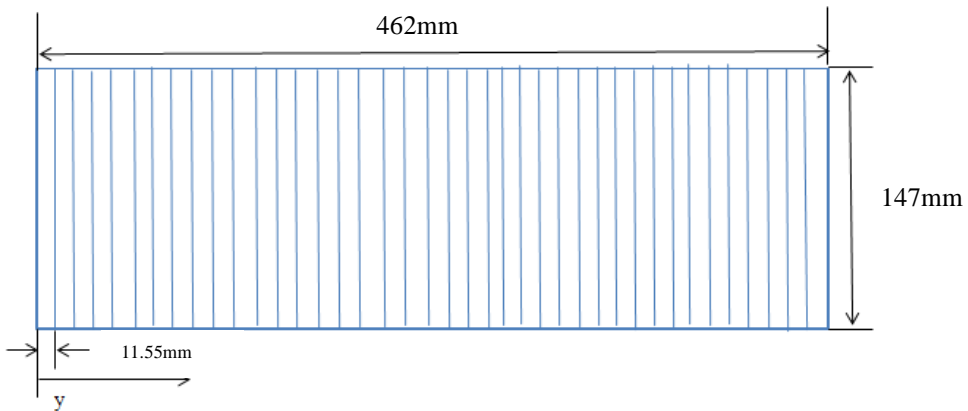


Fig. 2 Half span UAV wing divided into 40 sections for lift distribution calculation

For a 3kg UAV Wing, the Ultimate load was calculated as 167.75N. This was used for the estimation of the load distribution using the Schrenk method.

Trapezoidal Wing:

$$L(y) = \frac{2L}{b(1 + \lambda)} \left[1 - \frac{2y}{b} (1 - \lambda)\right] \tag{5}$$

Elliptical Lift:

$$L(y) = \frac{4L}{\pi b} \sqrt{1 - \left(\frac{2y}{b}\right)^2} \tag{6}$$

Trapezoidal Wing at $y=0$ $L(0) = \frac{2 \times 167.75}{0.924 \times (1+1)} \left[1 - \frac{2(0)}{0.924} (1-1) \right] = 181.55 \text{ N/m}$

Elliptical Lift at $y=0$, $L(0) = \frac{4 \times 167.75}{3.141592 \times 0.924} \sqrt{1 - \left(\frac{2 \times 0}{0.924}\right)^2} = 231.155 \text{ N/m}$

$$L'(0) = \frac{181.55 + 231.155}{2} = 206.353 \text{ N/m}$$

Trapezoidal Wing at $y = 0.01155\text{m}$,

$$L(0.01155) = \frac{2 \times 167.75}{0.924 \times (1+1)} \left[1 - \frac{2(0.01155)}{0.924} (1-1) \right]$$

$$= 181.55 \text{ N/m}$$

Elliptical Lift at $y=0.01155$, $L(0.01155) = \frac{4 \times 167.75}{3.141592 \times 0.924} \sqrt{1 - \left(\frac{2 \times 0.01155}{0.924}\right)^2}$

$$= 231.083 \text{ N/m}$$

$$L'(0.01155) = \frac{181.55 + 231.083}{2} = 206.3165 \text{ N/m}$$

Where L is the Limit load; b is the span length of the wing; λ is the taper ratio; $L(y)$ is the lift distribution in N/m.

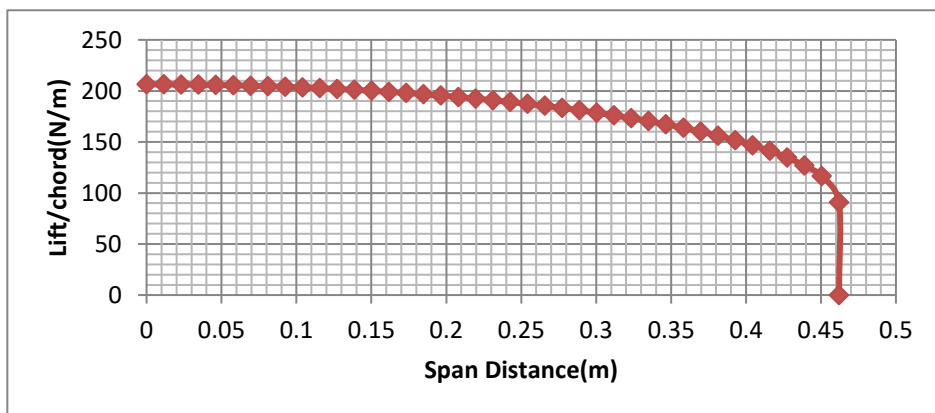


Fig. 3 Lift distribution over the half-span wing calculated using Schrenk method (3kg UAV)

2.3. Load and Boundary Conditions

The Load distribution across the wing span was estimated using the Schrenk method. The weight of the structure is automatically calculated by considering the material input into

ABAQUS pre-processing. ENCASTE boundary condition was applied to the root ribs which interfaces the fuselage. This would prevent rotation and translation in all direction. The wing tip is free from constraint in all degree of freedom. The overall loads and boundary conditions acting on the model are shown in figure 4:

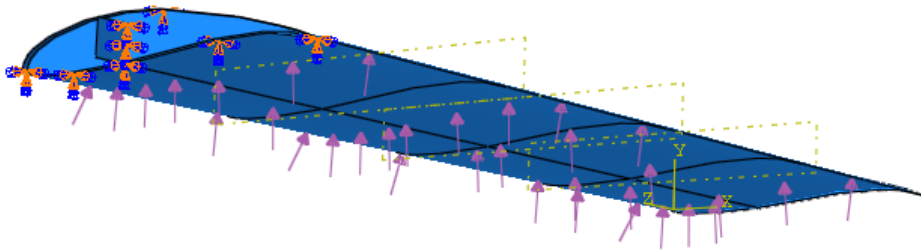


Fig. 4 ENCASTE boundary condition was applied to the root rib and the load pressure distribution applied to the lower wing region based on Schrenk method.

2.4. Meshing

Mesh Convergence study was conducted for a global size mesh of 5mm to 0.35mm. The global size of the mesh was chosen for the whole model with the size of approximately 0.5mm after the mesh convergence study [4]. The mesh control was activated for regulating the shape of the element and meshing technique. Quad-dominated shape element and free meshing technique was used. The ribs, contains many curved edges, the meshing technique used was free meshing technique and triangular element was used.

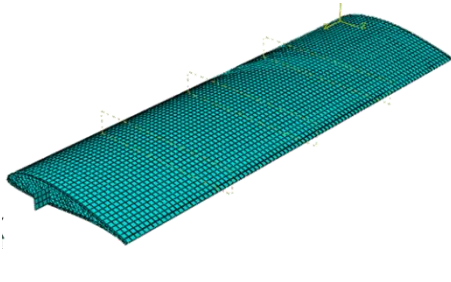


Fig. 5 Meshed result of the unmanned aerial vehicle wing for 5mm global size mesh

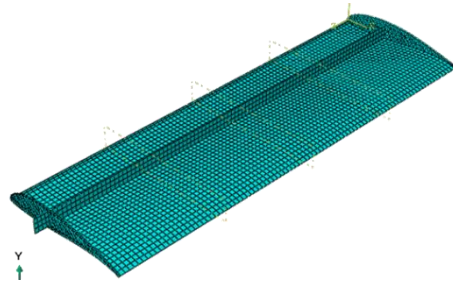


Fig. 6 Meshed result for the inner structure of the unmanned aerial vehicle wing for 5mm global size mesh

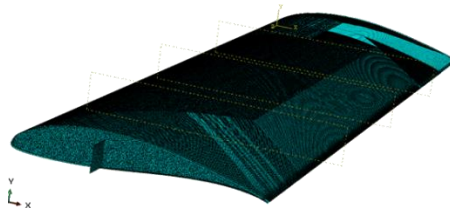


Fig. 7 Meshed result of the unmanned aerial vehicle wing for 0.5mm global size mesh

2.5 Composite Failure Theory Criterion

Failure Criterion is used to measure the ability of the structure to withstand a given load, whether it fails or not. The Tsai Hill and Tsai Wu failure criterion can be used to examine the failure of a composite material like the composite Unmanned Aerial Vehicle Wing.

2.5.1 Tsai Hill Failure Criterion

The Tsai-Hill failure criterion is based on distortion energy theory of Von Mises distortion energy yield criterion. The distortion energy is part of the strain energy of the body. The strain energy consists of two parts; the first part is as a result of change in volume of the body and it is known as the dilation energy and the second part of the strain energy is due to the change in shape of the body and is called distortion energy. The failure of the body occurs when the distortion energy is greater than the distortion energy of the material. Based on the distortion energy theory Tsai and Hill proposed that a lamina will fail if it does not satisfy Equation 7:

$$(G_2 + G_3)\sigma_1^2 + (G_1 + G_3)\sigma_2^2 + (G_1 + G_2)\sigma_3^2 - 2G_3\sigma_1\sigma_2 - 2G_2\sigma_1\sigma_3 - 2G_1\sigma_2\sigma_3 + 2G_4\tau_{23}^2 + 2G_5\tau_{13}^2 + 2G_6\tau_{12}^2 < 1 \quad (7)$$

is violated. Where:

$$G_1 = \frac{1}{2} \left[\frac{2}{[(\sigma_2^T)_{ult}]^2} - \frac{1}{[(\sigma_1^T)_{ult}]^2} \right] \quad (8)$$

$$G_2 = \frac{1}{2} \left(\frac{1}{[(\sigma_1^T)_{ult}]^2} \right) \quad (9)$$

$$G_3 = \frac{1}{2} \left(\frac{1}{[(\sigma_1^T)_{ult}]^2} \right) \quad (10)$$

$$G_6 = \frac{1}{2} \left(\frac{1}{[(\tau_{12})_{ult}]^2} \right) \quad (11)$$

Unidirectional lamina is assumed to be under plane stress, therefore $\sigma_3 = \tau_{13} = \tau_{23} = 0$

The equation reduces to [13, 14]:

$$\left[\frac{\sigma_1}{(\sigma_1^T)_{ult}} \right]^2 - \left[\frac{\sigma_1\sigma_2}{(\sigma_1^T)_{ult}^2} \right] + \left[\frac{\sigma_2}{(\sigma_2^T)_{ult}} \right]^2 + \left[\frac{\tau_{12}}{(\tau_{12})_{ult}} \right]^2 < 1 \quad (12)$$

Tsai-Hill theory considers the interaction among the three unidirectional lamina parameter. One of the drawbacks of the Tsai-Hill failure theory is that it does not distinguish between compressive and tensile strength in the equation. This can result to the underestimation of the maximum load that can be applied when compared to other failure theories. Tsai-Hill failure criterion can underestimate the failure stress of a component because the transverse strength of the unidirectional lamina is less than the transverse compressive strength.

2.5.2 Tsai Wu Failure Criterion

Tsai-Wu applied the failure criterion to a lamina in plane stress. A lamina is considered to fail if it does not satisfy the equation 13 [4,10]:

$$H_1\sigma_1 + H_2\sigma_2 + H_6\tau_{12} + H_{11}\sigma_1^2 + H_{22}\sigma_2^2 + H_{66}\tau_{12}^2 + 2H_{12}\sigma_1\sigma_2 < 1 \quad (13)$$

Tsai-Wu failure criterion is more general than the Tsai-Hill failure criterion because it distinguishes between the compressive strength and tensile strength of lamina. Where:

$$H_1 = \frac{1}{(\sigma_1^T)_{ult}} - \frac{1}{(\sigma_1^C)_{ult}} \tag{14}$$

$$H_{11} = \frac{1}{(\sigma_1^T)_{ult}(\sigma_1^C)_{ult}} \tag{15}$$

$$H_2 = \frac{1}{(\sigma_2^T)_{ult}} - \frac{1}{(\sigma_2^C)_{ult}} \tag{16}$$

$$H_6 = 0 \tag{17}$$

$$H_{66} = \frac{1}{(\tau_{12})_{ult}^2} \tag{18}$$

$$H_{12} = -\frac{1}{2(\sigma_1^T)_{ult}^2} \tag{19}$$

as per Tsai Hill failure theory [13,14].

Where $(\sigma_1^T)_{ult}$ is the tensile strength in fiber direction, $(\sigma_1^C)_{ult}$ is the compressive strength in the fibre direction, $(\sigma_2^T)_{ult}$ is the tensile strength in transverse direction, $(\sigma_2^C)_{ult}$ is the compressive strength in transverse direction, and $(\tau_{12})_{ult}$ is the shear strength.

2.6 Procedure for Loading of UAV Wing During Structural Test

The assembled UAV wing was subjected to structural test. Firstly, a gripping region was created at the root of the wing. The gripping region was created using the sisal fibre and the epoxy/hardener in order to simulate a fixed region. The gripping region acts as a holder during structural testing. The gripping region was used to ensure a fixed wing-fuselage interface region during testing. The Figure 8 shows the UAV wing being subjected to loading using sandbags and the deflection of wing being recorded using dial guage. The gripping region is shown in figure 9 and figure 10 shows the arrangement of the spar and ribs on the UAV wing skin. Figure 11 shows the fully assembled UAV wing. The UAV wing was inverted during testing since the wing loading is expected to be acting at the bottom of the wing. After gripping the UAV wing, the wing was divided into four equal sections. The UAV wing was subjected to wing loading as calculated using the Schrenk method for UAV of different masses. The deflection was recorded using a dial guage at the wing tip. The results were recorded and compared to simulation result.

The wing was subjected to various loadings under the regulations of Federal Aviation Regulation (FAR) part 23: Airworthiness Standard [8]. The limit load factor that was used was 3.8. It is used to find the maximum wing loading which would be experienced during flight and is multiplied with a safety factor of 1.5 to attain the ultimate load factor of 5.7. For a 3kg UAV the ultimate load is calculated as follows: . The UAV wing is divided into four sections using Schrenk method. The distributed load is divided into four sections: Section 1: 23.72/9.81=2.42kg; Section 2 = 22.78/9.81= 2.32kg; Section 3: 20.56/9.81 =2.10kg; Section 4: 15.74/9.81=1.61kg. The Ultimate load was divided by 2 since the simulated wing and tested was a half span [12, 13].

For a 3.5kg UAV the ultimate load was calculated as follows: . The distributed load was divided into four sections: Section 1: 27.63/9.81=2.82kg; Section 2: 26.54/9.81= 2.71kg; Section 3: 23.95/9.81 =2.44kg; Section 4: 18.334/9.81 =1.87kg. Refer to Table 4.



Figure 8 UAV wing subjected to loading using sandbags to determine its structural strength at the mechanical workshop, Bayero University Kano.



Figure 9 Fixture made from Sisal fibres and Epoxy Matrix attached to the root of the UAV wing to simulate the fuselage wing interface



Figure 10 Placement of the Spar on the wing skin and image of the ribs



Figure 11 Complete Unmanned Aerial Vehicle Wing

3. Result and Discussion

3.1 Performance Evaluation of UAV Wing Using Abacus Finite Element Method Software

Tsai Hill and Tsai Wu's failure criterion was used to analyze the failure of the UAV wing using Abacus FEM software. The Mechanical Properties used for Finite element Analysis includes Young's Modulus: E1, E2, Poissons Ratio: ν_{12} , Shear Modulus: G12, G13 and G23. Furthermore, other Strength parameters needed for the Tsai-Hill and Tsai-Wu failure criterion includes Longitudinal Tensile Strength, Longitudinal compressive Strength, Transverse Tensile Strength and Transverse Compressive Strength, in-plane shear strength and density(ρ). The section shows the images of the simulations results conducted for the UAV wing while subjecting the wing to various loading. The wing loading is based on the total mass of the UAV multiplied by ultimate load factor of 5.7 and acceleration due to gravity 9.81m/s². The factor is based on Federal Aviation regulation [11].

Mesh convergence studies was performed using h-refinement by reducing the size of elements to find the point at which the solution converges. The mesh convergence study graph is shown in figure 12. The Ultimate load used for the mesh convergence study was 167.5N (3kg). The result from the mesh convergence study is shown in Table 3. The result shows that as the number of element changes there is a significant change in the Tsai Hill, Tsai Wu failure criterion and the deflection of the UAV wing. Initially, a Global seed mesh size of 5mm was used to attain a Tsai Hill Value of 0.1274, as the mesh size was reduced to 4mm, the Tsai Hill value attained was 0.1335. The Tsai Hill value increased by a percentage of 4.79% from the 5mm size to 4mm. For the Global seed mesh from 0.5mm to 0.4mm. The Tsai Hill value increased by a percentage of 2.24%. The result showed a minimum increase in percentage difference as a result of increasing number of elements. A global seed mesh of 0.5mm was chosen for other simulations. The Element type chosen was the S3R S4R. The number of elements used for the simulations are 627574 and the no of nodes used are 606365.

S3R- 3-node triangular general-purpose or conventional shell/displacement shell with reduced integration and finite membrane strains. The nodes have six degree of freedom.

S4R is a 4-node quadrilateral, stress/displacement shell element, reduced integration with hourglass control and a large-strain formulation. The nodes have six degree of freedom [9].

Table 3. Mesh convergence study of the UAV wing

Value (Tsai Hill)	Tsai Wu	Deflection(mm)	No of Nodes	Number of Elements	Global Seed(mm)
0.1274	0.1319	4.846	6354	6644	5
0.1335	0.1382	4.834	9678	10100	4
0.1415	0.1465	4.826	17382	18055	3
0.1628	0.1700	4.817	151457	156861	1
0.1701	0.1780	4.816	269500	278638	0.75
0.1782	0.1872	4.815	606365	627574	0.50
0.1822	0.1918	4.815	945663	978263	0.4
0.1850	0.1949	4.815	1236069	1278832	0.35

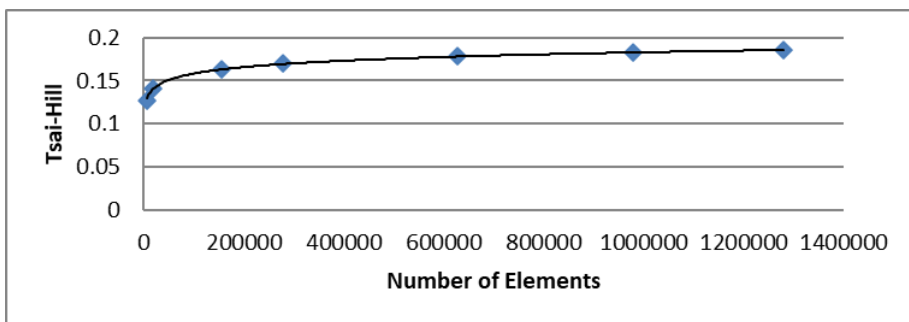


Fig. 12 Mesh convergence study of the UAV wing

The simulation results show the UAV wing response to wing loading. Tsai Hill, Tsai Wu failure criterion and deflections of the UAV wing is used to analyze the failure response of the wing.

The Figure 13-15 shows the Tsai Hill, Tsai Wu failure criterion value and the deflection of the UAV wing. The result in figure 13 shows that when a load of 167.75N (3kg UAV) is applied to the UAV wings the wing has a Tsai Hill failure value of 0.1767, Tsai Wu value of 0.1856 and a maximum wing deflection of 4.757mm. The Tsai Hill and Tsai Wu failure values are both less than 1 meaning that it satisfies their failure criterion.

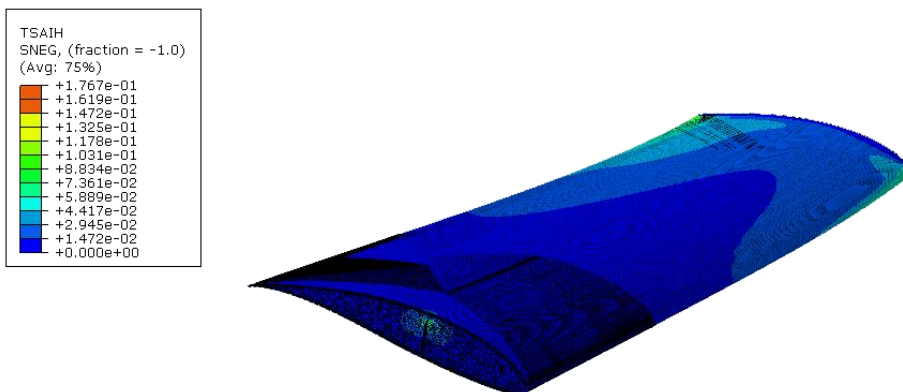


Fig. 13 Failure analyses of 3kg UAV (Tsai Hill)

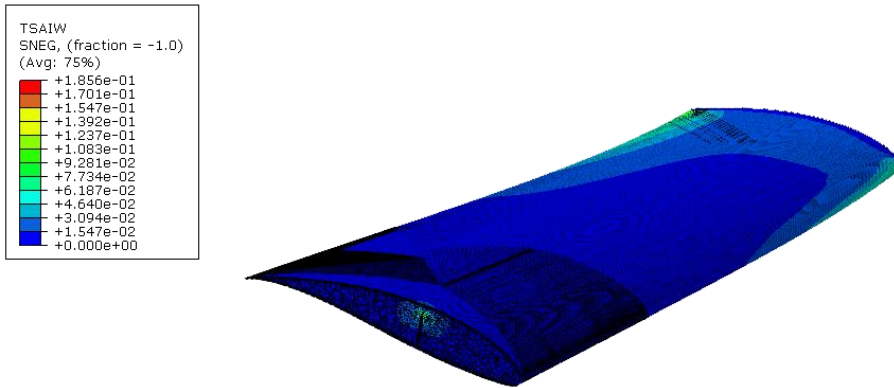


Fig. 14 Failure analyses of 3kg UAV (Tsai Hill)

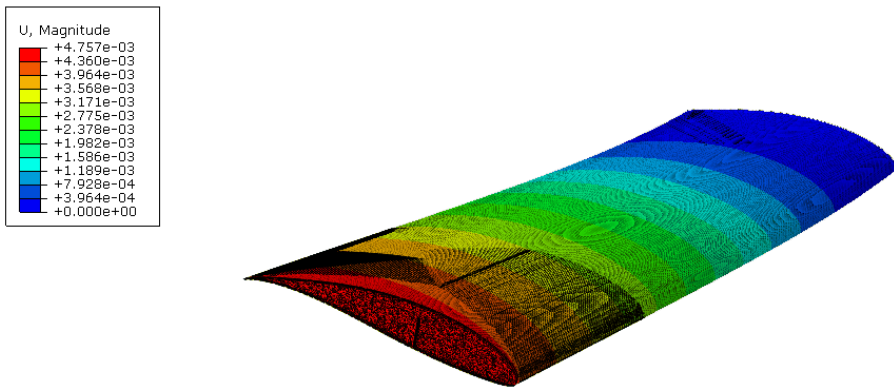


Fig. 15 Deflection of 3 kg unmanned aerial vehicle wing in meters

For figure 16-18, the load applied for a 4.5kg UAV wing was 251.63N distributed over both wings. Since half span of the wing was subjected to the simulation, half of the load was distributed over the wing. The result showed that after subjecting the UAV wing to wing loading, the wing had a Tsai Hill, Tsai Wu and deflection value of 0.265, 0.2784 and 7.135mm respectively. The Tsai Hill and Tsai Wu value satisfies their failure criterions because both values are less than 1.

For figure 19-21, the load applied for a 16kg UAV wing was 895N distributed over both wings. The result showed that after subjecting the UAV wing to wing loading, the wing had a Tsai Hill, Tsai Wu and deflection value of 0.9422, 0.9899 and 25.37mm respectively. The Tsai Hill and Tsai Wu value satisfies their failure criterions because both values are less than 1. Simulation was also performed using Carbon fibre epoxy as the material for the UAV wing. The UAV wing was subjected to wing loading of 167.5N to 951N. The Tsai Hill value was between 0.004667 to 0.02644 respectively and the Tsai Wu value was between 0.004740-0.0266 respectively for a wing loading of 167.5N to 951N. The deflection of the UAV wing was between 0.09576mm to 0.5427mm respectively. The results clearly showed that Carbon fibre epoxy composite has higher resistance to failure and higher resistance to deflection. The result of the Carbon fibre epoxy wing analysis is shown in table 6. At the wing loading of 895N, the SterculiaSetigeraDelile fibre- PterocarpusErinaceus epoxy composite wing had a Tsai-Hill value (0.9425), Tsai-Wu (0.9902) and deflection

(25.37mm) for deflection while for the Carbon fibre epoxy composite wing had a Tsai-Hill value (0.0249), Tsai-Wu (0.02528) and deflection (0.5107mm) respectively.

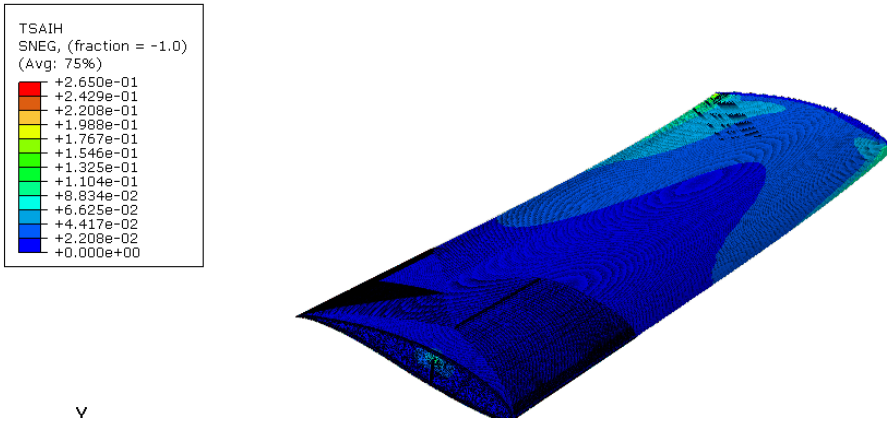


Fig. 16 Failure analyses of 4.5 kg UAV (Tsai Hill).

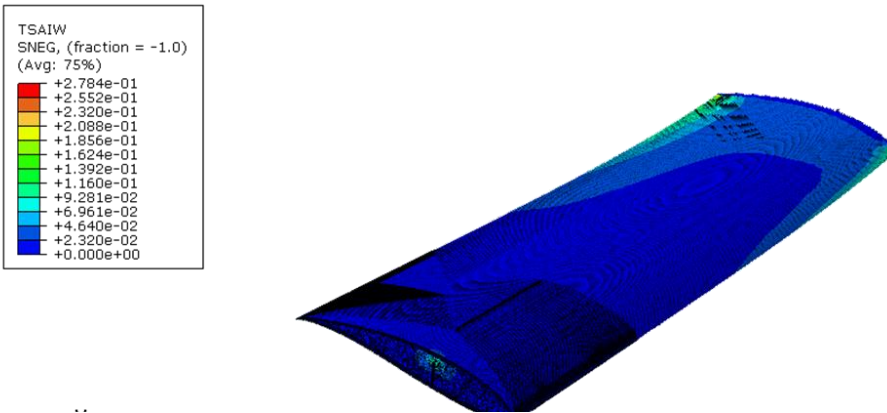


Fig. 17 Failure analyses of 4.5 kg UAV (Tsai Wu)

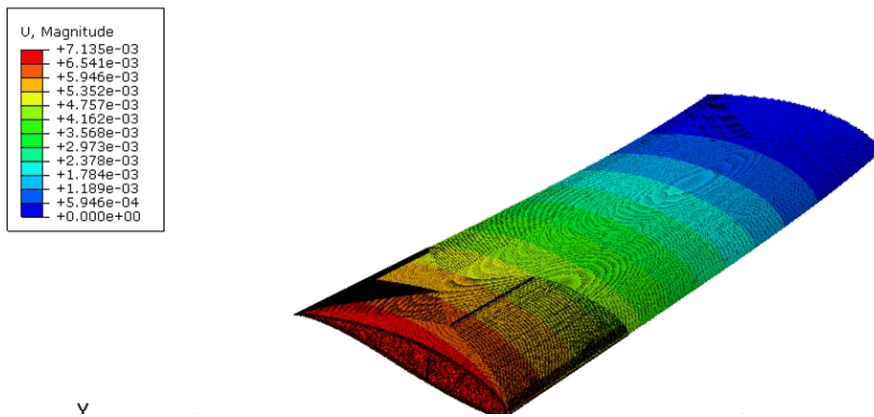


Fig. 18 Deflection of 4.5 kg unmanned aerial vehicle in meters

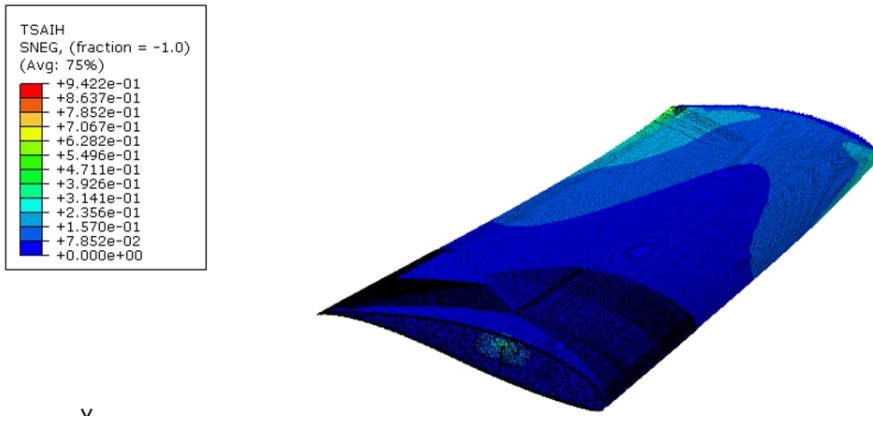


Fig. 19 Failure analyses of 16kg UAV (Tsai Hill)

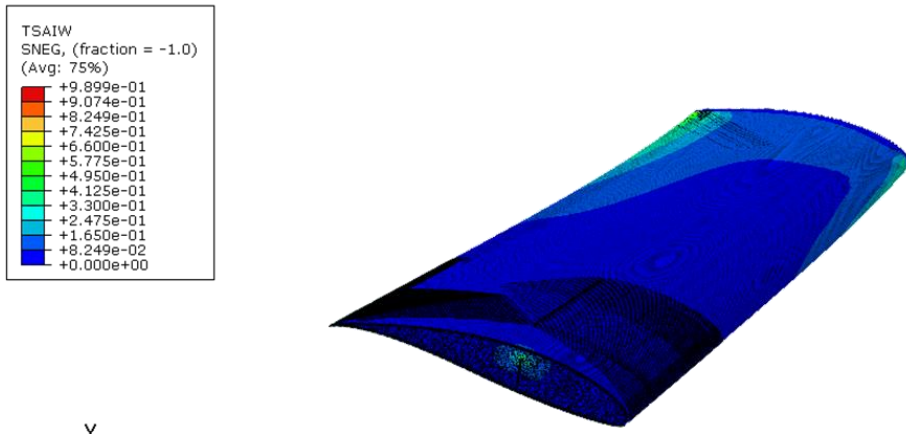


Fig. 20 Failure analyses of 16kg UAV (Tsai Wu)

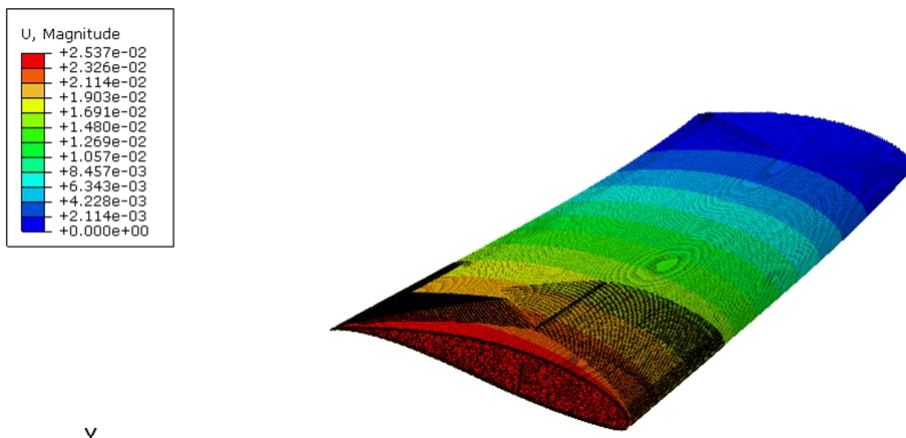


Fig. 21 Deflection of 16 kg unmanned aerial vehicle in meters

3.2 Structural Testing of the Unmanned Aerial Vehicle Wing

Structural test was performed on the wing with a wing loading from 167.75 to 335.50N (3 to 6kg UAV). The result shows the maximum deflection of the Unmanned Aerial Vehicle wing when subjected to wing loading using sand bag is shown in Table 4. The results were compared to result obtained from simulation using Abaqus Simulia software. The result showed that the UAV wing could withstand a wing loading of 335.50N (6kg).

Table 4. Loads placed in different sections of the UAV wing and its deflections

Ultimate load(N)	Section 1(kg)	Section 2(kg)	Section 3(kg)	Section 4 (kg)	Maximum Deflection at wingtip(mm)	
					Simulation Result	Experimental Result
167.5(3kg)	2.42	2.322	2.10	1.61	4.757	5
195.71 (3.5kg)	2.82	2.71	2.44	1.87	5.550	6
223.668 (4kg)	3.224	3.10	2.80	2.14	6.342	8
251.63 (4.5kg)	3.63	3.48	3.14	2.40	7.135	10
279.585 (5.0kg)	4.024	3.86	3.49	2.67	7.935	11
335.502 (6.0kg)	4.83	4.64	4.186	3.20	9.519	13

Table 5. Tsai-Hill, Tsai-Wu failure criterion and deflection of UAV wing

Ultimate load(N)	Tsai Hill failure index	Tsai Wu failure index	Maximum Deflection at wingtip (mm)		% Difference between Experimental and Simulation Deflection
			Simulation Result	Experimental Result	
167.5 (3kg)	0.1767	0.1856	4.757	5	5.11
195.71 (3.5kg)	0.2061	0.2166	5.550	6	8.10
223.668N (4kg)	0.2356	0.2475	6.342	8	26.14
251.63(4.5 kg)	0.2650	0.2784	7.135	10	40.15
279.585 (5.0kg)	0.2947	0.3096	7.935	11	38.63
335.502 (6.0kg)	0.3535	0.3714	9.519	13	36.57
447.336 (8.0kg)	0.4711	0.4950	12.69	-	-
559.17 (10kg)	0.5893	0.6191	15.87	-	-
726.921 (13kg)	0.7656	0.8043	20.61	-	-
838.755 (15kg)	0.8838	0.9286	23.80	-	-
895 (16kg)	0.9425	0.9902	25.37	-	-
951 (17kg)	1.002	1.053	26.98	-	-

The Ultimate load the wing can withstand from Table 5 was 895N based on the TsaiHill and Tsai Wu failure Index. In order to find the Ultimate load factor, for a 4.5kg UAV the Ultimate load factor was found using:

$$UL=nW$$

$$895=n \times 4.5 \times 9.81$$

$$n=20.27$$

Table 6. Tsai-Hill, Tsai-Wu failure criterion and Deflection of UAV wing for woven carbon fibre epoxy

Ultimate load(N)	Tsai Hill failure index	Tsai Wu failure index	Maximum Deflection at wingtip (mm)
			Simulation Result for woven carbon fibre epoxy material
167.5 (3kg)	0.004667	0.004740	0.09576
195.71 (3.5kg)	0.005445	0.005530	0.1117
223.668N (4kg)	0.006222	0.006320	0.1277
251.63 (4.5kg)	0.007000	0.007110	0.1436
279.585 (5.0kg)	0.007778	0.007900	0.1596
335.502 (6.0kg)	0.009333	0.009479	0.1915
447.336 (8.0kg)	0.01244	0.01264	0.2544
559.17 (10kg)	0.01556	0.01580	0.3192
726.921 (13kg)	0.02022	0.2054	0.4150
838.755 (15kg)	0.02333	0.02370	0.4788
895 (16kg)	0.0249	0.02528	0.5107
951 (17kg)	0.02644	0.02686	0.5427

3.3 Comparison Between Simulation and Experimental Testing of the UAV Wing

The material selected for the composite UAV wing was the Cold SSD 5% PTE wood dust 7.5% at 0-degree orientation. The UAV wing performance was simulated using the ABACUS software with various wing loadings on the wing. In this research Tsai Hill and Tsai Wu failure criteria were used to examine the ability of the optimum composite material to withstand load [15]. The results from Table 5 have shown that the UAV wing produced satisfies the Tsai-Hill and Tsai Wu failure criterion of being less than 1. Simulation result shows that the UAV wing could withstand a wing loading from 167.75N to 895N. Structural test was performed on the wing with a wing loading from 167.75 to 335.50N (3 to 6kg UAV). The UAV wing successfully resisted the loading. However, for the wing tip deflection there was a variation between 5.11%-40% between the maximum wing deflection simulations to the experimental result. The result showed that the wing could withstand the most critical flight load distribution in conformation with the Federal Aviation Regulation (FAR) part 23 Airworthiness for a normal category general aviation airplane with an Ultimate design load factor of 5.7. At the point of failure the wing could withstand

an Ultimate load factor of 20.27 which is 255.6% higher than the prescribed Ultimate design load factor of 5.7. This means that the UAV wing can withstand a load factor that is 255.6% higher than the prescribed ultimate load factor 5.7. For good comparison between the simulation and experimental result, the UAV manufacturer needs to ensure good bonding at the interface between the wing and the fuselage which is the key to good wing performance [5, 7].

3.4 Comparison Between Carbon Fibre Epoxy Composite and SSD fibre/PTE Wood Dust Epoxy Composite Wing

For the Carbon fibre epoxy composite UAV wing an Ultimate load of 251.63N(4.5kg mass UAV) was applied to the wing, the maximum wing deflection recorded from the Abaqus simulation result was 0.1436mm as shown in table 6 while result for the SSD fibre/PTE wood dust epoxy composite wing simulation the recorded result was 7.135mm. There is a percentage difference of 98% in the maximum deflection between the two materials. The carbon fibre has greater resistance to deflection. For Carbon fibre epoxy composite an Ultimate load of 895N (16kg mass UAV) was applied to the UAV wing, the maximum deflection recorded from the Abaqus simulation result was 0.5107mm while result for the SSD fibre/PTE wood dust epoxy composite wing simulation the recorded result was 25.37mm. There is a percentage difference of 98% in the maximum deflection between the two materials. The carbon fibre has greater resistance to deflection. The carbon fibre epoxy composite UAV wing as expected has higher resistance to wing deflection. However, both the materials can withstand the wing loading requirement of the Federal Aviation Regulation. The advantages of SSD fibre/PTE wood dust epoxy composite when compared to the carbon-epoxy material is that the material is renewable, environmentally friendly, less pollution in the production of material and lower cost. The SSD fibre/PTE wood dust performance could be improved by optimization techniques.

4. Conclusion

In this research a 3 dimensional model of UAV wing was drawn, assembled and simulated using Abaqus software. The simulation results showed that the UAV wing could withstand a wing loading of 167.75 to 895N (3kg to 16kg UAV) meaning an Ultimate load factor of 20.27. This means that it could withstand an Ultimate load factor of 20.27 for a UAV with a 4.5kg mass. The Ultimate load factor of the wing was found by dividing the Ultimate load the Wing could withstand which was 895N by the UAV weight of 4.5kg multiplied by the acceleration due to gravity. The ultimate load factor given by the Federal Aviation Regulation was 5.7 meaning that the UAV wing should be able to withstand an ultimate load factor of 5.7. The 167.75 to 895N are the forces distributed incrementally on the UAV wing to analyze whether the wing could withstand the Ultimate load factor given by the Federal Aviation Regulation. The result means that components of higher weight such as weaponry and standard high quality cameras could be attached to the UAV. The UAV wing was successfully manufactured and structurally tested to validate the results from the simulation. The UAV wing was subjected to wing loading 167.75N to 335.50N (3kg to 6kg UAV mass). The UAV wing was able to withstand the pressure applied using sandbags successfully. The distribution of pressure was found using Schrenk method. In summary light weight Unmanned Aerial Vehicle wing was successfully produced using Wood fibre and wood dust epoxy composite and it was able to withstand the estimated wing loading. The composite produced has the potential to be used in the Aerospace industry due to its low density. Weight is an important factor in the aerospace industry as it affects the fuel consumption of aerospace vehicles. Furthermore, the production of synthetic fibres for composites has a negative impact on the environment. The use of natural fibre hybrid composite provides locally available wood fibres and wood dust for potential production of the Unmanned Aerial vehicles.

References

- [1] Warsi FA, Hazry D, Ahmed FS, Joyo M K, Tanveer MH, Kamarudin H. Yaw, Pitch and Roll controller design for fixed-wing UAV under uncertainty and perturbed condition. IEEE 10th International Colloquium On Signal Processing and its Applications. Kuala Lumpur, 2014. <https://doi.org/10.1109/CSPA.2014.6805738>
- [2] Rana S, Figueiro R. Advanced Composite Material for Aerospace Engineering: Processing Properties and Applications., Duxford, United Kingdom, Wood head Publishing, 2016. <https://doi.org/10.1016/B978-0-08-100037-3.00001-8>
- [3] Hsu TR. Applied Engineering Analysis, New Jersey, USA, John Wiley and Sons Ltd, 2018.
- [4] Rumayshah K, Prayoga A, Moelyadi MA. Design of High Altitude Long Endurance UAV: Structural Analysis of Composite Wing using Finite Element Method. IOP Conference Series: Journal of Physics: Conference Series 1005. IOP Publishing, 2018. <https://doi.org/10.1088/1742-6596/1005/1/012025>
- [5] Sullivan R, Hwang Y, Rais-Rohani M, Lacy T. Structural Analysis and Testing of an Ultralight Unmanned-Aerial-Vehicle Carbon-Composite Wing. Journal of Aircraft, 2009; 46(3): 814-820. <https://doi.org/10.2514/1.36415>
- [6] Kanesan G, Mansor S, Abdul-Latif A. Validation of UAV Wing Structural Model for Finite Element Analysis. Jurnal Teknologi, 2014; 71(2): 1-5. <https://doi.org/10.11113/jt.v71.3710>
- [7] Hutagalung MA, Latif AA, Israr HA. Structural Design Of UAV Semi-Monoque Composite Wing. Journal of Transport System Engineering, 2016; 3(1): 26-34.
- [8] Airfoiltools. WORTMANN FX 63-137 AIRFOIL (fx63137-il) Xfoil prediction polar at RE=200,000 Ncrit=9. [Internet]. Airfoiltools; 2021, Available from <http://airfoiltools.com/polar/details?polar=xf-fx63137-il-200000>
- [9] Dassault Systems. Abaqus 6.11: Abaqus/CAE User's Manual. Rhode Island: Dassault Systems, 2011.
- [10] Tahir NM, Alhaji AU and Abdullahi I. (In press). Optimization Of Mechanical Properties Of Hybrid Biocomposite From Sterculia Setigera Delile Fibre And Pterocarpus Erinaceus Wood Dust Epoxy. Wood Industry and Engineering.
- [11] Federal Aviation Administration. User's Guide for FAR23 Loads Program [Internet]. Federal Aviation Administration; 1997. Available from: <http://www.tc.faa.gov/its/worldpac/techrpt/ar96-46.pdf>
- [12] Soemaryanto A, Rosid N. Verification Of Schrenk Method For Wing Loading Analysis Of Small Unmanned Aircraft Using Navierstokes Based Cfd Simulation. Jurnal Teknologi Dirgantara, 2018; 15(2): 161-166. <https://doi.org/10.30536/j.jtd.2017.v15.a2747>
- [13] Kaw A. Mechanics of composite materials, 2nd edition, Florida, U.S.A, Taylor and Francis, 2006. <https://doi.org/10.1201/9781420058291>
- [14] Kolios AJ, Proia S. Evaluation of the Reliability Performance of Failure Criteria for Composite Structures. World Journal of Mechanics, 2012; 5: 162-170. <https://doi.org/10.4236/wjm.2012.23019>
- [15] Rajanish M, Nanjundaradhya NV, Sharma RS and Bhaskar PA. Review Of Failure Of Composite Materials. International Journal of Engineering Research and Applications (IJERA), 2013; 3(2):122-124.



Research Article

Adhesion strength evaluation for plasma-sprayed coatings based on intensity of singular stress

Nikolay Dolgov^{1,2,a}, Maris Hauka^{*3,b}, Leonids Vinogradovs^{3,c}

¹G.S.Pisarenko Institute for Problems of Strength, Nat. Ac. Sci. of Ukraine, 2 Timiryazevska Str, Kyiv, Ukraine

²National Transport University, 1 Omelianovycha-Pavlenka Str, Kyiv, Ukraine

³Department of Aeronautics, Riga Technical University, Riga, Latvia

Article Info

Article history:

Received 13 Nov 2021

Revised 9 May 2022

Accepted 6 June 2022

Keywords:

Finite Element Method;
Plasma-sprayed coatings;
Tensile testing;
Coated specimens;
Co-Cr alloy;

Abstract

This paper presents a new test method, including coated specimen, shear testing procedure, and algorithm for evaluation of critical intensity of singular stress for coating, for more accurate and complete characterization of adhesion strength.

A procedure for determining the critical intensity of singular stress for coating is presented in this paper. In this paper, the coated specimen has been analysed in terms of the intensity of singular stress field. The adhesion strength of plasma-sprayed coatings was estimated in terms of the intensity of singular stresses in the vicinity of the free edge of the coating. The finite element analysis for normal and tensile stress distributions of the coated specimens are obtained by using different mesh sizes (fine, medium, and coarse size). Tensile testing of flat metal samples with plasma-sprayed coatings of Co-Cr alloy of various thicknesses (90, 100, 160 μm) was performed. The results show that the adhesion strength of the tested coatings can be represented by a critical stress of 1.34, 0.94, 0.88 $\text{MPa m}^{0.43}$ for thicknesses of 90, 100, 160 μm , respectively.

© 2022 MIM Research Group. All rights reserved

1. Introduction

Experimental studies of specimens with coatings indicate, that the delamination of the coating from the substrate initiates from the free edge of the coating even in absence of an initial crack in the interface [1-4]. The coating delamination of the item initiates from the free edge due to the singularity of stresses. The existing studies of the stress state in deformed coating are taking into account only the concentration of shear stresses in the nearby area of the free edge of the coating [5-7]. So, it is necessary to finally study the stress fields singularity dependency on the coated specimen geometric characteristics, as well as the substrate and coating elasticity characteristics.

The study of the singularity of stress fields was initiated in [8], in which the singularity of stresses in plates of various configurations, from homogeneous as well as composite materials was determined. The distribution of stress in a body formed by dissimilar isotropic elastic materials was considered in the work [9]. The distribution of stress in systems of dissimilar materials was also investigated in the work [10]. The problem for an anisotropic material consisting of a system of anisotropic layers separated by isotropic layers was solved in the work [11]. The problem of determining the singularity of stress fields for wedges made of two different materials was considered in numerous works [12-16].

*Corresponding author: maris.hauka@rtu.lv

^a orcid.org/0000-0002-3962-7551; ^b orcid.org/0000-0003-2134-7647; ^c orcid.org/0000-0003-2257-8607;

DOI: <http://dx.doi.org/10.17515/resm2022.365ma1113>

Res. Eng. Struct. Mat. Vol. 8 Iss. 4 (2022) 695-706

Research of this field is well covered in reviews [17, 18]. There are various approaches to assessing the stress state in layered materials, both analytical methods [19-23], and numerical methods [23, 24]. The investigation of the stress fields singularity in case of thermal barrier coatings deduced that, if the angle of the free edge is decreases to an angle of 60 degree, the coating durability increases [25, 26]. The goal of this paper is to investigate the singular stress fields that cause the coating delamination.

2. The Evaluation of Stress Fields Intensity in A Coated Sample

The field of stress is determinate as [27, 28]:

$$\begin{aligned}
 \sigma_r^c &= \frac{K}{r^{1-\lambda}} f_r^c(\lambda, \theta); \\
 \sigma_r^s &= \frac{K}{r^{1-\lambda}} f_r^s(\lambda, \theta); \\
 \sigma_\theta^c &= \frac{K}{r^{1-\lambda}} f_\theta^c(\lambda, \theta); \\
 \sigma_\theta^s &= \frac{K}{r^{1-\lambda}} f_\theta^s(\lambda, \theta); \\
 \tau_{r\theta}^c &= \frac{K}{r^{1-\lambda}} f_{r\theta}^c(\lambda, \theta); \\
 \tau_{r\theta}^s &= \frac{K}{r^{1-\lambda}} f_{r\theta}^s(\lambda, \theta),
 \end{aligned}
 \tag{1}$$

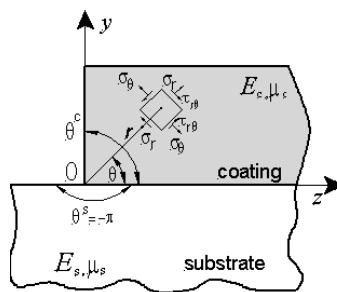


Fig. 1. The detail of “coating”-“substrate” system [28]

The equations for the normal σ_θ^c and shear $\tau_{r\theta}^c$ stresses in the coating from (1) can be written as:

$$\begin{aligned}
 \sigma_\theta^c &= K_1 r^{\lambda-1} ; \\
 \tau_{r\theta}^c &= K_2 r^{\lambda-1} ;
 \end{aligned}
 \tag{2}$$

Where,

$$K_1 = K f_\theta^c(\lambda, \theta);$$

$$K_2 = K f_{r\theta}^c(\lambda, \theta);$$

Transform the equations (2) to look as:

$$\lg \tau_{r,\theta}^c = \lg K_2 + (\lambda - 1) \lg r \quad (3)$$

$$\lg \sigma_{\theta}^c = \lg K_1 + (\lambda - 1) \lg r$$

From equations (3) it can be determined that there is a linear relationship between stresses and distance r if plotting graphs in logarithmic coordinates. If $\lg \sigma_{\theta}^c$ is shown related to $\lg r$, the graph-line has a slope $\lambda - 1$, the graph will intersect the ordinate axis at a point with a y-coordinate $\lg K_1$. Therefore, knowing the value, $\lg \sigma_{\theta}^c$ at $\lg r = 0$, it is possible to determine the value of $K_1 = 10^{\lg \sigma_{\theta}^c}$.

3. Methods and Materials

The Co-Cr coating [29, 30] with thickness of 90, 100 and 160 μm has been plasma sprayed on stainless steel substrate (1Kh18N9 stainless steel, containing 0.9% C, 16.7% Cr, 7.8% Ni, 0.37% Si, and 1.47% Mn) thickness 1.5 mm (Fig. 2). The coating was sprayed only partially on steel substrate so as to leave out free edge of the coating (Fig.1). The elastic characteristics of the substrate and the coating were determined under static tension of coated specimen following methodology described in [30].



Fig. 2. Specimen with the plasma sprayed coating (Co- Cr alloy coating; Left view) before the tensile test.

The thickness of the coating is comparatively thick so it is measure using a micrometre. Delamination moment can be fixed through visual observation, as acoustic emission techniques have shown that the moment of coating delamination visually gives an error within 2% boundaries (Not explained further in this study as it is not the object of the research).

The thickness of coating was chosen based on both its intended functionality- to increase wear and corrosion resistance and economic considerations- to not have wasted material. It was proven that coating thickness of 90 μm would start providing some functionality, while thicker coating, while increasing functionality, would increase expenditure in larger scale (Not explained further in this study as it is not the object of the research).

4. Results and Discussion

It should be noted, that the use of the K_{cr} value as a criterion is also possible for coatings in which the angle of the free edge is not equal to 90° . Such coatings are widely used and the deposition of coatings with a free edge angle $\theta_c < 90^\circ$ is recommended by the technological process of plasma coating spraying [31]. The results show that the intensity of singular stresses for the tested metal coatings is dependent weakly on the

thickness of the coating. It can be seen, that the analytical method for determining the singularity factor λ is more accurate than the method based on the approximation of stresses obtained using finite element modelling. The critical intensity of singular stress K_{cr} , measured using the proposed technique, can be used as a criterion to evaluate adhesion strength for coatings.

To determine the critical singular stresses that would cause the failure of the coating, the specimen was subjected to tensile load.

The delamination of the coating (sample with coating thickness $90 \mu\text{m}$) occurs under stress that corresponds to the moment when the load on the uncoated substrate reach $\sigma_{sub} = 752 \text{ MPa}$.

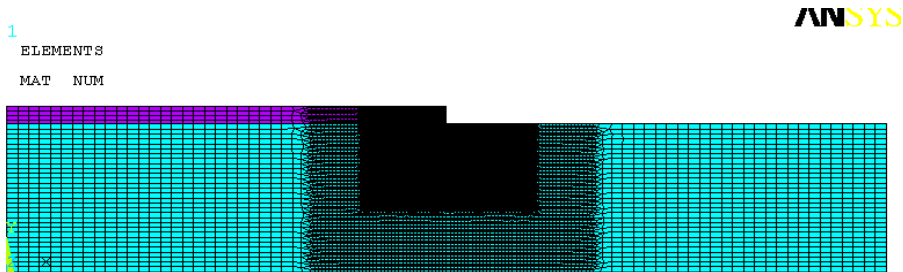


Fig. 3. Coated specimen's finite elements model. Minimal size of mesh $0.2 \mu\text{m}$.

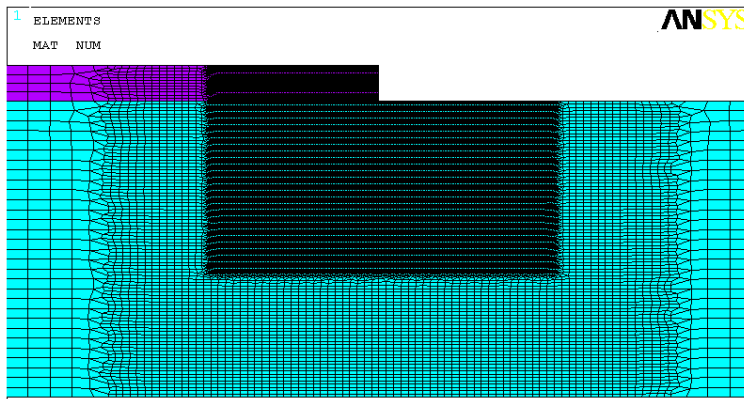


Fig. 4. Part of the finite element mesh model near the free edge of coating and the stress singularity area

The critical stress intensity factor K_{cr} was determined by Finite Element Method (FEM). Specimen's finite element mesh is shown on (Fig.3). The mesh was constructed using half of the specimen. Numerical calculus for elastic solid was made using ANSYS. The finite element mesh in the area of the singularity was made finer. A fragment of the finite element mesh in the area of stress singularity is shown in (Fig.4); the tensile load was applied to the end face of sample. The minimal size of mesh in the area of

stress singularity is 0.2 μm (Fig. 4). The elasticity characteristics of both the coating, and the substrate, were calculated after the tension test as listed in [31], see Table 1.

Table 1. Elasticity characteristics of the coating and its substrate.

	Material	Elastic modulus E , GPa	Poisson Ratio, μ
Substrate	1X18H9	199	0.28
Coating	Co- Cr alloy	70	0.3

The distribution of normal and shear stresses in the area of adhesive contact between the substrate and the coating at a distance r (0.07 ... 100 μm) from the free edge of the coating at $\sigma_{sub} = 752 \text{ MPa}$ are shown in (Fig.5) (logarithmic coordinates). The distribution of stresses in the sample during the delamination of the coating can be seen in (Fig.6) to (Fig.8).

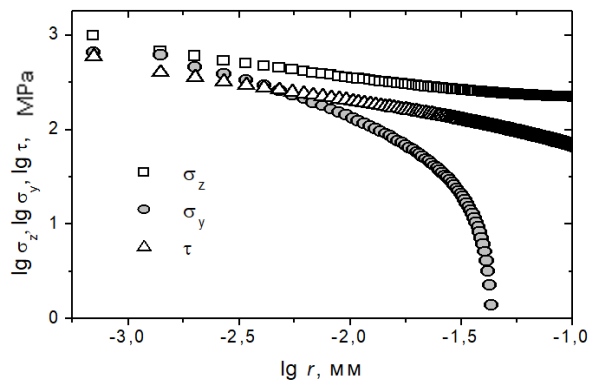


Fig. 5. The distribution of normal and shear stresses in the area of adhesive contact between the substrate and the coating at a distance r (0.07 ... 100 μm) from the free edge of the coating at $\sigma_{sub} = 752 \text{ MPa}$

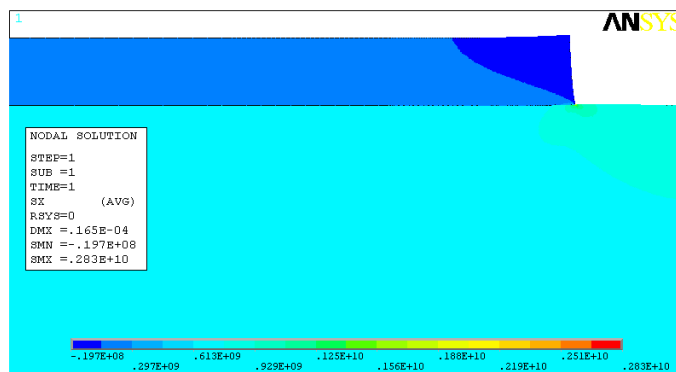


Fig. 6. The distribution of normal stresses σ_z under coating of the specimen during delamination near free edge ($\sigma_{sub} = 752 \text{ MPa}$).

Deviations from linearity seen in Fig.5 are related to the method used to describe fracture mechanics and estimating the singularity of stresses in the vicinity of a singular point, in particular it is caused by the logarithmic scale

(Fig.5) shows that the normal tensile stresses σ_z and shear stresses τ vary approximately linearly in the area corresponding to $r = 0.7 \mu\text{m}$ ($\lg r = -3.15$) to $r \approx 14.4 \mu\text{m}$ ($\lg r \approx -1.84$). This character of the distribution shows that the stress can be described by the formula given in (2). At $r > 14.4 \mu\text{m}$ the character of these expressions ceases to be linear till eventually the singularity disappears. Normal stresses of the σ_y are linear in a much narrower range of r ($0.7 \mu\text{m} < r < 4.8 \mu\text{m}$).

The stress σ_y near the free edge of the coating exceeds the shear stresses τ (Fig.5), meaning, in the area of the coating; the free edge delamination occurs due to the predominant action of normal shear stresses σ_y . Consequently, the investigation of how stress singularity affects the coating adhesion failure must be carried out as for normal delamination stresses σ_y .

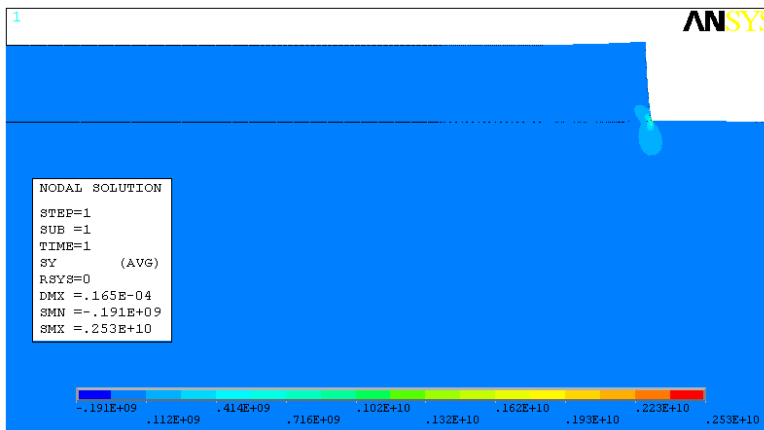


Fig. 7. Normal stresses σ_y distribution under specimen coating delamination near free edge ($\sigma_{sub} = 752 \text{ MPa}$)

As a result of the singularity of the stress near coating free edge [28], the value of the stress might be dependent on how fine the finite element mesh is. To make sure that, the accuracy of K_{cr} does not depends on minimal size of finite element mesh (FEMesh), the simulation was made for three different FEMeshes: sizes; fine $0,2 \mu\text{m}$ (Fig.8); medium $0.7 \mu\text{m}$ (Fig. 9); and coarse $6.2 \mu\text{m}$ (Fig. 10). These simulations allowed to evaluate the area of stress singularity under load σ_{sub} that causes the metal coating delamination. In (Fig.11) normal delamination stresses distribution is shown in three graphs of FEMeshes. Though in the area of the free edge of the coating the stress value depends on FEMeshes size, the curve slope $\lambda-1$, does not depend on FEMesh in graph's linear part $\lg\sigma_y$ compared to $\lg r$. The stresses change is linear in a wide range of r , regardless if fine, middle and coarse FEMeshes. The angle of curve slope for expression (3) can be found analytically [28] or by curve-fitting the linear graph part $\lg\sigma_y$ to $\lg r$. Usually such approximation is made using The Least Square Method (LSM). The analytical approach is more accurate than LSM and also allows to determinate two factors of singularity order (the roots λ_1 and λ_2 for characteristic equation).

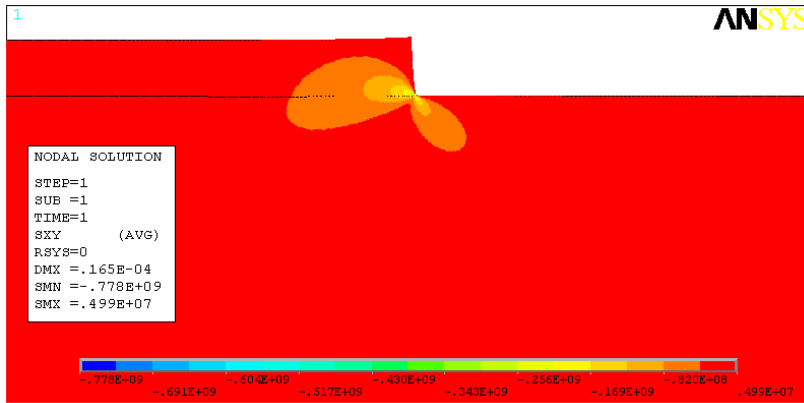


Fig. 8. The shear stresses τ area in a specimen during the coating delamination near its free edge ($\sigma_{sub} = 752$ MPa)

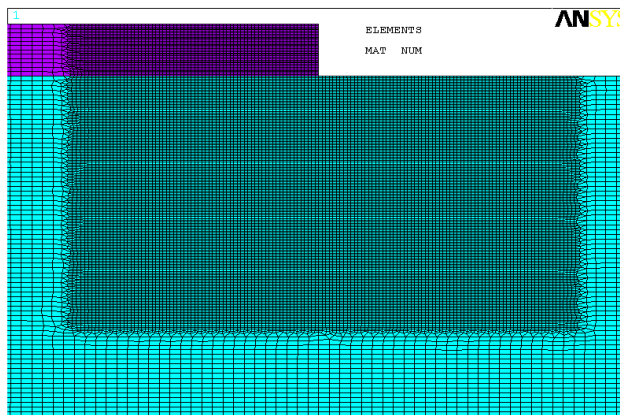


Fig. 9. The FEM of coated specimen (minimal mesh size is $0.7 \mu\text{m}$)

When comparing the singularity order calculated by the analytical method with the value obtained by linear approximation by the LSM, it can be concluded that the approximation has errors corresponding to the size of the FEMesh.

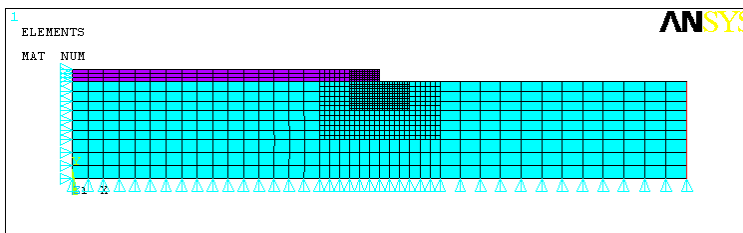


Fig. 10. The FEM of coated specimen (minimal mesh size is $6.2 \mu\text{m}$)

The σ_y values obtained by the FEM can be compared with the stresses in accordance with equations (1). The error associated with numerical calculations can be reduced by creating a finer mesh of finite elements.

Table 2. The Results of Adhesion Properties of plasma-sprayed Coating (Co-Cr alloy) Investigation

Coating thickness $h, \mu\text{m}$	Factors of stress singularity		Ratio $\frac{\lambda}{\lambda_{num}}$	Critical stress intensity K_{cr}	Physical dimension K_{cr} [MPa·m ^{1-λ]}
	The analytical method [25]	The LSM λ_{num}			
90	0.5687	0.5517	1.031	1.34	MPa·m ^{0,43}
100		0.5033	1.130	0.94	
160		0.5429	1.048	0.88	

Plasma-sprayed coatings with a thickness of 100 μm and 160 μm delaminates under loads cause corresponding to stresses of 625 and 340 MPa in the substrate material's uncoated area. A specimen with a coating with a thickness of 160 μm after tensile tests is shown in (Fig. 12). The indicators of the critical stress intensity K_{cr} , as well as the order of the stress singularity, calculated analytically and found using the approximation method, are given in Table. 2. The stress distribution σ_y near the free edge of the coating during delamination of coatings of various thicknesses is shown in (Fig.13).

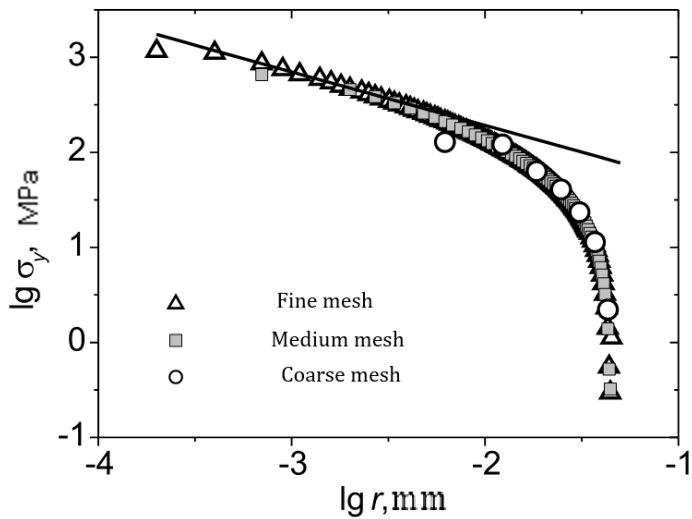


Fig. 11. Impact of FEMeshes size on stress distribution σ_y

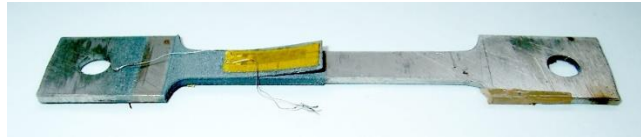


Fig. 12. Plasma-coated (Co-Cr alloy, thickness 160 μm) Sample after tensile load test

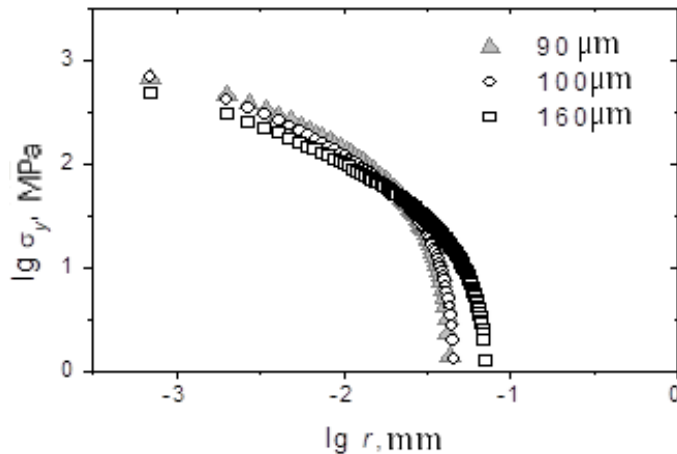


Fig. 13. Stress σ_y distribution during delamination of plasma-sprayed coating of various thicknesses.

5. Conclusion

Analysis of the test results shows that the value of K_{cr} for the tested metal coatings is weakly dependent on the thickness of the coating. Thus, the K_{cr} value can be used as a criterion for adhesive destruction of coatings. In addition, it should be noted, that the use of the K_{cr} value as a criterion is also possible for coatings in which the angle of the free edge is not equal to 90° . Such coatings are widely used and the deposition of coatings with a free edge angle $\theta^c < 90^\circ$ is recommended by the technological process of plasma coating spraying. The results show that the intensity of singular stresses for the tested metal coatings is weakly dependent on the thickness of the coating. It can be seen, that the analytical method for determining the singularity factor is more accurate than the method based on the approximation of stresses obtained using finite element modelling. The critical intensity of singular stress, measured using the proposed technique, can be used as a criterion to evaluate adhesion strength for coatings.

Acknowledgement



This work has been supported by the European Regional Development Fund within the Activity 1.1.1.2 "Post-doctoral Research Aid" of the Specific Aid Objective 1.1.1 "To

increase the research and innovative capacity of scientific institutions of Latvia and the ability to attract external financing, investing in human resources and infrastructure” of the Operational Programme “Growth and Employment” (No. 1.1.1.2/VIAA/2/18/326)

Nomenclature

E - elastic modulus (index c refers to coating, index s refers to substrate);

K - stress intensity factor,

K_{cr} - critical stress intensity factor;

K_1, K_2 - mode 1 and mode 2 stress intensity factors;

$f_r^c, f_r^s, f_\theta^c, f_\theta^s, f_{r\theta}^c, f_{r\theta}^s$ - correcting factor for stresses (index c refers to coating, index s refers to substrate);

r, θ - local polar coordinates;

λ - order of stress singularity.

μ - Poisson Ratio (index c refers to coating, index s refers to substrate);

Q_{sub} - the remote stress applying to the substrate in the z direction;

$Q_r, Q_\theta, Q_{r\theta}$ - stress components (index c refers to coating, index s refers to substrate)

σ_y - peeling stress;

σ_z - normal tensile stress;

τ - interfacial shear stress;

FEM - Finite Element Method;

FEMesh - finite element mesh;

LSM - Least Square Method

References

- [1] Lyashenko BA, Veremchuk VS, Dolgov NA, Ivanov VM. Strength and deformation properties of compositions with plasma-sprayed coatings. Strength of Materials.1996; 28;452-454. <https://doi.org/10.1007/BF02209316>
- [2]. Shinde SV, Sampath S.. Interplay between cracking and delamination in incrementally deposited plasma sprayed coatings. Acta Materialia, 2021:215; 117074. <https://doi.org/10.1016/j.actamat.2021.117074>
- [3]. Hafez M, Akila S, Khder M, Khalil A. Reducing Cracks and Delamination in Plasma-Sprayed Coatings of Calcia and Magnesia Stabilized-Zirconia. Microscopy and Microanalysis. 2021: 27(S1); 2360-2362. <https://doi.org/10.1017/S1431927621008497>
- [4]. Xiao YQ, Yang L, Zhu W, Zhou YC, Pi ZP, Wei YG. Delamination mechanism of thermal barrier coatings induced by thermal cycling and growth stresses. Engineering Failure Analysis 2021;121:105202. <https://doi.org/10.1016/j.engfailanal.2020.105202>
- [5] Jiang T, Huang R, Zhu Y. Interfacial Sliding and Buckling of Monolayer Graphene on a Stretchable Substrate. Adv Funct Mater 2013;24:396–402. <https://doi.org/10.1002/adfm.201301999>

- [6] Wu K, Wang YQ, Yuan HZ, Zhang JY, Liu G, Sun J. Interfacial stress transfer mechanism of Cu-Zr amorphous films on polyimide substrates: Effect of deformation-induced devitrification. *Journal of Alloys and Compounds* 2019;783:841–7. <https://doi.org/10.1016/j.jallcom.2019.01.016>
- [7] Panin AV, Shugurov AR, Kazachenok MS, Sergeev VP. Effect of the nanostructuring of a Cu substrate on the fracture of heat-resistant Si-Al-N coatings during uniaxial tension. *Tech Phys* 2012;57:779–86. <https://doi.org/10.1134/s1063784212060205>
- [8] Williams ML. Stress Singularities Resulting From Various Boundary Conditions in Angular Corners of Plates in Extension. *Journal of Applied Mechanics* 1952;19:526–8. <https://doi.org/10.1115/1.4010553>
- [9] Bogy DB. Edge-Bonded Dissimilar Orthogonal Elastic Wedges Under Normal and Shear Loading. *Journal of Applied Mechanics* 1968;35:460–6. <https://doi.org/10.1115/1.3601236>
- [10] Hess MS. The End Problem for a Laminated Elastic Strip — II. Differential Expansion Stresses. *Journal of Composite Materials* 1969;3:630–41. <https://doi.org/10.1177/002199836900300404>
- [11] Puppo AH, Evensen HA. Interlaminar Shear in Laminated Composites Under Generalized Plane Stress. *Journal of Composite Materials* 1970;4:204–20. <https://doi.org/10.1177/002199837000400206>
- [12] Chue C-H, Liu C-I. A general solution on stress singularities in an anisotropic wedge. *International Journal of Solids and Structures* 2001;38:6889–906. [https://doi.org/10.1016/s0020-7683\(01\)00015-4](https://doi.org/10.1016/s0020-7683(01)00015-4)
- [13] Luo Y, Subbarayan G. A study of multiple singularities in multi-material wedges and their use in analysis of microelectronic interconnect structures. *Engineering Fracture Mechanics* 2007;74:416–30. <https://doi.org/10.1016/j.engfracmech.2006.04.032>
- [14] Tan M.A. Analysis of bimaterial wedges using a new singular finite element/ M.A.Tan, S.A.Meguid // *International Journal of Fracture*. 1997; 88(4):373-391. <https://doi.org/10.1023/A:1007427506134>
- [15] Bogy DB, Wang KC. Stress singularities at interface corners in bonded dissimilar isotropic elastic materials. *International Journal of Solids and Structures* 1971;7:993–1005. [https://doi.org/10.1016/0020-7683\(71\)90077-1](https://doi.org/10.1016/0020-7683(71)90077-1)
- [16] Dempsey JP, Sinclair GB. On the stress singularities in the plane elasticity of the composite wedge. *J Elasticity* 1979;9:373–91. <https://doi.org/10.1007/bf00044615>
- [17] Sinclair G. Stress singularities in classical elasticity—I: Removal, interpretation, and analysis. *Applied Mechanics Reviews* 2004;57:251–98. <https://doi.org/10.1115/1.1762503>
- [18] Sinclair G. Stress singularities in classical elasticity—II: Asymptotic identification. *Applied Mechanics Reviews* 2004;57:385–439. <https://doi.org/10.1115/1.1767846>
- [19] Agrawal DC, Raj R. Measurement of the ultimate shear strength of a metal-ceramic interface. *Acta Metallurgica* 1989;37:1265–70. [https://doi.org/10.1016/0001-6160\(89\)90120-x](https://doi.org/10.1016/0001-6160(89)90120-x)
- [20] Dolgov NA, Lyashenko BA, Rushchitskii YaYa, Veremchuk VS, Terletskii VA, Kovalenko AP. Effects of elasticity differences between substrate and coating on the state of stress and strain in a composite. Part 2. Coating tensile stress distribution. *Strength Mater* 1996;28:373–5. <https://doi.org/10.1007/bf02330856>
- [21] Rizov V. Analysis of cylindrical delamination cracks in multilayered functionally graded non-linear elastic circular shafts under combined loads. *Frattura Ed Integrità Strutturale* 2018;12:158–77. <https://doi.org/10.3221/igf-esis.46.16>

- [22] Bulbuk O, Velychkovych A, Mazurenko V, Ropyak L, Pryhorovska T. Analytical estimation of tooth strength, restored by direct or indirect restorations. 105267/jEsm 2019:193–204. <https://doi.org/10.5267/j.esm.2019.5.004>
- [23] Li L-A, Li R-J, Wang S-B, Wang Z-Y, Li T, Li C-W. Stress analysis of film-on-substrate structure under tensile loads. *Mechanics of Materials* 2018;120:1–14. <https://doi.org/10.1016/j.mechmat.2018.02.003>
- [24] Leguillon D, Li J, Martin E. Multi-cracking in brittle thin layers and coatings using a FFM model. *European Journal of Mechanics - A/Solids* 2017;63:14–21. <https://doi.org/10.1016/j.euromechsol.2016.12.003>
- [25] Brodin H, Li XH, Sjoestroem S. Influence on Thermal Barrier Coating Delamination Behaviour of Edge Geometry. *Fracture of Nano and Engineering Materials and Structures* n.d.:273–4. https://doi.org/10.1007/1-4020-4972-2_134
- [26] Sjöström S, Brodin H. Influence of TBC end geometry on the TMF life of an APS TBC. *Procedia Engineering* 2010;2:1363–71. <https://doi.org/10.1016/j.proeng.2010.03.148>
- [27] Bogy DB. Two Edge-Bonded Elastic Wedges of Different Materials and Wedge Angles Under Surface Traction. *Journal of Applied Mechanics* 1971;38:377–86. <https://doi.org/10.1115/1.3408786>
- [28] Dolgov NA, Soroka EB. Stress singularity in a substrate-coating system. *Strength Mater* 2004;36:636–42. <https://doi.org/10.1007/s11223-005-0010-5>
- [29] Besov AV, Maslyuk VA, Stepanchuk AN, Napara-Volgina SG, Orlova LN. Cobalt-Chromium Powder Alloys and Retention Coatings Made from Them for Orthopaedic Stomatology. *Powder Metall Met Ceram* 2005;44:207–10. <https://doi.org/10.1007/s11106-005-0082-6>
- [30] Dolgov NA, Lyashenko BA, Veremchuk VS, Dmitriev YuV. Determining elasticity characteristics for protective coatings. *Strength Mater* 1995;27:392–4. <https://doi.org/10.1007/bf02209364>
- [31] Handbook of thermal spray technology. (2004) Edited by J.R. Davis. Materials Park, OH: ASM International.



Research Article

Experimental investigation on bamboo fibre reinforced mortar using artificial neural network – a comparative study

Prem Kumar V^a, Vasugi V^{*b}

School of Civil Engineering, Vellore Institute of Technology, Chennai Campus, Tamil Nadu, India

Article Info

Article history:

Received 28Mar 2022

Revised 04 Jun 2022

Accepted 25 Jun 2022

Keywords:

*Bamboo Fibre;
Bamboo Stem Ash;
Sustainable Building
Material;
Taguchi's Design of
Experiment;
Artificial Neural
Network.*

Abstract

The increase in population promotes the construction industry to exploit the conventional building materials. This phenomenon leads to use of alternative building materials in the construction field. One of the effective natural materials is bamboo. In this paper, the Bamboo Fibre (BF) is used as an additive in the mortar at various percentages (1% to 4%) and Bamboo Stem Ash (BSA) is used as an alternative binder material to replace the cement at different proportions (2.5% to 10%). To increase the property of mortars, Styrene butadiene rubber (SBR) is used a super plasticizer from 0.5% to 2%. Due to high raising demand of river sand, Copper slag (CS) is used partially to replace the fine aggregate at constant percentage (50%) for all the mix proportion. W/B ratio is proportioned from 0.35 to 0.5 at different level. The design of experiment is conducted through Taguchi's design and the experimental values are validated by Artificial Neural Network (ANN) tool for obtaining the predicted results with respect to dry density, water absorption, compressive strength and flexural strength. The experimental investigation proved that BF and BSA have a potential sign to be used as an alternative sustainable building material. From the comparative analysis of experimental results with ANN, it is revealed that the mortars show an acceptable prediction of physical and strength properties with a maximum error of 8.11%.

© 2022 MIM Research Group. All rights reserved.

1. Introduction

Bamboo is a perennial sustainable grass which falls under "Poaceae" family [1]. The use of bamboo in construction field is in practice since ancient time due to its significant engineering properties [2]. Many researches are carried out to replace the conventional construction materials by many naturally available materials [3–5] especially in the field of bamboo to use bamboo and its derivatives in the construction industry [6,7]. Bamboo's stem can be used as reinforcement and its culm can be peeled off to obtain Bamboo Fibre (BF) that can be used as an additive in cement mortar and concrete to strengthen its mechanical properties [8]. The use of bamboo fibre in concrete may result in the reduction of density and at the same time increases the flexural properties of the concrete. Though it has significant advantages, it promotes the water absorption and thus swelling of concrete takes place [[9]. To overcome this phenomenon of moisture content due to addition of natural fibres into the concrete, proper treatment should be done to the fibres before adding it into the concrete to serve its need [10]. To replace the ordinary Portland cement content by alternative pozzolanic materials, bamboo stem ash and bamboo leaf ash can be a better solution. The waste culm parts and the leaves of bamboo are abundantly available which the solid waste to be disposed. The bamboo stem and leaf can be burnt into an ash to be used for the partial replacement of conventional cement material since Bamboo Stem Ash (BSA) possess good pozzolanic property [11]. The use of

*Corresponding author: vasugi.v@vit.ac.in

^aorcid.org/0000-0002-3641-2520; ^borcid.org/0000-0002-0757-6593

DOI: <http://dx.doi.org/10.17515/resm2022.424ma0328>

Res. Eng. Struct. Mat. Vol. 8 Iss. 4 (2022) 707-720

BF and BSA in cement mortar and concrete influences the compressive and flexural strength. It also reduces the density and water absorption capacity of the concrete which therefore, reduces the self-weight and moisture content as well respectively. The optimization of water-cement ratio and the percentage of superplasticizer was studied by using bamboo leaf ash to obtain high performance concrete [12]. The experimental results proved the optimization at 0.128% for superplasticizer and 0.360 for water-cement ratio.

Due to high raise in the demand of the river sand, there is a need for alternative fine aggregate. Copper slag is one of the important waste products in the manufacture of copper. This possesses good mechanical properties to be used as aggregate and also significant chemical compositions to be used as a replacement of cement [13,14]. Styrene butadiene rubber (SBR) has a potential to reduce the early strength of the concrete and also decreases the water absorption capacity of the concrete [15].

In this research, the promotion of the use of bamboo wastes in the construction filed was addressed. Many researches was undergone for the use of natural fibres (BF) [16] and ashes (BSA) [14] in the mortar and concrete but the combination of both BF and BSA in the same mortar and concrete was not addressed. The novelty in this research is to use BF and also BSA by utilising BSA has a complementary binder and BF has an additive to the same mortar. BF was added at various percentages (1%, 2%, 3% and 4%) to the mortar and BSA was used at different percentages (2.5%, 5%, 7.5% and 10%) to replace the cement. To improve the workability and enhance the property of the mortar, SBR was used at different percentages (0.5%, 1%, 1.5% and 2%) at different levels. To obtain the good combination of proportions, Taguchi's method of design of experiment was adopted. The experimental values and the predicted results by ANN validation obtained an acceptable percentage of error.

2. Material Properties

2.1. Bamboo Fibre (BF)

Bamboo fibre was used as an additive in the mortar mix after proper treatment to remove the wax and moisture content [10]. The bamboo culm was cut into pieces to extract fibre mechanically. Each fibre was cut for a length of 25 mm by maintaining a diameter of 1 mm. After the extraction process of fibre, it was treated by immersing in 10% concentration of a sodium hydroxide solution for two days. Then the treatment of fibre was ended by washing the fibre with water and drying in sun for 48 hours [16]. The compositions of BF are listed in Table 1.

Table 1. Constituents of bamboo fibre

Constituents of BF	Chemical Compositions (%)
Cellulose (%)	73
Hemicellulose (%)	13
Lignin (%)	12
Wax (%)	2

2.2. Bamboo Stem Ash (BSA)

To replace the cement by BSA, the stem of bamboo was cut into small pieces and dried completely in sun for 24 hours [14]. Then it was incinerated using furnace for about 120 minutes at 800°C. The burnt BSA was sieved using 0.075 mm diameter sieve to replace

the ordinary Portland cement (OPC). The composition of OPC and BSA are shown in Table 2.

Table 2. Chemical constituents of OPC and BSA

Chemical Composition	Ordinary Portland Cement (%)	BSA (%)
SiO ₂	20	69.74
MgO	0.8	8.83
Al ₂ O ₃	5.2	0.25
CaO	62.7	18.92
Na ₂ O	0.35	0.74
Fe ₂ O ₃	3.5	0.16
K ₂ O	0.74	0.86
LOI	6.71	0.5

2.3. Copper Slag

At the process of extraction of copper metal, the waste material is obtained from the refinery plants called as copper slag [17]. For the effective use of CS in the concrete or cement mortar and to get reduced moisture absorption and voids, river sand can be replaced by CS up to 50% [18]. The properties of CS are observed in Table 3.

Table 3. Properties of Copper Slag

Properties	Value
Silica (%)	33.5
Water absorption (%)	0.24
Bulk density (kg/m ³)	1899
Fineness modulus	3.3
Specific gravity	3.47

2.4. Styrene Butadiene Rubber (SBR)

SBR is a super plasticizer used in the cement mortar and concrete due to its high bonding efficiency, resistance to abrasion and crack and aging characteristics [15]. It is a copolymer liquid in white colour with a specific gravity and solid content of 1.04 and 45% respectively [19]. Use of SBR at 1.5% in the mortar performed good compressive strength.

3. Methodology

3.1. Design of Experiments

In this research, four parameters are considered to study the performance of bamboo fibre reinforced mortar are: (i) water-cement ratio, (ii) binder (cement+BSA), (iii) Super plasticizer (SP) and (iv) Bamboo Fibre (BF). Each parameter is concentrated for four levels and shown in Table 4. To minimise the number of trials, Taguchi's design of experiment is adopted [20–22]. The layout of the developed combination of trials is shown in Fig. 1.

The ratio maintained for Bamboo fibre reinforced mortar was 1:2.75 with respect to ASTM C109 standard [10]. The sixteen trials obtained from the taguchi's design of experiment are illustrated in Table 5. Fine aggregate for all the trials was replaced constantly by 50% of copper slag.

Table 4. Description of parameters and variation levels

Parameters	Parameter label	L1	L2	L3	L4
W/B ratio	A	0.5	0.45	0.4	0.35
Binder (Cement + BSA) (%)	B	97.5 + 2.5	95 + 5	92.5 + 7.5	90 + 10
SP (%)	C	0.5	1	1.5	2
BF (%)	D	1	2	3	4

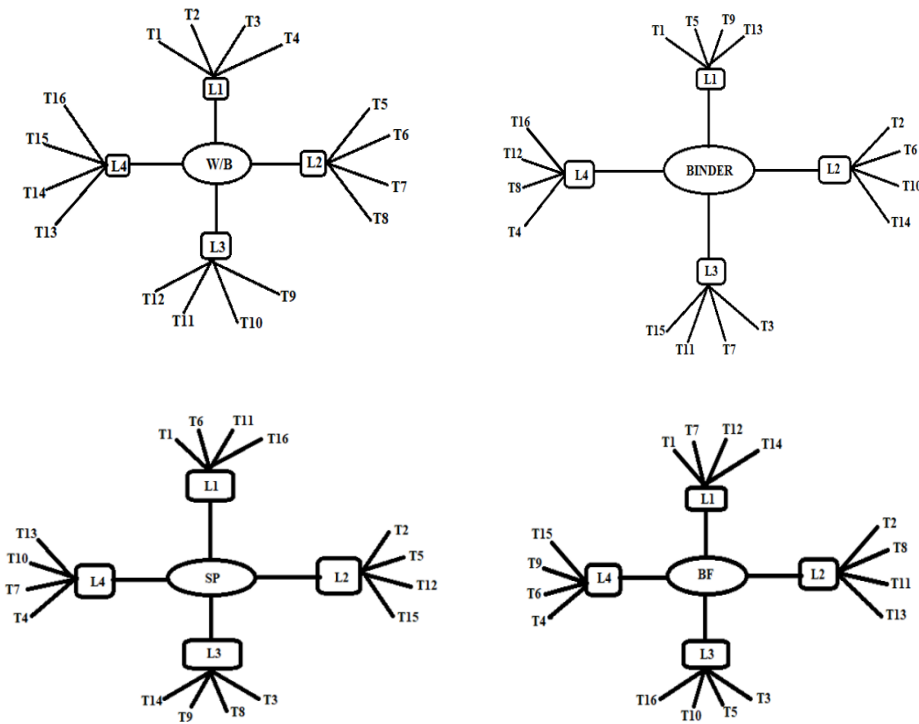


Fig. 1 Orthogonal array of Taguchi's design of experiment (L16)

3.2. Artificial Neural Networks (ANN)

ANN is a framework designed to analyze and process the information activity like the human brain. This neural network has an ability to recognize and generalize from the accessible data and bring pertinent solutions from the incomplete or inaccuracy input parameters [23–25]. ANN tool is implemented to rectify and distinguish the investigation results obtained from the other methods. It holds enormous neuron which is interlinked like networks and each and every neuron from the input (X_i) will produce individual output (Y) with the mentioned equation (1). The terms (f) represent the activation function and (H) denotes input parameters that are obtained from the equation (2). The term (b) in the equation (2) is used to direct the function and commonly known as bias co-efficient [26–30].

$$Y = f(H) = \frac{1}{1 + e^{-H}} \tag{1}$$

$$H = \sum_{i=1}^n X_i W_i + b \tag{2}$$

Table 5. Mix Proportion of Mortar

Exp. No	W/B	Binder (Cement + BSA) (%)	SP (%)	BF (%)	FA (Sand + CS) (%)
Ctrl	0.5	100 + 0	0	0	50 + 50
T1	0.5	97.5 + 2.5	0.5	1	50 + 50
T2	0.5	95 + 5	1	2	50 + 50
T3	0.5	92.5 + 7.5	1.5	3	50 + 50
T4	0.5	90 + 10	2	4	50 + 50
T5	0.45	97.5 + 2.5	1	3	50 + 50
T6	0.45	95 + 5	0.5	4	50 + 50
T7	0.45	92.5 + 7.5	2	1	50 + 50
T8	0.45	90 + 10	1.5	2	50 + 50
T9	0.4	97.5 + 2.5	1.5	4	50 + 50
T10	0.4	95 + 5	2	3	50 + 50
T11	0.4	92.5 + 7.5	0.5	2	50 + 50
T12	0.4	90 + 10	1	1	50 + 50
T13	0.35	97.5 + 2.5	2	2	50 + 50
T14	0.35	95 + 5	1.5	1	50 + 50
T15	0.35	92.5 + 7.5	1	4	50 + 50
T16	0.35	90 + 10	0.5	3	50

The ANN is identified as Multilayer Perception (MLP) due to its three apparent layers. The feeding of network with outside data is done in the first layer. The connection between the input and output layer is performed in the second layer which is commonly known as computational or hidden layer. The prediction is executed in the output form in the third component which is preferably known as output layer. The input layer consist of five independent parameters and the output layer contains four dependent variables using which ANN predicts the dry density, water absorption, compressive and flexural strength.

In this research work, the ANN framework was created in MATLAB R2018a to estimate the mechanical strength developed at 7 and 28 days of experimental mortars. Figure 2 shows the Lavenberg-Marquardt algorithm of the ANN framework.

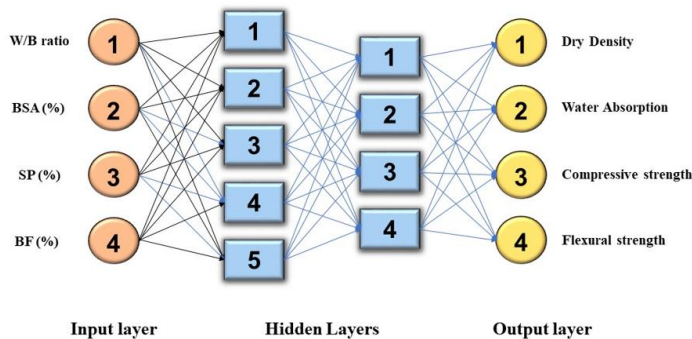


Fig. 2 ANN framework of the present research

3.3. Test Samples Preparation

All the materials were weighted as per the mix proportions followed by dry mixing. Then the wet mixing was carried out for 2 to 3 minutes by gradual addition of water. The total mix was transferred into a flat container and mixing was performed manually so that the fibre won't get segregated in the mortar mix. After even distribution of the bamboo fibres, the fresh mortar mix was casted by filling into the 100 x 100 x 100 mm³ and 40 x 40 x 160 mm³ mould sizes. Then the mortar was kept under curing to get hardened for testing its flexural and compressive strength.

3.4. Experimental Program

After the curing period of 7 and 28 days for the developed cubes, the compressive strength was conducted as per ASTM C109 with a compression testing machine of 2000 kN capacity and valued for each trial with an average of three samples. The load was applied gradually at a loading rate of 0.75 kN/s. The flexural test was performed on prism samples of size 40 x 40 x 160 mm³ after 7 and 28 days of curing as per ASTM C348 on all the samples using 10 kN capacity, universal testing machine under three point loading. Physical testing of water absorption was done on all the sample cubes as per BS 1881-122 standard [31]. The water cured mortar specimens were taken at 28 days and dried using oven at temperature of 100°C for 24 hours. The oven dried mortar specimens were weighted for its mass to calculate the dry density. To determine the physical testing of water absorption, the specimens were immersed in water up to 240 minutes [32]. The wet mortar specimens were taken away from the water and weighted for its mass at 10 minutes, 20 minutes, 30 minutes, 60 minutes, 120 minutes, 180 minutes and 240 minutes, and finally the water absorption percentage was calculated.

4. Experimental and Predicted Results Using ANN Model

4.1. Effect of Addition of BSA and BF on Water Absorption and Dry Density

Dry density results of all the experimental samples with varying percentage of BF and BSA is shown in Fig. 3. It was observed that the increase in percentage of bamboo stem ash (BSA) decreased the dry density of the mortar due to its low density than cement. However, there was marginal increase in the dry density of mortar for 7.5% to 10% replacement of cement by BSA because of 3% to 4% addition of bamboo fibre. The replacement of cement by 5% of BSA and 1.5% of bamboo fibre reduced the dry density of mortar by 22.8% in comparison with the dry density of conventional mortar. The increase in bamboo fibre content had made cement composite more porous like other fibres[10]. The porous structure had given accommodation for the water molecules to occupy[16]. Bamboo fibre concentration seems to be directly proportional to the increase of moisture content of mortar. However, the water absorption percentage got decreased for all the trial mortars because of the NaOH treatment adapted to the bamboo fibre before adding it in the mortar mix. Figure 4 shows that all the trial mortar water absorption percentage was less in comparison with control mix. The maximum water absorption at 240 minutes for the conventional mortar was 12.19% and the maximum and minimum water absorption for the trial mortars were 5.89% and 1.47% respectively. This showed that there was maximum and minimum reduction of water absorption for the trial mortars by 6.3% and 11.43% respectively.

4.2. Effect of Addition of BSA and BF on Compressive and Flexural Strength

There was a decline of compressive strength on mortars with the addition of BSA and BF [10]. The water to binder ratio and dosage of super plasticizer also had significant effect in increase or decrease of compressive strength. The replacement of cement by 2.5% of BSA with 0.5% of BF had given equivalent compressive strength of control mortar. The

strength of this trial mortar was achieved by adding 0.5% of SBR at w/b ratio of 0.5. With decrease in w/b ratio for the same dosage of BSA% and BF%, the decrease in strength was observed. However, the increase in SBR% gradually increased the strength of mortars of 5% to 10% replacement of cement by BSA and 3% to 4% addition of BF at 0.5 w/b ratio. The replacement of cement by 10% of BSA with 2% of bamboo fibre and 2% of SBR% at 0.5 w/b ratio increased the compressive strength by 77.89% as compared with the compressive strength of control mortar for 28 days. Figure 5(a) & (b) shows the compressive strength of control and all the trial mortar of 7 days and 28 days. The flexural strength was increased up to 20% than control mortar with fibre dosage of 1% at w/b of 0.5 and the flexural strength results of trials is shown in Fig. 6(a) & (b). The strength started to gradually decrease in increase with fibre percentage. However, this phenomenon was overcome by increased percentage of SBR%. For the same w/b ratio of 0.5, the flexural strength of mortar with 4% BF was increased with increase in SBR%. The treatment of BF with NaOH solution before using in mortar and increased percentage of SBR% are the important reason for the increase of flexural strength.

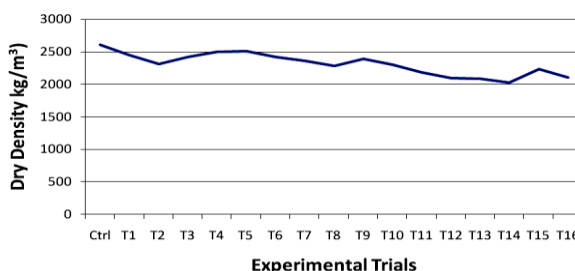


Fig. 3 Effect of BF and BSA incorporated mortar on dry density

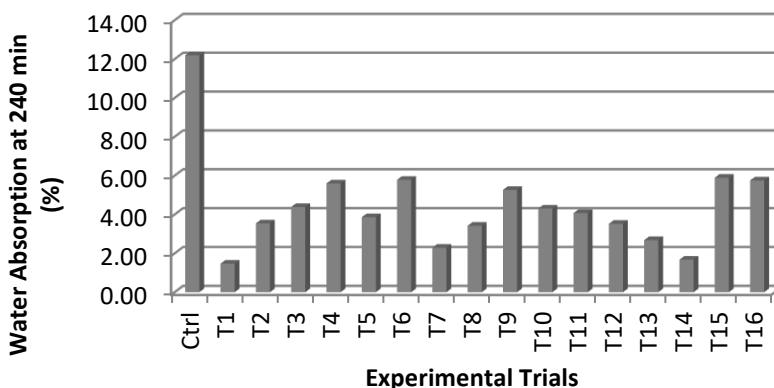


Fig. 4 Effect of BF and BSA incorporated mortar on water absorption

4.3. Prediction of Physical and Strength Properties from ANN Model

The selected range of variables of input and output in the ANN database is shown in Table 6 and the precision in the data obtained from the network are calculated by the prediction of error percentage formula [33]

$$\text{Prediction of error (\%)} = \frac{\text{Experimental results} - \text{ANN results}}{\text{Experimental results}} \times 100$$

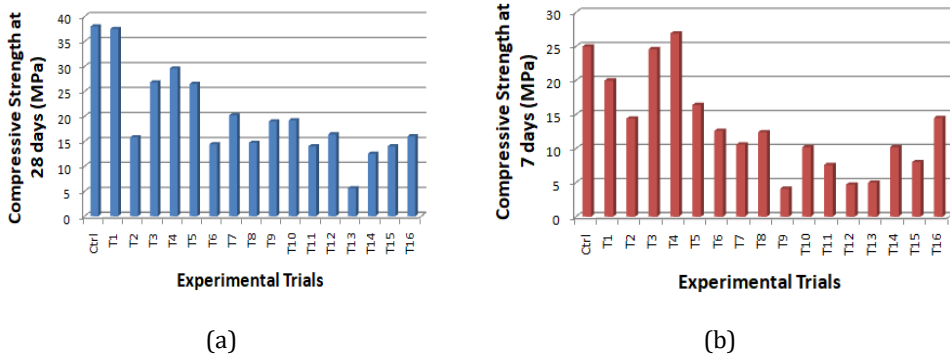


Fig.5(a) Compressive strength at 7 days (b) Compressive strength at 28 days

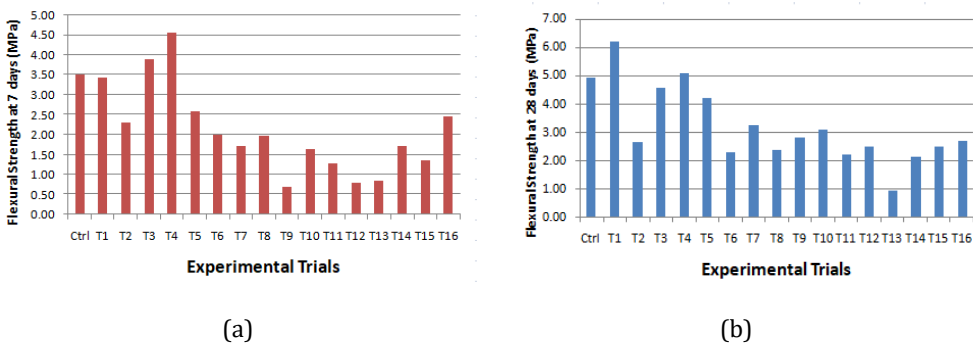


Fig.6(a) Flexural strength at 7 days (b) Flexural strength at 28 days

Table 6. Range of variables in ANN database

Variables	Range	Remarks
W/B ratio	0.35 – 0.5	Input variables
BSA (%)	2.5 – 10	
SP (%)	0.5 – 2	
BF (%)	1 – 4	
CS (%)	50	
Dry density (kg/m ³)	2030 – 2608	Target variables
Water absorption (%)	1.47 – 12.19	
Compressive strength (MPa)	4.1 – 38	
Flexural strength (MPa)	0.7 – 6.19	

The error percentage of bamboo fibre reinforced mortars for its dry density, water absorption, compressive and flexural strength were shown in Table 7. The percentage of error obtained from the ANN tool is acceptable as it is less than 10%. From all the trials, flexural strength of T1 for 7 days recorded a maximum error percentage of 8.11%.

Figure 7 illustrates the predicted and experimental dry density values of 16 trials and the control mortar at 28 days. Also, Figure 8 shows the experimental and ANN results of water absorption at the end of 28 days at 240 minutes. Figure 9 & 10 depicts the compressive strength and flexural strength comparison of experimental results with

predicted results using ANN of all the trial mortars and control mortar at the end of 7 days and 28 days. From all these comparison graphs, it was indentified that the experimental results and the predicted results are marginal and equivalent.

Table 7. Error percentage values of physical and strength property values from the ANN model

Mix ID	Dry density	Water Absorption	Compressive Strength		Flexural Strength	
			7 days	28 days	7 days	28 days
Ctrl	0.22	-2.50	-0.84	-1.96	0.19	0.39
T1	-0.33	-2.72	-0.55	2.11	8.11	-2.10
T2	0.26	-1.13	-0.69	5.13	2.31	-3.56
T3	0.04	1.80	3.32	-0.52	-0.40	-0.57
T4	-0.65	-1.43	0.59	-1.96	1.09	-0.79
T5	-0.33	-1.90	-0.06	1.98	4.22	-0.66
T6	-0.32	-2.03	0.60	2.57	1.00	-5.58
T7	0.20	4.37	-0.65	0.23	-0.30	-0.55
T8	0.27	-2.34	-0.20	-2.18	-2.80	-0.26
T9	-0.03	-1.14	-2.52	0.26	-5.37	-2.61
T10	-0.27	1.91	-0.88	-2.45	3.07	-5.18
T11	0.26	-0.81	0.26	0.79	-4.65	2.23
T12	-0.36	5.35	-2.57	-0.79	2.50	-0.10
T13	0.11	-1.30	-7.60	0.34	-3.43	-0.65
T14	0.12	4.07	0.34	-2.31	-0.93	2.14
T15	0.21	-2.88	1.38	-0.14	0.30	-0.24
T16	0.13	-1.04	-6.83	-1.49	3.24	1.10

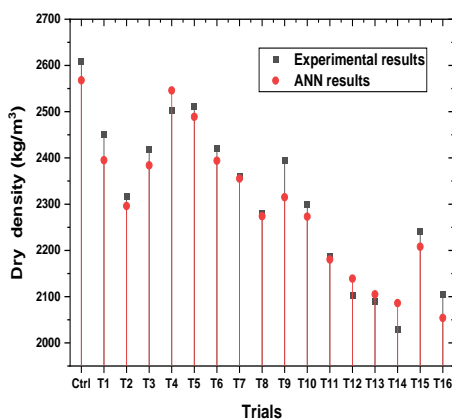


Fig. 7 Comparison of actual and ANN results of dry density

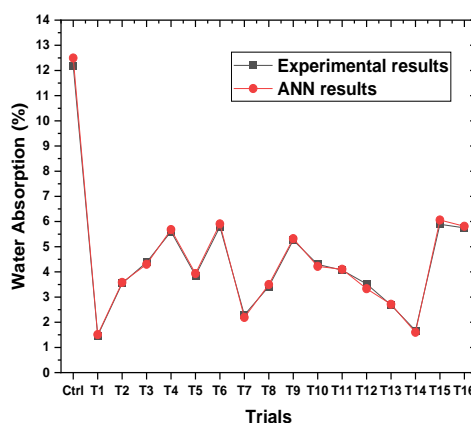


Fig. 8 Comparison of actual and ANN results of water absorption

Figure 11-16 shows the ANN predicted execution (regression plots) of dry density, water absorption, compressive and flexural strength (target variables). The three-phase combination correlation co-efficient recorded for compressive strength test at 7 days and 28 days are 0.96801 and 0.95995 respectively as shown in Fig.11 & 12. Similarly, the three phase combination correlation co-efficient obtained for flexural strength for 7 and 28 days are 0.97585 and 0.97686 respectively and for dry density and absorption are

0.96015 and 0.9683 respectively. This reveals the less error results of experimental results and ANN outcomes depicted in Fig 7-10.

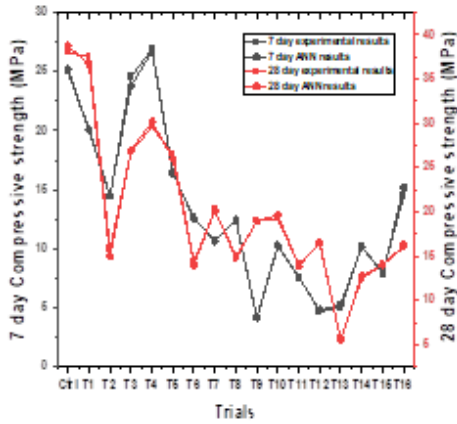


Fig. 9 Comparison of actual and ANN results of compressive strength at 7 and 28 days

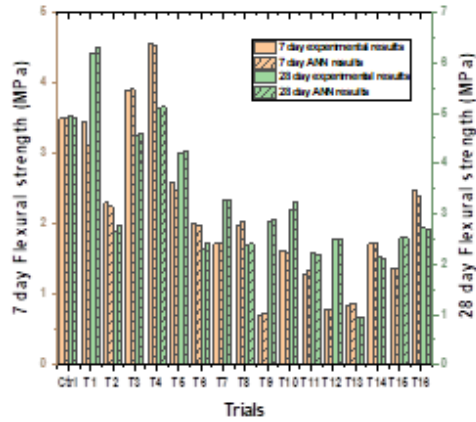


Fig. 10 Comparison of actual and ANN results of flexural strength at 7 and 28 days

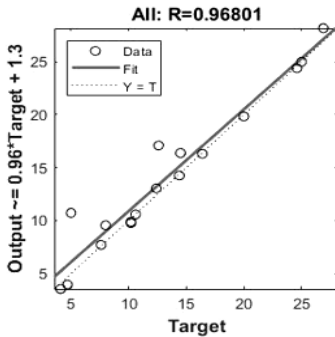


Fig.11 Prediction execution of Compressive strength for 7 days

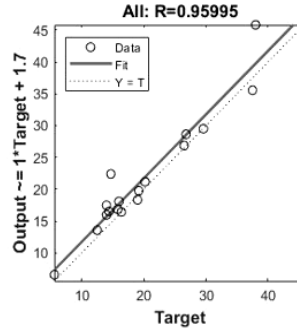


Fig. 12 Prediction execution of Compressive strength for 28 days

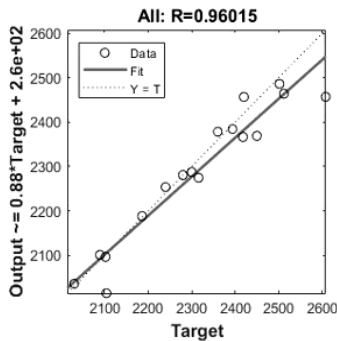


Fig. 13 Prediction execution of dry density for 28 days

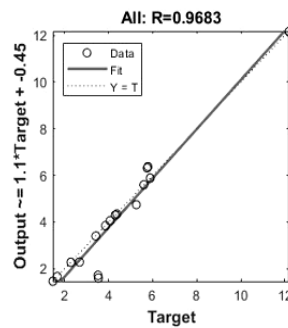


Fig. 14 Prediction execution of water absorption for 28 days

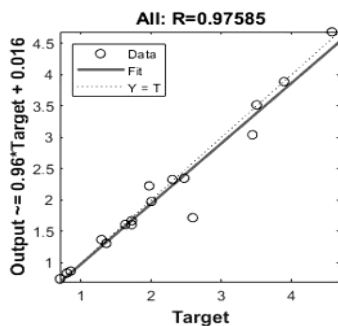


Fig. 15 Prediction execution of flexural strength for 7 days

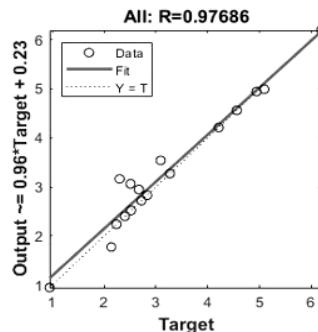


Fig. 16 Prediction execution of flexural strength for 28 days

5. Conclusions

This research focuses on incorporating an alternative sustainable building material by utilizing waste bamboo materials (BF and BSA) in mortar to enhance its mechanical strengths. Here are the following conclusions drawn from this experimental research.

- Bamboo stem ash (BSA) has potential to reduce the density of the mortar due to its low density than cement[11]. Due to addition of bamboo fibre (BF) from 3% to 4%, there was a marginal increase in the dry density of mortars for 7.5% to 10% replacement of cement by BSA. The BSA with 5% and BF with 1.5% can be chosen has an optimum dosage since it reduced the dry density by 22.8% than control mortar.
- The 10% concentration of NaOH treatment for BF as per the literature [16]reduced the water absorption capacity. For the control mortar, the maximum water absorption percentage was recorded as 12.19% at 28 days whereas, the maximum and minimum percentage of water absorption of trial mortars were 5.89% and 1.47%. The recorded results revealed that treated bamboo fibre reinforced mortar with the bamboo stem ash as a complementary binder has potential to reduce the water absorption capacity of the mortar.
- It is observed that compressive strength got declined with increase in the percentage of BF [10]and BSA. However, by increasing the SBR% at higher water cement ratio of 0.5, gradually increased the strength of mortars of 5% to 10% replacement of cement by BSA with 3% to 4% addition of BF. The mortar sample with 10% of BSA, 2% of BF and 2% of SBR% at water cement of ratio of 0.5, increased the compressive strength by 77.89% as compared to the control mortar.
- The flexural strength gradually decreased with increase in fibre percentage[10]. However, the flexural strength was raised up to 20% than control mortar. This was achieved by treatment of BF with NaOH solution and increased percentage of SBR.
- The ANN framework construction in this research was noticed to be suitable with results in judging the dry density, water absorption, compressive and flexural strength values of bamboo fibre reinforced mortar mixes.

Future Work

The output obtained from the experimental investigation should be analysed and validated through Taguchi's approach. The analysis of variance is to be performed to identify the percentage of contribution of each parameter. Finally the experimental program should be executed for the obtained optimum dosage of the mortar based on the output performance indices.

References

- [1] Kaware A, Awari UR, Wakchaure MR. Review of Bamboo as Reinforcement Material in Concrete Structure. International Journal of Innovative Research in Science, Engineering and Technology, 2013; 2:6 2461-4.
- [2] Science E. Bamboo materials in cement, geopolymer and reinforced concrete as sustainable solutions for better tomorrow Bamboo materials in cement , geopolymer and reinforced concrete as sustainable solutions for better tomorrow. IOP Conference Series: Earth and Environmental Science, 2020; 573: 012036. <https://doi.org/10.1088/1755-1315/573/1/012036>
- [3] Arunkumar K, Muthukannan M, Sureshkumar A, Chithambarganesh C, R RK. Mechanical and durability characterization of hybrid fibre reinforced green geopolymer concrete. Res. Eng. Struct. Mater., 2022; 8:1 19-43.
- [4] Arunkumar K, Muthukannan M, Kumar AS, Ganesh AC, Devi RK. Cleaner environment approach by the utilization of low calcium wood ash in geopolymer concrete. Applied Science and Engineering Progress. 2022; 15:1. <https://doi.org/10.14416/j.asep.2021.06.005>
- [5] Kilani A, Fapohunda C, Adeleke O, Metiboba C. Evaluating the effects of agricultural wastes on concrete and composite mechanical properties: a review. Res. Eng. Struct. Mater., 2022; 8(2): 307-336. <https://doi.org/10.17515/resm2021.339st0912>
- [6] Ghavami K. Bamboo as reinforcement in structural concrete elements, Cement and Concrete Composites. 2005; 27:6 637-49. <https://doi.org/10.1016/j.cemconcomp.2004.06.002>
- [7] Xie X, Zhou Z, Yan Y. Flexural properties and impact behaviour analysis of bamboo cellulosic fibers filled cement based composites. Construction and Building Materials. 2019 Sep 30; 220:403-14. <https://doi.org/10.1016/j.conbuildmat.2019.06.029>
- [8] Kushwaha PK, Kumar R. Effect of silanes on mechanical properties of bamboo fiber-epoxy composites. Journal of reinforced plastics and composites. 2010; 29:57 18-24. <https://doi.org/10.1177/0731684408100691>
- [9] Yvonne KS, Mahani Y, Razak W, Sofiyah MR, Razali MH. Properties of epoxy-hybrid composite using bamboo fiber and Salacczalacca fruit skin powder. Materials Today: Proceedings. 2018; 5: 21759-21764. <https://doi.org/10.1016/j.matpr.2018.07.029>
- [10] Raut AN, Gomez CP. Thermal and mechanical performance of oil palm fiber reinforced mortar utilizing palm oil fly ash as a complementary binder. Construction and Building Materials. 2016; 126:15 476-483. <https://doi.org/10.1016/j.conbuildmat.2016.09.034>
- [11] Ikeagwuani CC, Nwonu DC, Obetule DA, Omeje MU, Festus T. Potential of bamboo stem ash as supplementary cementitious material in concrete production. International Journal of Engineering Research & Technology. 2019; 8:08 75-80. <https://doi.org/10.17577/IJERTV8IS080028>
- [12] Odeyemi SO, Adisa MO, Dotun O. Optimal water-cement ratio and volume of superplasticizers for blended cement-bamboo leaf ash high-performance concrete Research on Engineering Structures and Materials. x (xxxx): 1-13.
- [13] Al-Jabri KS, Al-Saidy AH, Taha R. Effect of copper slag as a fine aggregate on the properties of cement mortars and concrete. Construction and Building Materials. 201; 25:2 933-938. <https://doi.org/10.1016/j.conbuildmat.2010.06.090>

- [14] Rodier L, Bilba K, Onésippe C, Arsène MA. Study of pozzolanic activity of bamboo stem ashes for use as partial replacement of cement. *Materials and structures*. 2017; 50:87. <https://doi.org/10.1617/s11527-016-0958-6>
- [15] Atiyah AA, Farid SB, Kadhim AS. High Performance Concrete Improvement by Styrene-Butadiene Rubber Addition. *Engineering and Technology Journal*. 2016; 34:12 2296-2309.
- [16] Chin SC, Tee KF, Tong FS, Ong HR, Gimbin J. Thermal and mechanical properties of bamboo fiber reinforced composites. *Materials Today Communications*. 2020; 23: 100876. <https://doi.org/10.1016/j.mtcomm.2019.100876>
- [17] Soni MM, Mangroliya JR. Performance of Copper Slag on Strength as Partial Replacement of Fine Aggregate in Concrete. *International Journal of Engineering Research and Technology*. 2018; 7:1 347-349. <https://doi.org/10.17577/IJERTV7IS010156>
- [18] Patnaik B, Seshadri S, Rao SC. Strength and durability properties of copper slag admixed concrete. *IJRET Int. J. Res. Eng. Technol*. 2015: 2319-1163.
- [19] Grinys A, Balamurugan M, Augonis A, Ivanauskas E. Mechanical properties and durability of rubberized and glass powder modified rubberized concrete for whitetopping structures. *Materials*. 2021; 14:9 2321. <https://doi.org/10.3390/ma14092321>
- [20] Nuruddin MF, Bayuaji R. Application of Taguchi's approach in the optimization of mix proportion for microwave incinerated rice husk ash foamed concrete. *International Journal of Civil & Environmental Engineering*. 2009; 9:09 121-129.
- [21] Antony J, Perry D, Wang C, Kumar M. An application of Taguchi method of experimental design for new product design and development process. *Assembly automation*. 2006. <https://doi.org/10.1108/01445150610645611>
- [22] Sabarish KV, Remo MA, Paul P. Optimizing the concrete materials by Taguchi optimization method. In *IOP Conference Series: Materials Science and Engineering* 2019; 574:1, 012002. <https://doi.org/10.1088/1757-899X/574/1/012002>
- [23] Barbuta M, Diaconescu RM, Harja M. Using neural networks for prediction of properties of polymer concrete with fly ash. *Journal of Materials in Civil Engineering*. 2012; 24:5 523-528. [https://doi.org/10.1061/\(ASCE\)MT.1943-5533.0000413](https://doi.org/10.1061/(ASCE)MT.1943-5533.0000413)
- [24] Chaitanya M, Manikandan P, Kumar VP, Elavenil S, Vasugi V. Prediction of self-healing characteristics of GGBS admixed concrete using Artificial Neural Network. In *Journal of Physics: Conference Series* 2020; 1716:1 012019. <https://doi.org/10.1088/1742-6596/1716/1/012019>
- [25] Ahmadi M, Naderpour H, Kheyroddin A. ANN model for predicting the compressive strength of circular steel-confined concrete. *International Journal of Civil Engineering*. 2017; 15:2 213-221. <https://doi.org/10.1007/s40999-016-0096-0>
- [26] Manikanta C, Manikandan P, Duraimurugan S, Elavenil S, Vasugi V. Pozzolanic properties of agro waste ashes for potential cement replacement predicted using ANN. In *Journal of Physics: Conference Series* 2020; 1716:1 012018. <https://doi.org/10.1088/1742-6596/1716/1/012018>
- [27] Oh JW, Lee IW, Kim JT, Lee GW. Application of Neural Networks for Proportioning of. *ACI Materials Journal*. 1999; 96:1. <https://doi.org/10.14359/429>
- [28] Noorzaei J, Hakim SJ, Jaafar MS, Thanoon WA. Development of artificial neural networks for predicting concrete compressive strength. *International Journal of engineering and Technology*. 2007; 4:2 141-153.
- [29] Bilim C, Atiş CD, Tanyildizi H, Karahan O. Predicting the compressive strength of ground granulated blast furnace slag concrete using artificial neural network. *Advances in Engineering Software*. 2009; 40:5 334-340. <https://doi.org/10.1016/j.advengsoft.2008.05.005>

- [30] Nazari A, Torgal FP. Predicting compressive strength of different geopolymers by artificial neural networks. *Ceramics International*. 2013; 39:3 2247-2257. <https://doi.org/10.1016/j.ceramint.2012.08.070>
- [31] N.d. "BS-1881-122-2011_TOAZ.INFO.pdf".
- [32] Jung CT, Siang TC, Kwong TH, Boon K. Compressive strength and water absorption of mortar incorporating silica fume. *Int J Civ Eng*. 2019; 6:8 39-43. <https://doi.org/10.14445/23488352/IJCE-V6I8P106>
- [33] Natrayan L, Kumar MS. An integrated artificial neural network and Taguchi approach to optimize the squeeze cast process parameters of AA6061/Al₂O₃/SiC/Gr hybrid composites prepared by novel encapsulation feeding technique. *Materials Today Communications*. 2020; 25: 101586. <https://doi.org/10.1016/j.mtcomm.2020.101586>



Research Article

Effect of ZrO₂ on morphological and adhesion properties of hydroxyapatite reinforced poly- (lactic) acid matrix hybrid coatings on Mg substrates

Mehmet Topuz

Department of Mechanical Engineering, Van Yüzüncü Yıl University, Van, Turkey

Article Info

Abstract

Article history:

Received 20 May 2022

Revised 07 Jul 2022

Accepted 22 Aug 2022

Keywords:

Magnesium;
Hydroxyapatite;
Zirconia (ZrO₂);
Poly- (lactic) acid;
Hybrid dip-coatings

The study aimed to reduce the high biodegradability of magnesium (Mg) as well as local infections due to the hydrogen gas formation because of pH increase around biological tissues. Composite coatings of poly- (lactic acid)/hydroxyapatite (PLA/HA) are commonly employed, although their adhesive strength to the metallic substrates are insufficient. In this study, PLA/HA-zirconia (ZrO₂) hybrid coatings were successfully coated on Mg surfaces by means of dip-coating method to enhance this insufficient adhesion strength at the coating - Mg substrate interface with desired surface morphology. Scanning electron microscopy (SEM) micrographs were used to examine the surface morphologies of the coatings, both energy dispersive spectroscopy (EDS) and X-ray diffraction (XRD) analyses to characterize them elementally and phase formation, respectively. Micro-Vickers hardness measurements were taken on coatings and tape tests were carried out following ASTM D3359 standard to reveal the adhesion strengths. The agglomeration size on the coating surfaces decreased as the ZrO₂ reinforcement increased, and the Mg surface was entirely sealed with 30 wt% ZrO₂ reinforcement, according to the SEM micrographs. The presence of both HA and ZrO₂ in the coating was confirmed by XRD analysis, which also demonstrated that it was crystalline. Adhesion strengths were determined 1B, 3B, 4B, and 5B for HA, HA-10%ZrO₂, HA-20%ZrO₂, and HA-%30 ZrO₂ reinforced hybrid coatings, respectively. As a result, it was concluded that hybrid coatings which reinforcements of ZrO₂ particles to the PLA/HA composite coatings reduced agglomeration and enhance the coating - substrate adhesion at the interface.

© 2022 MIM Research Group. All rights reserved.

1. Introduction

Materials, used in a living environment, are expected to be able to withstand mechanical reactions (muscle movements and body weight), chemical interactions (corrosion and degradation), factors originating from temperature and radiation, and osseointegration (interacting with tissues) properties. In this way, biomaterials can be defined as any material that is safe, harmless, economically, and physiologically acceptable to the body during use as a part of the body [1]. They are also in contact with the surrounding living tissues from the moment they are placed in the body and fulfil the task of the missing limb. Biocompatibility is also another important term that can be defined as the chemical interaction of this biomaterials with body fluids during use in the body and whether the physiological consequences of these interactions cause harm to the body [2]. For this reason, it is a prerequisite for the biomaterial to be accepted by the environment in which it is defined as biocompatible.

Corresponding author: mehmettopuz@vyu.edu.tr

orcid.org/0000-0003-3692-796X

DOI: <http://dx.doi.org/10.17515/resm2022.434me0520>

Res. Eng. Struct. Mat. Vol. 8 Iss. 4 (2022) 721-733

Metals and their alloys are frequently used in biomedical fields as biomaterials. Today the most commonly used metallic biomaterials are titanium and its alloys (such as commercially pure titanium, Ti6Al4V), stainless steels (such as 316L), and cobalt-chromium (such as Co-Cr) alloys [3]. They are used in the body in many places such as hip prostheses, orthopaedic applications, heart valves, stent applications, and dental implants [4]. These materials also have a high load-carrying capacity with sufficient wear and corrosion properties [5,6]. Thus, the plastic deformation of the metallic biomaterials will be delayed and their life cycle can be extended in the body. On the other hand, two features have come to mind in terms of compatibility with the surrounding tissues. The first one is structural compatibility, which means the most suitable adaptation of the material to the mechanical behaviour of body tissues. When we consider the structural integrity, it is necessary to mention the Young's modulus mismatch (Wolf's law) between the implant and the bone. As Wolf's law mentioned, when Young's modulus (also known as the Stress-Shielding effect) between bone and metallic biomaterial is increased, osteoporosis which is inadequate regeneration of bone can occur [7,8]. The second one is surface compatibility: it means that a biomaterial should have physically, chemically, and tribologically suitable for tissues. Magnesium (Mg) and its alloys are preferable among metallic biomaterials for low density, lower Young's modulus, and high specific strength features [9]. On the other hand, Mg and its alloys are not very advanced in terms of surface compatibility due to their high biodegradability properties. One of them can be explained with its high corrosion tendency. As a result of corrosion that may occur on the Mg implant, the material loss may occur which will reduce the strength of the implant, and more importantly, the interaction of metal ions with the surrounding tissues may lead to undesirable results [10]. On the other hand, the high degradation rate of Mg in the physiological environment is encountered as a significant drawback in clinical applications [11]. Some reactions occur because of the interaction of Mg with the surrounding tissues which most important one is the formation of H₂ gas ($Mg + 2H_2O \rightarrow Mg(OH)_2 + H_2$) resulted in undesired interactions at implant-tissue interface [12]. Furthermore, the formability of this reaction increased with implant-tissue interaction with body fluids, because of this reason, it is very important to seal Mg and its alloys from surrounding tissue with biological compounds. However, as a result of recent studies, especially coating with organic polymers, these desired surface compatibilities can be increased [12-15].

Polymer coatings are preferred in many applications to ensure that the interface to be formed between the implant material and the living tissue has the desired properties [16]. Thin and enhanced adhesion properties of polymeric coatings not only isolate the material against direct contact with body fluid but also provide the desired biological response. For this reason, choosing the right polymer coating can both improve the corrosion behaviour of the Mg and prevent any complications during the application. Poly- (lactic) acid (PLA) has received considerable attention due to its controllable properties such as biodegradability - biocompatibility, well-defined formulation techniques, easy handling, thermal barrier properties, and high machinability with traditional technologies (extrusion, injection moulding, compression moulding, and blow moulding) [17,18]. Certain properties such as poor mechanical properties of PLA can be increased with composite blending, co-polymerization, etc. [19]. Owing to these advantages of PLA, absorbable fixation components have been studied for decades experimentally before clinical use [20]. The mechanical properties and bioactivity of PLA materials are decisive for bone regeneration and degradation rate [17]. On the other hand, as a result of PLA's high hydrophobic properties, adequate wettability cannot be achieved during implant-tissue interaction [21]. For this reason, researchers have generally been carried out on PLA-hydroxyapatite (HA: Ca₁₀(PO₄)₆(OH)₂) composites [22]. Owing to its similarity to bone structure in terms of calcium: Ca- and phosphor: P- with the Ca/P ratio (1.67), HA is frequently used in biomaterial applications, especially to increase the biocompatibility of

coating applications [23–25]. Studies conducted by many researchers aim to use the advanced biocompatibility features of HA together with the high corrosion resistance and adhesion strength of PLA in coatings. Nowadays, researchers have widely investigated hybrid composites to further improve these properties by addition of various reinforcements to PLA/HA coatings [11,26,27]. Zirconia (ZrO_2) ceramics have been commonly used as coating reinforcements due to its non-cytotoxicity to the human body (except for an acidic environment like an oral cavity), non-degradable *in-vivo* conditions, high fracture toughness, and chemical durability [16].

The method used in the surface coatings should be selected by taking into consideration of thickness, surface roughness, crystallinity, price of the equipment, and safety. Recently, many methods commercially used for surface coatings on metallic materials such as plasma spray [28], cold spray [29], magnetron sputtering [30], electrochemical deposition [31], and dip-coating [23,24]. The dip-coating method is notable among them since not dependent on the shape, high purity and homogeneity can be obtained, and inexpensive [32]. The dip-coating method can be defined as immersing the substrate material to be coated into the prepared solution under certain atmospheric conditions and speed and then removing it again. When the material is withdrawn from the coating liquid, a stable liquid film is carried along with the material surface due to surface tensions. To obtain a thin film on the material surface, the thin liquid film must be evaporated without allowing any chemical reaction. Normally, post-treatments such as curing or sintering are required to obtain thin coatings [33]. With the dip-coating method, the coating can be obtained in a few seconds depending on the volatile components. In this way, the method is frequently used in industrial and laboratory applications due to its simple processing stages, and high coating quality.

As stated a recent study conducted by Harb *et al.* [34], suggested that poly (methyl methacrylate) (PMMA)- TiO_2 and PMMA- ZrO_2 reinforcement to organic-based additives such as HA and β -tricalcium phosphate (β -TCP) could enhance implants surface features. They stated that the surface roughness, hydrophilicity, surface free energies, and corrosion resistance were increased with HA reinforced PMMA- ZrO_2 coatings. While no adhesion test was performed in the study, the effect of the ZrO_2 fraction was also not investigated. Unlike the aforementioned study, PLA/HA- ZrO_2 hybrid coatings were successfully coated on Mg substrates as a possible candidate for biomedical applications in this study. Investigation of both morphological and adhesive effects of ZrO_2 in PLA/HA composite coatings on Mg substrates was investigated in detail. In this way, it was aimed that the hybrid composite coatings which were reinforced with both HA and ZrO_2 , prolonged the lifetime of the implant.

2. Materials and Methods

2.1. Substrate and Coating Preparation

In all coated specimens, high purity (99.9%) Mg was employed as the coating substrate (Merck, 7439-95-4). Cylindrical specimens were cut from rod-shaped Mg with a precision cutter machine (Metkon, Micracut 152) in dimensions of 12.7×3 mm. All substrates were sandblasted (Mikro dental, MKK975) with $250 \mu m$ sized Al_2O_3 particles at 6 bar for 1 min to promote adhesion at the coating-substrate interface [32]. A series of ultrasonic surface cleaning in distilled water and ethanol for 15 min each was applied for degrease and remove sand particles from the substrates. Chloroform has been used in coating procedures to dissolve PLA. While the size of irregular shaped and agglomerated HA powders ranges from 3–5 μm , sharp-edged ZrO_2 powders have a maximum size of 49 μm and a purity of 99.7% (Fig. 1). PLA was first dissolved in chloroform at room temperature for 2 h. To synthesize PLA/HA composite coatings HA reinforcement was held constant at

50% by weight. On the other hand, 10, 20, and 30 wt% ZrO_2 reinforcement to HA balanced of 50 wt% (Table 1). Both possible delamination and sedimentation occurrence were effective in using the 50 wt% PLA fraction in the coatings. The hybrid mixture was stirred for another 2 h to ensure uniform dispersion of the reinforcement powders (HA and ZrO_2) in the PLA. To avoid particle agglomeration, it was then homogenized for 5 min in an ultrasonic homogenizer (MTI, MSK-USP-3N). The coating was carried out by using the dip-coating method, substrates kept in hybrid mixtures for 5 s, and pulled up at 45° to prevent clumping at the corners of Mg substrates. Finally, to prevent absorbing moisture from the atmosphere, coatings were stored in a desiccator containing silica gel at room temperature until the tests were carried out. On behalf of clarification, the abbreviations for PLA/HA and 10, 20, and 30 wt% ZrO_2 reinforced PLA/HA- ZrO_2 coatings will be used as PH, PHZ1, PHZ2, and PHZ3, respectively (Table 1).

Table 1. Abbreviations and compositions of coatings

Substrate	Coatings	Abbreviation	Composition (wt%)		
			PLA	HA	ZrO_2
Magnesium	PLA/HA	PH	50	50	0
	PLA/HA- ZrO_2 10 wt%	PHZ1	50	40	10
	PLA/HA- ZrO_2 20 wt%	PHZ2	50	30	20
	PLA/HA- ZrO_2 30 wt%	PHZ3	50	20	30

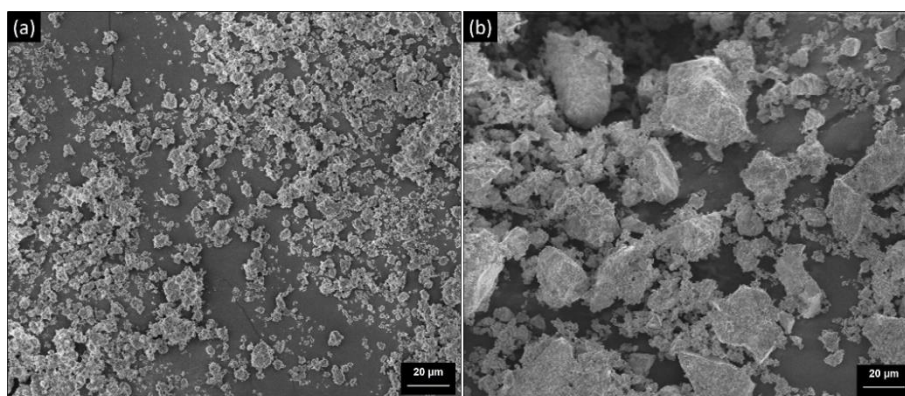


Fig. 1 SEM morphologies of the (a) HA and (b) ZrO_2 powders

2.2. Characterization

The morphological changes on coatings were investigated by scanning electron microscopy (SEM, Zeiss Sigma 300). In SEM morphological investigations, a thin Au-Pd coating was applied to coatings to increase the electrical conductivity of coatings for better observation. Energy dispersive spectroscopy analysis (EDS, Oxford INCA) was used for the elemental evaluation of coated Mg substrates which attached to the SEM. The phase analysis of hybrid composite coatings was determined using X-ray diffraction (XRD, PANalytical Empyrean) analysis. XRD analysis was carried out with a K-tube and a step rate of 0.02 at a wavelength of 1.5406 (between 25 and 55 2θ angles). Following adhesion tests, optical microscopy (OM) was used to better clarification of the adhesive behaviour of coatings.

2.3. Micro-Vickers and Adhesion Tests

The micro-Vickers hardness (DMHV100EDV, HARDWAY) device was used to determine the hardness values of the coatings. In the hardness measurements, a load of 100 gf (HV.0,1) was applied for 20 seconds and the hardness value was measured from five different regions. Adhesion testing was conducted according to ASTM D3359 [35]. In short, the test method covers the evaluation of the adhesion strength of the coatings on the substrate, using pressure-sensitive tape with several scratches. Adhesion tests were conducted with method B which claimed that firstly lattice patterns with numerous scratches (preferably more than 6) in every 90° directions were made on a coated substrate then pressure-sensitive tape (Elcometer 99, Elcometer, USA) is applied over scratches, finally removed from coated specimens. Adhesion resistance was evaluated by comparison with local delamination of coatings as visually. According to the separation rate of coatings from substrates as spatially, less than 0%, 5%, 5-15%, 15-35%, 35-65% and greater than 65% were defined as 5B, 4B, 3B, 2B, 1B, and 0B, respectively.

3. Results and Discussion

In Fig. 2a-d, SEM surface morphology images of PH, PHZ1, PHZ2, and PHZ3 coatings are presented, respectively. The first striking point of the SEM surface morphologies is the presence of agglomeration structures on all surfaces. While this agglomeration size is large in the PH coating, it is seen that the agglomeration size decreases with the increase of ZrO₂ reinforcements to PLA/HA composite composition (Fig. 2b, c). Moreover, with the 30% ZrO₂ (PHZ3) reinforcement, it was determined that these agglomerations were considerably reduced and were almost completely covered with PLA. Similar surface morphologies have been obtained by other researchers [12]. Considering the general morphology, it is predicted that while the smaller size of agglomeration is a desirable morphology for implant-tissue interaction in the biomedical usage of coatings, the biodegradability may increase but the adhesion strength of the coatings, which important parameter for coatings, may decrease. On the other hand, it has been stated in other studies that these properties will increase in PHZ3 coatings as a result of both the reduced agglomeration size and the fact that PLA completely covers the Mg surfaces [12]. It was concluded that ZrO₂ decreased the agglomeration rate between PLA/HA as a result of the increasing weight fraction. It is thought that the total agglomeration on the surface decreases as a result of the particle size of ZrO₂ is quite large compared to HA and resulted in HA agglomeration around the ZrO₂ particles. The main reason for this is thought to be inorganic - organic interactions between ZrO₂ and HA [36]. The increase in the tendency of this interaction with the increasing ZrO₂ fraction may have resulted in SEM morphologies which are presented in Fig. 2b-d. It can be said that morphological changes in PLA, HA, and ZrO₂ composition are highly affected by the components and their fractions. On the other hand, it is thought that the decrease in micropores on the surface together with the increasing ZrO₂ reinforcement will increase the stability of the coatings in the body fluid, thus increasing the service life of the implant (Fig. 2a-d). According to a study conducted by Jin *et al.* [11], similar surface morphology was obtained with the increasing PLA fraction in the coating, while it was mentioned that the completely sealed Mg would increase the possible corrosion resistance. Unlike the aforementioned study, it is thought that the similar coating morphologies obtained with the increase of the ZrO₂ fraction rather than increasing the PLA fraction will be more effective on the adhesion strength.

The EDS analyses carried out to reveal the elemental compositions in the coatings are given in Figs. 3a-b. As seen in Fig. 3a, in the analysis of the point indicated by the white square, no elemental finding was found for the base material Mg, while Ca and P elements were found due to their HA structure. In Fig. 3b, in EDS analyses taken from a surface similar to the PHZ morphology (Fig. 2d), the Zr element was also found in addition to Ca and P.

Among these findings, the presence of Ca, P, and Zr in the structure as well as the absence of Mg substrate and the fact that the coatings are crack-free and homogeneous can be presented as proof that the coatings can be successful in use as implant material.

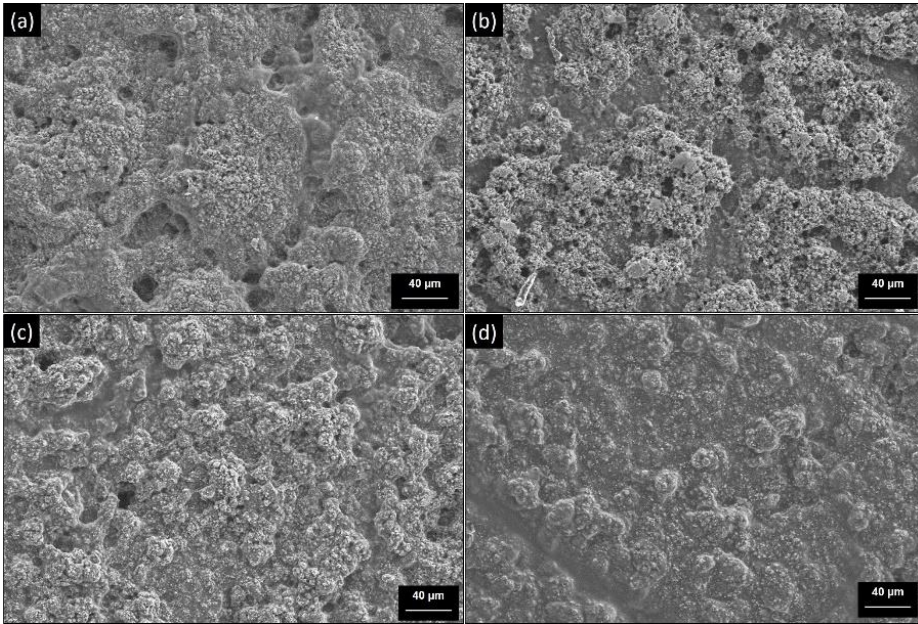


Fig. 2 SEM surface morphologies of coatings with different compositions: (a) PH, (b) PHZ1, (c) PHZ2, and (d) PHZ3

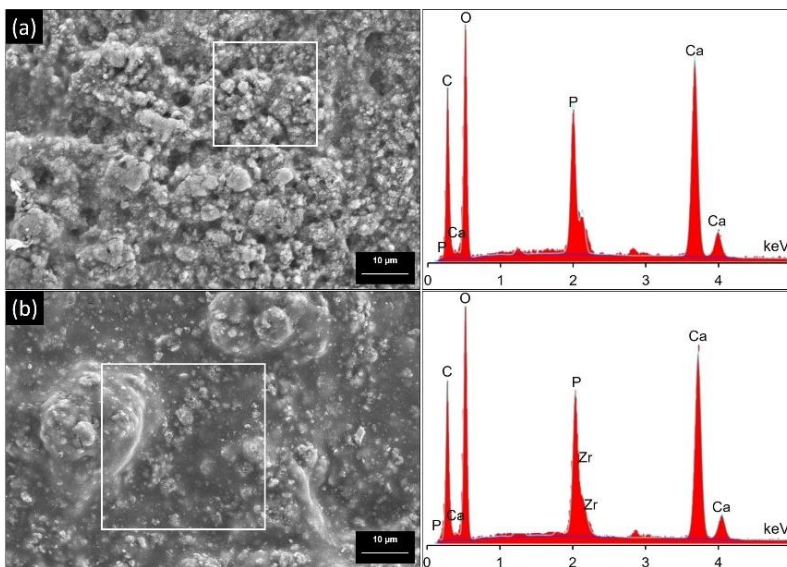


Fig. 3 EDS elemental analysis of (a) PH and (b) PHZ3 coatings

The elemental composition of the coatings on Mg substrates is given in EDS elementally. However, the results of XRD analysis carried out to investigate the presence of these elements formed in the HA phase are presented in Fig. 4. As indicated by the black line in

Fig. 4, characteristic HA peaks were encountered in the 30–32 2θ angle range in PH coatings and the accuracy of the HA phase in the structure was revealed (ICDD: 01-074-9780). It is well known that compared to other Ca–P bio ceramics (such as TCP: $\text{Ca}_3(\text{PO}_4)_2$), HA exhibits lower solubility as a result of its high crystallinity. Due to these features, the coating dissolves more slowly and is more stable in the body, and increases the service life of the implant material. On the other hand, the presence of ZrO_2 in PHZ coatings was found at ~ 30.4 , ~ 31 , 31.2 , and ~ 35.1 2θ angles (JCPDS: 81-1314), respectively, as shown by the red line in the figure [37]. Unlike the study by Yuan *et al.* [26], the crystallinity of the HA phase is quite high, although no heat treatment was applied to the coatings. As a result, since HA will reduce the dissolution rate of the coatings, it provides controllability of the implant service time [38].

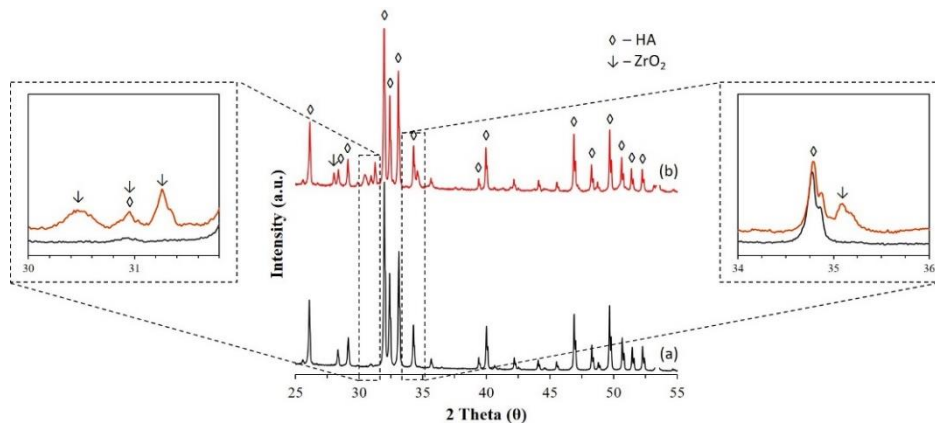


Fig. 4 XRD analysis results of coatings: (a) PH and (b) PHZ, with detailed peaks at 30–31.8 and 34–36 2θ degrees

In Table 2, the micro-Vickers hardness and thickness results of the coatings are presented with standard deviations. It is seen that the hardness increases with the increasing ZrO_2 fraction ratio. The reason for this is thought to be due to the higher hardness value of ZrO_2 compared to HA. On the other hand, it is noteworthy that the coating thickness increased with ZrO_2 10 wt% reinforcement, but remained almost constant with 20 wt% and 30 wt% reinforcements, but the standard deviation decreased. With such a decreasing standard deviation, it can be said that the coating thickness was found to be the most stable in the PHZ3 coating. The surface morphologies in Fig. 2 confirm this change in coating thickness. As it is known, the increase in coating thickness is an important factor that will decrease the adhesion strength between the substrate and the coating film. However, as can be seen from Figs. 5–6, the adhesion strength of the coatings increased with the addition of ZrO_2 . It is predicted that this may be the result of both ZrO_2 preventing agglomeration and the higher affinity of ZrO_2 to Mg than HA.

Table 2. Micro-Vickers hardness and thickness of coatings

Coatings	Hardness (HV)	Thickness (μm)
PH	135.6 ± 3.8	74 ± 14
PHZ1	219.8 ± 4.1	94 ± 11
PHZ2	241.4 ± 2.6	97 ± 9
PHZ3	279.2 ± 4.7	96 ± 4

Undoubtedly, it is very important for the coating to remain on the substrate for a long time after any coating on Mg alloys, in protecting the Mg from the physiological environment against aggressive media. Accordingly, the coatings must be firmly attached to the substrate (advanced adhesion property). Tape test results, which are an indication of the adhesion strengths performed in this direction, are given for PH, PHZ1, PHZ2, and PHZ3 coatings in Fig. 5a-d, respectively. In the figure, the black areas represent the substrate material (Mg), while the orange areas represent the presence of coatings. The first finding that draws attention after the adhesion tests is the coating structure that occurs in PH coatings and deforms completely in some parts in various areas (Fig. 5a). On the other hand, partial black coating removal was observed around the scratches on the PHZ1 coating (Fig. 5b). In Fig. 5c, black areas were found on the scratches on the PHZ2 coating, and no coating remained around the scratch. As a result of the increased ZrO_2 reinforcement fraction, on the PHZ3 coating, there were no areas of the substrate material either on the scratch or around the scratches (Fig. 5d). In some studies, a similar adhesion strength increase was observed with increasing PLA fraction [11]. Based on this, it has been revealed that the adhesion strength is not only affected by the PLA fraction, but also by the agglomeration of PLA matrix composite coatings. Briefly, it is thought that high adhesion strength can be obtained as a result of the smoother surface morphology and lack of agglomeration with the increased ZrO_2 reinforcement in this study.

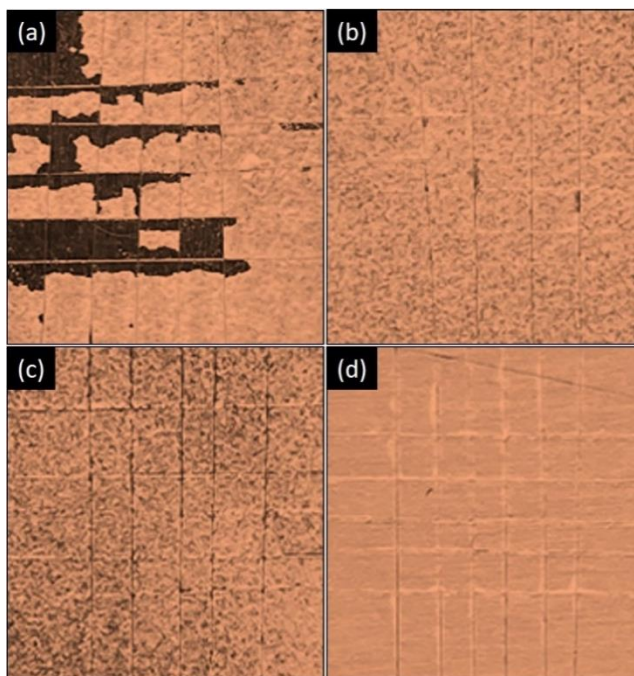


Fig. 5 Tape test results of (a) PH, (b) PHZ1, (c) PHZ2, and (d) PHZ3 coatings, respectively, in accordance with ASTM D3359 standard

In Fig. 6a-d, OM images are presented to reveal the behaviour of the PH, PHZ1, PHZ2, and PHZ3 coatings, especially around the scratches, after the adhesion tests, respectively. Based on this, the adhesion strength of the coatings, as specified in the ASTM D3359 standard, is 1B, 3B, 4B, and 5B for PH, PHZ1, PHZ2, and PHZ3, respectively [35]. In Fig. 6a, the presence of both substrate and partial coatings in the PH coating is shown. The partial coating in the middle of the scratches is thought to have higher strength in the middle part

of the coating. The reason for this result is that the adhesion strength is weak in the sharp corners close to the scratch traces. Although the traces of scratches are not fully visible in Fig. 5b, c, these traces are visible in Fig. 6b, c, so it has been determined that the scratch traces have reached the base material. It is thought that increased adhesion strength with the increased reinforcement fraction of ZrO_2 may be the result of the decreased agglomeration presented in Fig. 2. Another factor is that the polymer and ceramic structures of PLA and HA have less affinity with the metallic substrate (Mg), and metal-polymer/ceramic bonding may have increased with the reinforcement of metal oxide (ZrO_2). The last phenomenon that increases the adhesion strength is thought to be the result of decreasing PLA/HA agglomeration with increasing ZrO_2 fraction and increasing the contact angle between PLA and HA- ZrO_2 reinforcement.

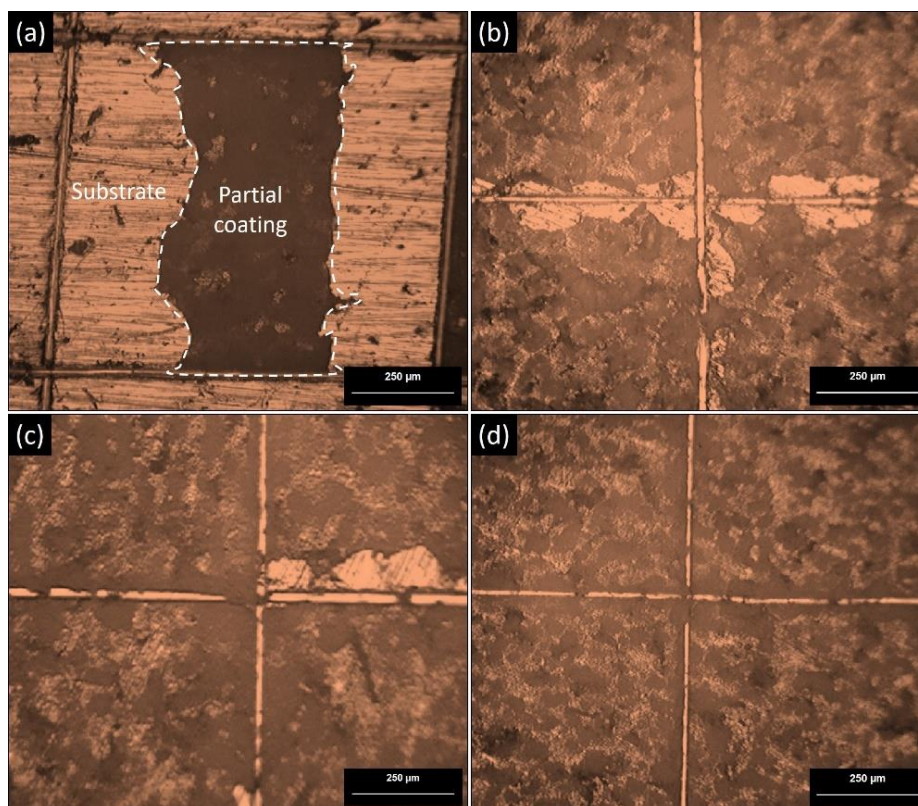


Fig. 6 OM microphotographs of (a) PH, (b) PHZ1, (c) PHZ2, and (d) PHZ3 coatings for the examination of adhesion scratches, respectively

In Fig. 7, a mechanism is proposed for the relationship of coatings with different compositions and fractions to the proposed surface morphology, such as morphology, possible implant-tissue interface interaction, solubility, and adhesion behaviour. A smoother surface was obtained as seen in Fig. 7 with ZrO_2 reinforcement (also can be seen in Fig. 2d). As a result of the proposed mechanism, there are agglomerations and micro porosities in PLA/HA coatings that will increase the implant-tissue interaction. However, this surface morphology can also lead to fast biodegradability and low adhesion strength of coatings. On the other hand, it has been determined that the decrease in the size of these agglomerations as a result of increasing ZrO_2 contribution and the fact that the coatings are increasingly smooth and homogeneous lead to an increase in the biodegradability and

adhesion strength of PLA/HA-ZrO₂ coatings. Similar surface morphology and coating interface were reported by Chen *et al.* [39], which can be said that the high adhesion strength obtained has a similar mechanism.

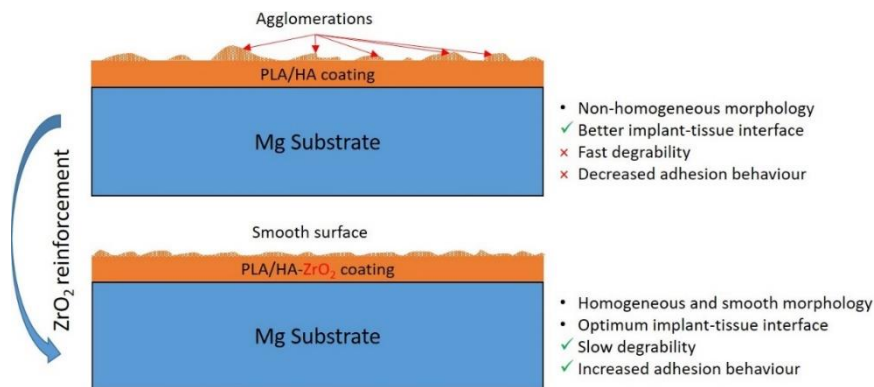


Fig. 7 The proposed mechanism for the effects on the surface morphology and coating structure as a result of ZrO₂ reinforcement

5. Conclusions

The morphological and adhesion properties of poly- (lactic) acid/hydroxyapatite-zirconia (PLA/HA-ZrO₂) coatings were successfully proven within the scope of the study, with the goal of both limiting the rapid biodegradation process of Magnesium (Mg) biomaterials and minimizing the H₂ gas formation. To investigate the ZrO₂ reinforcement in PLA/HA-ZrO₂ hybrid coatings, 10, 20, and 30 wt% ZrO₂ doped coatings, were successfully coated on Mg using the dip-coating method. In SEM surface morphologies, a large agglomeration was observed in PLA/HA coating, it was observed that these agglomerations' sizes decreased with increasing ZrO₂ reinforcement (10 and 20 wt%). Furthermore, it was discovered that the surface has a smooth structure and entirely seals the Mg substrate with the 30 wt% ZrO₂ reinforcement. Additionally, EDS analyses confirmed the presence of Ca, P, and Zr in the coating. XRD analysis revealed the HA and ZrO₂ phases, confirming that the elemental presence of Ca and P in the coatings is HA and revealing their amorphous-crystalline characteristics. It was found that HA did not decompose into different structures such as TCP as a result of not applying heat treatment in the production of coatings. While the hardness values of the coatings increased with the ZrO₂ reinforcement, they increased further with the increasing ZrO₂ fraction. On the other hand, it was concluded that the coating thicknesses did not change much with the increasing ZrO₂ fraction, but the roughness on the surfaces of the coatings decreased, also confirmed by the decrease in the standard deviation in thickness. As a consequence of the adhesive strength, which is arguably the most expected feature of all biomedical coatings, it has been discovered that the adhesion strength of the coatings increased with the increase of ZrO₂ reinforcement (1B, 3B, 4B, and 5B for PH, PHZ1, PHZ2, and PHZ3, respectively). The OM examinations performed after the adhesion tests corroborated these findings. The study found that adding a third-phase reinforcement to PLA/HA composite coatings can modify the physical properties of the coating. High biodegradability and H₂ gas evolution, which limit the use of Mg in biomedical applications, are prevented by polymer-based hybrid composite coatings on it, and its prevalence is assumed to rise.

References

- [1] Santos-Coquillat A, Martínez-Campos E, Mora Sánchez H, Moreno L, Arrabal R, Mohedano M, Hybrid functionalized coatings on Metallic Biomaterials for Tissue Engineering. *Surface Coatings Technology*, 2021; 422(July). <https://doi.org/10.1016/j.surfcoat.2021.127508>.
- [2] Song J, Winkeljann B, Lieleg O. Biopolymer-Based Coatings: Promising Strategies to Improve the Biocompatibility and Functionality of Materials Used in Biomedical Engineering. *Advanced Materials Interfaces*, 2020; 7(17). <https://doi.org/10.1002/admi.202000850>.
- [3] Topuz M, Dikici B, Gavgalı M, Yilmazer Y. Effect of hydroxyapatite:zirconia volume fraction ratio on mechanical and corrosive properties of Ti-matrix composite scaffolds. *Transactions of Nonferrous Metals Society of China*, 2022; 32(3): 882–894. [https://doi.org/10.1016/s1003-6326\(22\)65840-0](https://doi.org/10.1016/s1003-6326(22)65840-0).
- [4] Topuz M, Dikici B, Gavgalı M. Titanium-based composite scaffolds reinforced with hydroxyapatite-zirconia: Production, mechanical and in-vitro characterization. *Journal of the Mechanical Behavior of Biomedical Materials*, June 2021; 118(March): 104480. <https://doi.org/10.1016/j.jmbbm.2021.104480>.
- [5] Çomaklı O. Improved structural, mechanical, corrosion and tribocorrosion properties of Ti45Nb alloys by TiN, TiAlN monolayers, and TiAlN/TiN multilayer ceramic films. *Ceramics International*, 2021; 47(3): 4149–4156. <https://doi.org/10.1016/j.ceramint.2020.09.292>.
- [6] Songur F, Dikici B, Niinomi M, Arslan E. The plasma electrolytic oxidation (PEO) coatings to enhance in-vitro corrosion resistance of Ti–29Nb–13Ta–4.6Zr alloys: The combined effect of duty cycle and the deposition frequency. *Surface and Coatings Technology*, 2019; 374(April): 345–354. <https://doi.org/10.1016/j.surfcoat.2019.06.025>.
- [7] Niinomi M, Nakai M. Titanium-Based Biomaterials for Preventing Stress Shielding between Implant Devices and Bone. *International Journal of Biomaterials*, 2011;2011:1–10. <https://doi.org/10.1155/2011/836587>.
- [8] Topuz M, Dikici B, Gavgalı M, Kaseem M. Processing of Ti/(HA+ZrO₂) biocomposite and 50% porous hybrid scaffolds with low Young's modulus by powder metallurgy: Comparing of structural, mechanical, and corrosion properties. *Materials Today Communications*, 2021; 29(August): 102813. <https://doi.org/10.1016/j.mtcomm.2021.102813>.
- [9] Rahman M, Li Y, Wen C. HA coating on Mg alloys for biomedical applications: A review. *Journal of Magnesium and Alloys*, 2020; 8(3): 929–943. <https://doi.org/10.1016/j.jma.2020.05.003>.
- [10] Gao J, Su Y, Qin YX. Calcium phosphate coatings enhance biocompatibility and degradation resistance of magnesium alloy: Correlating in vitro and in vivo studies. *Bioactive Materials*, 2021; 6(5): 1223–1229. <https://doi.org/10.1016/j.bioactmat.2020.10.024>.
- [11] Sarian MN, Iqbal N, Sotoudehbagha P, Razavi M, Ahmed QU, Sukotjo C, et al. Potential bioactive coating system for high-performance absorbable magnesium bone implants. *Bioactive Materials*, 2022; 12(October 2021): 42–63. <https://doi.org/10.1016/j.bioactmat.2021.10.034>.
- [12] Li X, Weng Z, Yuan W, Luo X, Wong HM, Liu X, et al. Corrosion resistance of dicalcium phosphate dihydrate/poly(lactic-co-glycolic acid) hybrid coating on AZ31 magnesium alloy. *Corrosion Science*, 2016; 102: 209–221. <https://doi.org/10.1016/j.corsci.2015.10.010>.
- [13] Shi P, Niu B, E S, Chen Y, Li Q. Preparation and characterization of PLA coating and PLA/MAO composite coatings on AZ31 magnesium alloy for improvement of corrosion

- resistance. Surface and Coatings Technology, 2015;262:26–32. <https://doi.org/10.1016/j.surfcoat.2014.11.069>.
- [14] Jin J, Chen X, Zhou S. Biocorrosion evaluation and bonding strength of HA-CS/PLA hybrid coating on micro-arc oxidised AZ91D magnesium alloy. Materials Technology, 2020; 00(00): 1–8. <https://doi.org/10.1080/10667857.2020.1863556>.
- [15] Yamada S, Yamamoto A, Kasuga T. Poly(l-lactic acid)/vaterite composite coatings on metallic magnesium. Journal of Materials Science: Materials in Medicine, 2014; 25(12): 2639–2647. <https://doi.org/10.1007/s10856-014-5302-5>.
- [16] Li H yang, Huang D ni, Ren K feng, Ji J. Inorganic-polymer composite coatings for biomedical devices. Smart Materials in Medicine, 2021; 2(August 2020): 1–14. <https://doi.org/10.1016/j.smaim.2020.10.002>.
- [17] Vacaras S, Baciut M, Lucaciu O, Dinu C, Baciut G, Crisan L, et al. Understanding the basis of medical use of poly-lactide-based resorbable polymers and composites—a review of the clinical and metabolic impact. Drug Metabolism Reviews, 2019; 51(4): 570–588. <https://doi.org/10.1080/03602532.2019.1642911>.
- [18] Liu S, Qin S, He M, Zhou D, Qin Q, Wang H. Current applications of poly(lactic acid) composites in tissue engineering and drug delivery. Composites Part B: Engineering, 2020; 199(May). <https://doi.org/10.1016/j.compositesb.2020.108238>.
- [19] Zan J, Qian G, Deng F, Zhang J, Zeng Z, Peng S, et al. Dilemma and breakthrough of biodegradable poly-L-lactic acid in bone tissue repair. Journal of Materials Research and Technology, 2022; 17: 2369–2387. <https://doi.org/10.1016/j.jmrt.2022.01.164>.
- [20] Narayanan G, Vernekar VN, Kuyinu EL, Laurencin CT. Poly (lactic acid)-based biomaterials for orthopaedic regenerative engineering. Advanced Drug Delivery Reviews, 2016; 107: 247–276. <https://doi.org/10.1016/j.addr.2016.04.015>.
- [21] Chen Y, Geever LM, Killion JA, Lyons JG, Higginbotham CL, Devine DM. Review of Multifarious Applications of Poly (Lactic Acid). Polymer-Plastics Technology and Materials, 2016; 55(10): 1057–1075. <https://doi.org/10.1080/03602559.2015.1132465>.
- [22] Roointan A, Kianpour S, Memari F, Gandomani M, Gheibi Hayat SM, Mohammadi-Samani S. Poly(lactic-co-glycolic acid): The most ardent and flexible candidate in biomedicine! International Journal of Polymeric Materials, 2018; 67(17): 1028–1049. <https://doi.org/10.1080/00914037.2017.1405350>.
- [23] Dikici B, Niinomi M, Topuz M, Koc SG, Nakai M. Synthesis of biphasic calcium phosphate (BCP) coatings on β -type titanium alloys reinforced with rutile-TiO₂ compounds: adhesion resistance and in-vitro corrosion. Journal of Sol-Gel Science and Technology, September 27, 2018; 87(3): 713–724. <https://doi.org/10.1007/s10971-018-4755-2>.
- [24] Dikici B, Niinomi M, Topuz M, Say Y, Aksakal B, Yilmazer H, et al. Synthesis and Characterization of Hydroxyapatite/TiO₂ Coatings on the β -Type Titanium Alloys with Different Sintering Parameters using Sol-Gel Method. Protection of Metals and Physical Chemistry of Surfaces, May 16, 2018; 54(3): 457–462. <https://doi.org/10.1134/S2070205118030255>.
- [25] Yigit O, Dikici B, Ozdemir N, Arslan E, Senocak TC, Ozdemir N. Plasma electrolytic oxidation of Ti-6Al-4V alloys in nHA/GNS containing electrolytes for biomedical applications: The combined effect of the deposition frequency and GNS weight percentage. Surface and Coatings Technology, July 2021; 32(March): 127139. <https://doi.org/10.1007/s10856-021-06514-w>.
- [26] Yuan Q, Wu J, Qin C, Xu A, Zhang Z, Lin S, et al. Spin-coating synthesis and characterization of Zn-doped hydroxyapatite/polylactic acid composite coatings. Surface and Coatings Technology, 2016; 307: 461–469. <https://doi.org/10.1016/j.surfcoat.2016.09.021>.
- [27] Pitjamit S, Thunsiri K, Nakkiew W, Wongwichai T, Pothacharoen P, Wattanutchariya W. The Possibility of Interlocking Nail Fabrication from FFF 3D Printing PLA/PCL/HA

- Composites Coated by Local Silk Fibroin for Canine Bone Fracture Treatment. *Materials* (Basel), March 28, 2020; 13(7): 1564. <https://doi.org/10.3390/ma13071564>.
- [28] Heimann RB. Plasma-Sprayed Hydroxylapatite-Based Coatings: Chemical, Mechanical, Microstructural, and Biomedical Properties. *Journal of Thermal Spray Technology*, 2016; 25(5): 827–850. <https://doi.org/10.1007/s11666-016-0421-9>.
- [29] Dikici B, Topuz M. Production of Annealed Cold-Sprayed 316L Stainless Steel Coatings for Biomedical Applications and Their in-vitro Corrosion Response. *Protection of Metals and Physical Chemistry of Surfaces*, March 5, 2018; 54(2): 333–339. <https://doi.org/10.1134/S2070205118020168>.
- [30] Kong D, Long D, Wu Y, Zhou C. Mechanical properties of hydroxyapatite-zirconia coatings prepared by magnetron sputtering. *Transactions of Nonferrous Metals Society of China*, 2012; 22(1): 104–110. [https://doi.org/10.1016/S1003-6326\(11\)61147-3](https://doi.org/10.1016/S1003-6326(11)61147-3).
- [31] He DH, Wang P, Liu P, Liu XK, Ma FC, Zhao J. HA coating fabricated by electrochemical deposition on modified Ti6Al4V alloy. *Surface and Coatings Technology*, 2015; 277: 203–209. <https://doi.org/10.1016/j.surfcoat.2015.07.038>.
- [32] Dikici B, Niinomi M, Topuz M, Say Y, Aksakal B, Yilmazer H, et al. Synthesis and Characterization of Hydroxyapatite/TiO₂ Coatings on the β -Type Titanium Alloys with Different Sintering Parameters using Sol-Gel Method. *Protection of Metals and Physical Chemistry of Surfaces*, May 2018; 54(3): 457–462. <https://doi.org/10.1134/S2070205118030255>.
- [33] Mohseni E, Zalnezhad E, Bushroa AR. Comparative investigation on the adhesion of hydroxyapatite coating on Ti-6Al-4V implant: A review paper. *International Journal of Adhesion and Adhesives*, 2014; 48: 238–257. <https://doi.org/10.1016/j.ijadhadh.2013.09.030>.
- [34] Harb SV, Bassous NJ, de Souza TAC, Trentin A, Pulcinelli SH, Santilli CV, Webster TJ, Lobo AO, Hammer P. Hydroxyapatite and β -TCP modified PMMA-TiO₂ and PMMA-ZrO₂ coatings for bioactive corrosion protection of Ti6Al4V implants. *Materials Science and Engineering: C*, 2020; 116: 111149. <https://doi.org/10.1016/j.msec.2020.111149>.
- [35] ASTM D3359-09. Standard Test Methods for Measuring Adhesion by Tape Test, 2012. <https://doi.org/10.1520/D3359-09E02.2>.
- [36] Silina YE, Gernaey KV, Semenova D, Iatsunskyi I. Application of Organic-Inorganic Hybrids in Chemical Analysis, Bio- and Environmental Monitoring. *Applied Sciences*, 2020; 10(4): 1458. <https://doi.org/10.3390/app10041458>.
- [37] Rauta PR, Manivasakan P, Rajendran V, Sahu BB, Panda BK, Mohapatra P. Phase transformation of ZrO₂ nanoparticles produced from zircon. *Phase Transitions*, 2012; 85(1–2): 13–26. <https://doi.org/10.1080/01411594.2011.619698>.
- [38] Topuz, M. Dikici, B. Two simple methods for surface modification of lithium disilicate dental blocks with hydroxyapatite, *Research on Engineering Structures and Materials (RESM)*, 2019; 1: 97-104. <https://doi.org/10.17515/resm2019.132me0506tn>.
- [39] Chen QZ, Blaker JJ, Boccaccini AR. Bioactive and Mechanically Strong Bioglass®-Poly(D,L-Lactic Acid) Composite Coatings on Surgical Sutures. *Journal of Biomedical Materials Research – Part B*, 2005; 76B(2): 354-363. <https://doi.org/10.1002/jbm.b.30379>.

Blank Page



Research Article

Weldability of interlocked-end friction stir welding of aluminum alloy: single and double-sided welding

Olatunji Oladimeji Ojo^{*1,3,a}, Gbadebo Samuel John^{2,3,b}

¹Department of Industrial and Production Engineering, Federal University of Technology Akure, Nigeria.

²Department of Mechanical Engineering, Ogun State Institute of Technology Igbesa, Nigeria.

³Department of Mechanical Engineering, Federal University of Technology Akure, Nigeria.

Article Info

Article history:

Received 30 May 2022

Revised 05 Aug 2022

Accepted 07 Aug 2022

Keywords:

Weldability;
Interlocked end friction stir welding;
Aluminum alloy;
Weld structure;
Tensile strength;
Fracture

Abstract

The weldability of the interlocked-end friction stir welding (IFSW) of aluminum plates was studied via the use of single and double-sided welding procedures. The abutting ends of the Al plates were milled into equidistant slots (with 5 mm rise and 10 mm span) and an interlocked/meshed end profile was formed when two slotted plates were brought together. The friction stir welding of the interlocked end of the plates was carried out at different tool rotational (700 – 1120 rpm) and traverse (21 – 63 mm/min) speeds while the structure, tensile strength, and fracture behaviors of the resultant welds were examined. The results showed the presence of flow-induced defects in the welds irrespective of the adopted welding procedure. Relative to the single-sided welds, the severity of the weld defect was significantly reduced in the double-sided welds due to dual material plasticization, material consolidation, and twofold recrystallization advantages. Improved tensile strength (from 39.6 to 69.1 MPa), reduced area fraction of flow-induced defect, and a large area with ductile features are obtained in the double-sided IFSW weld. A double-sided welding procedure is recommended for the interlocked-end friction stir welding process.

© 2022 MIM Research Group. All rights reserved.

1. Introduction

Aluminum alloys are used in automotive, aerospace, marine applications, and high-speed train manufacturing because of their high strength, corrosion resistance, and high ductility [1]. Welding of Al alloy with fusion and other means always introduces challenges like distortion, porosity and blowholes, hot cracking, and excess heat to aluminum welds [2]. Solid-state friction stir welding (FSW) of Al alloy can effectively remove these challenges as the FSW process takes place at a temperature below the melting point of Al alloys [3][4]. Tool design modifications [5][6], process parameter optimization [7-10], and variance of the FSW/FSSW process [11-15] have been successfully utilized in improving the mechanical properties of friction stir welds of Al alloys in literature. Meanwhile, modification of joint-line/configuration is adjudged as a worthy alternative/route for improving the performance of dissimilar and similar friction stir welds, which is yet to receive concerted efforts in literature. Limited studies have been carried out on the alteration of joint-line/configuration for the improvement of weld strength [5][16][17]. Thus, this paper attempts to modify/change the abutting line of the conventional friction stir welding process to an interlocked end and studies the weld strength and fracture behavior of the resultant joints under varied process parameters.

Some of the existing works in the literature on the modifications of joint-line/configuration have shown good prospects while improvements are still pertinent via continuous studies.

*Corresponding author: ojoomadimeji90@yahoo.com

^a orcid.org/0000-0002-6581-1168; ^b orcid.org/0000-0001-6693-0188

DOI: <http://dx.doi.org/10.17515/resm2022.439me3005>

Res. Eng. Struct. Mat. Vol. 8 Iss. 4 (2022) 735-749

For instance, cuboid-shaped grooves were machined at the abutting ends of the Ti-6Al-4V and aluminum alloys before the lap-butt friction stir welding of the alloys in the studies of Li et al. [18]. It was reported that up to 92 % of the Al alloy's tensile strength was achieved as the tensile fracture resistance of the joint. Kumar et al. [11] also utilized the same lap-butt joint configuration (cuboid-shaped grooves) to join AA6061-T6 and AZ31B magnesium alloys, and a joint efficiency of 61% was obtained. Acharya et al [19] investigated the double-butt-lap (DBL) joint configuration of the AA6061-T6 Al alloy and the obtained result was compared with that of the single-square-butt (SSB) joints. The DBL joints showed better tensile strength as compared to the SSB joints. Pankul et al. [5] investigated the friction stir welding of the AA6063 aluminum alloy by changing the conventional butt geometry to an inclined butt (scarf configuration). This welding approach was reported to be susceptible to undesirable flow defects such as tunnel, hooking, kissing, and zigzag line due to the inherent low inclined angle of 26° to the vertical. In addition, the scarf configuration-produced joint was acknowledged to have low loadbearing resistance in comparison to the butt/conventional friction stir welded counterparts. In the search for better strength in scarf configuration, Sethi et al. [20] increased the angle of inclination to 60° using AA6061-T6 Al alloy as the base material. The increase in the angle of inclination improved the tensile strength of the joint by 13.5% over the sample produced by the square butt configuration. Similarly, Reza-E-Rabby et al. [16] also investigated the dovetail (head-tail) FSW of the rolled homogeneous armor steel (as the head) and AA6061 Al (as the tail) alloys. An improvement in tensile strength (4000 N/mm) was obtained via this welding approach.

Recently, Zhang et al [21] conducted tooth-shaped joint configuration-based friction stir welding on dissimilar copper and aluminum alloy. The tooth was designed to have equal width and height of 3 mm. It was reported that the disparity in the properties of the base materials negatively affected the flowability and the resultant metallurgical bonding of the joint. The impact of tooth-shaped joint configuration on the properties of similar alloys is yet to be explicated in the literature. This study utilizes a somewhat similar joining approach, otherwise referred to as the interlock-end friction stir welding process to join Al alloy sheets having equal thicknesses to unravel the gap in literature. Rises and spans were machined along the abutting ends of the Al plates in such a manner that when the plates were brought together, they formed an interlocked end. The rise of the interlocked end was designed to be higher than the span to form a symmetric profile after the machined ends of the sheets were brought together in this study. The AA1050 aluminum alloy has industrial applications in the fabrication of chemical process plant equipment, architectural flashings, lamb reflectors, and food containers due to its high corrosion resistance [22]. Thus, the AA1050 Al alloy was employed as the base material for this study. This paper investigated the weldability of the interlock-end friction stir welding (IFSW) of AA1050 Al alloy while areas such as the structure, tensile strength, and fracture behaviors of the IFSW joints were covered.

2. Materials and Method

Commercial rolled AA1050 aluminum alloy plates having a thickness of 6 mm were utilized as the base metal. Table 1 reveals the chemical composition of the base metal. The as-received Al plates were cleaned with acetone to remove the inherent dirt and were subsequently cut into the dimensions of 100 x 50 mm x 6 mm on a guillotine machine. Before the interlocked-end friction stir welding (IFSW) process, the preliminary edge preparation (or cutting of the rise and span) was performed on the abutting ends of the Al plates on a milling machine. Fig. 1 shows the equidistant slots (having a rise of 5 mm and a span of 10 mm) that were milled out along the 100 mm length of the cut Al samples.

Table 1. Chemical Composition of base metal (Wt %)

Element	Mg	Si	Mn	Ni	Zn	Fe	Ti	Ga	Al
Wt%	0.011	0.065	0.003	0.004	0.003	0.336	0.026	0.018	Bal.

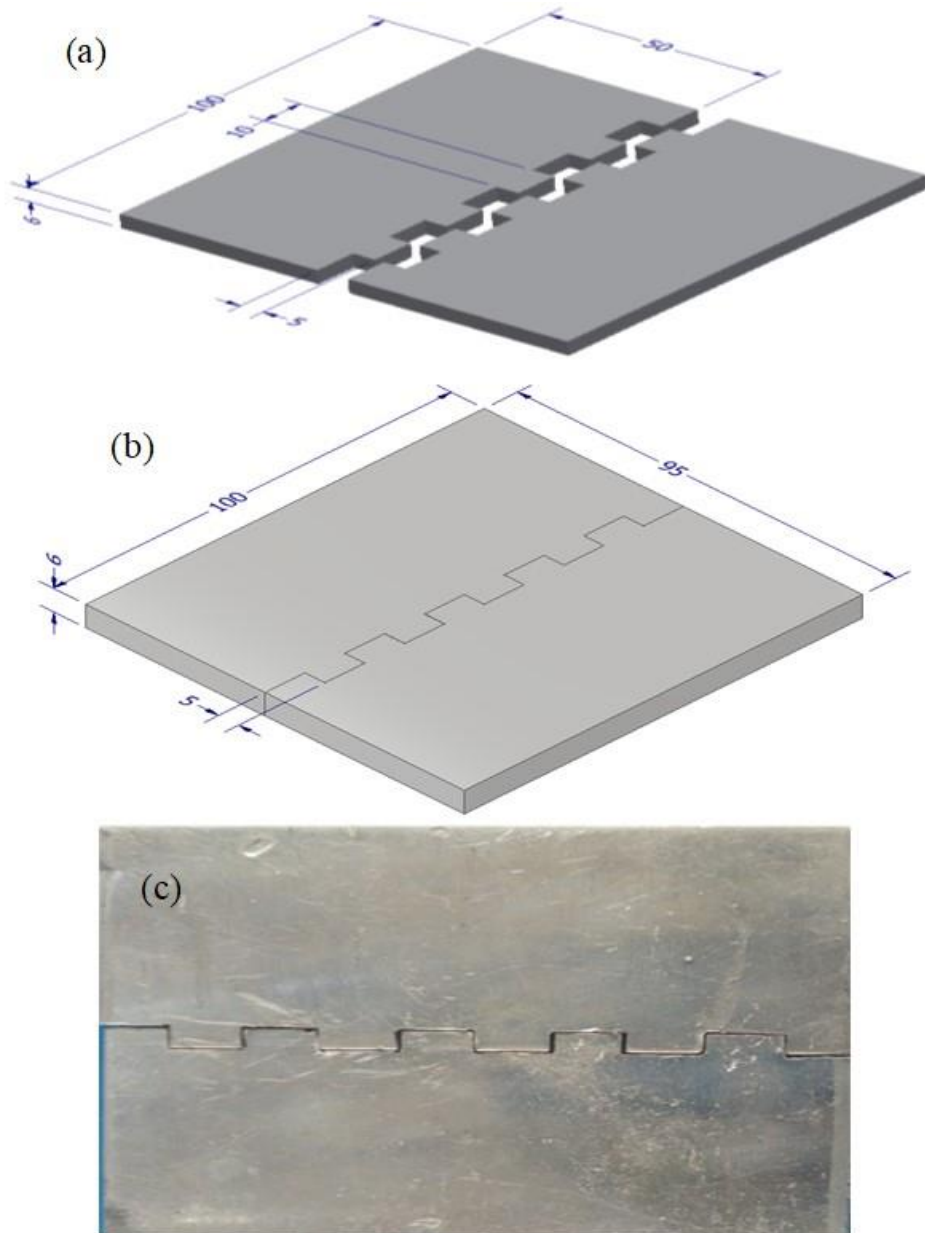


Fig. 1 Interlock-end configuration for the welding process: (a) schematic of the milled ends showing rises and spans (b) schematic of the meshed/interlocked ends (c) actual meshed/interlocked-ends

The interlocked-end friction stir welding (IFSW) process was then carried out along the interlocked/meshed end of the plates. A 20 mm diameter HSS tool steel was selected for

the welding process. Pin and pinless tools were fabricated from the HSS tool for the welding process. Meanwhile, the design of the pin tool was based on the joint configurations. Since the rise in the interlock-end was 5 mm (see Fig.1), the pin diameter of 7 mm was fabricated to accommodate the interlocked zone and ensure proper intermixing when the pin is plunged into the setup of the workpiece. Fig. 2 shows the welding tools (pin and pinless) that were utilized for the IFSW process. The application of the pin tool in welding the setup (shown in Fig.1c) at one side is referred to as a single-sided IFSW welding while the welding of both Al sides with a pin tool (upper side) and pinless tool (bottom side) is referred to double-sided IFSW welding in this paper. The single and double-sided IFSW processes were performed at varied tool rotational speeds (710, 900, and 1120 rpm) and traverse speeds (21, 40, and 63 mm/min) based on the outcomes of the preliminary study. The preliminary studies were based on the visual assessment of the stirred paths and the hammer impact-knock-off (HIKO) assessment. First, the process parameters of the welds having no surface flow-induced discontinuities or defects were accepted and the resultant/accepted weld samples were subjected to hammer impact-knock off (HIKO) processing. Before the HIKO test, an accepted weld sample was clamped to a bench vice in a manner that the weld line/path was left above the jaws of the vice. Repeated hammer impact loads were progressively employed to bend the weld sample to the righthand side and the reverse/opposite side of the vice respectively until the knockoff of the unclamped section of the weld sample ensued. The weld samples that could not bear up to 3 side-bends were rejected. Based on this, the process parameters were selected for this study. The plates in the single-sided welds were first welded together using a pin tool as shown in Fig.3a and 3b. The double-sided IFSW welding was carried out in a step-wise manner under the same welding conditions except that the pin tool was replaced with the pinless tool for the welding of the bottom side of the Al plates. It should be noted that the plate was turned over in such a way that the advancing side (AS) during the single-sided IFSW welding became the retreating side (RS) during the pinless welding of the opposite/bottom side.

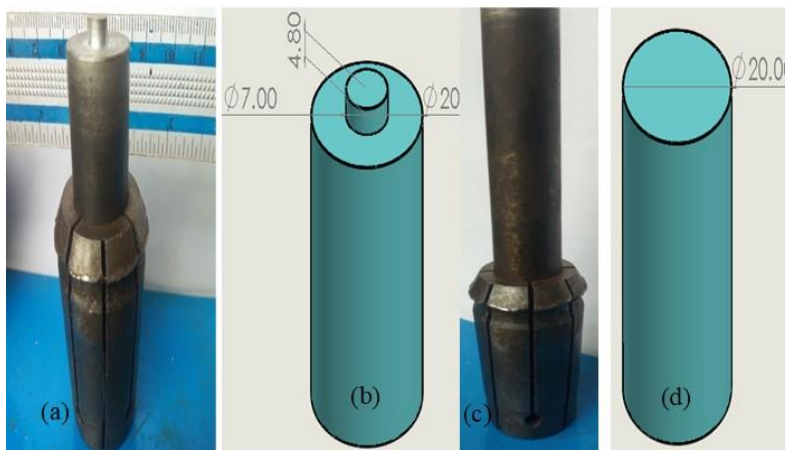


Fig. 2 Welding tool used for the IFSW process: (a) Pin tool with collet, (b) Schematic of the pin tool (c) Pinless tool with collect, (d) Schematic of the pinless tool (All dimensions are in mm)

The single- and double-sided IFSW'ed samples were cut perpendicular to the welding direction, ground, polished, and etched in Keller's reagent (1 ml HF + 1.5 ml HCL + 2.5 mlNH₃ + 95 ml H₂O). The microstructure of the etched samples was examined under an OMAX computerized optical microscope (OM). The tensile samples were obtained

according to the illustration shown in Fig.4a. The samples for the tensile test were cut in triplicates perpendicular to the welding direction (see Fig.4b) and subsequently wet milled to the dimensions provided in Fig.4a. For the preparation of the tensile samples, the start and stop (keyhole) ends of the weld sample were cut off via the use of a guillotine machine, and additional 3 cut samples were obtained for the wet milling process. The obtained 3 cut samples were stacked together with two (2) unwelded Al plates. The unwelded plates were placed above and below the weld samples and rigidly clamped before the start of the machining process. The stacked samples were gradually milled to the dimensions provided in Fig.4a under the continuous flow of the soluble oil cutting fluid. The removal of the heat generated (by friction and metal shearing) during the cutting process was aided by the cutting fluid to mitigate the impact of the cutting zone temperature on the samples. The INSTRON 5582 model Universal Testing Machine (UTM) was used to determine the tensile properties of the joint at a strain rate of 5 mm/s according to the ASTM E8M/B557 standard. Scanning Electron Microscope (SEM) was then used to examine the fracture surfaces of the joints.

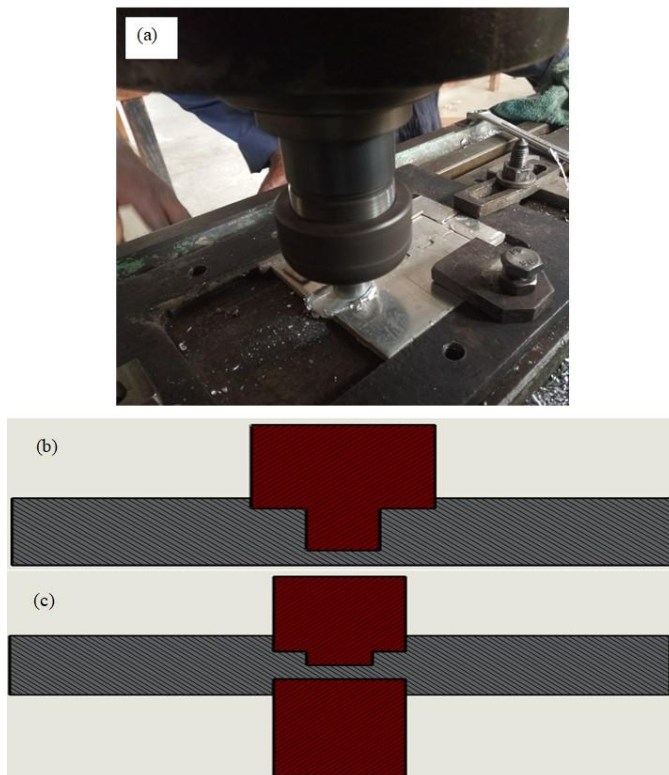


Fig. 3 Schematic representation of the IFSW processes: (a) single-sided IFSW welding (welding of the first side), (b) schematic illustration of the single-sided IFSW, (c) double-sided IFSW welding

3. Results and Discussion

3.1 Surface Appearance and Structure of Welds

The front and back views of the single- and double-sided IFSW welds are shown in Fig.5. The front views of the single and double-sided welds appear to be the same in Fig.5a and

5c due to the processing of the welds with the same pin tool. Deformation/plasticization and tool travel-induced onion rings, exit pinholes, and shearing-induced weld flashes are present on the top surface of the welds in Fig.5a and 5c. The high strain and strain rates attributable to the welding process aid the extrusion of the deformed/plasticized material as the weld flash at the retreating side (RS) of the weld. The interlocking profile remains at the back of the single-sided IFSW weld (see Fig.5b) while the pinless friction stir welding process eliminates this profile in the double-sided IFSW weld (see Fig.5d).

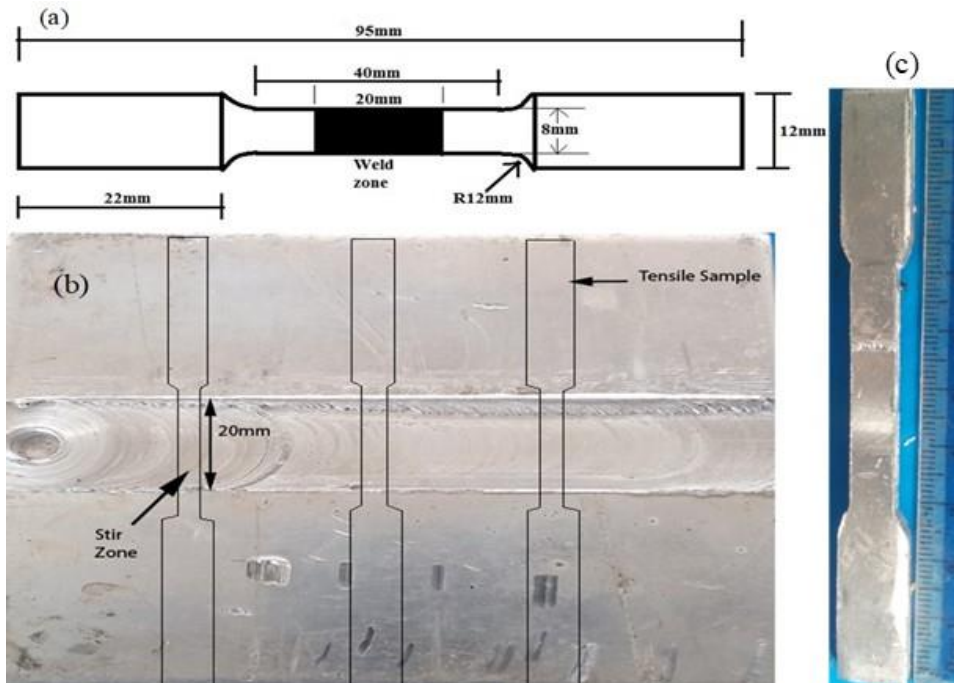


Fig. 4 Tensile test samples: (a) Schematic representation of the tensile sample (b) regions where the tensile samples were taken from on the welded plate (c) sample of the actual tensile sample

traverse speed of 40 mm/min and different rotational speeds (710, 900, and 1120 rpm) are shown in Fig. 6. It is obvious that a change in the tool rotational speed and welding choice (single and double-sided welding) significantly influences the level of flow-induced defects in the IFSW welds (see Fig.6). A similar defect was referred to as a cavity defect in the studies of Du et al. [23] and it was reported that the defect was material flow-related due to the inherent material flow's converging line. The flow-induced defect owing to the new joint configuration shows up as a crack-like defect in the double-sided IFSW weld (see Fig.6d) and as twin crack-like paths along the rise of the joint configuration in the single-sided IFSW welds (see Fig.6a) at 710 rpm. The least area fraction of flow-induced defect is obtained in the IFSW welds produced at 710 rpm in both single and double-sided welds. The increase in the tool rotational speed (from 710 to 900 rpm) caused an increase in the area fraction of the inherent flow-induced defect in the IFSW welds while a decrease in the area fraction of the flow-induced defect ensued as the tool rotational speed was further increased to 1120 rpm (see Fig.6). This behavior could be linked to the non-traditional joint-line morphology (new configuration), variance in heat input, and complex material flow at the interlocked ends of the IFSW welds. To a certain degree, a better inter-material flow (at the joint-lines) and bonding between the interlocked ends of the welds are

obtained in Fig.6a and 6d in relation to the other welds due to satisfactory plasticization at low heat input (at 710 rpm). A further increase in the heat input (at 900 rpm) caused an unsatisfactory flow and a wider flow-defect or flow-induced unbonded span and partly bonded rise (in the single-sided weld in Fig.6b) while tunnel-like flow defects at the corners of the rise were found in the double-sided weld in Fig.6c. The highest heat input (at 1120 rpm) further reduced the inherent flow-induced defect at the joint-line/interlocked end of the joint relative to the samples welded at 900 rpm. It can be affirmed that the increase in the tool rotational speed (from 710 to 1120 rpm) does not have a direct relationship with the area fraction of the inherent flow-induced defect in the IFSW welds owing to the joint configuration.

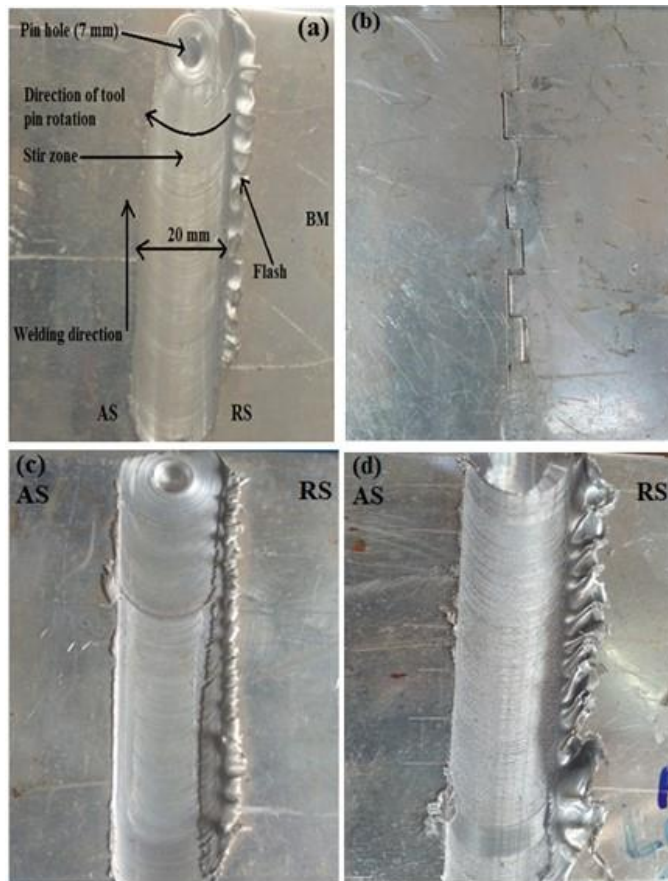


Fig. 5 Surface appearances of IFSW welds: (a) front view of the single-sided IFSW weld (b) Back view of the single-side weld (c) front view of the double-sided IFSW weld (d) Back view of double-sided IFSW weld.

The macrographs of the interlocked friction stir welded (IFSW) joints made at a constant. Meanwhile, some degree of flow defect is found along the interlocked-ends/joint-lines of all the IFSW weld samples (both single and double-sided welds) but the severity of the defect is to some extent reduced in the double-sided welds as compared to the single-sided weld counterparts fabricated under the same process parameters. The double-sided IFSW process is considered to have provided a synergetic combination of pin and pinless-assisted (dual) material plasticization, consolidation of material flow, and twofold

recrystallization effects on the IFSW joint. These phenomena are reckoned to have favored the reduction in the area fraction (level) of the flow-induced defect in the double-sided IFSW welds as compared to their single-sided counterparts in Fig. 6.

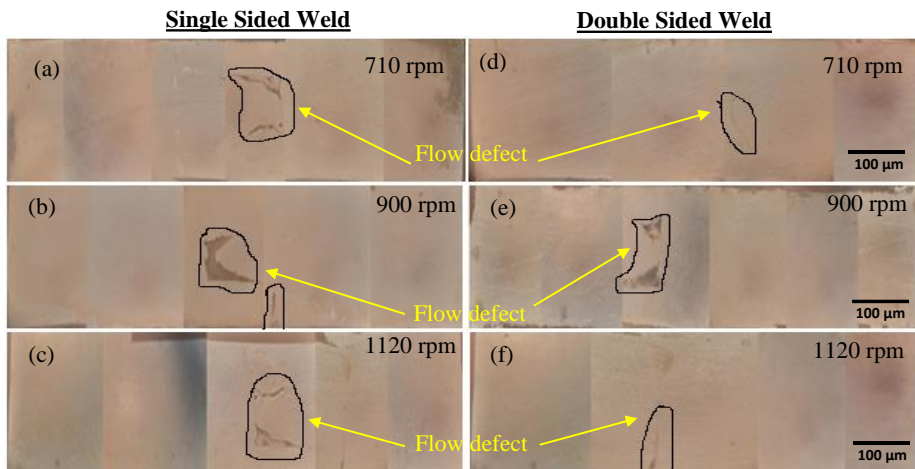


Fig. 6 Macrographs of IFSW welds obtained at constant 40 mm/min and different rotational speeds: single-sided welds at (a) 710 rpm, (b) 900 rpm, (c) 1120 rpm, and double-sided welds at (d) 710 rpm, (e) 900 rpm, and (f) 1120 rpm

Overcoming flow-defect is important for the integrity of the IFSW welds. There are many strategies for lessening or eliminating flow defects such as flash, void, and tunnels in literature [24]. Optimization studies and parameter settings that eliminate abnormal stirring, and excessive or insufficient heat input are required for the prevention of defects in FSW welds [25] [26]. As a result, the flow defect found in this study could be further mitigated via process parameter optimization with appropriate tool designs. It has been reported that optimized heat input and flow behavior, effective selection of FSW parameters, and relatively large tool shoulder with sufficient pin length are necessary for the mitigation of flow defects in FSW Welds [27]. Flow enhancing features such as threading was also acknowledged to aid the elimination of void defect in the studies of Mohammadi-pour et al. [28].

3.2 Tensile Strength of IFSW Welds

Fig. 7 shows the average tensile strengths of the single and double-sided IFSW joints obtained at different processing parameters. The stress-strain curves obtained from the tensile tests are presented in the appendix (Fig. A1 and A2). It is obvious from the plot that the double-sided welds have better tensile strengths compared to that of the single-sided counterparts. The maximum tensile strengths of the single and double-sided IFSW welds are 39.6 and 69.1 MPa respectively (at 700 rpm and 40 mm/min). This is due to the lesser area fraction of flow-induced defect together with the additional pinless tool-induced material consolidation and twofold recrystallization effects in the double-sided IFSW welds. This phenomenon favors a better loadbearing resistance of the double-sided IFSW welds compared to the single-sided IFSW welds having profound and larger area fractions of flow-induced defects along the joint-line/interlocked ends of the IFSW welds. Also, the strengthened welding interface has been reported as a factor responsible for strength improvement in the double-sided friction stir spot welded joints in the studies of Wang et al. [29].

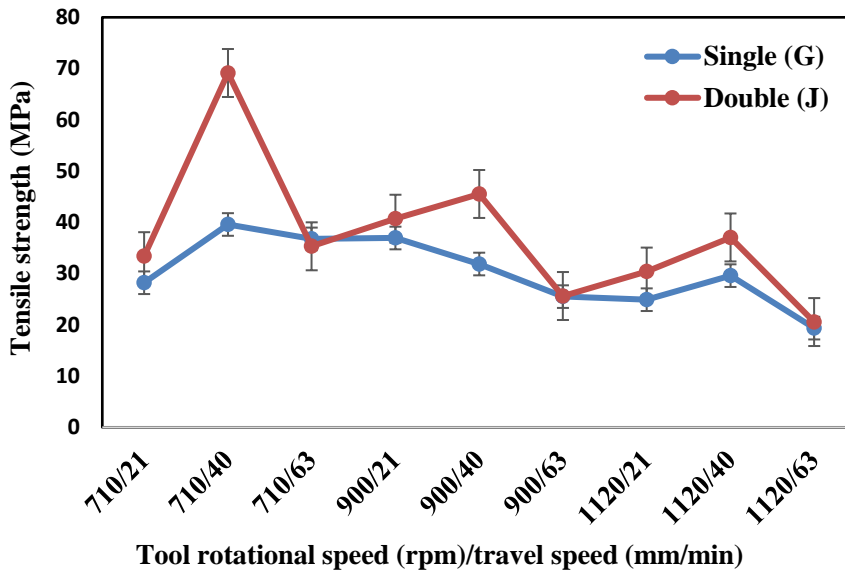


Fig. 7 Effect of varying welding parameters of the tensile strength of single and double-sided IFSW welds of Al-alloy

The assessment of the plot (see Fig.7) reveals that the welds fabricated at 40 mm/min irrespective of the levels (700, 900, and 1120 rpm) of the tool rotational speed show an improvement in the weld strength. The traverse speed of 40 mm/min produced the maximum tensile strength at different tool rotational speeds (see Fig.7) owing to ideal/sufficient material stirring, and heat input required for good metallurgical bonding in the IFSW joints. The tensile strength of the IFSW welds increases as the traverse speed increases from 21 to 40 mm/min and a further increase in the traverse speed to 63 mm/min causes the strength of the welds to decrease. A decline in the tensile strength of the IFSW joints is obtained at traverse speeds below and beyond 40 mm/min due to the prolonged tool stirring (excessive heat input) and insufficient stirring (low heat input) effects respectively.

The increase in tool rotational speed beyond 710 rpm also caused a decline in the tensile strength of the IFSW welds. This occurrence might be attributed to the direct correlation between heat input and tool rotational speed. Elevated temperature or heat input at higher tool rotational speed has been reported to aid thermal softening, and grain coarsening effects in Al alloys [30][31]. This attribute is adjudged to have impaired the tensile strength of the IFSW welds as the tool rotational speed of the weld was increased. Also, the area fraction of the flow-induced defect has been revealed to increase as the tool rotational speed was increased to 900 rpm. These stress-raisers (flow defects) are crack initiation sites in welds and the coalescence of the inherent defects in the samples having profound flow-induced defects leads to quicker weld failure and reduced tensile strength.

3.3 Weld Fracture Behavior

The fracture paths and their equivalent illustrations for the single and double-sided IFSW welds are studied in Fig.8 to understand the fracture behavior of the IFSW welds. The role of the advancing side (AS) and the retreating side (RS) on the weld failure/fracture of the IFSW welds (single and double-sided welds) cannot be ascertained in Fig.8. This might be

due to the dominant influence of the inherent flow defects (at the joint lines) on the failure mode of the IFSW welds.

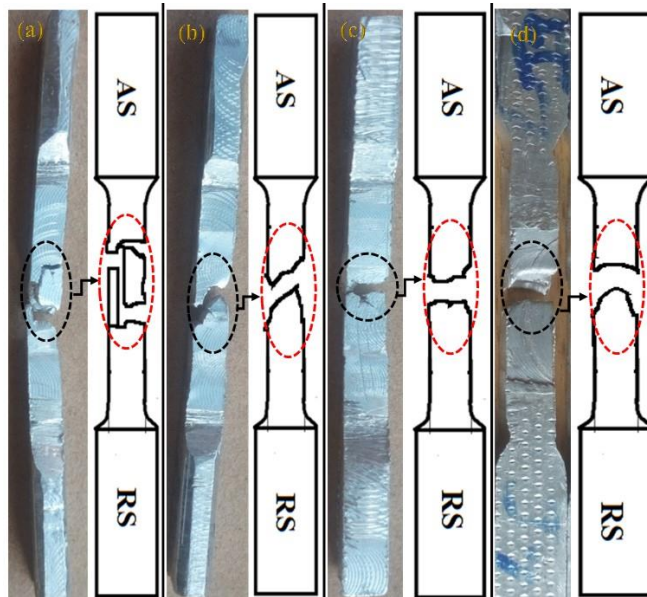


Fig. 8 Fracture paths and their equivalent illustrations for the IFSW welds: (a) single-sided weld at 1120 rpm/40 mm/min, (b) single-sided weld at 710 rpm/40 mm/min, (c) double-sided weld at 1120 rpm/40 mm/min, (d) double-sided weld at 710 rpm/40 mm/min

The fracture path of the single and double-sided IFSW welds takes place along the stirred zone of the joints in Fig.8. However, it is important to note as observed in Fig.8a that the fracture path of the single-sided joint (1120 rpm/40 mm/min) occurred along the joint-line or interlocked ends of the IFSW weld. This is a confirmation of the presence of stress-concentration along the interlocked ends of the weld, and this also provides evidence that the weld offers little loadbearing resistance before its eventual failure upon tensile loading/test. Tang et al. [32] reported that the micro-void features (of the zigzag line defect) in the FSW weld promoted crack propagation under loading. Meanwhile, the single-sided IFSW weld fabricated at 710 rpm/40 mm/min (see Fig.8b) shows a fracture path across the bonded joint-line of the weld, which is contrary to that of Fig.8a. The deviation of the fracture path away from the interlocked ends/paths (see Fig.8b) confirms that the tensile strength of the single-sided weld (obtained at 710 rpm/40 mm/min) to be better than that of Fig.8a. On the other hand, the fracture paths of the double-sided IFSW welds (see Fig.8c and d) are close to that of the single-sided one in Fig.8b, which also confirms that the weld failure is not significantly influenced by the bonded joint-line (interlocked ends). The inherent flow defect in the double-sided IFSW weld produced at 1120 rpm/40 mm/min (see Fig.8c) aids the failure across the joint whereas some level of ductility is experienced by its counterpart welded at 710 rpm/40 mm/min.

Fig. 9 shows and compares the fracture surfaces of the failed IFSW samples after the tensile tests. Flow-induced macro/micro-defects and mixed fracture (brittle and ductile) characterized the fracture surfaces of the single-sided welds in Fig.9a-c whereas the surfaces of the double-sided welds were predominated by ductile fractures in Fig.9d-f. The single-sided weld fabricated at 710 rpm and 40 mm/min had a flow defect (tunnel-like)

surrounded by uneven fracture layers having large dimples and brittle-like appearances in Fig.9a. Apart from the stress raiser (flow defect) in Fig.9a, the fracture features of the weld confirm that mixed fracture (with a large area fraction of ductile mode) ensued in the single-sided IFSW weld. This occurrence justifies the improved tensile strength of the single-sided joint fabricated at 710 rpm and 40 mm/min as compared to the other single-sided welds having brittle/mixed fracture appearances in Fig.9b and c. Flow-induced cavities with minimal ductile features are present in the single-sided weld produced at 900 rpm and 40 mm/min (see Fig.9b) while the presence of brittle facets and a few dimple appearances are found in the single-sided weld produced at 1120 rpm and 40 mm/min (see Fig.9c). It can be concluded that mixed fracture mode occurs in Fig.9b and c. On the other hand, the double-sided welding process significantly improved the IFSW welds (see Fig.9d-f) by significantly reducing the flow defects and making the welds exhibit some level of ductility and loadbearing attributes. For instance, the double-sided welds produced at 710 rpm and 40 mm/min (see Fig.9d) and at 900 rpm and 40 mm/min (see Fig.9e) have predominantly shallow and some large dimples. This observation is a confirmation of ductile fracture modes in the welds. This is in agreement with the studies of Xu et al [33] as large dimples on the fracture sites were reported as evidence of ductile fracture mode. Fig.9f also confirms the presence of some fine dimples and a flow defect (see the enclosed orange circle in Fig.9f) in the double-sided weld produced at 1120 rpm and 40 mm/min. This occurrence validates that the double-sided welding process improves the weld strength of the IFSW joints via attributes such as reduction in flow-induced defects, improved plasticization/material flow, and twofold recrystallization phenomena.

4. Conclusion

Weldability of the interlock-end friction stir welding (IFSW) of the AA1050 aluminum alloy was successfully investigated by employing single- and double-sided welding procedures. The structure, tensile strength, and fracture patterns of the single- and double-sided IFSW welds fabricated at different process parameters were studied and compared. The following findings were observed from this investigation:

- The joint lines of the interlocked friction stir welded (IFSW) joint have flow-induced defects in both weld categories (single- and double-sided IFSW welds) owing to the interlocked morphology.
- The severity of the inherent flow defect in the IFSW welds is significantly reduced in the double-sided IFSW welds as compared to the single-sided counterparts due to the advantage of dual material plasticization, material consolidation, and twofold recrystallization effects in the double-sided IFSW welds.
- The increase in the tool rotational speed (from 710 -1120 rpm) does not have a direct correlation with the area fraction of the inherent flow-induced defect in the IFSW joint.
- The double-sided welds have better tensile strengths compared to the single-sided weld counterparts due to the lesser area fraction of flow-induced defect or stress raiser. The maximum tensile strengths of the single and double-sided IFSW welds were 39.6 and 69.1 MPa respectively.
- The tensile strength of the IFSW welds increases as the traverse speed increases from 21 to 40 mm/min and a further increase in the traverse speed to 63 mm/min causes the strength of the welds to decrease.
- The fracture path/location of the single and double-sided IFSW welds takes place along the stir zone. The rotating tool-aided advancing and retreating sides do not influence the weld fracture location of the IFSW welds owing to the dominant influence of flow defect on the weld failure.

- A large expanse of ductile fracture features and brittle appearances characterized the fracture surfaces of the single and double-sided IFSW welds respectively.

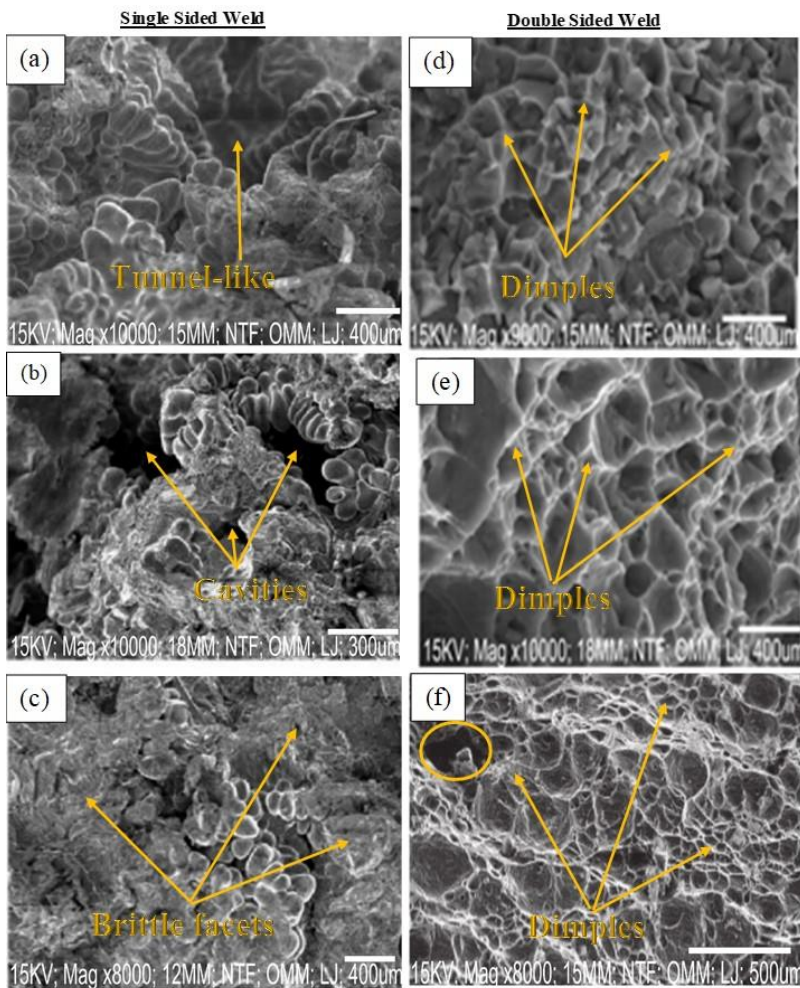


Fig. 12. Fracture surfaces of the IFSW welds: the single-sided welds at (a) 710 rpm/40 mm/min, (b) 900 rpm/40 mm/min, (c) 1120 rpm/40 mm/min; and double-sided welds at (d) 710 rpm/40 mm/min, (e) 900 rpm/40 mm/min, (f) 1120 rpm/40 mm/min

References

- [1] Thakur R, Bajwa PS. Friction stir welding of 5xxx series aluminum alloys: A literature survey. *International Journal of Scientific Research in Science, Engineering, and Technology*, 2016; 2(2): 1129-1131.
- [2] Qiao Q, Su Y, Li Z, Cui Q, Yu H, Ouyang Q, Zhang D. Effect of overlapping region on double-sided friction stir welded joint of 120 mm ultra-thick SiCp/Al composite plates. *Materials Science & Engineering A*, 2020; 782: 139238. <https://doi.org/10.1016/j.msea.2020.139238>
- [3] Hejazi I, Mirsalehi SE. Effect of pin penetration depth on double-sided friction stir welded joints of AA6061-T913 alloy. *Transaction of Nonferrous Metals Society of China*, 2016; 26: 676 - 683. [https://doi.org/10.1016/s1003-6326\(16\)64158-4](https://doi.org/10.1016/s1003-6326(16)64158-4)

- [4] Ma ZY, Feng AH, Chen DL, Shen J. Recent Advances in Friction Stir Welding/Processing of Aluminium Alloys: Microstructural Evolution and Mechanical Properties. *Critical Reviews in Solid State and Materials Sciences*, 2018; 43(4): 269-333. <https://doi.org/10.1080/10408436.2017.1358145>
- [5] Pankul G, Arshad NS, Noor ZK, Mohd AH, Zahid AK, Mustufa HA, Abdulrahman A. Investigation on the Effect of Tool Pin Profiles on Mechanical and Microstructural Properties of Friction Stir Butt and Scarf Welded Aluminium Alloy 6063. *Metals*, 2018; 8(1): 74. <https://doi.org/10.3390/met8010074>
- [6] Darmadi DB, Talice M. Improving the strength of friction stir welded joint by double side friction welding and varying pin geometry. *Engineering Science and Technology, an International Journal*, 2020; 24(3): 637-647. <https://doi.org/10.1016/j.jestch.2020.11.001>
- [7] Ojo OO, Taban E, Kaluc E. Understanding the role of welding parameters and tool profile on the morphology and properties of expelled flash of spot welds. *Materials and Design*, 2016; 108: 518-528. <https://doi.org/10.1016/j.matdes.2016.07.013>
- [8] Xu W, Wang H, Luo Y, Li W, Fu MW. Mechanical behavior of 7085-T7452 aluminum alloy thick plate joint produced by double-sided friction stir welding: Effect of welding parameters and strain rates. *Journal of Manufacturing Processes*, 2018; 35: 261-270. <https://doi.org/10.1016/j.jmapro.2018.07.028>
- [9] Zhou M, Morisada Y, Fujii H; Ishikawa, T. Mechanical properties optimization of AZX612-Mg alloy joint by double-sided friction stir welding. *Journal of Materials Processing Tech.*, 2018; 254: 91-99. <https://doi.org/10.1016/j.jmatprotec.2017.11.014>
- [10] Chen J, Fujii H, Yufeng SY, Morisada Y, Kondoh K. Optimization of mechanical properties of fine-grained non-combustive magnesium alloy joint by asymmetrical double-sided friction stir welding. *Journal of Materials Processing Technology*, 2017; 242: 117-125. <http://dx.doi.org/10.1016/j.jmatprotec.2016.11.021>
- [11] Kumar U, Acharya U, Saha SC, Roy BS. Microstructure and mechanical property of friction stir welded Al-Mg joints by adopting modified joint configuration technique. *Materials Today: Proceedings*, 2020; 26: 2083-2088. <https://doi.org/10.1016/j.matpr.2020.02.450>
- [12] Paidar M, Ojo OO, Ezatpour HR, Heidarzadeh A. Influence of multi-pass FSP on the microstructure, mechanical properties and tribological characterization of Al/B4C composite fabricated by accumulative roll bonding (ARB). *Surface and Coatings Technology*, 2019; 361: 159-169. <https://doi.org/10.1016/j.surfcoat.2019.01.043>
- [13] Chu Q, Li WY, Hou HL, Yang XW, Vairis A, Wang C, Wang WB. On the double-side probeless friction stir spot welding of AA2198 Al-Li alloy. *Journal of Materials Science & Technology*, 2019; 35: 784-789. <https://doi.org/10.1016/j.jmst.2018.10.027>
- [14] Yang C, Zhang JF, Ma GN, Wu LH, Zhang XM, He GZ, Xue P, Ni DR, Xiao BL, Wang KS, Ma ZY. Microstructure and mechanical properties of double-side friction stir welded 6082Al ultra-thick plates. *Journal of Materials Science & Technology*, 2020; 41: 105-116. <https://doi.org/10.1016/j.jmst.2019.10.005>
- [15] Bhardwaj N, Narayanan RG, Dixit US, Hashmi MSJ. Recent developments in friction stir welding and resulting industrial practices. *Advances in Materials and Processing Technologies*, 2019; (5)3: 461-496. <https://doi.org/10.1080/2374068x.2019.1631065>
- [16] Reza-E-Rabby MD, Ross K, Whalen S, Hovanski Y, McDonnell M. Solid-State Joining of Thick-Section Dissimilar Materials Using a New Friction Stir Dovetailing (FSD) Process. *The Minerals, Metals and Materials Series*, 2017; 67-77. https://doi.org/10.1007/978-3-319-52383-5_8
- [17] Yan Z, Liu X, Fang H. Effect of sheet configuration on microstructure and Mechanical Behaviors of Dissimilar Al-Mg-Si/Al-Zn-Mg Aluminium Alloys Friction Stir Welding

- Joints. *Journal of Materials Science and Technology*, 2016; 32(12): 1378 – 1385. <https://doi.org/10.1016/j.jmst.2016.10.011>
- [18] Li Z, Zhang Y, Shen W, Hu LL. Dissimilar friction stir welding of Ti–6Al–4V alloy and aluminum alloy employing a modified butt joint configuration: Influences of process variables on the weld interfaces and tensile properties, *Materials & Design* 2014; 53: 838-848. <https://doi.org/10.1016/j.matdes.2013.07.019>
- [19] Acharya U, Medhi T, Sethi D, Choudhury S, Banik A, Saha SC, Roy BS. A study on the implication of modified joint configuration in Friction stir welding. *Soldagem & Inspeção*, 2021; 26: 2606. <https://doi.org/10.1590/0104-9224/SI26.07>
- [20] Sethi D, Acharya U, Shekhar S, Roy BS. Applicability of unique scarf joint configuration in friction stir welding of AA6061-T6: Analysis of torque, force, microstructure, and mechanical properties, *Defence Technology*. 2021; 1-16. <https://doi.org/10.1016/j.dt.2021.03.010>
- [21] Zhang W, Shen Y, Yan Y, Guo R. Dissimilar friction stir welding of 6061 Al to T2 pure Cu adopting tooth shaped joint configuration: Microstructure and mechanical properties. *Materials Science & Engineering A*, 2017; 690: 355 – 364. <http://dx.doi.org/10.1016/j.msea.2017.02.091355-364>
- [22] Mhedhbi M, Khelif M, Bradai C. Investigations of microstructural and mechanical properties evolution of AA1050 alloy sheets deformed by cold-rolling process and heat treatment annealing. *Journal of Materials and Environmental Sciences*, 2017; 8: 2967-2974
- [23] Du S, Liu H, Jian M, Hu Y, Zhou L. Eliminating the cavity defect and improving mechanical properties of TA5 alloy joint by titanium alloy supporting friction stir welding. *Journal of Manufacturing Processes*, 2021; 69: 215-222. <https://doi.org/10.1016/j.jmapro.2021.07.044>
- [24] Ojo OO, Taban E. Hybrid multi-response optimization of friction stir spot welds: failure load, effective bonded size and flash volume as responses. *Sadhana*, 2018; 43(6): 1-13. <https://doi.org/10.1007/s12046-018-0882-2>
- [25] Suresh S, Elango N, Venkatesan K, Lim WH, Palanikumar K, Rajesh S. Sustainable friction stir spot welding of 6061-T6 aluminum alloy using improved non-dominated sorting teaching learning algorithm. *Journal of Materials Research Technology*, 2020; 9: 11650-11674. <https://doi.org/10.1016/j.jmrt.2020.08.043>
- [26] Dialami N, Cervera M, Chiumenti M. Defect formation and material flow in Friction Stir Welding. *European Journal of Mechanics / A Solids*, 2020; 80: 103912. <https://doi.org/10.1016/j.euromechsol.2019.103912>
- [27] Kah P, Rajan R, Martikainen J, Suoranta R. Investigation of weld defects in friction-stir welding and fusion welding of aluminum alloys. *International Journal of Mechanical and Materials Engineering*, 2015; 10:26. <https://doi.org/10.1186/s40712-015-0053-8>
- [28] Mohammadi-pour M, Khodabandeh A, Mohammadi-pour S, Paidar M. Microstructure and mechanical properties of joints welded by friction-stir welding in aluminum alloy 7075-T6 plates for aerospace application. *Rare Metals*, 2016. <https://doi.org/10.1007/s12598-016-0692-9>
- [29] Wang X, Morisada Y, Ushioda K, Fujii H. Double-sided friction stir spot welding of ultra-high-strength C-Mn-Si martensitic steel by adjustable probes. *Journal of Materials Processing Technology*, 2022; 300: 117422. <https://doi.org/10.1016/j.jmatprotec.2021.117422>
- [30] Ojo OO, Taban E, Kaluc, E. Friction stir spot welding of aluminum alloys: a review. *Materials Testing*, 2015; 57(7-8): 609-627. <https://doi.org/10.3139/120.110752>
- [31] Heydari F, Amadeh A, Ojo OO, Hasanniya MH, Tamizifar M. Microstructure and mechanical properties of autobody steel joined by friction stir spot welding, *Sādhanā* 2019; 44(3): 1-10. <https://doi.org/10.1007/s12046-019-1057-5>

- [32] Tang W, Yang X, Li S, Li H. Zigzag line defect in friction stir butt-weld of ferritic stainless steel. *Materials Letter*, 2021; 288: 129361. <https://doi.org/10.1016/j.matlet.2021.129361>
- [33] Xu X, Liu Q, Hou H, Wang J, Ren X. Effect of incomplete penetration defects on mechanical and fatigue properties of friction-stir-welded 6802-T6 joint. *Journal of Materials Research and Technology*, 2021; 15: 4021-4031. <https://doi.org/10.1016/j.jmrt.2021.10.028>

Appendix

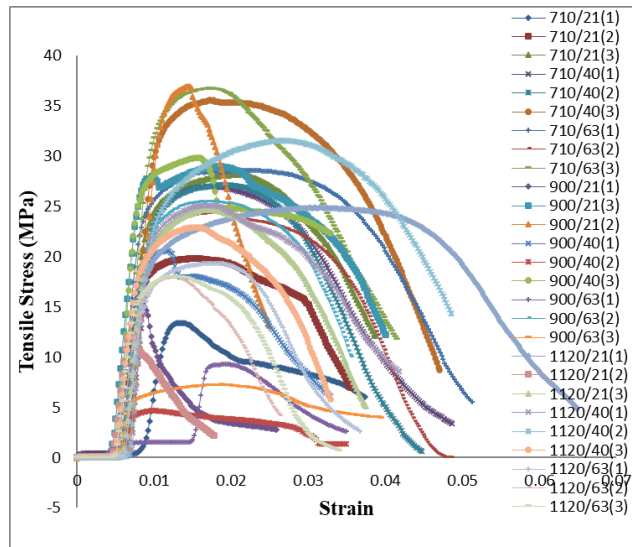


Fig. A1. Stress-strain curves of the single-sided IFSW welds

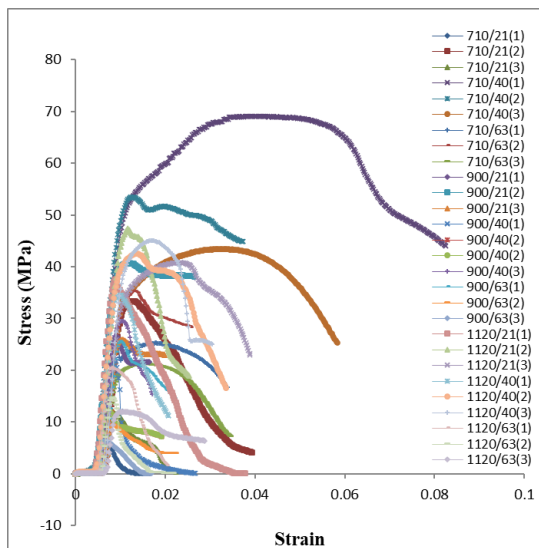


Fig. A2. Stress-strain curves of the double-sided IFSW welds

Blank Page



Research Article

Numerical investigation of the combined effects of coating layer properties and specific heat capacities of materials on the heat transfer mechanism in solidification of pure metals

Mehmet Hakan Demir

Department of Mechatronics Engineering, Iskenderun Technical University, Hatay, Turkey

Department of Mechanical and Industrial Engineering, University of Illinois at Chicago, Chicago, IL, USA

Article Info

Article history:

Received 02 Jun 2022

Revised 01 Aug 2022

Accepted 30 Aug 2022

Keywords:

Solidification;

Pure metal;

Casting;

Phase-change;

Heat transfer;

Finite difference;

Growth instability

Abstract

Mold coating has a critical importance to adjust the microstructure of the cast and regulate the heat transfer during the solidification. The phase change heat transfer problem during the solidification is solved numerically in the presence of the coating layer and finite thermal capacitances of materials. Previous studies have been expanded by considering the combined effects of the coating layer and specific heat capacities of the materials on growth instability. Also, the conditions are specified based on the process parameters for minimizing or eliminating the unstable growth of the shell. The complexity of the two-dimensional thermal problem is reduced by perturbation analysis. After that, the governing equations are solved numerically by using the variable time step and grid size based Lagrangian finite difference scheme. The effects of the thermal properties of the materials, coating properties and the thermal contact resistances on the thermoelastic instability process are studied in detail. According to the results obtained that a thicker coating layer causes more regular growing and better quality in the shell. However, the specific heats of the solidified layer and coating materials have stabilizing effects but an increase in the mold specific heat leads to a destabilizing effect on the thermoelastic instability. Also, the thermal conductivities have great impact on growth of the shell. The solution of this study can be used as thermal part in uncoupled and coupled problems in which the thermomechanical problems are investigated.

© 2022 MIM Research Group. All rights reserved.

1. Introduction

Almost all metals and alloys, some ceramic and polymer materials are liquid at some stage of their production and start to solidify when they are cooled below the melting temperature. The control of thermo-mechanical events that occur during casting is of great importance to increase the quality of the casting. Studies, in which the solidification during casting is analyzed theoretically and experimentally, reveal that thermo-mechanical phenomena at the solid/liquid interface (moving interface) has significant effect on the thermoelastic unstable growth that occurs during solidification. When the experimental studies are examined, it is seen that some undulations occur at the moving interface during the solidification of metals as an inevitable result of cooling [1]. The experiments reveal that these undulations continue from the beginning of solidification to a certain stage and then disappear. This behavior is explained as the thermal and mechanical phenomena occurring at the mold/shell interface affects the thermo-mechanical conditions at the moving interface and this situation gradually disappears with the increase of the solidified shell thickness. These non-uniform undulations occur because of the uneven heat flux at the mold/shell interface. This unstable undulation causes important faults such as

Corresponding author: mhakan.demir@iste.edu.tr

orcid.org/0000-0002-3934-2425

DOI: <http://dx.doi.org/10.17515/resm2022.441me0602>

Res. Eng. Struct. Mat. Vol. 8 Iss. 4 (2022) 751-772

micro/macro scaled cracks in the final casting [3]. This phenomenon during the solidification, which is called thermoelastic instability, is theoretically examined in two parts such as thermal and mechanical problems. The thermal problem and its solution are discussed in this study in detail.

The phase-change problems (moving interface problems) have great importance for the applications such as purification of metals, casting/welding processes and thermal energy storage systems [4]. The common property of phase change problems is a moving interface that occurs between the solid and liquid phases during the solidification or melting process and the location of this moving interface have to be determined with the solution. Stefan [5] dealt with the first theoretical work on solving the phase-change problem for the ice formation process. Evans [6] and Douglas [7] studied the existence and uniqueness of this problem's solution, respectively. Since then, despite many phase change problems appeared in literature but exact solution to this problem has been limited to idealized cases containing semi-finite or infinite regions with simple boundary and initial conditions. The history and some classical solutions to the Stefan problems were collected in Crank [8] and Hill [9]. Due to the nonlinear behavior of this problem, the superposition principle is not applicable and all cases are evaluated separately.

Barry and Cauce [10] solved Stefan type problem numerically and analytically by taking into the account of linear and nonlinear diffusivities. Song et al. [11] solved the Stefan problem by an underlying iso-geometric approximation with a sharp interface. For the solution of one-dimensional Stefan problems with moving boundaries, Reutskiy [12] developed a delta-shaped function based meshless numerical. Juric and Tryggvason [13] used the front tracking method and the fixed grid in space was used for determining the moving boundary's location and the interface heat sources were calculated by using the moving grid on the interface. An adapted grid procedure is applied by Murray and Landis [14] and they found that the moving interface location is determined more accurately with the adapted grid method. Also, an adaptive grid method is used by Segal et al. [15] for the free boundary in the 2D phase change problem and the movement of the grid was introduced into the system equations by use of Arbitrary Lagrangian-Eulerian (ALE) approach. Kutluay et al. [16] obtained a solution of Stefan problem by using boundary immobilization techniques with variable space grid. Caldwell et al. [17] solved 1D Stefan problem by using the nodal integral method with finite difference (FD) scheme. The methods for the numerical solution of one-dimensional Stefan problems for different geometries are compared in Caldwell and Kwan [18] in detail. A simple level set method was used to solve the Stefan problem in the dendritic solidification process by Chen et al. [19]. Font [20] solved the one-phase phase-change problem with size-dependent thermal conductivity. The boundary immobilization and finite difference scheme are used for numerical solution. Moreover, the phase-field modeled Stefan problems are investigated by Mackenzie and Robertson [21] and Sun and Beckermann [22]. Vynnycky and Mitchell [23] developed an algorithm for 1D time-dependent problem by use of the Keller box FD scheme and boundary immobilization technique. Myers and Mitchell [24] developed a solution method for solving Stefan problem based on the heat balance integral method that is called the combined integral method. This method breaks down like other integral methods when the boundary temperature approaches zero or oscillates.

The problem of solidification of metals with phase-change heat transfer has been specifically addressed in this paper and some studies about heat transfer during solidification are summarized below. Zabararas and Mukherjee [25] solved the phase change problem during the pure metal solidification process by convolution integrals and Green's functions based boundary element method. In Dursunkaya and Nair [26], the motion of a solidification front is analyzed by using a semi-analytical approach during the solidification of a finite one-dimensional medium with boundary temperature with oscillations.

Skrzypczak and Wergzyn-Skrzypczak [27] studied the mathematical and numerical modeling of the heat transfer problem during the pure metal solidification process by using the finite element method and the front tracking method based on the level set method were used for determining the position of the moving interface. Another useful method for analyzing Stefan problems is the perturbation method. Caldwell and Kwan [28] solved Stefan problems, which have time-dependent boundary conditions, by using perturbation method. Yu et al. [29] obtained a perturbation solution to the planar solidification problem with time-dependent heat generation. Yigit [30] used the linear perturbation method for solving a 2D phase-change Stefan problem during the solidification process in which the planar mold's outer surface has a periodic temperature boundary condition. Also, Yigit [31] used the same method to determine the heat transfer problem's solution during pure metal solidification on a mold with sinusoidal surfaces, and the governing equations were discretized by using the finite difference approach. A linear perturbation solution was used to obtain approximate analytical and numerical solutions of the 2D heat conduction problem for solidification on a planar mold surface by Yigit [32] and the effects of thermal diffusivity of shell on the unstable growth were determined. The previous paper was extended by taking into account the thermal diffusivity of the mold in Yigit [33] and the linear perturbation and the finite difference methods are used for the solution.

As it is mentioned above, the uneven shell growth leads to defects in the cast product because of the uneven heat transfer during the solidification. Mold coating is the one of the most used and effective techniques to control the heat transfer. It plays an effective role in ensuring controlled solidification by reducing the solidification rate of the liquid metal in the mold. Thus, the liquid proceeds without freezing in the metal mold and fills the entire mold. On the other hand, the mold coatings are used to prevent direct contact with the liquid metal with the mold steel and to increase the life of the mold by preventing corrosive effects and soldering. Another advantage of using mold coating is that it assists with casting release from the mold [34]. In the literature, there are many experimental studies in which the coating's effects are investigated in detail. However, the number of theoretical studies are much less than the experimental ones. Jafari et al. [35] studied experimentally on the mold coating effects on the thin-wall ductile iron casting. The effects of coating thickness on porosity percentage and imperfection during the casting process of Al-Si-Cu alloy are studied experimentally by Karimian et al. [36]. Also, the effects of mold coating properties and alloy composition on the heat transfer during the casting of Al alloys are determined by Hamasaiid et al. [37]. Demir and Yigit solved the heat transfer problem for the pure metal solidification on a coated planar mold in [4,38-40] for coupled and uncoupled processes by neglecting the effects of thermal diffusivities. The same problem is modeled for a sinusoidal mold and coating in Demir and Yigit [41] and the linear perturbation method was used to solve it analytically.

In this study, the numerical solution of the heat transfer problem for the early stages of the full solidification problem, in which the pure metal solidification occurs on the coated planar mold, is made by considering the finite thermal diffusivity of the materials. The previous studies are extended by investigating the combined effects of the properties of the coating layer and thermal diffusivities of the materials. The problem is modeled with the linear perturbation method for reducing the complexness of the problem and then, it is discretized by the variable time and grid size based Lagrangian finite difference scheme for numerical solution. After that, the effects of the coating properties are investigated theoretically and the key question is that how can be adjusted the coating layer's properties depending on the other process parameters. Also, other system parameters associated with the presence of the coating layer such as thermal contact resistances, specific heats of the layers, and thermal conductivity ratios between the materials are investigated in detail. This problem has extended the dissertation work given in [4] by adding the heat capacities of the materials and the solution obtained as a result of this

problem will be used in the realization of the thermo-mechanic solution, in which the thermal problem affects the mechanical problem.

This paper is organized as follows. The two-dimensional modeling and the perturbation analysis for simplifying the problem by reducing dimensionality are described in Sections 2 and 3, respectively. Section 3 introduces the terminology used throughout this paper. In Section 4, dimensionless variables are introduced which are used to simplify the complexity of the problem and generalize the solution. Section 5 shows the numerical algorithm used to solve the problem and Section 6 includes the results and their discussions which indicate the reliability of the proposed numerical algorithm and the effects of the system parameters. The conclusions of the study are given in Section 7.

2. Mathematical Formulation

The geometry of the considered solidification process is shown in Fig. 1. The coating, shell and mold layers are denoted with superscripts b , c and d respectively.

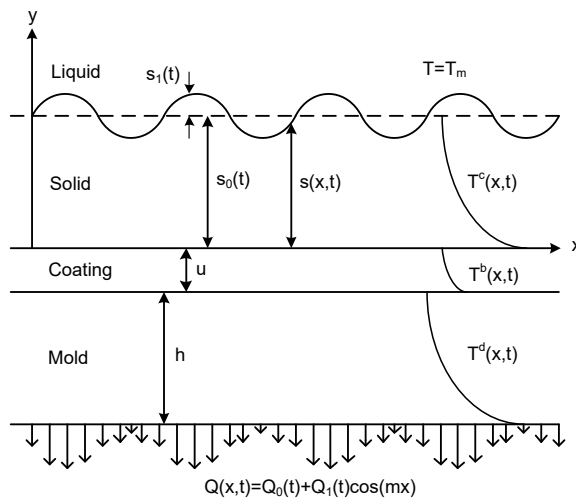


Fig. 1 Geometry of the casting process

There is a moving surface between the liquid/solid phases of shell material and it has a sharp structure. The reason for this is that the phase change during the pure metal solidification process occurs at a distinct temperature. The materials' properties don't change depending on the time and temperature. The temperature fields in these solid layers ($T^i(x, y, t)$, $i = c, b, d$) and instantaneous location of the freezing front ($s(x, t)$) are determined as a result of the solution. The liquid shell's temperature is assumed to be at the melting temperature T_m during the process. For this reason, the thermal effects of the liquid phase of the metal are not taken into account. This assumption provides us that the moving interface's temperature is always equal to T_m .

Since the thermal diffusivities of the materials are taken into account in this study, the solution is obtained numerically due to the non-linearity. In this numerical solution, a limiting solution to the problem is used for initial conditions. The limiting solution is obtained analytically [38] by assuming the thermal diffusivities of the materials are infinite. This makes the thermal capacitance of the solid layers are zero and the general heat conduction equations are solved analytically with boundary and initial conditions. The solution procedure is explained in Appendix and Ref. [38].

In Figure 1, h and u symbolize thicknesses of the mold and its coating, respectively. As it is mentioned that the thermal diffusivities are assumed to be finite and therefore, the distribution of thermal fields in the solid layers varies parabolically. The temperature fields have to satisfy the equations in Eq. (1).

$$\begin{aligned}\frac{\partial^2 T^c}{\partial y^2}(x, y, t) &= \frac{1}{\alpha^c} \frac{\partial T^c}{\partial t}(x, y, t) \\ \frac{\partial^2 T^b}{\partial y^2}(x, y, t) &= \frac{1}{\alpha^b} \frac{\partial T^b}{\partial t}(x, y, t) \\ \frac{\partial^2 T^d}{\partial y^2}(x, y, t) &= \frac{1}{\alpha^d} \frac{\partial T^d}{\partial t}(x, y, t)\end{aligned}\quad (1)$$

where α^i ($i = b, c, d$) denotes the thermal diffusivities of the materials. These equations are solved depending on the boundary conditions. The moving interface's temperature, which is equal to T_m is defined in Eq. (2).

$$T^c(x, s, t) = T_m \quad (2)$$

The energy balance at the moving interface due to heat conduction and the latent heat is;

$$K^c \frac{\partial T^c}{\partial y}(x, s, t) = L^c \rho^c \frac{ds}{dt}(x, t) \quad (3)$$

where L^c and ρ^c denote latent heat and density of the shell, respectively. K^i , ($i = c, b, d$) represents the thermal conductivities of the materials. Eqs. (4) and (5) show the heat flux continuity at the interfaces between the solid layers, respectively.

$$K^c \frac{\partial T^c}{\partial y}(x, 0, t) = K^b \frac{\partial T^b}{\partial y}(x, 0, t) \quad (4)$$

$$K^b \frac{\partial T^b}{\partial y}(x, -u, t) = K^d \frac{\partial T^d}{\partial y}(x, -u, t) \quad (5)$$

In the model, there are thermal contact resistances at the interface between the solid layers due to contaminant films and roughness. R_{sc} and R_{cm} symbolize these constant thermal resistances at the interfaces. The subscript "sc" denotes the shell-coating interface and subscript "cm" indicates the coating-mold interface. These contact resistances are assumed to be independent of the contact pressure. This is true for the uncoupled process in which the thermal problem affects the mechanical problem but vice versa does not come true. The uncoupled model is applicable for the early stages of the process and this means that the solution of this full solidification problem is eligible for very early stages. Eq. (6) define this relation between heat flux and thermal contact resistances.

$$\begin{aligned}K^c \frac{\partial T^c}{\partial y}(x, 0, t) &= \frac{1}{R_{sc}} [T^c(x, 0, t) - T^b(x, 0, t)] \\ K^b \frac{\partial T^b}{\partial y}(x, -u, t) &= \frac{1}{R_{cm}} [T^b(x, -u, t) - T^d(x, -u, t)]\end{aligned}\quad (6)$$

At the mold's lower surface, there is a heat flux, $Q(x, t)$, and it has small spatial variation to perform the uneven heat transfer. The heat flux extracted from the mold is given in Eq. (7).

$$K^d \frac{\partial T^d}{\partial y}(x, -u - h, t) = Q(x, t) \quad (7)$$

3. Perturbation Analysis

The conditions at the interfaces between the solid layer control the resulting properties of the final cast and the solidification rate. In this method, it is assumed that an x-dependent perturbation grows on the unperturbed process. The parameters of the unperturbed process affect the development of this perturbation. The unperturbed and perturbed processes are called as zeroth-order and first-order processes, respectively. The amplitudes of the perturbed quantities are very smaller than the zeroth-order quantities and the perturbation is linear. So, this provides us to use Fourier transformation in x and the dimensionality and complexity of the problem are reduced.

The new forms of the heat flux, the temperature fields, and the moving interface's position are

$$Q(x, t) = Q_0(t) + Q_1(t)\cos(mx) \quad (8)$$

$$T(x, y, t) = T_0(y, t) + T_1(y, t)\cos(mx) \quad (9)$$

$$s(x, t) = s_0(t) + s_1(t)\cos(mx) \quad (10)$$

Subscript 0 and 1 define the zeroth-order process and the first-order process, respectively. The constant m and λ denote the wavenumber and the wavelength and they depend each other with $\lambda = 2\pi/m$. Also, the slope of the moving front, $\partial s/\partial x$, is very much less than unity. If the readers need more information about the perturbation method, they refer to Yigit's paper in Refs. [32] and [33].

Accordingly, the perturbation added forms of temperature field in Eq. (9) substitutes into Eq. (1), and then the periodic and uniform terms are separated. The obtained uniform (zeroth-order) terms from heat conduction equations are;

$$\begin{aligned} \frac{\partial^2 T_0^c}{\partial y^2}(y, t) &= \frac{1}{\alpha^c} \frac{\partial T_0^c}{\partial t}(y, t) \\ \frac{\partial^2 T_b^c}{\partial y^2}(y, t) &= \frac{1}{\alpha^b} \frac{\partial T_b^c}{\partial t}(y, t) \\ \frac{\partial^2 T_0^d}{\partial y^2}(y, t) &= \frac{1}{\alpha^d} \frac{\partial T_0^d}{\partial t}(y, t) \end{aligned} \quad (11)$$

The obtained periodic (first-order) terms from separating heat conduction equations are;

$$\begin{aligned} \frac{\partial^2 T_1^c}{\partial y^2}(y, t) - m^2 T_1^c(y, t) &= \frac{1}{\alpha^c} \frac{\partial T_1^c}{\partial t}(y, t) \\ \frac{\partial^2 T_1^b}{\partial y^2}(y, t) - m^2 T_1^b(y, t) &= \frac{1}{\alpha^c} \frac{\partial T_1^b}{\partial t}(y, t) \\ \frac{\partial^2 T_1^d}{\partial y^2}(y, t) - m^2 T_1^d(y, t) &= \frac{1}{\alpha^c} \frac{\partial T_1^d}{\partial t}(y, t) \end{aligned} \quad (12)$$

Temperature fields are expanded in form of Taylor series at the vicinity of $y = s_0(t)$. The boundary conditions are rearranged similarly to heat equations and the second and higher-order terms are eliminated due to their negligible effects. The zeroth and first order boundary conditions to be used in the solution of the equations in Eqs. (11) and (12) are determined by using perturbed forms in Eqs (8)-(10). The procedure is described in detail in Ref [33]. See this reference for details.

The zeroth-order boundary conditions are;

$$T_0^c(s_0, t) = T_m \quad (13)$$

$$K^c \frac{\partial T_0^c}{\partial y}(s_0, t) = L_c \rho_c \frac{ds_0}{dt}(x, t) \quad (14)$$

$$K^c \frac{\partial T_0^c}{\partial y}(0, t) = K^b \frac{\partial T_0^b}{\partial y}(0, t) \quad (15)$$

$$K^b \frac{\partial T_0^b}{\partial y}(-u, t) = K^d \frac{\partial T_0^d}{\partial y}(-u, t) \quad (16)$$

$$K^c \frac{\partial T_0^c}{\partial y}(0, t) = \frac{1}{R_{sc}} [T_0^c(0, t) - T_0^b(0, t)] \quad (17)$$

$$K^b \frac{\partial T_0^b}{\partial y}(-u, t) = \frac{1}{R_{cm}} [T_0^b(-u, t) - T_0^d(-u, t)] \quad (18)$$

$$K^d \frac{\partial T_0^d}{\partial y}(-u - h, t) = Q_0(t) \quad (19)$$

The first order boundary conditions are;

$$s_1(t) \frac{\partial T_0^c}{\partial y}(s_0, t) + T_1^c(s_0, t) = 0 \quad (20)$$

$$K^c \left[\frac{\partial T_1^c}{\partial y}(s_0, t) + s_1(t) \frac{\partial^2 T_0^c}{\partial y^2}(s_0, t) \right] = L_c \rho_c \frac{ds_1}{dt}(x, t) \quad (21)$$

$$K^c \frac{\partial T_1^c}{\partial y}(0, t) = K^b \frac{\partial T_1^b}{\partial y}(0, t) \quad (22)$$

$$K^b \frac{\partial T_1^b}{\partial y}(-u, t) = K^d \frac{\partial T_1^d}{\partial y}(-u, t) \quad (23)$$

$$K^c \frac{\partial T_1^c}{\partial y}(0, t) = \frac{1}{R_{sc}} [T_1^c(0, t) - T_1^b(0, t)] \quad (24)$$

$$K^b \frac{\partial T_1^b}{\partial y}(-u, t) = \frac{1}{R_{cm}} [T_1^b(-u, t) - T_1^d(-u, t)] \quad (25)$$

$$K^d \frac{\partial T_1^d}{\partial y}(-u - h, t) = Q_1(t) \quad (26)$$

4. Dimensionless Presentation

To reduce the complexness of the problem and generalize the solution, the dimensionless parameters are described as follows.

$$Y = my, \quad S(\beta) = ms(t), \quad H = mh, \quad U = mu, \quad \beta = m^2 \frac{K^c T_m}{\rho^c L^c} t, \quad (27)$$

$$\bar{T}(Y, \beta) = \frac{T(y, t)}{T_m}, \quad \bar{Q} = \frac{Q}{mK^c T_m}, \quad \bar{R}_{sc} = mK^c R_{sc}, \quad \bar{R}_{cm} = mK^c R_{cm} \quad (28)$$

$$\zeta_1 = \frac{K^c}{K^b}, \quad \zeta_2 = \frac{K^b}{K^d}, \quad \zeta_3 = \frac{K^c}{K^d}, \quad \epsilon_c = \frac{K^c T_m}{\alpha^c \rho^c L^c}, \quad \epsilon_b = \frac{K^c T_m}{\alpha^b \rho^c L^c}, \quad \epsilon_d = \frac{K^c T_m}{\alpha^d \rho^c L^c} \quad (29)$$

The dimensionless forms of the zeroth order heat conduction equations are given below.

$$\begin{aligned} \frac{\partial^2 \bar{T}_0^c}{\partial Y^2}(Y, \beta) &= \epsilon_c \frac{\partial \bar{T}_0^c}{\partial \beta}(Y, \beta) \\ \frac{\partial^2 \bar{T}_0^b}{\partial Y^2}(Y, \beta) &= \epsilon_b \frac{\partial \bar{T}_0^b}{\partial \beta}(Y, \beta) \\ \frac{\partial^2 \bar{T}_0^d}{\partial Y^2}(Y, \beta) &= \epsilon_d \frac{\partial \bar{T}_0^d}{\partial \beta}(Y, \beta) \end{aligned} \quad (30)$$

The dimensionless zeroth-order boundary conditions used to obtain zeroth-order temperature distributions ($\bar{T}_0^i(x, y, t), i = c, b, d$) from these equations are;

$$\bar{T}_0^c(S_0, \beta) = 1 \quad (31)$$

$$\frac{\partial \bar{T}_0^c}{\partial Y}(S_0, \beta) = \frac{dS_0(\beta)}{d\beta} \quad (32)$$

$$\frac{\partial \bar{T}_0^c}{\partial Y}(0, \beta) = \zeta_1 \frac{\partial \bar{T}_0^b}{\partial Y}(0, \beta) \quad (33)$$

$$\frac{\partial \bar{T}_0^b}{\partial Y}(-U, \beta) = \zeta_2 \frac{\partial \bar{T}_0^d}{\partial Y}(-U, \beta) \quad (34)$$

$$\frac{\partial \bar{T}_0^c}{\partial Y}(0, \beta) = \frac{1}{\bar{R}_{sc}} [\bar{T}_0^c(0, \beta) - \bar{T}_0^b(0, \beta)] \quad (35)$$

$$\frac{\partial \bar{T}_0^b}{\partial Y}(-U, \beta) = \frac{\zeta_1}{\bar{R}_{cm}} [\bar{T}_0^b(-U, \beta) - \bar{T}_0^d(-U, \beta)] \quad (36)$$

$$\frac{\partial \bar{T}_0^d}{\partial Y}(-U - H, \beta) = \zeta_3 \bar{Q}_0(\beta) \quad (37)$$

The dimensionless forms of the first order heat conduction equations are given below.

$$\frac{\partial^2 \bar{T}_1^c(Y, \beta)}{\partial Y^2} - \bar{T}_1^c(Y, \beta) = \epsilon_c \frac{\partial \bar{T}_1^c}{\partial \beta}(Y, \beta) \quad (38)$$

$$\frac{\partial^2 \bar{T}_1^b(Y, \beta)}{\partial Y^2} - \bar{T}_1^b(Y, \beta) = \epsilon_b \frac{\partial \bar{T}_1^b}{\partial \beta}(Y, \beta)$$

$$\frac{\partial^2 \bar{T}_1^c(Y, \beta)}{\partial Y^2} - \bar{T}_1^c(Y, \beta) = \epsilon_c \frac{\partial \bar{T}_1^c}{\partial \beta}(Y, \beta)$$

The dimensionless first-order boundary conditions used to obtain first-order temperature distributions ($\bar{T}_1^i(x, y, t), i = c, b, d$) from these equations are;

$$\bar{T}_1^c(S_0, \beta) \frac{\partial \bar{T}_0^c}{\partial Y}(S_0, \beta) + \bar{T}_1^c(S_0, \beta) = 0 \quad (39)$$

$$\frac{\partial \bar{T}_1^c}{\partial Y}(S_0, \beta) + S_1(\beta) \frac{\partial^2 \bar{T}_0^c}{\partial Y^2}(S_0, \beta) = \frac{dS_1(\beta)}{d\beta} \quad (40)$$

$$\frac{\partial \bar{T}_1^c}{\partial Y}(0, \beta) = \zeta_1 \frac{\partial \bar{T}_1^b}{\partial Y}(0, \beta) \quad (41)$$

$$\frac{\partial \bar{T}_1^b}{\partial Y}(-U, \beta) = \zeta_2 \frac{\partial \bar{T}_1^d}{\partial Y}(-U, \beta) \quad (42)$$

$$\frac{\partial \bar{T}_1^c}{\partial Y}(0, \beta) = \frac{1}{R_{sc}} [\bar{T}_1^c(0, \beta) - \bar{T}_1^b(0, \beta)] \quad (43)$$

$$\frac{\partial \bar{T}_1^b}{\partial Y}(-U, \beta) = \frac{\zeta_1}{R_{cm}} [\bar{T}_1^b(-U, \beta) - \bar{T}_1^d(-U, \beta)] \quad (44)$$

$$\frac{\partial \bar{T}_1^d}{\partial Y}(-U - H, \beta) = \zeta_3 \bar{Q}_1(\beta) \quad (45)$$

After obtaining dimensionless equations, the numerical solution procedure for the heat transfer problem has been obtained due to a non-available closed-form solution.

5. Numerical Solution Procedure

In the heat transfer problems, the exact solutions are generally obtained just for idealized cases in which semi-finite or infinite regions are considered with simple initial/boundary conditions. Since the nonlinear behavior of this problem, the superposition principle is not applicable and all cases are evaluated separately. When the exact solution of the full Stefan problem is not calculated analytically, the numerical methods are developed to solve these problems. In this study, zero and first-order heat conduction equations (Eq. (30) and Eq. (38)) do not exist in closed form with their respective boundary conditions. For this reason, the temperature distributions and the position of the moving interface have been obtained with a numerical solution. In the current study, the Lagrange scheme, which is an explicit finite difference method, was applied to obtain the solution to the heat transfer problem during the solidification.

In the numerical solution algorithm, the shell's thickness is divided into N elements at each step. Thus, the space step width at each time step becomes $\delta = \frac{S_0(\beta)}{N}$ with the $N + 1$ number of nodes in the average solidified metal thickness ($0 < Y < S_0(\beta)$). In this case, the final node ($N + 1^{th}$) in the solidifying solid always corresponds to the position of the zero-order solid-liquid moving surface. Due to the increase in the average solid thickness as time progresses, the nodal points change for each new time step, and space is recalculated for

the step width. The average solidified metal thickness in the next time step depending on the time increase (τ) is calculated by the backward finite difference formulation of Eq. (32).

$$S_0^{j+1} = S_0^j + \frac{\tau}{2\delta_c} \left(3\bar{T}_{0_{N+1}}^{c_j} - 4\bar{T}_{0_N}^{c_j} + \bar{T}_{0_{N-1}}^{c_j} \right) \quad (46)$$

In this equation, the temperature in the moving interface ($\bar{T}_{0_{N+1}}^j$) is constant during the process according to Eq. (31). The temperature distributions in the solidified metal are obtained for the space variable values $Y = (i - 1)\delta$, ($i = 1, 2, \dots, N + 1$) for $N+1$ nodes. The temperatures in the nodes in the solidified metal ($i = 2, 3, \dots, N$ nodes) are found for each time step with Eq. (47) which is the central finite difference formulation of the general heat conduction equation in Eq. (30a).

$$\bar{T}_{0_i}^{c_{j+1}} = \bar{T}_{0_i}^{c_j} + \frac{\tau}{\epsilon_c \delta_c^2} \left(\bar{T}_{0_{i+1}}^{c_j} - 2\bar{T}_{0_i}^{c_j} + \bar{T}_{0_{i-1}}^{c_j} \right), \quad (i = 2, 3, \dots, N) \quad (47)$$

Here the subscript “ i ” refers to the i^{th} node location to derive the temperature in the solidified shell while the superscript “ j ” is the time step counter.

In this problem, it is necessary to update with the inclusion of the convective terms in the algorithm to calculate the temperatures at the node points whose positions change depending on fixed elements number, as the thickness of the shell solidifies as time progresses.

$$\bar{T}_{0_i}^{c_{j+1}} = \bar{T}_{0_i}^{c_j} + (i - 1) \frac{\delta_c^{j+1} - \delta_c^j}{\delta_c^j} \left(\bar{T}_{0_{i+1}}^{c_{j+1}} - \bar{T}_{0_i}^{c_{j+1}} \right), \quad (i = 2, 3, \dots, N) \quad (48)$$

Similarly, the coating layer and mold are divided into a fixed number of elements J and M , respectively. Therefore, $J + 1$ and $M + 1$ number of nodes are formed in the coating and mold for temperature distribution derivation. As time progresses, the locations of the nodes in these layers are fixed because there is no change in coating and mold thicknesses. The temperatures for nodes ($k = 2, 3, \dots, J$ and $p = 2, 3, \dots, M$) in these layers are calculated by Eq. (49), which is the central finite difference formulation of Equation (30b) and Eq. (30c).

$$\begin{aligned} \bar{T}_{0_k}^{b_{j+1}} &= \bar{T}_{0_k}^{b_j} + \frac{\tau}{\epsilon_b \delta_b^2} \left(\bar{T}_{0_{k+1}}^{b_j} - 2\bar{T}_{0_k}^{b_j} + \bar{T}_{0_{k-1}}^{b_j} \right), \quad (k = 2, 3, \dots, J) \\ \bar{T}_{0_p}^{d_{j+1}} &= \bar{T}_{0_p}^{d_j} + \frac{\tau}{\epsilon_d \delta_d^2} \left(\bar{T}_{0_{p+1}}^{d_j} - 2\bar{T}_{0_p}^{d_j} + \bar{T}_{0_{p-1}}^{d_j} \right), \quad (p = 2, 3, \dots, M) \end{aligned} \quad (49)$$

After determining the temperatures at the nodes in the solid layers, the temperatures at the interfaces and at the mold's bottom surface are derived by using boundary conditions. For nodes, $i = 1$ and $k = J + 1$ corresponding to the solidified shell/coating interface, the temperatures are found using Eqs. (33) and (35). Similarly, the temperatures at the $k = 1$ and $p = M + 1$ nodes at the coating and mold interface are obtained using finite difference formulations of boundary conditions in Eqs. (34) and (36). Finally, the temperature of the node at the mold's lower surface ($p = 1$) is found by using Eq.(38).

The first-order solution is made using the same method as the above zeroth-order solution and the first-order temperatures at the nodes in the solid layers are obtained with $S_1(\beta)$. $S_1(\beta)$ is found by Eq. (50) which is derived through the backward finite difference formulation of Eq. (40).

$$S_1^{j+1} = S_1^j \left(1 + \frac{\tau}{\delta_c^2} \left(2\bar{T}_{0\ N+1}^{c\ j} - 5\bar{T}_{0\ N}^{c\ j} + 4\bar{T}_{0\ N-1}^{c\ j} - \bar{T}_{0\ N-2}^{c\ j} \right) \right) + \frac{\tau}{2\delta_c} \left(3\bar{T}_{1\ N+1}^{c\ j} - 4\bar{T}_{1\ N}^{c\ j} + \bar{T}_{1\ N-1}^{c\ j} \right) \quad (50)$$

Similar to the zeroth degree solution, the first order node temperatures are calculated using the heat conduction equations in Eq. (38) and the first-order boundary conditions in Eq. (39) and Eqs. (41) - (45).

Another important factor is the adjustment of the time increment variable (τ) in the algorithm. The discretization of both time and dimensional variables is of great importance for the reliability of the results obtained by the numerical solution. For this reason, when choosing the value of τ , attention should be paid to the acceptance of numerical convergence, to maintain stability and to provide calculation efficiency. The maximum time step for stability is proportional to $\epsilon_c \delta_c^2$. Therefore, the stability condition imposes a restriction on τ when good spatial accuracy is required, which usually requires very small δ values. In this case, the numerical stability for this model occurs when the conditions in Eq. (51) are provided.

$$\frac{\tau}{\epsilon_c \delta_c^2} < 0.5, \quad \frac{\tau}{\epsilon_b \delta_b^2} < 0.5, \quad \frac{\tau}{\epsilon_d \delta_d^2} < 0.5 \quad (51)$$

When solidification begins, $S_0(\beta)$ and δ are of very small values. Hence, a very small time step is needed to fulfill the requirement in Eq.(51a). But choosing the time step so small causes the algorithm to be very slow. In the continuation of solidification, the time step is allowed to increase without loss of stability due to the increase in $S_0(\beta)$ and δ . However, the conditions in Eq.(51b) and Eq.(51c) significantly limit this increase in T due to the constant δ_b and δ_d during solidification. Therefore, it is necessary to use a very small initial δ value during the solidification process to keep both space and time steps under conditions and obtain a reliable result.

Also, the nodes must not overlap for the algorithm used for the numerical solution. For this reason, solidification is not desired to start at $S_0(\beta) = 0$. To overcome this problem, an appropriate initial condition must be created and the solution of the limiting problem under certain assumptions is used for this purpose. In the early stages, the limited solution is of acceptable accuracy. Therefore, the numerical solution of the considered problem, in which the material thermal diffusivities are included, was started by using this limiting solution with a very small finite $S_0(\beta)$. The solution to this limiting problem is presented by Demir and Yigit [38] and the expressions used as the initial condition for the numerical solution are given in the Appendix.

6. Results and Discussion

In this study, the numerical solution of the heat transfer problem, which is one of the sub-parts of the thermoelasticity problem that occurs during solidification, was carried out, and especially the roles of the coating layer on the thermoelastic instability were dealt with. The theoretical model developed by Demir and Yigit [38], which examines the heat transfer problem at the early stages of the process, was used as the initial condition in the solution of the full heat transfer problem, in which the thermal capacities of the solidifying metal, coating layer and mold materials are not considered zero (the thermal diffusivities of the materials are assumed to have finite values).

At the beginning of the analysis, obtained numerical results are compared with the previous results in Yigit [33] in which the heat transfer problem during the solidification

of pure metal on planar mold without a coating layer. Therefore, the coating layer's effects on the process is neglected for proving the correctness of the solution by assuming $U + H = 10, \bar{R}_{cm} \ll 1, \zeta_2 = 1, \epsilon_2 = \epsilon_3 = 10, \zeta_1 = \zeta_3 = 2, \bar{R}_{sc} = \bar{R}_0$ when $\bar{R}_0 = 0.3, \zeta_1 = 2$ for approaching the model in Yigit [33].

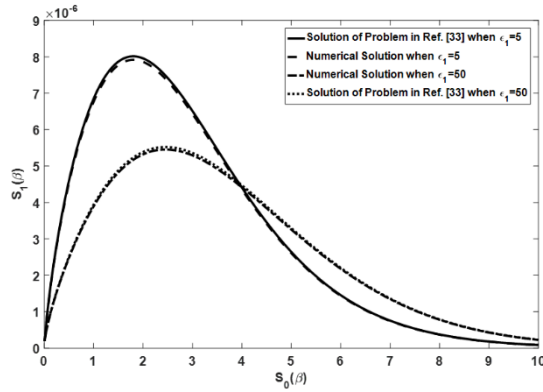


Fig. 2 The comparison between the numerical solution and the limiting solution in Yigit [33] when $\epsilon_1 = 5$ and $\epsilon_1 = 50$ ($U + H = 10, \bar{R}_{cm} \ll 1, \zeta_2 = 1, \epsilon_2 = \epsilon_3 = 10, \zeta_1 = \zeta_3 = 2, \bar{R}_{sc} = \bar{R}_0 = 0.3$)

The mold and coating are assumed to make of the same material and \bar{R}_{cm} is considered very small. Thus, we converge to the solution given in Fig. 4 in Ref [33] where $H = 10, \zeta = 2, \bar{R}_0 = 0.3, \epsilon_1 = 5$ and $\epsilon_2 = 10$. The comparison results are given in Fig. 2 for different values of ϵ_1 . Fig. 2 shows the variation of $S_1(\beta)$ as a function of $S_0(\beta)$ for the numerical solution and Yigit's problem solution when $\epsilon_1 = 5$ and $\epsilon_1 = 50$. The results of the present model go to limiting solutions due to Yigit [33] and it is indicated that these results are important in terms of proving the accuracy and reliability of the developed finite-difference algorithm and the numerical solution procedure. Thus, it can be said that the results examining the effects on the problem of heat transfer during solidification in which the coating layer is included in the later stages are reliable and reflect the actual process within certain assumptions. After that, the influences of the coating's thickness on the thermoelastic stability during the solidification are examined.

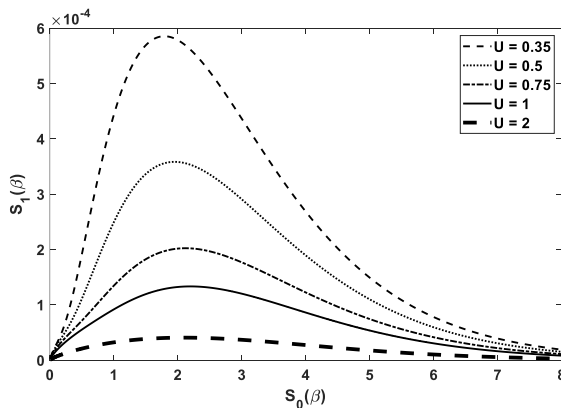


Fig. 3 The variation of $S_1(\beta)$ as a function of $S_0(\beta)$, at selected values of U when $H = 5, \zeta_1 = \zeta_2 = 0.5, \epsilon_1 = \epsilon_2 = \epsilon_3 = 10$ and $\bar{R}_{sc} = \bar{R}_{cm} = 0.3$

Fig. 3 shows the variation of $S_1(\beta)$ for different coating thickness. Other parameters are assumed $H = 5$, $\zeta_1 = \zeta_2 = 0.5$, $\epsilon_1 = \epsilon_2 = \epsilon_3 = 10$ and $\bar{R}_{sc} = \bar{R}_{cm} = 0.3$. The results indicate that the coating layer controls the heat transfer during solidification and it leads to stabilizing effect. In other words, the thicker coating layer should be chosen as much as possible to achieve more stable growth and better quality final casting. It should also be mentioned here that increasing the coating thickness for all solidification parameter combinations creates a stability-enhancing effect. These effects of the coating layer are shown in the following figures in detail. Likewise, it is seen that the thickness of the mold has a similar effect and it is concluded that this supports the fact that increasing the layer thickness directly enables the heat transfer rate to be controlled.

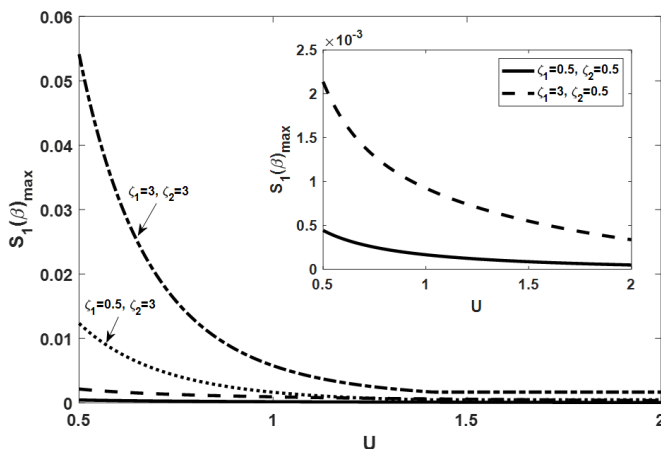


Fig. 4 The variation of $S_1(\beta)_{max}$ as a function of U for four combinations of ζ_1 and ζ_2 ($H = 5$, $\epsilon_1 = 2$, $\epsilon_2 = \epsilon_3 = 5$, $\bar{R}_{sc} = \bar{R}_{cm} = 0.3$)

Then, the effect of the thickness of the coating layer is focused depending on the other important process parameters such as conductivity ratios and thermal capacities. Fig. 4 shows the variation of $S_1(\beta)_{max}$ as a function of coating thickness, U , for different values of thermal conductivity ratios between materials of the shell, mold and its coating when $\epsilon_1 = 2$, $\epsilon_2 = \epsilon_3 = 5$, $\bar{R}_{sc} = \bar{R}_{cm} = 0.3$. $S_1(\beta)_{max}$ denotes the maximum amplitude of the perturbed undulation on the mean shell thickness. The aim here is to establish the relationship between the choice of mold, coating, and casting materials and the coating thickness and to create clues for the most efficient casting. The results show that the thermal conductivity ratios have an important effect on growth instability and the sensitivity to coating thickness. It is indicated that the coating's thickness has stabilizing impact for all combinations of ζ_1 and ζ_2 . However, it is seen that this effect varies considerably according to the values of these parameters. The ζ_1 and ζ_2 values selected in this figure represent various orders of material thermal conductivities relative to each other. $\zeta_1 = 0.5 - \zeta_2 = 0.5$, $\zeta_1 = 3 - \zeta_2 = 0.5$, $\zeta_1 = 0.5 - \zeta_2 = 3$ and $\zeta_1 = 3 - \zeta_2 = 3$ represent the cases in which the values of the thermal conductivities are ranked as $K^d > K^b > K^c$, $K^c > K^d > K^b$, $K^b > K^c > K^d$ and $K^c > K^b > K^d$, respectively. The results show that $\zeta_1 = 0.5 - \zeta_2 = 0.5$ case leads to more uniform growth than the other cases and the most unstable growth occurs when ζ_1 and ζ_2 are equal to 3. In other words, $K^c > K^b > K^d$ state causes the most unstable growth, while $K^d > K^b > K^c$ the condition causes the most stable growth. Also, much lower amplitude perturbations occur when $K^d > K^b > K^c$ and $K^c > K^d > K^b$. This means that if the coating material is chosen from a material whose thermal conductivity is smaller than that of the mold material, the growth instability is minimized to obtain the best quality casting piece, regardless of the shell's thermal

conductivity. Besides, the smaller thermal conductivity of the casting material compared to that of both the mold and the coating material ensures the most efficient solidification. The most unstable growth occurs when the mold's thermal conductivity is the smallest. In those cases, where the shell's conductivity is greater than that of the mold, the coating's thermal conductivity should be chosen higher than that of the material to be cast for quality solidification.

Furthermore, it can be seen from this figure that the sensitivity to the change of coating thickness varies according to the thermal conductivities. For $\zeta_1 = 3 - \zeta_2 = 3$, it is seen that the change in x according to the change of the coating thickness of the process is the most and the sensitivity to the coating thickness is the most in this case. Following this case, coating thickness sensitivity for $\zeta_1 = 0.5 - \zeta_2 = 3$ is also higher than in other cases. Thus, it can be said that in the case where the mold's thermal conductivity is the smallest, the sensitivity of the solidification process to the thickness increases. Relatively, for cases where $\zeta_1 = 0.5 - \zeta_2 = 0.5$, $\zeta_1 = 3 - \zeta_2 = 0.5$, it is seen that the sensitivity to the coating thickness decreases. Therefore, in cases where the sensitivity to coating thickness is to be lowered, the mold's thermal conductivity should be chosen greater than that of the coating regardless of the thermal conductivity of the metal to be solidified. However, it should be studied where the coating's thermal conductivity is greater than that of the other solid layers to minimize the sensitivity to the coating thickness. According to the results, the thermal conductivity ratios play an important role on the growth instability. Fig. 5 shows the variation of $S_1(\beta)_{max}$ depending on the thermal conductivity ratios (ζ_1 and ζ_2) when $U = 0.5, H = 5, \epsilon_1 = \epsilon_2 = \epsilon_3 = 5$ and $\bar{R}_{sc} = \bar{R}_{cm} = 0.3$. The curves in the figure were obtained by keeping one of the thermal conductivity ratios constant and changing the other so that the effects of the change of thermal conductivity of the materials relative to each other on the growth instability were observed.

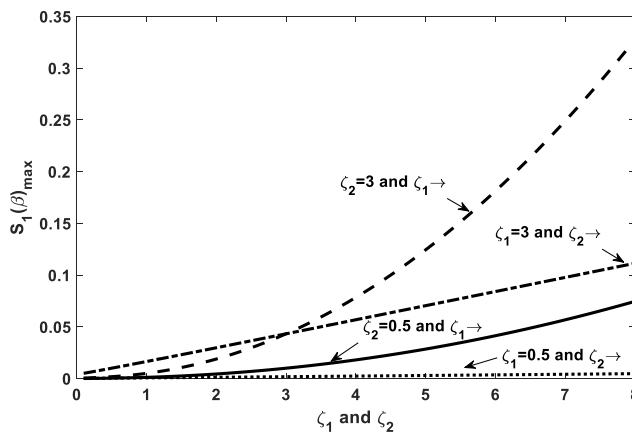


Fig. 5 The variation of $S_1(\beta)_{max}$ as a function of ζ_1 and ζ_2 for the case where $U = 0.5, H = 5, \epsilon_1 = \epsilon_2 = \epsilon_3 = 5$ and $\bar{R}_{sc} = \bar{R}_{cm} = 0.3$

The results show that the increases in both ζ_1 and ζ_2 increase the amplitude of the perturbations at the moving interface and have negative effects on the growth instability. It can be also seen that it is seen that the change of ζ_2 varies the amplitude of the perturbations least when $\zeta_1 = 0.5$. In this case, it appears that the solidification process has less sensitivity to ζ_2 , and changing the value of K^d for $K^b > K^c$ has less effect on growth instability. It is observed that an increase in ζ_1 leads to increase in the sensitivity of the process to change of ζ_2 . This means that the variation of the mold's thermal conductivity

affects the thermoelastic stability much more when the shell's conductivity is higher than the coating's conductivity. Similarly, for $\zeta_2 = 0.5$ and $\zeta_2 = 3$, the effect of changing ζ_1 also appeared to increase instability. Again, according to the value of ζ_2 , the sensitivity of the process to ζ_1 varies. It is seen that the sensitivity to ζ_1 increases when ζ_2 is greater than 1 than the case where ζ_2 is less than 1. This means that both growth instability and sensitivity to the coating's and shell's conductivities are increased when the coating thermal conductivity is greater than that of the mold, compared to the case where it is smaller than the mold's conductivity.

On the other hand, the specific heats of the materials vary the coating layer's effects on the process. Fig. 6 shows the variation of $S_1(\beta)_{max}$ as a function of coating thickness for the different combinations of the specific heat values of the solid layer's materials when $H = 5$, $\zeta_1 = \zeta_2 = 2$ and $\bar{R}_{sc} = \bar{R}_{cm} = 0.3$. All specific heat values are taken as 3, 10 and 50 and compared with the case where all specific heat values are equal to 10. As mentioned earlier, the stability-enhancing effect of the coating thickness is seen for all considered specific heats combinations and it is seen that the change of the specific heat values changes the sensitivity to the coating thickness.

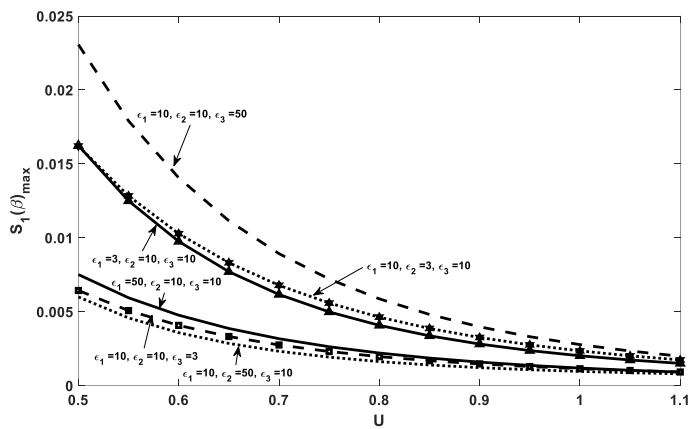


Fig. 6 The variation of $S_1(\beta)_{max}$ depending on U for the different values of ϵ_1 , ϵ_2 and ϵ_3 ($H = 5$, $\zeta_1 = \zeta_2 = 2$ and $\bar{R}_{sc} = \bar{R}_{cm} = 0.3$)

The results show that the increase in ϵ_3 appears to cause larger amplitude perturbation for a given coating thickness, while the increases in ϵ_1 and ϵ_2 cause lower amplitude perturbations. Therefore, the decrease in $S_1(\beta)_{max}$ due to the increase in coating thickness occurs when the value of ϵ_3 is large. Thus, it can be said that increasing the specific heat of the mold material increases the sensitivity to coating thickness. Considering the stability-enhancing effects of ϵ_1 and ϵ_2 , it is seen that the sensitivity to coating thickness is high when ϵ_1 and ϵ_2 are small. It is also observed that the sensitivity to the coating thickness is reduced for large values of ϵ_1 and ϵ_2 and for small values of ϵ_3 . Physically, this result raises the requirement that certain temperatures of the solidified metal and the material of the coating layer should be low or the mold should be selected from the material with a certain temperature in order to reduce the dependence of the solidification process on the coating thickness. It can be also noted that the effects of the specific heat of the materials of the solid layers on the growth instability are opposite and these effects of the specific heats have been examined in Fig. 7.

The variation of $S_1(\beta)_{max}$ depending on the specific heat values of materials (ϵ_1 , ϵ_2 , ϵ_3) is shown in Fig. 7 when $U = 0.5$, $H = 5$, $\zeta_1 = 0.5$ and $\zeta_2 = 3$. The specific heats change from

0.1 to 20 for each curve in the figure and the curves are drawn for the cases where each specific heat changes, whereas the other two specific heats are equal to 10. The results indicate that the specific heat of each solid layer has different effects on the unstable shell growth and the sensitivity of the solidification process to these specific heat variations is also different. It is seen that the specific heats of solidified shell and coating materials have stabilizing effects on the growth stability during the solidification. This means that they should be selected higher specific heats (lower thermal diffusivities) for more uniform growth and higher quality final cast. However, the higher specific heat of mold material causes an increase in $S_1(\beta)_{max}$, and hence, it reduces growth stability. As can be seen, while ϵ_1 and ϵ_2 increase stability, ϵ_3 has an increasing effect on unstable shell growth for the considered case. When analyzes are made for all cases, it is seen that the specific heats of the materials have a similar effect on the process. Therefore, it can be said that the effects of the specific heat of the solidified metal and the coating layer (ϵ_1 and ϵ_2) and the mold's specific (ϵ_3) on the perturbation growth neutralize each other. It can also be stated that the sensitivity of the growth instability to ϵ_2 variation during the solidification process is quite low, but the sensitivities to ϵ_1 and ϵ_3 variations are high.

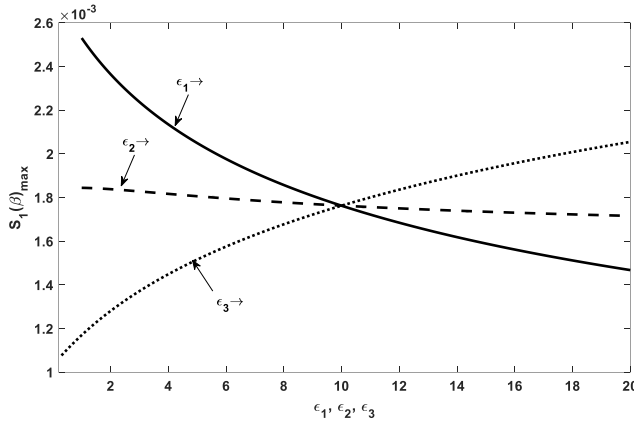


Fig. 7 The variation of $S_1(\beta)_{max}$ as a function of ϵ_1, ϵ_2 and ϵ_3 for the case where $U = 0.5, H = 5, \zeta_1 = 0.5, \zeta_2 = 3$ and $\bar{R}_{sc} = \bar{R}_{cm} = 0.3$

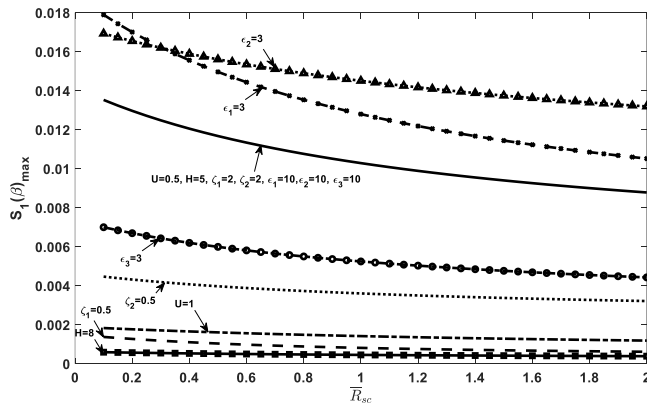


Fig. 8 The variation of $S_1(\beta)_{max}$ as a function of \bar{R}_{sc} for the different values of system parameters

The effects of the thermal contact resistances ($\bar{R}_{sc}, \bar{R}_{cm}$) are analyzed in Fig. 8 and Fig. 9, respectively. These figures show the variation of $S_1(\beta)_{max}$ as a function of thermal contact resistances. They are changed from 0.1 to 2 because the aforementioned effects were found to be unchanged for the values greater than 2. Additionally, it was observed how the effects of thermal resistances on growth instability changed for different values of other system parameters. Firstly, the variation of $S_1(\beta)_{max}$ is observed as a function of \bar{R}_{sc} in Fig. 8. The straight line curve represents the case in which the other system parameters are assumed to be equal as $U = 0.5, H = 5, \zeta_1 = \zeta_2 = 2, \bar{R}_{cm} = 0.3$ and $\epsilon_1 = \epsilon_2 = \epsilon_3 = 10$.

The result indicates that an increase in \bar{R}_{sc} causes a decrease in the maximum amplitude of perturbation at the freezing front. This indicates that the thermal resistance at the shell/coating interface should be increased for more stable growth and better quality final cast. The other cases in the figure show the cases that occur by changing only one of the values of the system parameters given for the situation specified with the straight-line curve. It also appears that the same stabilizing effect applies to all cases in the figure. Although the variation of system parameters generally does not change the stability-enhancing effect of \bar{R}_{sc} , it has been observed that the sensitivity of the process to \bar{R}_{sc} varies with the values of the system parameters. It is seen from the results that the decrease in ζ_1 and ζ_2 has decreased sensitivity to \bar{R}_{sc} . Similarly, it was found that the increase in U and H decrease this sensitivity. Then, if the sensitivity to thermal contact resistance at this interface is to be reduced, it is necessary to increase the thickness of the coating and mold, to choose the thermal conductivity of the casting material smaller than the coating material, and to choose the coating material from the material with thermal conductivity less than the mold's conductivity. When the specific heats of materials are examined, it is seen that the sensitivity to \bar{R}_{sc} increases with the decrease of ϵ_1 but does not change significantly with the decrease of ϵ_2 and ϵ_3 . From this situation, it is seen that the sensitivity to thermal contact resistance between this layer and the coating layer can be adjusted by changing the shell's specific heat.

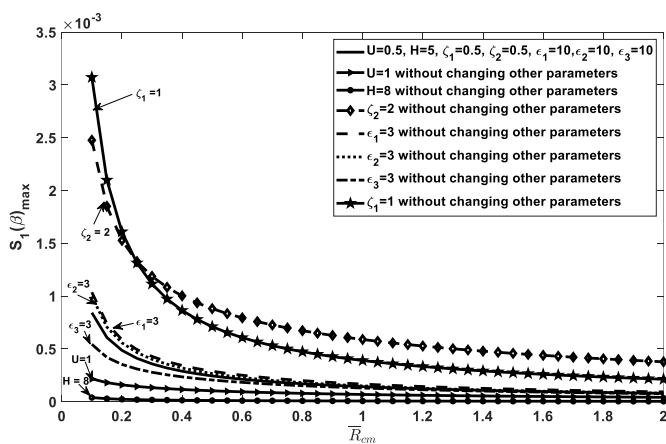


Fig. 9 The variation of $S_1(\beta)_{max}$ with respect to \bar{R}_{cm} for the different values of system parameters

The effects of \bar{R}_{cm} are investigated in Fig. 9 in which the variation of $S_1(\beta)_{max}$ as a function of \bar{R}_{cm} for different values of other system parameters. Similar to Fig. 8, the straight-line curve is the main curve in which the system parameters are assumed to be equal as $U = 0.5, H = 5, \zeta_1 = \zeta_2 = 0.5, \bar{R}_{sc} = 0.3$ and $\epsilon_1 = \epsilon_2 = \epsilon_3 = 10$ and other cases represent the cases in which only one system parameter is changed. The results show that $S_1(\beta)_{max}$

decreases when \bar{R}_{cm} is increased. This means that both \bar{R}_{sc} and \bar{R}_{cm} have stabilizing effects on the shell's growth. Physically, these thermal contact resistances should be increased for better quality final cast. It is also seen that the sensitivity of the process to \bar{R}_{cm} is greater than the sensitivity to \bar{R}_{sc} . Similar to the results in Fig. 9, the sensitivity of \bar{R}_{cm} decreases when ζ_1 and ζ_2 decrease. Moreover, increases in U and H also decrease this sensitivity. It is also noteworthy that decreases in ϵ_1 and ϵ_2 cause an increase in the sensitivity of \bar{R}_{cm} but on the contrary, the decrease in ϵ_3 decreases the sensitivity. Therefore, it can be said that the shell's and coating's specific heats should be selected higher and the mold's specific heat should be selected lower for reducing dependence to \bar{R}_{cm} . These results mean that thicker coating and mold lead to a decrease in the effect of \bar{R}_{cm} on the proses and the coating's thermal conductivity should be selected higher than the shell's conductivity for reducing the dependence on changes of \bar{R}_{cm} . Also, this dependence of the process can be reduced by the selection of the mold's thermal conductivity greater than the coating's conductivity.

7. Conclusion

A theoretical model is developed to study the effects of the coating layer on the growth instability mechanism during the solidification of pure metal on a coated mold of finite thickness. The phase change heat transfer problem, which is one of the two main sub-problems of thermoelastic instability during solidification, is considered, modeled, and solved numerically in this study. This study extends previous studies by taking into account the combined effects of coating layer properties and thermal capacitances of solid layers. The spatial dimension of the modeled heat transfer problem was reduced from two to one dimensional with the linear perturbation method. The finite acceptance of thermal diffusivities provides that the obtained full solidification model has to be solved numerically due to the nonlinear behavior of phase change problems. Therefore, the governing equations are discretized by the Lagrangian finite difference scheme for numerical solution. In this numerical solution, a limiting solution is used as initial conditions, and this limiting solution is obtained analytically in [38] by assuming the thermal diffusivities of the materials are infinite. The key question is how the properties of the coating layer are selected according to the other parameters.

The results show that an increase in the coating's thickness causes a positive effect on the thermoelastic instability and the thicker coating layer should be chosen as much as possible to achieve more stable growth and better quality final casting. Also, a thicker coating layer creates a stability-enhancing effect for all solidification parameter combinations. But, it is observed that the stabilizing effect of this thickness varies considerably according to the values of other parameters.

The sensitivity to coating thickness is to be lowered when the mold's thermal conductivity should be chosen greater than that of the coating material regardless of the thermal conductivity of the metal to be solidified. However, it should be worked in the cases in which the coating's thermal conductivity is greater than that of the other solid layers in order to minimize the coating thickness's dependence of the process. When the effects of the specific heats on this coating thickness dependence of the process are investigated, it is also observed that the sensitivity to the coating thickness is reduced for large values of ϵ_1 and ϵ_2 and for small values of ϵ_3 . On the other hand, it is also stated that the increases in both ζ_1 and ζ_2 increase $S_1(\beta)$ and have negative effects on the thermoelastic stability. Moreover, ϵ_3 shows an increasing effect on growth instability while ϵ_1 and ϵ_2 increase the stability for all cases and this means that the effects of the shell's and coating's specific heats and the mold's specific heat neutralize each other. Finally, the thermal contact resistances have stabilizing effects for all cases but the sensitivities of the process to these resistances vary according to other parameters.

The solution of this study can be used in uncoupled and coupled problems in which the thermos-mechanical problem is investigated for analyzing the full solidification process.

Appendix

In this section, the limiting solution of the heat transfer problem during the pure metal solidification process on a coated planar mold is given. The limiting solution is obtained when the thermal diffusivities of the materials are assumed to be infinite ($\epsilon_c \rightarrow 0, \epsilon_b \rightarrow 0$ and $\epsilon_d \rightarrow 0$). An analytical solution for the temperature fields in the solid layer and the position of the moving interface are derived for the limiting case in which the effects of the materials' thermal capacity are negligible. This model is valid for only the early stages and in the full problem, in which thermal diffusivities are finite, this limiting solution is used as initial conditions. The limiting solution is obtained in Demir and Yigit [38] and the readers refer to this study for more details. In summary, the expressions that are important for this study and give the average shell thickness and node temperatures in solid layers for a very small time interval are given below.

Zeroth-order temperature fields are;

$$\begin{aligned} \bar{T}_0^c(Y, \beta) &= 1 + \bar{Q}_0(\beta)(Y - S_0(\beta)) \\ \bar{T}_0^b(Y, \beta) &= 1 + \bar{Q}_0(\beta)(\zeta_1 Y - S_0(\beta) - \bar{R}_{sc}) \\ \bar{T}_0^d(Y, \beta) &= 1 + \bar{Q}_0(\beta)(\zeta_3 Y - \zeta_1 U - S_0(\beta) + \zeta_3 U - \bar{R}_{sc} - \bar{R}_{cm}) \end{aligned} \tag{A.1}$$

The mean shell thickness is;

$$S_0(\beta) = \bar{Q}_0(\beta)\beta \tag{A.2}$$

First-order temperature fields are;

$$\begin{aligned} \bar{T}_1^c(Y, \beta) &= C_1(\beta) \sinh(Y) + C_2(\beta) \cosh(Y) \\ \bar{T}_1^b(Y, \beta) &= C_3(\beta) \sinh(Y) + C_4(\beta) \cosh(Y) \\ \bar{T}_1^d(Y, \beta) &= C_5(\beta) \sinh(Y) + C_6(\beta) \cosh(Y) \end{aligned} \tag{A.3}$$

The perturbed undulation on the mean shell thickness is given in Eq. (A4) as follows.

$$S_1(S_0(\beta)) = \frac{C_7 S_0(\beta)}{C_8 \cosh(S_0(\beta)) + C_9 \sinh(S_0(\beta))} \tag{A.4}$$

The coefficients are;

$$\begin{aligned} \bar{C}_1 &= A_{32} + A_{33}S_1(\beta), & \bar{C}_2 &= A_{34} + A_{35}S_1(\beta), & \bar{C}_3 &= A_{37} + A_{38}S_1(\beta) \\ \bar{C}_4 &= A_{39} + A_{40}S_1(\beta) & \bar{C}_5 &= A_{44} + A_{45}S_1(\beta), & \bar{C}_6 &= A_{42} + A_{43}S_1(\beta) \\ \bar{C}_7 &= A_{29}, & \bar{C}_8 &= A_{27}, & \bar{C}_9 &= A_{28} \end{aligned} \tag{A.5}$$

The coefficients $A_{1.....45}$ are given in the Appendix part of Demir and Yigit [38] paper.

References

[1] Hanao M, Kawamoto M, Yamanaka, A. Growth of solidified shell just below the meniscus in continuous casting mold. ISIJ International, 2009; 49(3): 365-374. <https://doi.org/10.2355/isijinternational.49.365>

- [2] Yigit F, Barber J. Effect of Stefan number on thermoelastic instabilities in unidirectional solidification. *International Journal of Mechanical Sciences*, 1994; 36(8): 707-723. [https://doi.org/10.1016/0020-7403\(94\)90087-6](https://doi.org/10.1016/0020-7403(94)90087-6)
- [3] Konishi J, Militzer M, Samarasekera IV, Brimacombe JK. Modeling the formation of longitudinal facial cracks during continuous casting of hypoperitectic steel. *Metallurgical and Materials Transactions B*, 2002; 33(3): 413-423. <https://doi.org/10.1007/s11663-002-0053-y>
- [4] Demir MH. (2016) Thermoelastic stability analysis of solidification of pure metals on a coated planar mold of finite thickness: effects of the coating layer. Ph. D. Dissertation, Yildiz Technical University, Istanbul. <https://doi.org/10.1007/s11663-016-0876-6>
- [5] Stefan J. Über die Theorie Der Eisbildung, insbesondere Über die Eisbildung im Polarmeere. *Annalen der Physik*, 1891; 278(2): 269-286. <https://doi.org/10.1002/andp.18912780206>
- [6] Evans GW. A note on the existence of a solution to a problem of Stefan. *Quarterly of Applied Mathematics*, 1951; 9(2): 185-193. <https://doi.org/10.1090/qam/43330>
- [7] Douglas J. A uniqueness theorem for the solution of a Stefan problem. *Proceedings of the American Mathematical Society*, 1957; 8(2): 402-402. <https://doi.org/10.1090/S0002-9939-1957-0092086-6>
- [8] Crank J. *Free and moving boundary problems*, Oxford University Press, UK, 1987.
- [9] Hill JM. *One-dimensional Stefan problems: An introduction*, Longman Sc & Tech., USA, 1987.
- [10] Barry SI, Counce J. Exact and numerical solutions to a Stefan problem with two moving boundaries. *Applied Mathematical Modelling*, 2008; 32(1): 83-98. <https://doi.org/10.1016/j.apm.2006.11.004>
- [11] Song T, Upreti K, Subbarayan G. A sharp interface isogeometric solution to the Stefan problem. *Computer Methods in Applied Mechanics and Engineering*, 2015; 284: 556-582. <https://doi.org/10.1016/j.cma.2014.10.013>
- [12] Reutskiy S. A meshless method for one-dimensional Stefan problems. *Applied Mathematics and Computation*, 2011; 217(23): 9689-9701. <https://doi.org/10.1016/j.amc.2011.04.053>
- [13] Juric D, Tryggvason G. A front-tracking method for dendritic solidification. *Journal of Computational Physics*, 1996; 123(1): 127-148. <https://doi.org/10.1006/jcph.1996.0011>
- [14] Murray WD, Landis F. Numerical and machine solutions of transient heat-conduction problems involving melting or freezing: Part I-Method of analysis and sample solutions. *Journal of Heat Transfer*, 1959; 81(2): 106-112. <https://doi.org/10.1115/1.4008149>
- [15] Segal G, Vuik K, Vermolen F. A conserving Discretization for the free boundary in a two-dimensional Stefan problem. *Journal of Computational Physics*, 1998; 141(1): 1-21. <https://doi.org/10.1006/jcph.1998.5900>
- [16] Kutluay S, Bahadır A, Özdeş A. The numerical solution of one-phase classical Stefan problem. *Journal of Computational and Applied Mathematics*, 1997; 81(1): 135-144. [https://doi.org/10.1016/S0377-0427\(97\)00034-4](https://doi.org/10.1016/S0377-0427(97)00034-4)
- [17] Caldwell J, Savovic' S, Kwan Y. Nodal integral and finite difference solution of one-dimensional Stefan problem. *Journal of Heat Transfer*, 2003; 125(3): 523-527. <https://doi.org/10.1115/1.1565091>
- [18] Caldwell J, Kwan Y. Numerical methods for one-dimensional Stefan problems. *Communications in Numerical Methods in Engineering*, 2004; 20: 535-545. <https://doi.org/10.1002/cnm.691>
- [19] Chen S, Merriman B, Osher S, Smerka P. A simple level set method for solving Stefan problems. *Journal of Computational Physics*, 1997; 135(1): 8-29. <https://doi.org/10.1006/jcph.1997.5721>

- [20] Font F. A one-phase Stefan problem with size-dependent thermal conductivity. *Applied Mathematical Modelling*, 2018; 63: 172-178. <https://doi.org/10.1016/j.apm.2018.06.052>
- [21] Mackenzie J, Robertson M. A moving mesh method for the solution of the one-dimensional phase-field equations. *Journal of Computational Physics*, 2002; 181(2): 526-544. <https://doi.org/10.1006/jcph.2002.7140>
- [22] Sun Y, Beckermann C. Sharp interface tracking using the phase-field equation. *Journal of Computational Physics*, 2007; 220(2): 626-653. <https://doi.org/10.1016/j.jcp.2006.05.025>
- [23] Vynnycky M, Mitchell S. On the numerical solution of a Stefan problem with finite extinction time. *Journal of Computational and Applied Mathematics*, 2015; 276: 98-109. <https://doi.org/10.1016/j.cam.2014.08.023>
- [24] Myers T, Mitchell S. Application of the combined integral method to Stefan problems. *Applied Mathematical Modelling*, 2011; 35(9): 4281-4294. <https://doi.org/10.1016/j.apm.2011.02.049>
- [25] Zabaras N, Mukherjee S. An analysis of solidification problem by the boundary element method. *International Journal for Numerical Methods in Engineering*, 1987; 24: 1879-1900. <https://doi.org/10.1002/nme.1620241006>
- [26] Dursunkaya Z, Nair S. Solidification of a finite medium subject to a periodic variation of boundary temperature. *Journal of Applied Mechanics*, 2003; 70(5): 633-637. <https://doi.org/10.1115/1.1604836>
- [27] Skrzypczak T, Węgrzyn-Skrzypczak E. Mathematical and numerical model of solidification process of pure metals. *International Journal of Heat and Mass Transfer*, 2012; 55(15-16): 4276-4284. <https://doi.org/10.1016/j.ijheatmasstransfer.2012.03.070>
- [28] Caldwell J, Kwan Y. On the perturbation method for the Stefan problem with time-dependent boundary conditions. *International Journal of Heat and Mass Transfer*, 2003; 46(8): 1497-1501. [https://doi.org/10.1016/S0017-9310\(02\)00415-5](https://doi.org/10.1016/S0017-9310(02)00415-5)
- [29] Yu Z, Fan L, Hu Y, Cen K. Perturbation solution to heat conduction in melting or solidification with heat generation. *Heat and Mass Transfer*, 2010; 46(4): 479-483. <https://doi.org/10.1007/s00231-010-0596-4>
- [30] Yigit F. A simplified analytical solution of a two-dimensional Stefan problem with a periodic boundary condition. *International Review of Mechanical Engineering*, 2007; 1: 703-714.
- [31] Yigit F. Perturbation solution for solidification of pure metals on a sinusoidal mold surface. *International Journal of Heat and Mass Transfer*, 2007; 50(13-14): 2624-2633. <https://doi.org/10.1016/j.ijheatmasstransfer.2006.11.023>
- [32] Yigit F. Approximate analytical and numerical solutions for a two-dimensional Stefan problem. *Applied Mathematics and Computation*, 2008; 202(2): 857-869. <https://doi.org/10.1016/j.amc.2008.03.033>
- [33] Yigit F. Sinusoidal perturbation solution for solidification of pure materials on a planar mold of finite thickness. *International Journal of Thermal Sciences*, 2008; 47: 25-34. <https://doi.org/10.1016/j.ijthermalsci.2007.01.016>
- [34] Sanz A. Tribological behavior of coatings for continuous casting of steel. *Surface and Coating Technology*, 2001; 146-147: 55-64. [https://doi.org/10.1016/S0257-8972\(01\)01475-X](https://doi.org/10.1016/S0257-8972(01)01475-X)
- [35] Jafari H, Idris MH, Ourdjini A, Karimian M, Payganeh G. Influence of gating system, sand grain size, and mould coating on microstructure and mechanical properties of thin-wall ductile iron. *Journal of Iron and Steel Research International*, 2010; 17(12): 38-45. [https://doi.org/10.1016/S1006-706X\(10\)60195-1](https://doi.org/10.1016/S1006-706X(10)60195-1)
- [36] Karimian M, Ourdjini A, Hasbullah Idris M, Jafari H. Effect of pattern coating thickness on characteristics of lost foam Al-Si-Cu alloy casting. *Transactions of Nonferrous Metals*

- Society of China, 2012; 22(9): 2092-2097. [https://doi.org/10.1016/S1003-6326\(11\)61433-7](https://doi.org/10.1016/S1003-6326(11)61433-7)
- [37] Hamasaiid A, Dargusch M, Davidson C, Tovar S, Loulou T, Rezaï-Aria F, Dour G. Effect of mold coating materials and thickness on heat transfer in permanent mold casting of aluminum alloys. *Metallurgical and Materials Transactions A*, 2007; 38(6): 1303-1316. <https://doi.org/10.1007/s11661-007-9145-2>
- [38] Demir MH, Yigit F. Uncoupled modeling of the effects of coating layer on the growth instability in pure metal solidification. *International Journal of Metalcasting*, 2021; 15, 326-337. <https://doi.org/10.1007/s40962-020-00470-x>
- [39] Demir MH, Yigit F. Effect of coating material on the growth instability in solidification of pure metals on a coated planar mold of finite thickness. *International Journal of Solids and Structures*, 2016; 99: 12-27. <https://doi.org/10.1016/j.ijsolstr.2016.08.010>
- [40] Demir MH, Yigit F. Thermoelastic stability analysis of solidification of pure metals on a coated planar mold of finite thickness, *Metallurgical and Materials Transactions B*, 2017; 48 (2), 966-982. <https://doi.org/10.1007/s11663-016-0876-6>
- [41] Demir MH, Yigit F. A theoretical heat transfer model for unidirectional solidification of pure metals on a coated sinusoidal mold with constant boundary temperature. *Arabian Journal for Science and Engineering*, 2019; 44(6): 5825-5837. <https://doi.org/10.1007/s13369-019-03736-7>



Research Article

Evaluation of mechanical properties for banana-carbon fiber reinforced nano-clay epoxy composite using analytical modeling and simulation

Tanvi Saxena^{*a}, V.K. Chawla^b

Department of Mechanical and Automation Engineering, Indira Gandhi Delhi Technical University for Women, Kashmere Gate, Delhi, India

Article Info

Abstract

Article history:

Received 19 Feb 2022

Revised 18 Jun 2022

Accepted 17 Aug 2022

Keywords:

Analytical models;
Composite material;
Effective elastic
properties;
Nano-clay;
Natural fibers

Nano-fillers are bringing impeccable development in the area of materials science and natural fibers reinforced composites. In this study, a composite consisting of banana-carbon fiber reinforced epoxy matrix filled with 1%, 3%, and 5% weight percentage of nano-clay particles (NC) and carrying a transverse load is investigated for its mechanical and elastic properties. Nano-clay layer with interphase are arranged in layers called nano-clay platelets. The elastic properties such as longitudinal elastic modulus, transverse elastic modulus, in-plane Poisson's ratio, in-plane and out-of-plane shear modulus for the proposed composite are calculated by using different analytical models namely, Mori-Tanaka, Bridging, Generalized Self-Consistent, and Modified Halpin-Tsai model. The strength and deformation of the proposed composite are analyzed by using the ANSYS APDL application. The proposed composite is modeled using two layers of banana fibers, two layers of carbon fiber, and one layer of nano-clay platelet. The fibers and nano-clay platelet are arranged in a specific sequence of banana fiber at 90°, carbon fiber at 0°, nano-clay platelet at 90°, carbon fiber at 0°, and banana fiber at 90°. The proposed composite reinforced with 3% nano-clay is showing the least deformation as compared to 1% and 5% reinforcement. It is also observed that the modified Halpin-Tsai model outperforms all the other models as it is yielding the most effective elastic properties for the proposed composite and Mori-Tanaka model is found to be the least effective model for the calculation of elastic features of the proposed composite. Additionally, the hybridization effect for the composite is also calculated to analyze the tensile failure strain characteristics for banana and carbon fibers in the hybrid composite.

© 2022 MIM Research Group. All rights reserved.

1. Introduction

Banana fibers come under the category of bast fibers and find applications in automobile and aviation industries due to their availability, high rigidity, and fire-defiant features [1-3, 10]. Natural fibers reinforced green composites are being extensively used these days due to their excellent features and eco-friendly aspect [15, 16]. For attaining sustainable development, Green Operations Management (GOM) is gaining wide attention from community [32]. Banana fibers blended with carbon fibers reinforced composites improves ductility and imparts high degree of flexibility. Carbon fibers due to their high strength and lightweight attributes find wide applications in aerospace, cycles, motorcycles, etc., where high strength-to-weight ratios are required [4]. Research has been carried out on enhancing the physical features of composites. Mechanical features of the composite like tensile, bending, and crushing strength get enhanced by increasing the

*Corresponding author: tanvi002phd18@igdtuw.ac.in

^aorcid.org/0000-0002-3229-6294; ^borcid.org/0000-0001-7386-1838

DOI: <http://dx.doi.org/10.17515/resm2022.403me0219>

Res. Eng. Struct. Mat. Vol. 8 Iss. 4 (2022) 773-798

core diameter of the composite structure [5]. A new invariant-based technique for describing the elastic features and failure of composites and laminates was found to be commendable in enhancing the design and manufacturing of carbon/epoxy composites [27, 28].

In the past few decades, nano-composites have witnessed a tremendous growth in gaining the attention of researchers. It is observed that among various nano-fillers reinforced natural fiber composites, the most favorable and encouraging nano-composite could be the one reinforced with nano-clay consisting of silicate MMT(montmorillonite) layers [4, 6]. Nano-clays have certain remarkable features like large aspect ratio and large surface exposure that can improve the mechanical features of the polymer. The infusion of 6 wt% of nano-clay particles into banana fibers with the help of alkaline (NaOH) chemical analysis gives superior tensile, thermal, and interfacial properties as compared to untreated banana fibers. A threefold rise in tensile modulus and a 53% rise in tensile strength were noticed in nano-clay-blended treated banana fibers over untreated banana fibers [7]. The nano-clay particles blended banana fibers blended epoxy polymer composites resulted in a rise of 25% in Young's modulus, 11% in yield stress, and 26% in ultimate tensile strength when compared with untreated banana fibers blended epoxy composite [8]. The mechanical strength of nano-clay filled carbon fiber reinforced interpenetrating polymer networks (IPN) matrix composite was studied by varying the percentage of nano-clay to 0%, 1%, 3%, 5%, 7% & 9%. The inclusion of nano-clay enhances the mechanical strength of the composite to many folds but only up to 5% nano-clay addition. Beyond that, 7% and 9% nano-clay infusion showed a decline in mechanical strength [9].

The factors that affect the structure of nanomaterials are very complicated. The factors include the substance type, particle size, arrangement of nano-crystals, and preparation methods. The structure of nanomaterials can be divided into two categories: the first type is composed of two forms of structure that consist of particles and grain boundaries, and all structural components have the size in nanometers [11]. The second type of nanomaterial has a less dense random network of structure material having numerous nano-sized cavities. The whole layout has nano crystalline fragments and nano systems. A continuum non-local modified gradient theory was proposed and found to be suitably implemented for examining nanoscopic static and dynamic behaviour of nano-sized elastic beams [17]. A non-local gradient theory of elasticity theory was proposed which found to be beneficially employed in the severe analysis of nano-technological devices [18]. A higher order elasticity theory was found to be utilized effectively for characterizing advanced nano-materials and structural components of nano-systems [19]. The non-local modified gradient elasticity theory was found to be suitable for providing a practical outlook to the nanoscopic examination of the field variables [20].

Numerical method approach have been used by the researchers for evaluating Young's modulus of a nano-clay particle blended nano-composite [21], simulation methods [22-25], or using both together [26]. Numerical procedures are being opted more nowadays due to the advancement of computational techniques; however analytical methods are always preferred first for multivariable problems [26, 31]. Experimental work has other limitations also like, considering all aspects of well-defined systems, like particle dimensions, particle distribution, and shape arrangements. The mechanical features of composites can be achieved better using analytical modeling methods [29]. Continuum micromechanical models like Halpin-Tsai [12], ROM [13, 14, 30], have been used successfully for determining equivalent elastic properties of polymer silicate nano-composites and structural study of micro composites.

From the above literature, it is evident that the composite of banana-carbon fiber and epoxy matrix blended with nano-clay particles had never been explored for its elastic and mechanical properties. Also, the value of the hybridization effect for the proposed composite has never been calculated before by any researcher. Therefore, to bridge the aforementioned research gaps, in this paper following research problems are addressed.

- A new composite banana-carbon fiber reinforced epoxy matrix filled with different weight percentages of nano-clay particles carrying a transverse load of 200KN (along -z direction) is modeled in ANSYS APDL.
- The elastic and mechanical features for the newly proposed composite are calculated by employing the Mori-Tanaka, Bridging, Generalized Self-Consistent, and Modified Halpin-Tsai model.
- The strength and deformation of the proposed composite reinforced with 1%, 3%, and 5% of nano-clay particles are analyzed at different orientation angles by using the ANSYS APDL application.
- The hybridization effect for the composite is also calculated to analyze the tensile failure strain for high and low elongation fibers for the proposed composite.

2. Background

2.1. Modeling of the Banana-Carbon Fiber-Reinforced Nano-Clay Epoxy Composite

The layers of banana fiber, carbon fiber, and nano-clay layers along with interphase are arranged to form a sandwich intercalated composite structure. Epoxy is used as a matrix. Intercalated nano-composite has a single layer of interphase, while exfoliated has two. Clay particles are arranged in layers composed of silicate platelets (having nano-thickness) and an interphase layer. The interphase layer is naturally developed due to physical interactions between the nano-clay and polymer matrix [71]. Nano-clay platelet is 0.5mm thick and length of the nano-clay platelet and interphase are considered as same (Fig. 2). The average particle size of nano-clay particles is between 50-100nm [33].

Both numerical homogenization and analytical models have been used consequently for determining the mechanical features of the nano-composite [16, 34]. Depending upon the structure and chemical constitution of nano-particles, nano-clay can be classified into various categories like illite, bentonite, kaolinite, and montmorillonite. Homogenization micromechanical models like Mori-Tanaka (M-T) [35, 36, 67], self-consistent [37, 34], and Lielen's model [38] have been employed for computing various properties of short fiber composites. Self-consistent and Mori-Tanaka models were employed for short fiber composites and the M-T model was found to give the best values for fillers with a large aspect ratio. For higher fiber volume fractions and strength parameters, Lielen's model [38] proved to be better than the M-T model.

3. Analytical Modeling Methods

The proposed composite is designed using semi-empirical and homogenization models, by varying the composition percentage of nano-clay and epoxy while keeping the percent weight of banana and carbon fiber fixed as given in Table 1. The elastic features of carbon and banana fiber, epoxy, and nano-clay are given in Table 2. The volume fractions of the fibers, matrix, and filler are evaluated using the following equations [3] and are given in Table 3. The volume fraction of the interphase is about one percent of the volume fraction of the nanoparticle [72].

$$V_{fb/mx/NC} = \frac{W_{fb/mx/NC}}{\rho_{fb/mx/NC}} \times \rho_C \tag{1}$$

Where

$$\rho_C = \frac{1}{\frac{W_{CF}}{\rho_{CF}} + \frac{W_{BF}}{\rho_{BF}} + \frac{W_{EP}}{\rho_{EP}} + \frac{W_{NC}}{\rho_{NC}}} \tag{2}$$

3.1. Homogenization Models

Analytical homogenization models depend on the comprehensive mechanical performance of the composite structure that belongs to the macroscopic frame and heterogeneous microscopic frame of materials (e.g. composition, properties, shape, volume fraction, inclination, etc.) [45]. Homogenization models aim to obtain the stress, and strain behavior at the microscopic and macroscopic frames [46, 47].

3.1.1. Mori-Tanaka Model

The Mori-Tanaka model was originally formed by [35]. This model is reckoned for developing various kinds of composite systems. This model uses the theory of Eshelby inclusion. The aim is to define the average behaviors of the fiber and matrix. As reported in [48], the longitudinal and transverse Young's moduli, in & out-of-plane moduli of rigidity, and in-plane Poisson's ratio is given by equations.

Table 1. Weight percentages of fibers, matrix, and nano-clay

Sequence	Banana fiber (%)	Carbon fiber (%)	Epoxy (%)	Nano-clay (%)
I	20	60	19	1
II	20	60	17	3
III	20	60	15	5

Table 2. Elastic features of fibers, matrix, nano-clay, and interphase

Properties	Carbon fiber [42]	Banana fiber [42]	Epoxy [43]	Nano-clay [44]	Interphase [44]
$E_1^{fb/mx} =$ (GPa)	230	3.48	35	$E_{NC} = 176$	$E_{IP} = 11.6$
$E_{22}^{fb} = E_{33}^{fb}$ (GPa)	15	---	---	---	---
$G_{12}^{fb/mx} =$ (GPa)	15	1.58	0.32	$G_{NC} = 70.4$	$G_{IP} = 4.55$
$G_{13}^{fb/mx}$ (GPa)	7	---	---	---	---
G_{23}^{fb} (GPa)	7	---	---	---	---
$\nu_{12}^{fb/mx} = \nu_{31}^{fb/mx}$	0.2	0.28	0.35	$\nu_{NC} = 0.25$	$\nu_{IP} = 0.275$
ν_{23}^{fb}	0.07	---	---	---	---
$\rho^{fb/mx}$ (kg/m ³)	2260	1350	1270	1980	1590

Table 3. Evaluated volume fractions of the fibers, matrix, nano-clay, and interphase

Sequence	Carbon (CF)	Banana (BF)	Epoxy	Nano-clay (NC)	Interphase (IP)
	V_{CF}	V_{BF}	V_{EP}	V_{NC}	V_{IP}
I	0.47	0.26	0.26	8.89×10^{-3}	8.89×10^{-5}
II	0.47	0.26	0.24	0.027	2.7×10^{-4}
III	0.48	0.27	0.21	0.045	4.53×10^{-4}

$$E_1 = V_{fb}E_1^{fb} + (1 - V_{fb})E^{mx} + 2V_{fb}(1 - V_{fb})Z_1(v_{12}^{fb} - v^{mx})^2 \tag{3}$$

$$E_2 = \frac{E_1}{[1 - (v^{mx})^2](Y_1 + Y_2)} \tag{4}$$

$$v_{12} = v^{mx} + 2V_{fb} \frac{Z_1}{E^{mx}} (v_{12}^{fb} - v^{mx})[1 - (v^{mx})^2] \tag{5}$$

$$G_{12} = \frac{E^{mx}}{2(1 - V_{fb})(1 + v^{mx})} \left[1 + V_{fb} - \frac{4V_{fb}}{1 + V_{fb} + 2(1 - V_{fb}) \frac{G_{12}^{fb}}{E^{mx}} (1 + v^{mx})} \right] \tag{6}$$

$$G_{23} = E^{mx} \left[2(1 + v^{mx}) + \frac{V_{fb}}{\frac{1 - V_{fb}}{8[1 - (v^{mx})^2]} + \frac{G_{23}^{fb}}{E^{mx} - 2G_{23}^{fb}(1 + v^{mx})}} \right]^{-1} \tag{7}$$

Where:

$$Y_1 = V_{fb}Z_1 \left(\frac{E_1^{fb}}{E^{mx}} \right) \left[\frac{1 + v^{mx}}{E^{mx}} - \frac{2}{E_1^{fb}} + \frac{1 + v_{23}^{fb}}{E_2^{fb}} \right] \tag{8}$$

$$Y_2 = \frac{1}{1 - (v^{mx})^2} + 2V_{fb} \left(\frac{E_1}{Z_2} \right) \left[1 + v_{23}^{fb} - \frac{E_2^{fb}}{E^{mx}} (1 - v^{mx}) \right] \tag{9}$$

$$Z_1 = \left\{ -2(1 - V_{fb}) \frac{(v_{23}^{fb})^2}{E_1^{fb}} + (1 - V_{fb}) \frac{1 - v_{23}^{fb}}{E_2^{fb}} + \frac{(1 + v^{mx})[1 + V_{fb}(1 - 2v^{mx})]}{E^{mx}} \right\} \tag{10}$$

$$Z_2 = E_2^{fb}(3 + V_{fb} - 4v^{mx})(1 + v^{mx}) + (1 - V_{fb})E^{mx}(1 + v_{23}^{fb}) \tag{11}$$

Thus for 1% nano-clay, the elastic features of the banana-carbon fiber-reinforced nano-clay epoxy composite can be evaluated using Eqs. (3)-(7):

$$E_1 = 119797.9MPa$$

Where: $Z_{1CF} = 16638.9$; $Z_{1BF} = 52356$; $Z_{1NC} = 2586.9$; $Z_{1IP} = 28423.25$ (Values calculated using Eq. (10))

$$E_2 = 1.7100 \times 10^{13}MPa; v_{12} = 0.24$$

Where: $Y_{1CF} = 5.2$; $Y_{2CF} = 4$ (Values calculated using Eq. (8) & (9))

$$G_{12} = 13882.08MPa + G_{NCP,12} = 13882.08MPa + 6.92 \times 10^6 = 6.93 \times 10^6MPa$$

$$G_{23} = 10485.6MPa + G_{NCP,23}$$

$$= 10485.6MPa + 6.92 \times 10^6MPa = 6.93 \times 10^6MPa$$

Likewise, similar elastic properties of the proposed composite are evaluated for 3% and 5% nano-clay and are given in Table 4.

3.1.2. Generalized Self-Consistent Model

The generalized self-consistent (GS-C) model was initially evolved by [49, 34] to determine the elastic features of isotropic spherical inclusions blended composite materials. This model can be further utilized to find out the elastic features of short fiber composites [50, 68]. In this model, a particulate having elastic properties of short fiber is supposed to be placed in a homogenous medium, where the surrounding medium has the undetermined elastic features of the composite that requires to be solved.

$$E_1 = E_1^{fb}V_{fb} + E^{mx}(1 - V_{fb}) + \frac{4V_{fb}(1 - V_{fb})(v_{12}^{fb} - v^{mx})^2}{\frac{(1-V_{fb})}{K_{23}^{fb}} + \frac{V_{fb}}{K_{23}^{mx}} + \frac{1}{G^{mx}}} \tag{12}$$

$$v_{12} = v_{12}^{fb}V_{fb} + v^{mx}(1 - V_{fb}) + \frac{V_{fb}(1 - V_{fb})(v_{12}^{fb} - v^{mx})\left(\frac{1}{K_{23}^{mx}} - \frac{1}{K_{23}^{fb}}\right)}{\frac{(1-V_{fb})}{K_{23}^{fb}} + \frac{V_{fb}}{K_{23}^{mx}} + \frac{1}{G^{mx}}} \tag{13}$$

$$K_{23} = K_{23}^{mx} + \frac{V_{fb}}{\frac{1}{K_{23}^{fb}-K_{23}} + \frac{1-V_{fb}}{K_{23}^{mx}+G^{mx}}} \tag{14}$$

$$G_{12} = G^{mx} \frac{G_{12}^{fb}(1 + V_{fb}) + G^{mx}(1 - V_{fb})}{G_{12}^{fb}(1 - V_{fb}) + G^{mx}(1 + V_{fb})} \tag{15}$$

$$G_{23} = G^{mx} \left(\frac{-B + \sqrt{B^2 - 4AC}}{2A} \right) \tag{16}$$

Where:

$$A = a_0 + a_1V_{fb} + a_2V_{fb}^2 + a_3V_{fb}^3 + a_4V_{fb}^4 \tag{17}$$

$$B = b_0 + b_1V_{fb} + b_2V_{fb}^2 + b_3V_{fb}^3 + b_4V_{fb}^4 \tag{18}$$

$$C = c_0 + c_1V_{fb} + c_2V_{fb}^2 + c_3V_{fb}^3 + c_4V_{fb}^4 \tag{19}$$

Where:

$$a_0 = -2(G^{mx})^2(2G^{mx} + K^{mx})[2G_{23}^{fb}G^{mx} + K_{23}^{fb}(G_{23}^{fb} + G^{mx}) + G^{mx}]\{2G_{23}^{fb}G^{mx} + K^{mx}(G_{23}^{fb} + G^{mx})\} \tag{20}$$

$$a_1 = 8(G^{mx})^2(G_{23}^{fb} - G^{mx})[2G_{23}^{fb}G^{mx} + K_{23}^{fb}(G_{23}^{fb} + G^{mx})][(G^{mx})^2 + G^{mx}K^{mx} + (K^{mx})^2] \tag{21}$$

$$a_2 = -12(G^{mx})^2(K^{mx})^2(G_{23}^{fb} - G^{mx})[2G_{23}^{fb}G^{mx} + K_{23}^{fb}(G_{23}^{fb} + G^{mx})] \tag{22}$$

$$a_3 = 8(G^{mx})^2[(G_{23}^{fb}G^{mx})^2K_{23}^{fb} + (G_{23}^{fb})G^{mx}K^{mx}(K_{23}^{fb} - G^{mx}) + (K^{mx})^2\{G_{23}^{fb}G^{mx}(G_{23}^{fb} - 2G^{mx}) + K_{23}^{fb}(G_{23}^{fb} - G^{mx})(G_{23}^{fb} + G^{mx})\}] \tag{23}$$

$$a_4 = 2(G^{mx})^2(G_{23}^{fb} - G^{mx})(2G^{mx} + K^{mx})[K_{23}^{fb}G^{mx}K^{mx} - G_{23}^{fb}(2G^{mx}(K_{23}^{fb} - K^{mx}) + K_{23}^{fb}K^{mx})] \quad (24)$$

$$b_0 = 4(G^{mx})^3[2G_{23}^{fb}G^{mx} + K_{23}^{fb}(G_{23}^{fb} + G^{mx})][2G_{23}^{fb}G^{mx} + K^{mx}(G_{23}^{fb} + G^{mx})] \quad (25)$$

$$b_1 = 8(G^{mx})^2K^{mx}(G_{23}^{fb} - G^{mx})[2G_{23}^{fb}G^{mx} + (G_{23}^{fb} + G^{mx})K_{23}^{fb}](G^{mx} - K^{mx}) \quad (26)$$

$$b_2 = -2a_2 \quad (27)$$

$$b_3 = -2a_3 \quad (28)$$

$$b_4 = -4(G^{mx})^3(G_{23}^{fb} - G^{mx})[K_{23}^{fb}G^{mx}K^{mx} - G_{23}^{fb}\{2G^{mx}(K_{23}^{fb} - K^{mx}) + K_{23}^{fb}K^{mx}\}] \quad (29)$$

$$c_1 = 8(G^{mx}K^{mx})^2(G_{23}^{fb} - G^{mx})[2G_{23}^{fb}G^{mx} + K_{23}^{fb}(G_{23}^{fb} + G^{mx})] \quad (30)$$

$$c_2 = a_2 \quad (31)$$

$$c_3 = a_3 \quad (32)$$

$$c_4 = -2(G^{mx})^2K^{mx}(G_{23}^{fb} - G^{mx})[K_{23}^{fb}G^{mx}K^{mx} - G_{23}^{fb}\{2G^{mx}(K_{23}^{fb} - K^{mx}) + K_{23}^{fb}K^{mx}\}] \quad (33)$$

Thus, with 1% nano-clay, the elastic features of the banana-carbon fiber-reinforced nano-clay epoxy composite can be evaluated using Eqs. (12)-(16):

$$E_1 = 119703.74MPa$$

Where:

$$K_{23}^{CF} = \frac{E}{3(1-2\mu)} = \frac{15000}{3(1-2 \times 0.07)} = 5814MPa; \text{ Similarly, } K_{23}^{BF} = 2636.4MPa,$$

$$K_{23}^{NC} = 117333.3MPa, K_{23}^{IP} = 12888.9MPa, K_{23}^{mx} = 38888.9MPa$$

$$\nu_{12} = 0.27; G_{12} = 8510.27MPa + G_{NCP,12} = 6.92 \times 10^6MPa$$

$$G_{23} = 65040650.2MPa + G_{NCP,23} = 7.2 \times 10^6MPa$$

Where: A, B, and C are calculated using Eqs. (17)-(19) and are given below:

$$A = -1.23 \times 10^{28}; B = -2.5 \times 10^{32}; C = -1.44 \times 10^{28}$$

Where:

$$a_0 = -2.43 \times 10^{28}, a_1 = 5.32 \times 10^{28}, a_2 = -7.35 \times 10^{28}, a_3 = 2.98 \times 10^{28}, a_4 = 2.89 \times 10^{27}$$

$$b_0 = 6 \times 10^{27}, b_1 = -4.5 \times 10^{28}, b_2 = 14.7 \times 10^{28}, b_3 = -5.96 \times 10^{28}, b_4 = -5.2 \times 10^{33}$$

$$c_0 = 1, c_1 = 4.9 \times 10^{28}, c_2 = -7.35 \times 10^{28}, c_3 = 2.98 \times 10^{28}, c_4 = -4.9 \times 10^{26} \text{ (Values calculated using Eqs. (20)-(33))}$$

Likewise, similar elastic properties of the proposed composite are evaluated for 3% and 5% nano-clay and are given in Table 4.

3.1.3. Bridging Model

The bridging micromechanical model (BM) was evolved by [51, 52] to determine the strength and rigidity of unidirectional composites. An easy version of this model was also developed [53] that gave closer results when compared to experimentally obtained values. The elastic features of the composite based on the bridging model are as follows [54]:

$$E_1 = E_1^{CF}V^{CF} + E_1^{BF}V^{BF} + E^{mx}V^{mx} + E^{NC}V^{NC} + E^{IP}V^{IP} \tag{34}$$

$$v_{12} = v_{12}^{CF}V^{CF} + v_{12}^{BF}V^{BF} + v^{mx}V^{mx} + v^{NC}V^{NC} + v^{IP}V^{IP} \tag{35}$$

$$E_2 = \frac{(V^{CF} + V^{mx}a_{11})(V^{CF} + V^{mx}a_{22})}{(V^{CF} + V^{mx}a_{11})(V^{CF}S_{22}^{CF} + a_{22}V^{mx}S_{22}^{mx}) + V^{CF}V^{mx}(S_{21}^{mx} - S_{21}^{CF})a_{12}} \tag{36}$$

Where:

$$S_{22} = \frac{1}{E_2}, S_{21} = \frac{-v_{21}}{E_2}, S_{23} = \frac{-v_{32}}{E_3} \tag{37}$$

$$a_{11} = \frac{E^{mx}}{E_1^{CF}}, a_{22} = a_{33} = a_{44} = 0.3 + 0.7 \left(\frac{E^{mx}}{E_2^{CF}} \right), a_{12} = \left(\frac{E_1^{CF}v^{mx} - E^{mx}v_{12}^{CF}}{E_1^{CF} - E^{mx}} \right) (a_{11} - a_{22}) \tag{38}$$

$$G_{12} = \frac{(V^{CF} + V^{mx}a_{66})G_{12}^{CF}G^{mx}}{V^{CF}G^{mx} + V^{mx}a_{66}G_{12}^{CF}} \tag{39}$$

$$G_{23} = \frac{0.5(V^{CF} + V^{mx}a_{44})}{V^{CF}(S_{22}^{CF} - S_{23}^{CF}) + V^{mx}a_{44}(S_{22}^{mx} - S_{23}^{mx})} \tag{40}$$

$$a_{66} = 0.3 + 0.7 \left(\frac{G^{mx}}{G_{12}^{CF}} \right) \tag{41}$$

Thus for 1% nano-clay, the elastic features of the banana-carbon fiber-reinforced nano-clay epoxy composite can be evaluated using equations (34)-(36):

$$E_1 = 119670.47MPa; v_{12} = 0.26$$

$$E_2 = 20609.87MPa$$

$$\begin{aligned} \because a_{11} &= 0.152, a_{22} = 1.933, a_{12} = -0.6713, S_{22}^{CF} = 6.67 \times 10^{-5}, S_{22}^{mx} = 2.86 \times 10^{-5}, \\ S_{21}^{mx} &= -1 \times 10^{-5}, S_{21}^{CF} = -8.69 \times 10^{-7} \\ &= 20609.87MPa + E_{NCP,22} \\ &= 1.7342 \times 10^{13}MPa \end{aligned}$$

$$G_{12} = 8645.6MPa$$

$$\begin{aligned} \because a_{66} &= 0.45 \\ &= 8645.6MPa + G_{NCP,12} \\ &= 6.93 \times 10^6MPa \end{aligned}$$

$$G_{23} = 9262.83MPa$$

$$\begin{aligned} \because a_{44} = a_{22} &= 1.933, S_{22}^{CF} = 6.67 \times 10^{-5}, S_{23}^{CF} = -4.67 \times 10^{-6}, S_{23}^{mx} \\ &= -1 \times 10^{-5}, S_{22}^{mx} = 2.86 \times 10^{-5} \end{aligned}$$

$$\begin{aligned}
 &= 9262.83MPa + G_{NCP,23} \\
 &= 6.93 \times 10^6 MPa
 \end{aligned}$$

Likewise, similar elastic properties of the proposed composite are evaluated for 3% and 5% nano-clay and are given in Table 4.

3.2. Semi-Empirical Model

Semi-empirical models also known as semi-physical models are found to rely on parameters having natural significance [55, 56]. Semi-empirical relations have corrected or fitting parameters that make design procedures simple and easy [57, 58]. A semi-empirical micromechanical model, also known as the modified Halpin-Tsai (Mod. H-T) model is developed by exhibiting the matrix modulus in terms of fiber diameter and by establishing an equivalent constant. This model helps in deciding the threshold weight and volume fraction of the inclusion so that the matrix modulus can be maintained more the needed level [56].

3.2.1. Modified Halpin-Tsai

This semi-empirical model was developed by Halpin-Tsai (Modified Halpin-Tsai) to rectify the Young's modulus in transverse direction as obtained by the rule of mixture method (ROM). A modified Halpin-Tsai method based on finite elemental research was suggested, considering the possibility of a numerous fiber arrangements [59]. The transverse Young's modulus and in-plane modulus of rigidity as proposed by [60] are given by:

$$E_2 = E^{mx} \left(\frac{1 + \xi_{E_2} \eta_{E_2} V^{CF}}{1 - \xi_{E_2} V^{CF}} \right) \tag{42}$$

$$G_{12} = G^{mx} \left(\frac{1 + \xi_{G_{12}} \eta_{G_{12}} V^{CF}}{1 - \eta_{G_{12}} V^{CF}} \right) \tag{43}$$

Where, $V^{CF} < 0.3$

$$\eta_{E_2} = \frac{\left(\frac{E_2^{CF}}{E^{mx}}\right) - 1}{\left(\frac{E_2^{CF}}{E^{mx}}\right) + \xi_{E_2}}; \xi_{E_2} = \{4.924 - 35.888V^{CF} + 125.118V^{CF^2} - 145.121V^{CF^3}\} \text{ if}$$

$$V_{CF} \geq 0.3; \xi_{E_2} = \{1.5 + 5500V^{CF^{18}} \text{ if } V_{CF} \geq 0.3$$

$$\eta_{G_{12}} = \frac{\left(\frac{G_{12}^{CF}}{G^{mx}}\right) - 1}{\left(\frac{G_{12}^{CF}}{G^{mx}}\right) + \xi_{G_{12}}}; \xi_{G_{12}} = 1 + 40V^{CF^{10}}$$

The longitudinal elastic modulus and in-plane Poisson's ratio will be the same as that in ROM.

$$E_1 = E_1^{CF} V^{CF} + E_1^{BF} V^{BF} + E^{mx} V^{mx} + E^{NC} V^{NC} + E^{IP} V^{IP} \tag{44}$$

$$v_{12} = v_{12}^{CF} V^{CF} + v_{12}^{BF} V^{BF} + v^{mx} V^{mx} + v^{NC} V^{NC} + v^{IP} V^{IP} \tag{45}$$

Thus for 1% nano-clay, the elastic features of the banana-carbon fiber-reinforced nano-clay epoxy composite can be evaluated using Eqs. (42)-(43) and Eqs. (44)-(45):

$$\eta_{E_2} = \frac{\left(\frac{15}{35}\right) - 1}{\left(\frac{15}{35}\right) + 1.5} = -1.1$$

$$\because \xi_{E_2} = 1.5 + 5500 \times 0.47^{18} = 1.5 (V^{CF} = 0.47)$$

$$\therefore E_2 = 5179.63 MPa + E_{NCP,22}$$

$$= 1.7342 \times 10^{13} MPa$$

$$\eta_{G_{12}} = \frac{\left(\frac{15000}{3200}\right) - 1}{\left(\frac{15000}{3200}\right) + 1.02} = 0.65$$

$$\because \xi_{G_{12}} = 1 + 40 \times 0.47^{10} = 1.02 (V^{CF} = 0.47)$$

$$\therefore G_{12} = 6034.13 MPa + G_{NCP,12}$$

$$= 6.94 \times 10^6 MPa$$

$$E_1 = 119670.47 MPa$$

$$v_{12} = 0.26$$

Likewise, similar elastic properties of the proposed composite are evaluated for 3% and 5% nano-clay and are given in Table 4.

3.3. Calculation of Elastic Properties for Nano-Clay Platelets

In an intercalated banana-carbon fiber-reinforced nano-clay epoxy composite, the nano-clay platelet is surrounded by a layer of interphase at the top surface, and epoxy is used as a binding medium. The relation between the thickness of silicate layer (t_{SL}), number of silicate sheets (N), and the interlayer gap between nano-clay platelets d_{gap} in composites are as follows [61].

$$t = (N - 1)d_{gap} + t_{SL} \tag{46}$$

The following formulae were proposed as per modified ROM for calculating elastic properties of nano-clay platelets (consisting of nano-clay and interphase) [62].

$$E_{NCP,11} = E_{NCP,33} = \chi_{NC}E_{NC} + \chi_{IP}E_{IP} \tag{47}$$

$$E_{NCP,22} = \frac{E_{NC}E_{IP}}{\chi_{NC}E_{IP} + \chi_{IP}E_{NC} - \chi_{NC}\chi_{IP}\beta E_{NC}E_{IP}} \tag{48}$$

$$v_{NCP,12} = v_{NCP,32} = \chi_{NC}v_{IP} + \chi_{IP}v_{NC} \tag{49}$$

$$v_{NCP,13} = \frac{\chi_{NC}v_{NC}E_{NC}(1 - v_{IP}^2) + \chi_{IP}v_{IP}E_{IP}(1 - v_{NC}^2)}{\chi_{NC}E_{NC}(1 - v_{IP}^2) + \chi_{IP}v_{IP}E_{IP}(1 - v_{NC}^2)} \tag{50}$$

$$G_{NCP,12} = G_{NCP,32} = \frac{G_{NC}G_{IP}}{\chi_{NC}G_{IP} + \chi_{IP}G_{NC} - \chi_{NC}\chi_{IP}\eta G_{NC}G_{IP}} \tag{51}$$

$$G_{NCP,13} = \frac{E_{NCP,11}}{2(1 + v_{NCP,13})} \tag{52}$$

Where:

$$\beta = \frac{v_{NC}^2 \frac{E_{IP}}{E_{NC}} + v_{IP}^2 \frac{E_{NC}}{E_{IP}} - 2v_{NC}v_{IP}}{\chi_{NC}E_{NC} + \chi_{IP}E_{IP}}$$

$$\eta = \frac{v_{NC}^2 \frac{G_{IP}}{G_{NC}} + v_{IP}^2 \frac{G_{NC}}{G_{IP}} - 2v_{NC}v_{IP}}{\chi_{NC}G_{NC} + \chi_{IP}G_{IP}}$$

For 1% nano-clay:

$$E_{NCP,22} = 1734.22 \times 10^{10} MPa$$

Where $\beta = 6.49 \times 10^{-4}$

$$G_{NCP,12} = G_{NCP,23} = 6.92 \times 10^6 MPa$$

Where:

$$\eta = 1.65 \times 10^{-3}$$

$$v_{NCP,13} = 0.27$$

4. Finite Element Work

4.1. Model Configuration

The composite sample is modeled and examined for its mechanical properties on ANSYS Mechanical APDL software. The sample measurements used in this examination are as per ASTM D3039 standards [42]: length of the sample = 30 mm, width of the sample = 200 mm and thickness of lamina = 0.5mm/layer. Number of sheets = 5.

The total depth of the samples = 2.5mm, Degree of Freedom = zero,

Both sides of the samples are constrained. After modeling the sample, it is meshed using a mesh tool. Number of mesh: Number of vertical element divisions = 20; Number of horizontal element division=15. Meshed model is shown in Fig. 1.

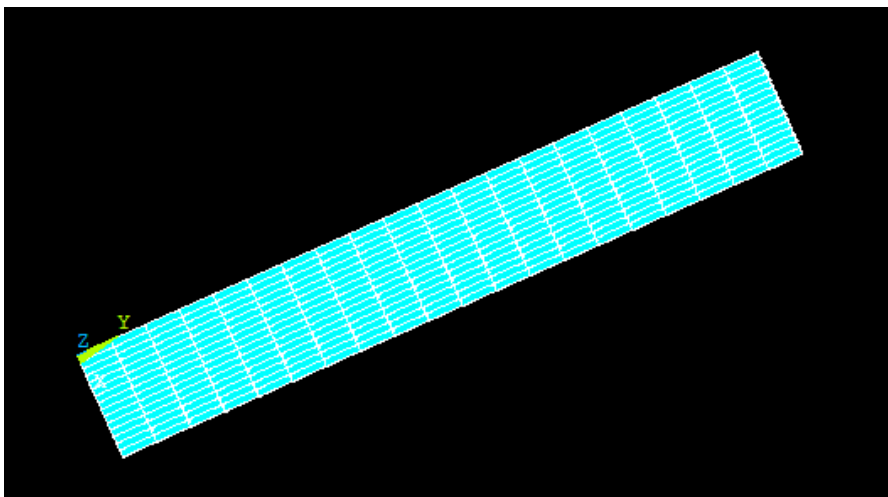


Fig. 1 Meshed model

4.2 Loads and Orientation of the Fibers

The examination of the properties is carried out by using element 3D 4 Shell 181. A point load of 200KN [42] is applied to the model at 21 nodes in a perpendicular direction (along -z axis) as shown in (Fig. 4). The sample is configured in the sequence of layers:

banana fiber - carbon fiber - nano-clay platelet - carbon fiber - banana fiber at orientation angles of 90°, 0°, 90°, 0°, and 90° respectively also portrayed in Fig. 2. The modeled layers in ANSYS APDL are shown in Fig. 3. The vector sum distortion for the proposed composite material is analysed for the proposed composite reinforced with 1%, 3%, and 5% nano-clay particles and is given in Table 4. The vector sum deformation plots developed by using the ANSYS APDL application for NC composition of 1%, 3% & 5% are also shown in Fig. 5.

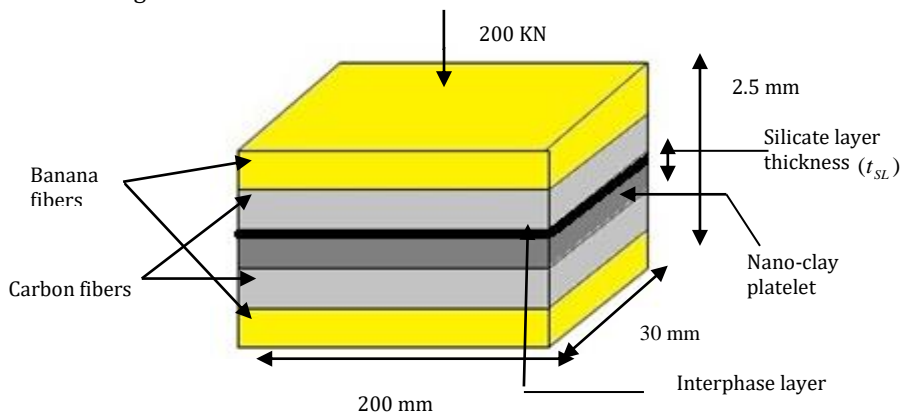


Fig. 2 Application of load on arrangement of fibers and nano-clay platelet.

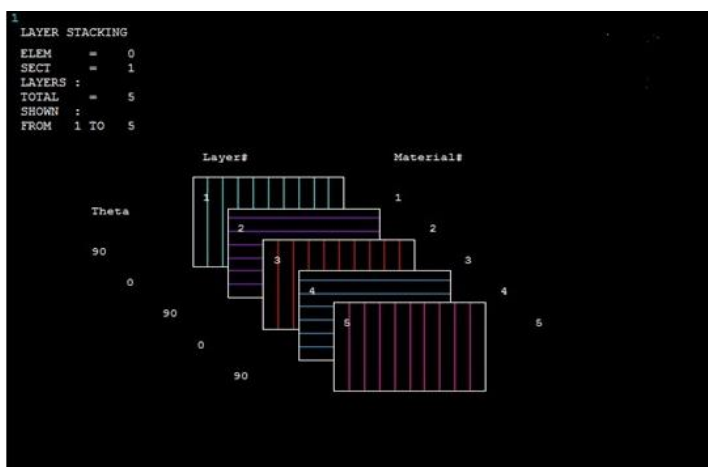


Fig. 3 Modelled layers in ANSYS APDL

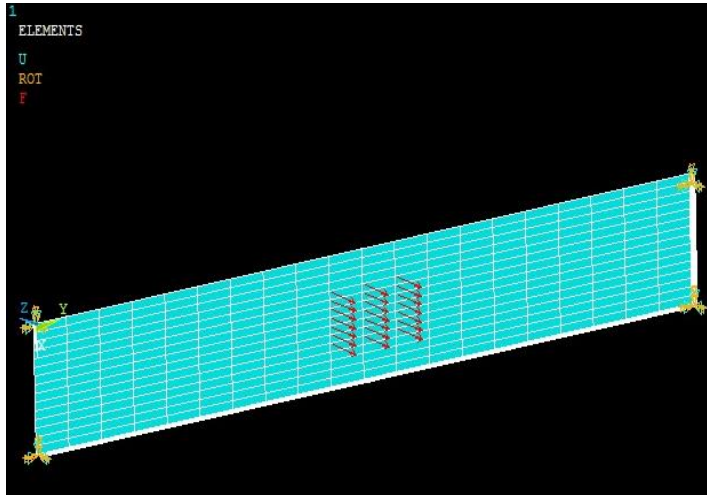
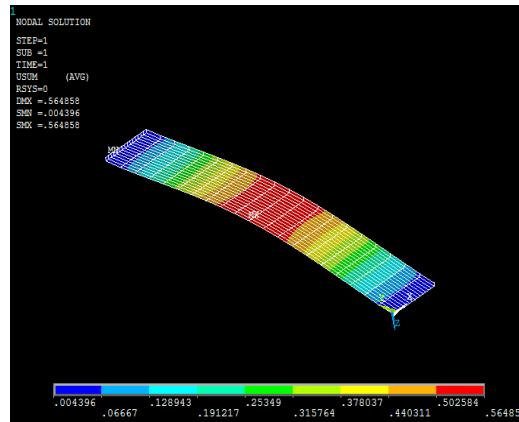
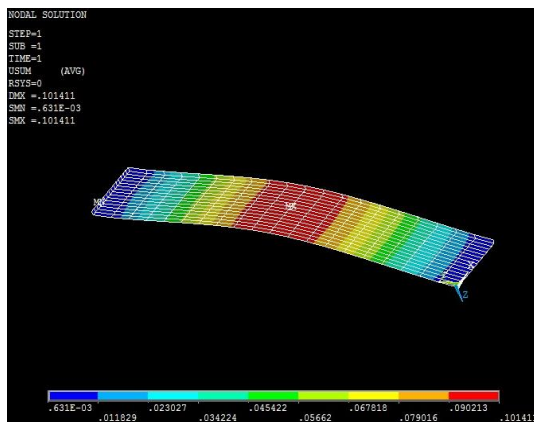


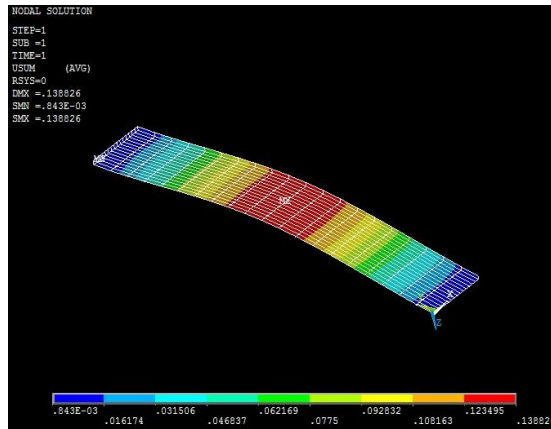
Fig. 4 FE model showing point load at 21 nodes (along -z axis)



(a)



(b)



(c)

Fig. 5 Vector sum deformation for banana-carbon fiber reinforced nano-clay epoxy composite having (a) 1 percent, (b) 3 percent and (c) 5 percent nano-clay.

Table 4. Elastic properties, vector sum deformation and FE model results for different percentages of NC filler in the proposed composite

Nano-clay %	Elastic Properties	Mori-Tanaka Model	Generalized Self-Consistent Model	Bridging Model	Modified Halpin-Tsai Model	Vector sum deformation from ANSYS(mm)	FE model
1%	E_1 (MPa)	119797.9	119703.74	119670.47	119670.47		116223.71
	ν_{12}	0.24	0.27	0.26	0.26		0.28
	E_2 (MPa)	1.7100×10^3	**	1.7342×10^{13}	1.7342×10^{13}	0.56485	1.6602×10^{13}
	G_{12} (MPa)	6.93×10^6	6.92×10^6	6.93×10^6	6.94×10^6		6.66×10^6
	G_{23} (MPa)	6.93×10^6	7.2×10^6	6.93×10^6	**		6.66×10^6
3%	E_1 (MPa)	122278.9	113792.3	122160	122160		117575.8
	ν_{12}	0.24	0.27	0.27	0.26		0.28
	E_2 (MPa)	3.86×10^5	**	3.97×10^5	392467.5	0.10141	3.67×10^5
	G_{12} (MPa)	7.02×10^6	7.02×10^6	7.02×10^6	7.03×10^6		6.75×10^6
	G_{23} (MPa)	7.02×10^6	6.12×10^6	7.02×10^6	**		6.75×10^6
5%	E_1 (MPa)	126742.3	130573.9	126614.8	126614.8		123050.7
	ν_{12}	0.25	0.26	0.26	0.26		0.27
	E_2 (MPa)	412231.3	**	402651.4	432231.2	0.13883	396376.2
	G_{12} (MPa)	8.11×10^6	8.11×10^6	8.11×10^6	8.20×10^6		7.87×10^6
	G_{23} (MPa)	8.11×10^6	7.09×10^6	8.11×10^6	**		7.87×10^6

5. Fiber Hybridization and Its Effect

The hybridization of fiber is a technique for improving the composite properties [63, 64]. The study of hybrid effect is significant in the analysis of the property of the proposed composite. The hybridization is important in understanding the behavior of the fibers in the hybrid composite. It, in general, predicts that the failure strain of a hybrid composite differs from the composites blended with either of the parent fibers alone. Fiber-hybrid composites are composed of high and low elongation fibers. In this study, high and low elongation fibers are banana and carbon fiber respectively. The outcome of placing a carbon fiber sheet in between glass fiber sheets was first reported by [65]. Carbon fiber layers failed in tension. The strain (ϵ_c) was noted to be increased by 40% (ϵ_c'). This increase is termed as the 'hybrid effect', that is normally expected for failure strain [65]. The hybrid effect (Eq. (53)) is the ratio of the failure strain of the hybrid composite to the failure strain of the low elongation fiber-blended composite [66].

$$\text{Hybridization effect} = \frac{\epsilon_c' - \epsilon_c}{\epsilon_c} \tag{53}$$

Where ϵ_c' = increased tensile strain of the hybrid composite at breaking point.

ϵ_c = tensile strain of the carbon fiber at breaking point.

The hybrid effect R_{hyb} as given by [66] is:

$$R_{hyb} = \frac{\bar{\epsilon}_{HEC}}{\bar{\epsilon}_{LEC}} = \sqrt{\frac{\bar{\epsilon}_{HEF}}{\bar{\epsilon}_{LEF}}} \left[\frac{\delta_h (k_h^q - 1)}{2\delta (k^q - 1)} \right]^{-1} \tag{54}$$

Where $\bar{\epsilon}_{LEF}$ = mean strain of the least elongated fiber at breaking point.

$\bar{\epsilon}_{HEF}$ = mean strain of the highest elongated fiber at breaking point.

q = Wei bulls shape parameter.

$$R_{hyb} = \left[\frac{\delta_h (k_h^q - 1)}{2\delta (k^q - 1)} \right]^{-1} \tag{55}$$

The ineffective length δ and δ_{\square} for the hybrid composite is given by [66]:

$$\delta = 1.531 \left(\frac{E_1 A_1 d}{gh} \right)^{1/2} \tag{56}$$

$$\delta_h = \frac{2}{\rho^{1/2}} \left(\frac{E_1 A_1 d}{Gh} \right)^{1/2} \frac{m_2^2 - m_1^2}{m_1(2 - m_1^2) - m_2(2 - m_2^2)} \tag{57}$$

Where: the ratio of fibers' extensional stiffness (ρ) is given by [66]:

$$\rho = \frac{E_1 A_1}{E_2 A_2}$$

$$\rho = \frac{3.48}{230} = 0.015$$

Where:

E_1A_1 = Denotative stiffness of LE fibers.

E_2A_2 = Denotative stiffness of HE fibers.

h= Matrix depth.

d= Fiber spacing.

G= Shear matrix modulus.

The strain and strain concentration parameters K and K_h respectively and a constant $m_{1,2}$ are given by [66]:

$$K = 1.293$$

$$K_h = 1 + \frac{m_2 - m_1}{m_1(2 - m_1^2) - m_2(2 - m_2^2)} \tag{58}$$

$$m_{1,2} = \left(\frac{\rho + 1 \pm (\rho^2 + 1)^{\frac{1}{2}}}{\rho} \right)^{\frac{1}{2}} \tag{59}$$

Substituting the value of ρ obtained above in Eq. (59), we get:

$$m_1 = 11.5 \text{ and } m_2 = 1.0.$$

Substituting the values of m_1 & m_2 obtained above in Eq. (58), we get:

$$K_h = 1.007 \approx 1.01$$

δ & δ_h are calculated using Eqs. (56) and (57) as:

$$\delta = 1.531 \left(\frac{230 \times 10^3 \times (200 \times 30) \times 30}{3200 \times 1 \times 1000^2} \right)^{\frac{1}{2}} = 5.5$$

$$\delta_h = \frac{2}{\sqrt{0.015}} (3.6) \left(\frac{1.0^2 - 11.5^2}{11.5(2 - 11.5^2) - 1.0(2 - 1.0^2)} \right) = 5.15$$

$$\therefore R_{hyb} = \left[\frac{5.15(1.01^5 - 1)}{2 \times 5.5(1.293^5 - 1)} \right]^{-1/2 \times 5} ; q \approx 5$$

$$= \frac{0.263}{28.75} = 1.6$$

The tensile failure strain of the banana-carbon fiber blended epoxy composite is 1.6 times more than the composites fabricated from carbon fibers alone.

6. Results and Discussion

In this study, the proposed composite reinforced with 1%, 3%, and 5% nano-clay particles is modeled in ANSYS APDL and various analytical equations are employed to find its effective elastic features. The main purpose is to analyze the comparison among the different elastic properties obtained using homogenization and semi-empirical

models, to calculate the average error and deformation for 1%, 3%, and 5% nano-clay reinforcements. The average error (E_{AV}) is calculated using the following equation [70]:

$$E_{AV} = \left| \frac{x_c - x_m}{x_m} \right| \times 100 \quad (60)$$

Where: x_c = Elastic values obtained by calculations

x_m = elastic values obtained by Finite element results

The average value of the tensile modulus obtained by different analytical models for the proposed composite blended with 1 wt% of nano-clay (with interphase) shows an increase of 88.35% on comparing it to the value of tensile modulus of 13950MPa for carbon fibers reinforced with 1 wt% of nano-clay filled IPN matrix [9]. For 3 wt% of nano-clay (with interphase), the average tensile modulus shows a rise of 88.1%, as compared to the tensile modulus value of 14550MPa [9]. From the results, it is observed that the inclusion of banana fibers increases the strength and toughness of nano-clay reinforced banana-carbon fibers composites.

The inclusion of 5 wt% of NC (with interphase) to the proposed composite shows an increase of 66 % on comparing it to the value of tensile modulus of 43000MPa obtained for NaOH treated banana fiber composite infused with 6 wt% of NC [7]. Therefore the results of FE model obtained for the proposed composite is validated with the analytical models used in this study and with experiments in literatures [7] and [9].

For 1%, 3% and 5% reinforcements of NC fillers, the average error values are evaluated for all the analytical models and for different elastic properties and are presented in Fig. 6. These errors show the percent deviation from the elastic values obtained from FEM results. The following points are highlighted from the results presented in Fig. 6(a) and 6 (b) for longitudinal elastic modulus(E_1) and in-plane Poisson's ratio (ν_{12}):

6.1. Longitudinal elastic modulus(E_1)

It can be observed from Fig. 6(a), that for 1% NC, all the models are in good concurrence with the FEM results as all the models are showing low average errors. For 3% NC reinforcement, the Mori-Tanaka model is yielding the largest variation from FEM value and for 5% NC, the Mori-Tanaka model gives the least percent error among all the other models used. It is evident from Fig. 6(a), that all the models for 1% NC are showing the best agreement with FEM results as compared to the error percent of all the models for 3% and 5% NC reinforcements. From the elastic values obtained for E_1 , it is found that among 1%, 3% and 5% reinforcements, the proposed composite reinforced with 5% NC gives the stiffer composite

In-plane Poisson's ratio. (ν_{12}): It can be observed from Fig. 6(b), that for 1% NC, only Generalized-Self Consistent model is showing good concurrence with FEM result. For 3% NC, both Generalized-Self Consistent model and Bridging model are yielding less variations from FEM values as compared to Mori-Tanaka and Modified Halpin-Tsai models. For 5% NC, the Mori-Tanaka model is showing the highest percent error. It is clear from Fig. 6(b) that all the models for 5% NC reinforcement, are showing the best agreement with FEM results as compared to error percent obtained for 1%, 3% and 5% NC.

The highlights for the result presented in Fig. 6(c) for transverse elastic modulus E_2 are

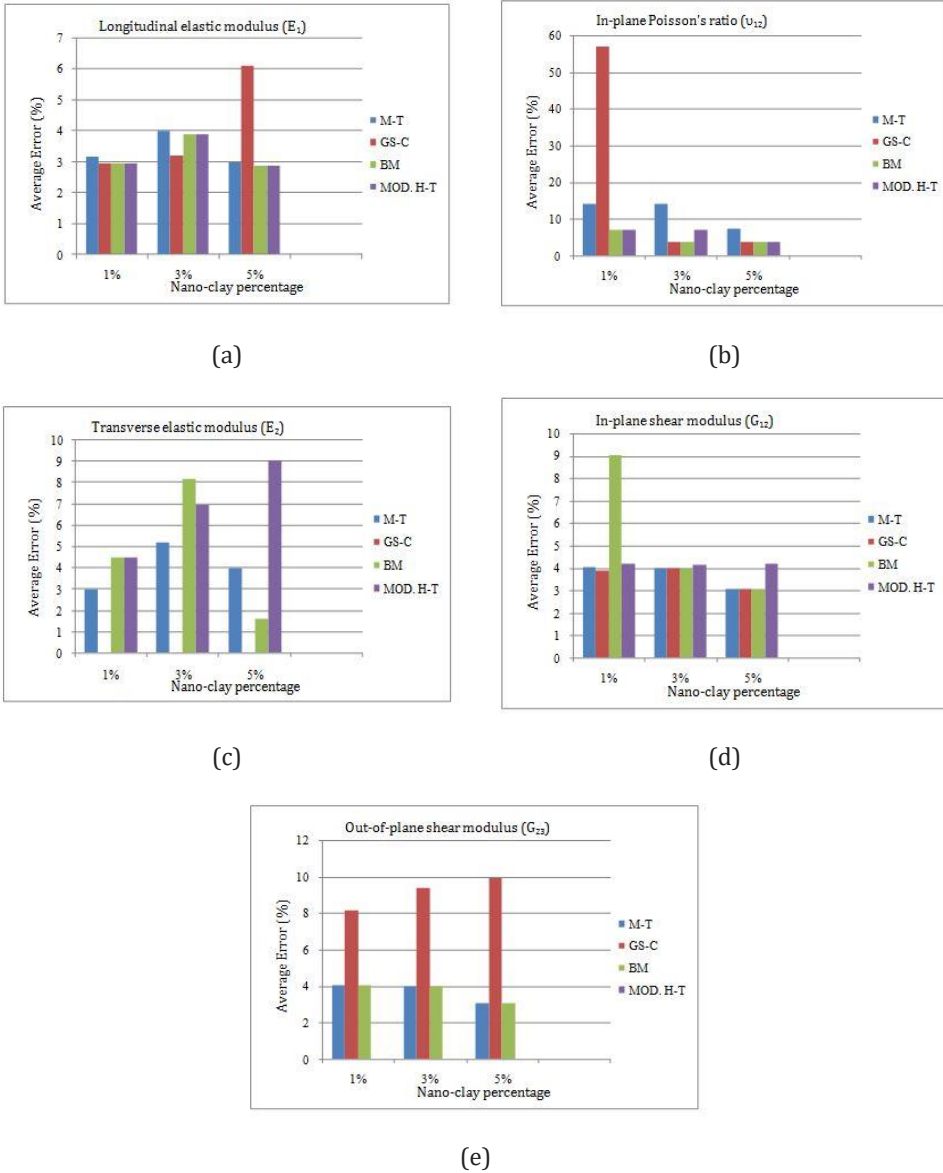


Fig. 6 Results for the average error for (a) Longitudinal elastic modulus (b) In-plane Poisson's ratio (c) Transverse elastic modulus (d) In-plane shear modulus (e) Out-of-plane shear modulus

6.2. Transverse elastic modulus(E_2)

From Fig. 6(c), it is clear that for 1% NC filler, all the models are showing good concurrence with the FEM results. For 3% NC, all the models are yielding high variations and for 5% NC, the Bridging model outperforms all the other models as it is showing the least percent error. It is evident from Fig. 6(c) that all the models for 1% NC are showing the best agreement with FEM results as compared to the error percent obtained for 3% and 5% NC reinforcements. From the elastic values obtained for E_2 , it can be deduced

that the proposed composite reinforced with 1% NC is stronger in the transverse direction as compared to 3% and 5% NC reinforcements.

The main highlights for the results of in-plane shear modulus (G_{12}) and out-of-plane shear modulus (G_{23}), presented in Fig. 6(d) and 6(e) respectively are:

6.3. In-Plane Shear Modulus (G_{12})

From Fig. 6(d), it is clear that all the models are showing good agreement with FEM results except the Bridging model for 1% NC reinforcement. It indicates that the NC reinforcement percentage does not have a significant influence on this property.

Out-of-plane shear modulus (G_{23}): All the models for 1%, 3% and 5% NC fillers are yielding low percent errors, as it can be observed from Fig. 6(e), except the Generalized-Self Consistent model is showing very high deviation from FEM results.

For the values of vector sum deformation given in Table 4, the following is observed:

6.4. Vector Sum Deformation

Banana and carbon-reinforced nano-clay epoxy composite for 3% nano-clay reinforcement is found the most suitable and for 1% nano-clay, the least suitable in terms of strength and deformation resistance as it is showing the lowest and highest total sum deformation respectively.

7. Conclusions

A novel composite material banana-carbon fiber-reinforced nano-clay epoxy composite is developed. The proposed composite is analyzed by using analytical models, namely Mori-Tanaka, Bridging, Generalized Self-Consistent, and Modified Halpin-Tsai model for the calculation of elastic properties like longitudinal and transverse elastic modulus, in-plane and out-of-plane shear modulus, and in-plane Poisson's ratio. The average error is calculated for all the elastic properties obtained from different models for 1%, 3%, and 5% nano-clay reinforcements. From the results of this study, the following points are deduced:

- The modified Halpin-Tsai method is yielding the most effective elastic properties for the proposed composite as it gives the lowest average error percent on comparing with FEM results, and the Mori-Tanaka model is giving the least effective results.
- The composite reinforced with 5% NC is stiffest, as it yields the higher values of longitudinal elastic modulus than the corresponding values obtained for 1% and 3% NC reinforcements.
- For different weight percentages of NC reinforcements, GS-C model is yielding the best elastic properties for 5% NC as compared to all the other models used in the study.
- On arranging fibers in the sequence of banana at 90°, carbon at 0°, nano-clay at 90°, carbon at 0°, and banana at 90°, the total sum deformation for 3% nano-clay composition is found to be least, so it can be deduced that the proposed composite reinforced with 3% NC can sustain the maximum load and is of higher strength as compared to the composite blended with 1% and 5% NC. The composite reinforced with 1% NC reinforcement is weakest in terms of strength as it gives the highest deformation.
- The value of hybridization obtained for the proposed composite is 1.6. It depicts that banana fiber (HE fiber) in the hybrid composite is 1.6 times stiffer than carbon fiber (LE fiber) in the hybrid composite. It is found that the inclusion of

banana fiber in the carbon fiber reinforced composites improves the failure strain rate of the hybrid composite. The hybrid composite becomes much stronger in terms of strength as the tensile failure strain characteristics increases in comparison to the failure strain of carbon fiber (LE fiber) blended non-hybrid composite.

Abbreviations

$V_{fb/mx/NC}$	The volume fraction of fiber, matrix, and nano-clay.
$W_{fb/mx/NC}$	The weight percentage of fiber, matrix, and nano-clay.
$\rho_{fb/mx/NC}$	The density of fiber, matrix, and nano-clay.
ρ_C	The density of composite.
$W_{CF}/W_{BF}/W_{EP}/W_{NC}$	The weight percentage of carbon fiber, banana fiber, epoxy, and nano-clay respectively.
$\rho_{CF}/\rho_{BF}/\rho_{EP}/\rho_{NC}$	The density of carbon fiber, banana fiber, epoxy, and nano-clay respectively.
$V_{CF}/V_{BF}/V_{EP}/V_{NC}/V_{IP}$	The volume fraction of carbon fiber, banana fiber, epoxy and nano-clay, and interphase.
E_{NC}/E_{IP}	Elastic modulus of nano-clay and interphase respectively.
G_{NC}/G_{IP}	Shear modulus of nano-clay and interphase respectively.
ν_{NC}/ν_{IP}	Poisson's ratio of nano-clay and interphase respectively.
$E_1^{fb/mx}$	Elastic modulus of fiber and matrix in longitudinal direction.
$E_{22}^{fb} = E_{33}^{fb}$	Elastic modulus of fiber and matrix in transverse direction.
$G_{12}^{fb/mx} = G_{13}^{fb/mx}$	In-plane shear modulus of fiber, matrix.
G_{23}^{fb}	Out-of-plane shear modulus of fiber.
$\nu_{12}^{fb/mx} = \nu_{31}^{fb/mx}$	In-plane Poisson's ratio of fiber, matrix.
ν_{23}^{fb}	Out-of-plane Poisson's ratio of fiber.
$\rho^{fb/mx}$	The density of fiber, matrix.
$K_{23}^{fb/mx}$	Strain bulk modulus of fiber, matrix.
K_{23}^{CF}/K_{23}^{BF}	Strain bulk modulus of fiber, matrix.

K_{23}	Plain strain bulk modulus.
α_{ij}	Coefficients of bridging matrix A [40, 41].
S_{21}^{CF}/S_{22}^{CF}	Coefficients of the compliance matrix of carbon fiber.
S_{21}^{mx}/S_{21}^{mx}	Coefficients of the compliance matrix of the epoxy matrix.
η_{E_2} $\eta_{G_{12}}$ ξ_{E_2} $\xi_{G_{12}}$	Dimensionless parameters.
E_1	Elastic modulus of the composite in longitudinal direction.
E_2	Elastic modulus of the composite in transverse direction.
ν_{12}	In-plane Poisson's ratio of the composite.
G_{12}	In-plane shear modulus of the composite.
G_{23}	Out-of-plane shear modulus of the composite.
$E_{NCP,11} = E_{NCP,33}$	Longitudinal elastic modulus of nano-clay platelet.
$E_{NCP,22}$	Transverse elastic modulus of nano-clay platelet.
$G_{NCP,12} = G_{NCP,32}$	In-plane shear modulus of nano-clay platelet.
$G_{NCP,13}$	Out-of-plane shear modulus of nano-clay platelet.
$\nu_{NCP,12} = \nu_{NCP,32}$	In-plane Poisson's ratio of nano-clay platelet.
$\nu_{NCP,13}$	Out-of-plane Poisson's ratio of nano-clay platelet/
χ_{NC}	Volume fraction of nano-clay.
χ_{IP}	Volume fraction of interphase.
t_{SL}	Thickness of silicate layer.
d_{gap}	Interlayer gap between nano-clay platelets.
N	Number of silicate sheets.

Acknowledgment

The author would like to express deep thanks to the editorial team and anonymous reviewers for their positive comments for previous version of this research paper.

References

- [1] Saxena T, Tomar P. Constitutive Performance Characterization of Diversified Bamboo Material-A Green Technology. Proceedings of International Conference on Sustainable Computing in Science, Technology and Management (SUSCOM), Amity University Rajasthan, Jaipur-India, Feb, 2008.
- [2] Parashar S, Tomar P. Synergy of sustainable bio-composite bamboo material in green technology-an explicit report. Proceedings of International Conference on Sustainable Computing in Science, Technology and Management (SUSCOM), Amity University Rajasthan, Jaipur-India, Feb, 2008.
- [3] Saxena T, Chawla VK. Effect of fiber orientations and their weight percentage on banana fiber-based hybrid composite. *Materials Today: Proceedings*. 2022;50:1275-81. <https://doi.org/10.1016/j.matpr.2021.08.149>
- [4] Saba N, Jawaid M, Asim M. Recent advances in nanoclay/natural fibers hybrid composites. *Nanoclay reinforced polymer composites*. 2016:1-28. https://doi.org/10.1007/978-981-10-0950-1_1
- [5] Kumar A, Angra S, Chanda AK. Analysis of the effects of varying core thicknesses of Kevlar Honeycomb sandwich structures under different regimes of testing. *Materials Today: Proceedings*. 2020;21:1615-23. <https://doi.org/10.1016/j.matpr.2019.11.242>
- [6] Usuki A, Kojima Y, Kawasumi M, Okada A, Fukushima Y, Kurauchi T, Kamigaito O. Synthesis of nylon 6-clay hybrid. *Journal of Materials Research*. 1993;8(5):1179-84. <https://doi.org/10.1557/JMR.1993.1179>
- [7] Mohan TP, Kanny K. Nanoclay infused banana fiber and its effects on mechanical and thermal properties of composites. *Journal of Composite Materials*. 2016;50(9):1261-76. <https://doi.org/10.1177/0021998315590265>
- [8] Mohan TP, Kanny K. Compressive characteristics of unmodified and nanoclay treated banana fiber reinforced epoxy composite cylinders. *Composites Part B: Engineering*. 2019;169:118-25. <https://doi.org/10.1016/j.compositesb.2019.03.071>
- [9] Suresh G, Vivek S, Babu LG, Bernard SS, Akash RM, Kanna SR, Kumar SB, Sethuramalingam P. Evaluation of mechanical behaviour of carbon fiber reinforced nanoclay filled IPN matrix composite. *Materials Research Express*. 2019;6(12):125311. <https://doi.org/10.1088/2053-1591/ab54ec>
- [10] Saxena T, Chawla VK. Banana leaf fiber-based green composite: An explicit review report. *Materials Today: Proceedings*. 2021;46:6618-24. <https://doi.org/10.1016/j.matpr.2021.04.099>
- [11] Yang G, Wang C, Wen P, Yin W. Performance characteristics of cold-mixed porous friction course with composite-modified emulsified asphalt. *Journal of Materials in Civil Engineering*. 2020;32(3):04019372. [https://doi.org/10.1061/\(ASCE\)MT.1943-5533.0003047](https://doi.org/10.1061/(ASCE)MT.1943-5533.0003047)
- [12] Brune DA, Bicerano J. Micromechanics of nanocomposites: comparison of tensile and compressive elastic moduli, and prediction of effects of incomplete exfoliation and imperfect alignment on modulus. *Polymer*. 2002;43(2):369-87. [https://doi.org/10.1016/S0032-3861\(01\)00543-2](https://doi.org/10.1016/S0032-3861(01)00543-2)
- [13] Kojima Y, Usuki A, Kawasumi M, Okada A, Fukushima Y, Kurauchi T, Kamigaito O. Mechanical properties of nylon 6-clay hybrid. *Journal of Materials Research*. 1993;8(5):1185-9.. <https://doi.org/10.1557/JMR.1993.1185>
- [14] Ji XL, Jing JK, Jiang W, Jiang BZ. Tensile modulus of polymer nanocomposites. *Polymer Engineering & Science*. 2002;42(5):983-93. <https://doi.org/10.1002/pen.11007>
- [15] Parashar S, Chawla VK. A systematic review on sustainable green fibre reinforced composite and their analytical models. *Materials Today: Proceedings*. 2021;46:6541-6. <https://doi.org/10.1016/j.matpr.2021.03.739>

- [16] Parashar S, Chawla VK. Evaluation of fiber volume fraction of kenaf-coir-epoxy based green composite by finite element analysis. *Materials Today: Proceedings*. 2022;50:1265-74. <https://doi.org/10.1016/j.matpr.2021.08.147>
- [17] Faghidian SA. Flexure mechanics of nonlocal modified gradient nano-beams. *Journal of Computational Design and Engineering*. 2021;8(3):949-59. <https://doi.org/10.1093/jcde/qwab027>
- [18] Faghidian SA. Higher order mixture nonlocal gradient theory of wave propagation. *Mathematical Methods in the Applied Sciences*. 2020; Sep 18.. <https://doi.org/10.1002/mma.6885>
- [19] Faghidian SA. Two-phase local/nonlocal gradient mechanics of elastic torsion. *Mathematical Methods in the Applied Sciences*. 2020 Sep 14. <https://doi.org/10.1002/mma.6877>
- [20] Faghidian SA. Contribution of nonlocal integral elasticity to modified strain gradient theory. *The European Physical Journal Plus*. 2021;136(5):559. <https://doi.org/10.1140/epjp/s13360-021-01520-x>
- [21] Kalaitzidou K, Fukushima H, Miyagawa H, Drzal LT. Flexural and tensile moduli of polypropylene nanocomposites and comparison of experimental data to Halpin-Tsai and Tandon-Weng models. *Polymer Engineering & Science*. 2007;47(11):1796-803. <https://doi.org/10.1002/pen.20879>
- [22] Hbaieb K, Wang QX, Chia YH, Cotterell B. Modelling stiffness of polymer/clay nanocomposites. *Polymer*. 2007;48(3):901-9. <https://doi.org/10.1016/j.polymer.2006.11.062>
- [23] Wang, H. W., Zhou, H. W., Peng, R. D., & MishnaevskyJr, L. (2011). Nanoreinforced polymer composites: 3D FEM modeling with effective interface concept. *Composites Science and Technology*, 71(7), 980-988. <https://doi.org/10.1016/j.compscitech.2011.03.003>
- [24] MishnaevskyJr L. Micromechanical analysis of nanocomposites using 3D voxel based material model. *Composites Science and Technology*. 2012;72(10):1167-77. <https://doi.org/10.1016/j.compscitech.2012.03.026>
- [25] Dai G, MishnaevskyJr L. Damage evolution in nanoclay-reinforced polymers: a three-dimensional computational study. *Composites science and technology*. 2013;74:67-77.. <https://doi.org/10.1016/j.compscitech.2012.10.003>
- [26] Andrianov IV, Awrejcewicz J, Danishevskyy VV. *Asymptotical mechanics of composites*. Cham, Germany: Springer. doi. 2018;10:978-3.. <https://doi.org/10.1007/978-3-319-65786-8>
- [27] Shah PD, Melo JD, Ciminijr CA, Ridha M. Evaluation of notched strength of composite laminates for structural design. *Journal of composite materials*. 2010;44(20):2381-92.. <https://doi.org/10.1177/0021998310372713>
- [28] Tsai SW, Melo JD. An invariant-based theory of composites. *Composites Science and Technology*. 2014;100:237-43. <https://doi.org/10.1016/j.compscitech.2014.06.017>
- [29] Xu W, Zeng Q, Yu A. Young's modulus of effective clay clusters in polymer nanocomposites. *Polymer*. 2012;53(17):3735-40. <https://doi.org/10.1016/j.polymer.2012.06.039>
- [30] Usuki A, Kojima Y, Kawasumi M, Okada A, Fukushima Y, Kurauchi T, Kamigaito O. Synthesis of nylon 6-clay hybrid. *Journal of Materials Research*. 1993;8(5):1179-84.. <https://doi.org/10.1557/JMR.1993.1179>
- [31] Cricri G, Garofalo E, Naddeo F, Incarnato L. Stiffness constants prediction of nanocomposites using a periodic 3D-FEM model. *Journal of Polymer Science Part B: Polymer Physics*. 2012;50(3):207-20. <https://doi.org/10.1002/polb.23001>
- [32] Gupta P, Chawla V, Jain V, Angra S. Green operations management for sustainable development: An explicit analysis by using fuzzy best-worst method. *Decision Science Letters*. 2022;11(3):357-66. <https://doi.org/10.5267/j.dsl.2022.1.003>

- [33] Yung KC, Wang J, Yue TM. Modeling Young's modulus of polymer-layered silicate nanocomposites using a modified Halpin-Tsai micromechanical model. *Journal of reinforced plastics and composites*. 2006;25(8):847-61. <https://doi.org/10.1177/0731684406065135>
- [34] Budiansky B. On the elastic moduli of some heterogeneous materials. *Journal of the Mechanics and Physics of Solids*. 1965;13(4):223-7. [https://doi.org/10.1016/0022-5096\(65\)90011-6](https://doi.org/10.1016/0022-5096(65)90011-6)
- [35] Mori T, Tanaka K. Average stress in matrix and average elastic energy of materials with misfitting inclusions. *Actametallurgica*. 1973;21(5):571-4. [https://doi.org/10.1016/0001-6160\(73\)90064-3](https://doi.org/10.1016/0001-6160(73)90064-3)
- [36] Benveniste Y. A new approach to the application of Mori-Tanaka's theory in composite materials. *Mechanics of materials*. 1987;6(2):147-57. [https://doi.org/10.1016/0167-6636\(87\)90005-6](https://doi.org/10.1016/0167-6636(87)90005-6)
- [37] Hill R. A self-consistent mechanics of composite materials. *Journal of the Mechanics and Physics of Solids*. 1965;13(4):213-22. [https://doi.org/10.1016/0022-5096\(65\)90010-4](https://doi.org/10.1016/0022-5096(65)90010-4)
- [38] Lielens G. (1999). Micro-macro modeling of structured materials, PhD thesis. UniversiteCatholique de Louvain, Louvain-la-Neuve, Belgium.
- [39] Tucker III CL, Liang E. Stiffness predictions for unidirectional short-fiber composites: review and evaluation. *Composites science and technology*. 1999;59(5):655-71. [https://doi.org/10.1016/S0266-3538\(98\)00120-1](https://doi.org/10.1016/S0266-3538(98)00120-1)
- [40] Huang ZM. Simulation of the mechanical properties of fibrous composites by the bridging micromechanics model. *Composites Part A: applied science and manufacturing*. 2001;32(2):143-72. [https://doi.org/10.1016/S1359-835X\(00\)00142-1](https://doi.org/10.1016/S1359-835X(00)00142-1)
- [41] Huang ZM. Micromechanical prediction of ultimate strength of transversely isotropic fibrous composites. *International journal of solids and structures*. 2001;38(22-23):4147-72. [https://doi.org/10.1016/S0020-7683\(00\)00268-7](https://doi.org/10.1016/S0020-7683(00)00268-7)
- [42] Dixit S, Padhee SS. Finite element analysis of fiber reinforced hybrid composites. *Materials Today: Proceedings*. 2019;18:3340-7. <https://doi.org/10.1016/j.matpr.2019.07.255>
- [43] Potluri R, Paul KJ, Prasanthi P. Mechanical properties characterization of okra fiber based green composites & hybrid laminates. *Materials Today: Proceedings*. 2017;4(2):2893-902. <https://doi.org/10.1016/j.matpr.2017.02.170>
- [44] Heydari-Meybodi M, Saber-Samandari S, Sadighi M. A new approach for prediction of elastic modulus of polymer/nanoclay composites by considering interfacial debonding: experimental and numerical investigations. *Composites science and technology*. 2015;117:379-85. <https://doi.org/10.1016/j.compscitech.2015.07.014>
- [45] Muc A, Jamróz M. Homogenization models for carbon nanotubes. *Mechanics of Composite Materials*. 2004;40(2):101-6. <https://doi.org/10.1023/B:MOCM.0000025484.92674.89>
- [46] Wang Y, Huang Z. A review of analytical micromechanics models on composite elastoplasticbehaviour. *Procedia engineering*. 2017;173:1283-90.. <https://doi.org/10.1016/j.proeng.2016.12.159>
- [47] Younes R, Hallal A, Fardoun F, Chehade FH. Comparative review study on elastic properties modeling for unidirectional composite materials. *Composites and their properties*. 2012;17:391-408.. <https://doi.org/10.5772/50362>
- [48] Abaimov SG, Khudyakova AA, Lomov SV. On the closed form expression of the Mori-Tanaka theory prediction for the engineering constants of a unidirectional fiber-reinforced ply. *Composite Structures*. 2016;142:1-6.. <https://doi.org/10.1016/j.compstruct.2016.02.001>

- [49] Hill R. Theory of mechanical properties of fibre-strengthened materials-III. Self-consistent model. *Journal of the Mechanics and Physics of Solids*. 1965;13(4):189-98.. [https://doi.org/10.1016/0022-5096\(65\)90008-6](https://doi.org/10.1016/0022-5096(65)90008-6)
- [50] Chou TW, Nomura S, Taya M. A self-consistent approach to the elastic stiffness of short-fiber composites. *Journal of Composite Materials*. 1980;14(3):178-88. <https://doi.org/10.1177/002199838001400301>
- [51] Huang ZM, Zhang YZ, Kotaki M, Ramakrishna S. A review on polymer nanofibers by electrospinning and their applications in nanocomposites. *Composites science and technology*. 2003;63(15):2223-53. [https://doi.org/10.1016/S0266-3538\(03\)00178-7](https://doi.org/10.1016/S0266-3538(03)00178-7)
- [52] Huang ZM, Ramakrishna S. Micromechanical modeling approaches for the stiffness and strength of knitted fabric composites: a review and comparative study. *Composites Part A: applied science and manufacturing*. 2000;31(5):479-501. [https://doi.org/10.1016/S1359-835X\(99\)00083-4](https://doi.org/10.1016/S1359-835X(99)00083-4)
- [53] Huang ZM. On micromechanics approach to stiffness and strength of unidirectional composites. *Journal of Reinforced Plastics and Composites*. 2019;38(4):167-96. <https://doi.org/10.1177/0731684418811938>
- [54] Huang ZM, Zhou YX. Bridging Micromechanics Model. In *Strength of Fibrous Composites 2011* (pp. 53-98). Springer, Berlin, Heidelberg. https://doi.org/10.1007/978-3-642-22958-9_3
- [55] Dahlen C, Springer GS. Delamination growth in composites under cyclic loads. *Journal of composite Materials*. 1994;28(8):732-81. <https://doi.org/10.1177/002199839402800803>
- [56] Ramakrishna S, Lim TC, Inai R, Fujihara K. Modified Halpin-Tsai equation for clay-reinforced polymer nanofiber. *Mechanics of Advanced Materials and Structures*. 2006;13(1):77-81. <https://doi.org/10.1080/15376490500343824>
- [57] Genin GM, Birman V. Micromechanics and structural response of functionally graded, particulate-matrix, fiber-reinforced composites. *International journal of solids and structures*. 2009;46(10):2136-50.. <https://doi.org/10.1016/j.ijsolstr.2008.08.010>
- [58] Alvinasab A. (2009). Nonlocal theory and finite element modeling of nano-composites. Ph.D. Dissertation, Clarkson University, New York.
- [59] Giner E, Vercher A, Marco M, Arango C. Estimation of the reinforcement factor ξ for calculating the transverse stiffness E_2 with the Halpin-Tsai equations using the finite element method. *Composite Structures*. 2015;124:402-8. <https://doi.org/10.1016/j.compstruct.2015.01.008>
- [60] Halpin JC. Effects of Environmental Factors on Composite Materials. Air Force Materials Lab Wright-Patterson AFB OH; 1969 Jun 1. <https://doi.org/10.21236/AD0692481>
- [61] Yung KC, Wang J, Yue TM. Fabrication of epoxy-montmorillonite hybrid composites used for printed circuit boards via in-situ polymerization. *Advanced Composite Materials*. 2006;15(4):371-84. <https://doi.org/10.1163/156855106778835203>
- [62] Tsai SW, Hahn HT. Introduction to composite materials, Technomic Publishing Co. Inc, Washington University, Routledge, USA, 2018.
- [63] Essabir H, Bensalah MO, Rodrigue D, Bouhfid R, Qaiss A. Structural, mechanical and thermal properties of bio-based hybrid composites from waste coir residues: Fibers and shell particles. *Mechanics of Materials*. 2016;93:134-44. <https://doi.org/10.1016/j.mechmat.2015.10.018>
- [64] Thwe MM, Liao K. Effects of environmental aging on the mechanical properties of bamboo-glass fiber reinforced polymer matrix hybrid composites. *Composites Part A: Applied Science and Manufacturing*. 2002;33(1):43-52. [https://doi.org/10.1016/S1359-835X\(01\)00071-9](https://doi.org/10.1016/S1359-835X(01)00071-9)
- [65] Hayashi T. On the improvement of mechanical properties of composites by hybrid composition. *Proceedings of 8th International Reinforced Plastics Conference*. 1972 (pp. 149-152).

- [66] Zweben C. Tensile strength of hybrid composites. *Journal of materials science*. 1977;12(7):1325-37. <https://doi.org/10.1007/BF00540846>
- [67] Patiño I, Isaza C. Mori-Tanaka-based statistical methodology to compute the effective Young modulus of polymer matrix nano-composites considering the experimental quantification of nanotubes dispersion and alignment degree. *Engineering Solid Mechanics*. 2022;10(1):79-98. <https://doi.org/10.5267/j.esm.2021.9.002>
- [68] Kumar U, Rathi R, Sharma S. Carbon nano-tube reinforced nylon 6, 6 composites: a molecular dynamics approach. *Engineering Solid Mechanics*. 2020;8(4):389-96. <https://doi.org/10.5267/j.esm.2020.2.002>
- [69] Barbero EJ. *Introduction to Composite Materials Design* (3rd Edition), Boca Raton, Florida, USA, 2018.
- [70] Golub GH, Van Loan CF. *Matrix computations*. Johns Hopkins University Press, (3rd edition), Baltimore, Maryland, 1996.
- [71] Huang J, Zhou J, Liu M. Interphase in polymer nanocomposites. *JACS Au*. 2022 Jan 13;2(2):280-91. <https://doi.org/10.1021/jacsau.1c00430>
- [72] DeArmitt C. Functional fillers for plastics. In *Applied plastics engineering handbook*, New York, 2011:455-468. <https://doi.org/10.1016/B978-1-4377-3514-7.10026-1>



Technical Note

On the effect of numerical parameters in finite element through thickness modeling for springback prediction

Bora Şener^{1,a}, Toros Arda Akşen^{2,b}, Emre Esener^{3,c}, Mehmet Firat^{*2,d}

¹Department of Mechanical Engineering, Yildiz Technical University, Istanbul, Turkey

²Department of Mechanical Engineering, The University of Sakarya, Sakarya, Turkey

³Department of Mechanical Engineering, Bilecik Seyh Edebali University, Bilecik, Turkey

Article Info

Article history:

Received 8 Mar 2022

Revised 9 May 2022

Accepted 16 May 2022

Keywords:

Springback;

TWIP980 steel;

U-Bending;

Finite Element Method

Abstract

The usage of advanced high strength steels (AHSS) presents important advantages in the reduction of the car body weight. However, these steels exhibit high springback behavior and causes to several problems in the manufacturing. Therefore, the prediction of the springback for AHSS is an important engineering task. In this study, the effect of numerical parameters in finite element through thickness modelling for springback prediction was investigated. U-draw bending process of transformation-induced plasticity-TWIP980 steel was performed as benchmark study. In the study, both shell and solid elements were taken into account. Number of integration points for shell elements and number of elements along the thickness direction for solid elements were evaluated. As a result, 5 integration points were determined as optimum value for shell elements however similar predictions results were obtained between the shell and solid elements.

© 2022 MIM Research Group. All rights reserved.

1. Introduction

Springback can be defined as deviation from the designed target shape after removal of the load. This phenomenon causes to difficulties in the subsequent manufacturing processes and assembly of the parts [1]. Accurate prediction of springback by finite element analysis (FEA) is a complicated task since numerous numerical and process parameters have effect on the prediction accuracy of springback. An accurate finite element modeling of a stamping process eliminates time-consuming stages especially at die compensation procedure [2-4]. From this perspective, finite element modelling stages must be well defined and optimized by means of accuracy and solution time. A great number of calculation parameters in finite element simulations effects the accuracy and the solution time of the simulation [5, 6]. Mesh design of the geometries and plasticity modeling steps dominates the accuracy of the simulations [7-9]. Mesh design generally includes element type, element number, and number of integration points (for shell elements). In the literature, Lee and Yang [10] investigated the effect of contact damping, penalty parameters, mesh size in the blank, number of elements on tool corners and punch velocity on springback prediction. They performed finite element (FE) simulations of U bending process with different values of the mentioned numerical parameters and determined that mesh size in the blank and number of elements on tool corners are the most important factors influencing springback prediction. Xu et al. [11] studied the effect of nodal damping value, number of integration point, mesh size in the blank and punch velocity on springback prediction of U bending process and determined the optimum values of the

*Corresponding author: fiat@sakary.edu.tr

^a orcid.org/0000-0002-8237-1950; ^b orcid.org/0000-0002-7087-3216; ^c orcid.org/0000-0001-5854-4834;

^d orcid.org/0000-0002-3973-4736

DOI: <http://dx.doi.org/10.17515/resm2022.415st0308tn>

Res. Eng. Struct. Mat. Vol. 8 Iss. 4 (2022) 799-809

numerical parameters. Chen et al. [12] performed finite element (FE) simulations of slit-ring cup and three automotive parts, namely fender load beam, a rail and a cross member in dynamic-explicit finite FE program Ls-Dyna. They studied the effect of mass scaling, contact method and material model on springback prediction. Authors determined that accuracy of springback prediction is improved by using selective mass scaling, smooth contact method and Yoshida-Uemori [13] nonlinear isotropic-kinematic hardening model. Yao et al. [14] investigated the effect of loading curve, mesh size, number of through thickness integration points and mass scaling factor. They determined that the decreasing of punch velocity, increasing of adaptivity level and number of integration points improve the springback prediction accuracy. Trzepieciniski and Lemu [15] researched the influence of a number of integration points, integration rule, the orientation of the blank and friction coefficient on the amount of springback in V bending process. From the numerical results, they determined that minimum five elements through the thickness direction for Gauss's integration rule are required to obtain compatible results, while similar results were obtained both Gauss and Simpson rules with seven or nine integration points. A comprehensive study was carried out by Firat et al. [16]. They investigated the effects of both numerical and process parameters on the springback prediction accuracy of U bending and an engine suspension bracket. The effects of element size and punch speed from numerical parameters and blank holder force (BHF), draw bead penetration and friction coefficient from process parameters were evaluated in their study. The interactions between the parameters and their effects on the springback and thinning behavior were determined by multi-linear regression and the optimum parameters were presented. Esener et al. [17] performed a sensitivity analysis for stamping process of a roof stiffener part manufactured from dual phase-DP600 steel and determined optimum numerical and process parameters which minimize the amount of springback. They investigated number of integration points through the thickness direction, shell element formulation, friction coefficient and BHF values and found the optimum parameters by using meta-model-based design of experiment.

As it seen from the literature studies, the effect of integration points through thickness was evaluated by several researchers in the past [10, 11, 14, 15]. However, comparisons were generally restricted to only the performance of the mesh sizes. The solution times were mostly ignored for the determination of the optimum mesh size. This study investigated the effect of the mesh size on spring-back prediction in terms of prediction performance and solution times. Moreover, an implicit solver was utilized in this work which is rare because explicit solvers have been preferred extensively for spring-back prediction due to the lower solution times.

On the contrary, implicit solvers have to calculate the stiffness matrix at all increments of the simulation, which increases the solution time. Therefore, implicit solvers provide consistent results for applications of plasticity. In addition, this study focuses on the effect of an anisotropic yield criterion on spring-back prediction. Although the influence of kinematic hardening is well known [13], the influence of the anisotropic yield criterion on spring-back prediction was not extensively investigated.

It can be seen that there is numerous studies that models the blank geometry using shell and solid elements. However, investigation of solid element number through the material thickness and number of integration points in shell elements for springback predictions is a challenge for process engineers. For this reason, presented study focused on finite element through thickness modelling for springback prediction. In this study, springback of TWIP980 sheet from advanced high strength steel (AHSS) was investigated by considering anisotropic plasticity model. U-draw bending process was performed and this process evaluated by using solid and shell elements with different trough thickness

modeling parameters. Finite element (FE) analyses were performed with a commercial implicit FE code and the predicted results were compared with experimental results.

2. Material and Method

In this study, U-draw bending process from the Numisheet93 benchmark is performed. Die tool geometries can be seen in Fig. 1. TWIP980 steel was used as material. TWIP steels consist of high manganese content and therefore it is fully austenitic at ambient temperature. The plastic deformation of this steel is carried out by both twinning and dislocation slip mechanisms [18]. Mechanical properties of the material can be seen in Table 1.

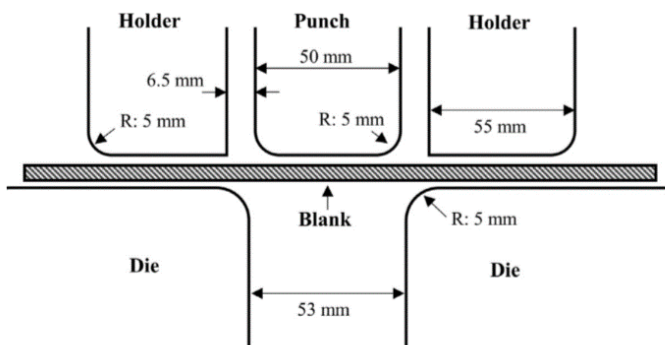


Fig. 1 Tool dimensions for U-draw bending [20]

Table 1. Mechanical properties of TWIP980 steel [20]

Angle (°)	Young modulus (MPa)	Yield Stress (MPa)	r-value
0°	207000	941.1	0.678
45°		896.9	1.147
90°		938.8	1.279

According to the additive plasticity approach, strain increment can be decomposed into the elastic and plastic components, as seen in Eq. (1).

$$d\varepsilon_{ij} = d\varepsilon_{ij}^e + d\varepsilon_{ij}^p \tag{1}$$

Cauchy stress tensor components can be decomposed into deviatoric and hydrostatic parts.

$$d\sigma_{ij} = dS_{ij} + d\sigma_m I \tag{2}$$

The deviatoric part is responsible for the shape-changing, while the hydrostatic part is responsible for the volume change. σ_m and I represent the mean stress and Kronecker delta, respectively. Eq. (3) establish a correlation between the elastic strain component and the deviatoric stress components.

$$dS_{ij} = 2Gd\varepsilon_{ij}^e \tag{3}$$

Ultimately, the yield criterion separating the elastic and plastic regions from each other in stress space can be expressed by Eq. (4).

$$f(\sigma_{ij}) = \sigma_{eqv}(\sigma_{ij}) - \sigma_0(\varepsilon_{ij}^p) = 0 \tag{4}$$

In this study, initial anisotropy of the material was defined with orthotropic quadratic Hill48 yield criterion [21] and the relationship between the plastic strain increments and stresses was defined with associated flow rule. The criterion has six coefficients for three-dimensional stress state and it could be written as follows:

$$f(\sigma_{ij}) = \{(F(\sigma_{22} - \sigma_{33})^2 + G(\sigma_{33} - \sigma_{11})^2 + H(\sigma_{11} - \sigma_{22})^2 + 2L\sigma_{23}^2 + 2M\sigma_{13}^2 + 2N\sigma_{12}^2)\}^{1/2} \tag{5}$$

where F, G, H, L, M and N are constants which define anisotropy. In this study, Lankford based identification was considered and F, G, H and N were determined by following equations. The remaining coefficients L and M were used as 1.5 due to neglecting of anisotropy along thickness direction.

$$F = \frac{r_0}{r_{90}(1+r_0)}, \quad G = \frac{1}{1+r_0}, \quad H = \frac{r_0}{1+r_0}, \quad N = \frac{(r_0+r_{90})(1+2r_{45})}{2r_{90}(1+r_0)} \tag{6}$$

r_0, r_{45} and r_{90} denote Lankford coefficients along the three main directions. Hill48 plasticity model coefficients were given in Table 2 for TWIP980 steel. Prediction performance of the Hill48 model was evaluated with directionality estimations for TWIP980 steel. Fig. 2 illustrates the r value, the yield stress ratio and the yield surface predictions of Hill48 plasticity model for TWIP980 steel.

Table 2. Hill48 coefficients of TWIP980

F	G	H	L	M	N
0.316	0.596	0.404	1.5	1.5	1.502

The experimental r values were accurately captured as expected (Fig. 1a). Nevertheless, some deviations were seen between the analytical yield ratio predictions and the experimental ones (Fig 1b). The associated flow rule (AFR) was employed to establish a relation between the Cauchy stress components and plastic strain components, and the AFR is given in Eq. (7).

$$d\varepsilon_{ij}^p = d\lambda \frac{df}{d\sigma_{ij}} \tag{7}$$

In the equation above, $d\lambda$ is the proportionality factor. In the study, isotropic hardening assumption and was considered and hardening of the material was defined with Swift hardening law. The hardening parameters are given in Table 3 and the Swift law was given in Eq. (8).

$$\sigma = K(\varepsilon_0 + \varepsilon_p)^n \tag{8}$$

Table 3. Swift model parameters of TWIP980 [20]

K(MPa)	ε_0	n
2349.9	0.167	0.502

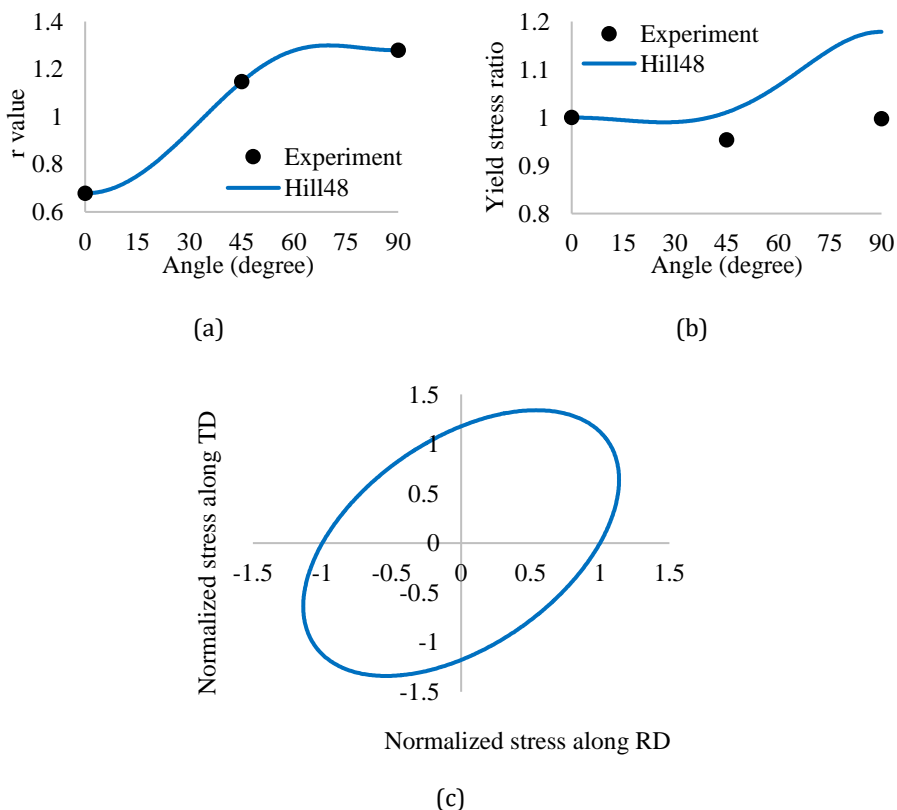


Fig. 2 (a) r value, (b) yield stress ratio, (c) yield surface predictions of the Hill48 criterion for TWIP980 steel

3. Application Study

In this study, U-draw bending process was modeled with implicit FE code Marc [21]. Blank part was modeled as deformable body, while other die tools were modeled as rigid body. Control nodes were assigned for punch and blank holder so as to apply the necessary boundary conditions. In simulations, two element types were considered, and blank was separately meshed with shell and solid elements. Bilinear, four-node fully integrated shell elements, including transverse shear effects, were adopted for shell element formulation. On the other hand, fully integrated hexahedral constant dilatational elements were used for solid element formulation. Both elements are free from shear locking [21, 22]. In the first case, 1, 2, 3, and 4 solid elements were used through the thickness and in the second case shell elements with 3, 5, 7 and 9 integration points were evaluated. For both element type, half of the geometry was modelled due to symmetry conditions. The Coulomb bilinear friction model was employed, and the friction coefficient between the blank and the tools was assumed to be 0.13 [20]. Node to segment contact algorithm coupled with penalty factor was utilized to eliminate the penetration. The FE model of the process was shown in Fig 3. In the FE model, blank holder force was assigned as 10 kN, 25 kN, and 50 kN separately and the punch displacement was performed as 70 mm.

Cross section of the deformed geometry was investigated following FE analyses, and three parameters were taken into account for springback measurement recommended in the literature studies that used U-draw bending [23, 24]. θ_1 and θ_2 angles and the sidewall

radius (ρ) can be seen in Fig. 4. θ_1 , θ_2 and ρ parameters were predicted for each FE analysis and the results were compared with experiments obtained in Numisheet93 benchmark. The comparison between the numerical and experimental results for shell and solid elements were shown in Fig. 5 and Fig. 6, respectively.

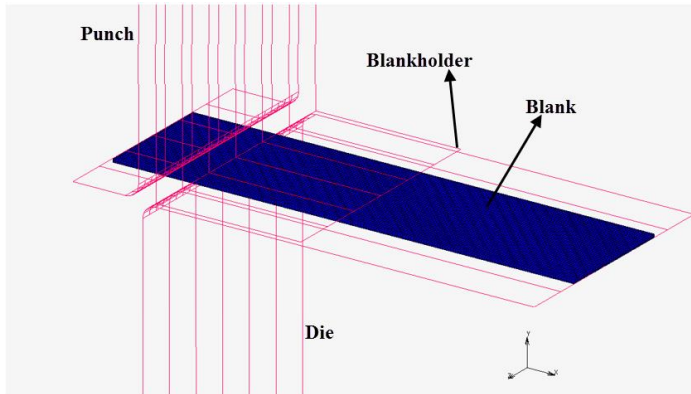


Fig. 3 FE model of U-draw bending

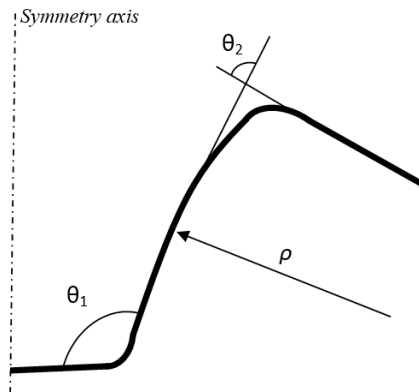


Fig. 4 Springback parameters in U-draw bending process

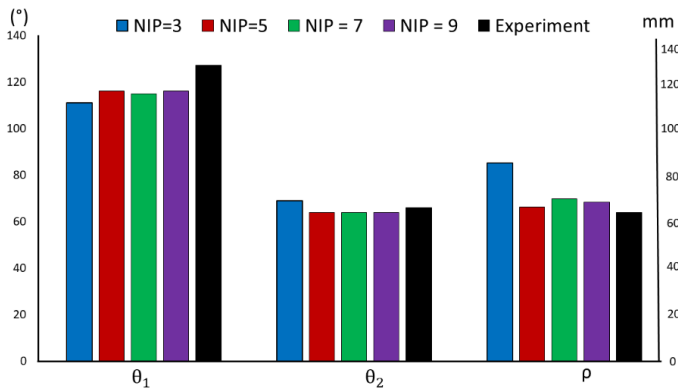


Fig. 5 Comparison results for shell elements with different integration point numbers

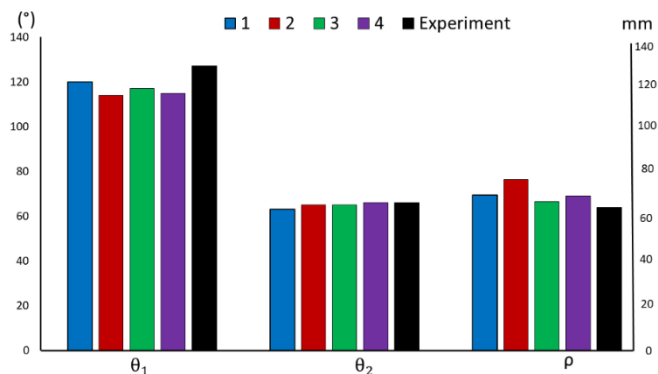


Fig. 6 Comparison results for different number of solid elements that used trough the thickness

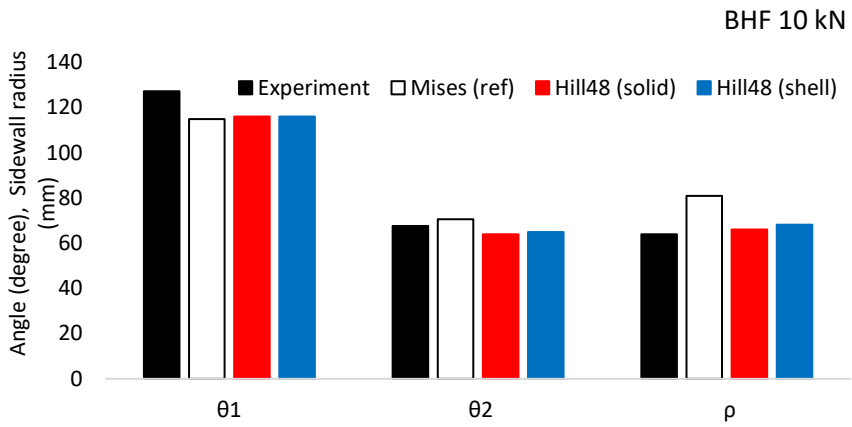
It can be seen from the figures, for shell elements, no significant differences were observed between the predicted and experimental springback angles (θ_1 – θ_2) when the more than 5 integration points were used. However, minor differences were observed for sidewall radius. When it comes to solid elements, it was observed that increasing of the number of elements in thickness direction has not an important effect on the prediction accuracy of springback for U-draw bending process. The solution times of different element numbers and integration points through-thickness directions were also compared, and Table 4 shows the CPU solution times.

Table 4. CPU solution times

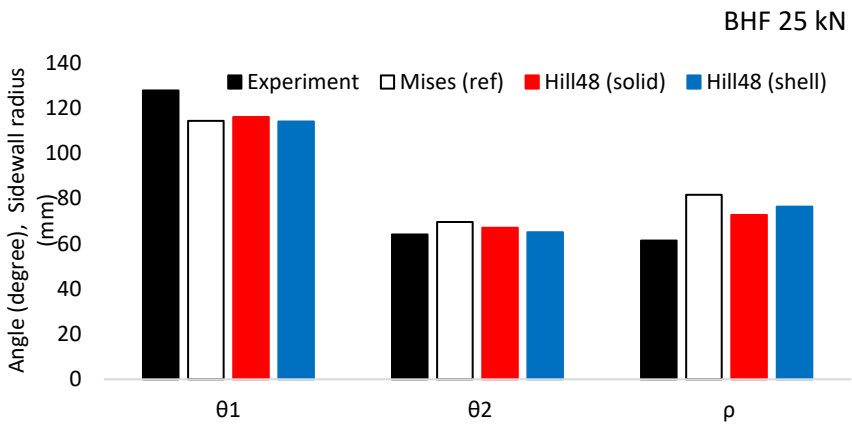
Element Number		1	2	3	4
Solid	Solution Time (s)	6424.86	11106.77	11805.89	13856.98
	Iteration (Cycle)	2816	2694	2367	2135
NIP		3	5	7	9
Shell	Solution Time (s)	6564.08	4149.25	5418.34	10902.21
	Iteration (Cycle)	2818	1865	2016	2132

It was observed that higher solution times were obtained for the simulations with the solid element formulation. In addition, the solution times increase with the increase in through-thickness element number or NIP. However, for the results obtained by the 3 NIP in thickness, the solution time was increased. It may be a consequence that the models have difficulty converging because the total iteration number of 3 NIP was considerably higher than the others. Correspondingly, an increase in the NIP through-thickness may lead to an improvement in the convergence performance. Moreover, for shell element formulation, after the 3 NIP iteration numbers suddenly decreased and from 5 NIP to 9 NIP, iteration numbers increased.

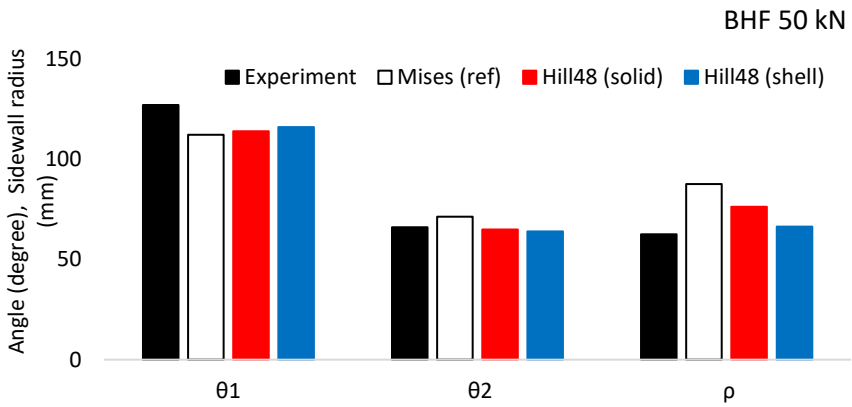
The equal number of integration layers in thickness was considered to properly compare the performances of shell element and solid element formulations. From this point of view, the FE models with 2 elements in thickness for solid and 5 NIP through-thickness for shell element formulations were selected for further studies. In order to evaluate the performance of the Hill48 criterion on the spring-back prediction, U draw bending simulations were carried out for BHF 10 kN and 25 kN as well. The results were compared with the experimental results and literature studies [20]. Fig 7 demonstrates the numerical and experimental spring back outcomes for 10 kN, 25 kN, and 50 kN BHF.



(a)



(b)



(c)

Fig. 7 Springback parameters for a) BHF = 10 kN, b) BHF = 25 kN, c) BHF = 50 kN

The von Mises results were taken from the Ref. [20]. Hill48 results obtained by solid and shell element formulations were compared with the reference Mises results and experimental results simultaneously. For all BHF values, Mises overpredicted the θ_1 while underpredicted the θ_2 and ρ . On the other hand, Hill48 results for both element formulations improved prediction performance and better agreed with the experimental results for all spring back parameters. However, a slight difference between both element formulations of Hill48 was observed. Shell element formulation was found to be more suitable and practical for spring-back prediction when considering the CPU solution times.

4. Conclusions

In this study, the effect of FE parameters on the prediction accuracy of the springback was investigated. U-draw bending process was selected as benchmark study and springback of TRIP980 sheet from AHSS was predicted with implicit FE code Marc. Element type, NIP, the number of elements in thickness direction were taken as variables and FE analyses were performed with different numerical parameters and different BHF values. Two angles between the sidewall and the deformed profile and also sidewall radius was selected as springback measurement. The predicted results from FE analyses were compared with experimental results and numerical results obtained from the literature study. The conclusions are as follows.

- It was found from the comparisons that increasing of NIP has no significant effect on the springback angle predictions. However, only minor differences were observed in sidewall radius predictions.
- It was determined that the usage of 5 integration points through the thickness direction was adequate for shell elements. When comparing the CPU solution times, the model with 5 NIP was found to be lower than the others. This situation is attributed to the improved convergence performance.
- Significant differences between the predictions were not observed when the number of elements in thickness direction increased for solid elements. When the solution times were regarded, a noticeable difference was not observed for different element numbers through the thickness.
- Simulations were repeated for different BHF values using solid, and shell element formulations utilizing the models with the optimum element numbers and NIP through the thickness. The models with 2 elements and 5 NIP through-thickness for solid and shell element formulations were selected for these analyses. Numerical results were compared with the experimental results and reference isotropic criterion results. The prediction accuracy was enhanced for both element formulations when the Hill48 criterion was employed.
- A noticeable difference was not observed between the solid and shell element formulations in terms of predicted spring back angles and sidewall radius. However, shell element formulation was found to be more practical and suitable for spring-back prediction in terms of CPU solution times.

References

- [1] Wagoner RH, Lim H, Lee M-G. Advanced issues in springback. *International Journal of Plasticity*, 2013; 45: 3-20. <https://doi.org/10.1016/j.iijplas.2012.08.006>
- [2] Zhang L, Li, H, Bian T, Wu C, Gao Y, Lei C. Advances and challenges on springback control for creep age forming of aluminum alloy. *Chinese Journal of Aeronautics*, 2021. <https://doi.org/10.1016/j.cja.2021.10.019>

- [3] Wang H, Zhou J, Zhao TS, Liu LZ, Liang Q. Multiple-iteration springback compensation of tailor welded blanks during stamping forming process. *Materials & Design*, 2016; 102: 247-254. <https://doi.org/10.1016/j.matdes.2016.04.032>
- [4] Jianjun WU, Zhang Z. An improved procedure for manufacture of 3D tubes with springback concerned in flexible bending process. *Chinese Journal of Aeronautics*, 2021; 34(11): 267-276. <https://doi.org/10.1016/j.cja.2020.05.036>
- [5] Navarro M, Ivorra S, Varona, FB. Parametric finite element analysis of punching shear behaviour of RC slabs reinforced with bolts. *Computers & Structures*, 2020; 228, 106147. <https://doi.org/10.1016/j.compstruc.2019.106147>
- [6] Greve L, van de Weg B. Surrogate modeling of parametrized finite element simulations with varying mesh topology using recurrent neural networks. *Array*; 2022; 14: 100137. <https://doi.org/10.1016/j.array.2022.100137>
- [7] Jiang HJ, Ren YX, Lian JW, Xu WL, Gao NH., Wang XG, Jia CS. A new predicting model study on U-shaped stamping springback behavior subjected to steady-state temperature field. *Journal of Manufacturing Processes*, 2022; 76: 21-33. <https://doi.org/10.1016/j.jmapro.2022.02.004>
- [8] Yoshida F. Description of elastic-plastic stress-strain transition in cyclic plasticity and its effect on springback prediction. *International Journal of Material Forming*, 2022; 15(2): 1-17. <https://doi.org/10.1007/s12289-022-01651-1>
- [9] Solfronk P, Sobotka J, Koreček D. Effect of the Computational Model and Mesh Strategy on the Springback Prediction of the Sandwich Material. *Machines*, 2022; 10(2): 114. <https://doi.org/10.3390/machines10020114>
- [10] Lee SW, Yang DY. An assessment of numerical parameters influencing springback in explicit finite element analysis of sheet metal forming process. *Journal of Materials Processing Technology*, 1998; 80-81: 60-67. [https://doi.org/10.1016/S0924-0136\(98\)00177-0](https://doi.org/10.1016/S0924-0136(98)00177-0)
- [11] Xu WL, Ma CH, Li CH, Feng WJ. Sensitive factors in springback simulation for sheet metal forming. *Journal of Materials Processing Technology*, 2004; 151: 217-222. <https://doi.org/10.1016/j.jmatprotec.2004.04.044>
- [12] Chen X, Shi M, Zhu X, Du C, Xie ZC, Xu S, Wang C-T. Springback prediction improvement using new simulation technologies. *SAE Technical Paper Series*, 2009. <https://doi.org/10.4271/2009-01-0981>
- [13] Yoshida F, Uemori T. A model of large-strain cyclic plasticity describing the Bauschinger effect and work hardening stagnation. *International Journal of Plasticity*, 2002; 18; 661-686. [https://doi.org/10.1016/S0749-6419\(01\)00050-X](https://doi.org/10.1016/S0749-6419(01)00050-X)
- [14] Yao H, Liu SD, Du C, Hu Y. Techniques to improve springback prediction accuracy using dynamic explicit FEA codes. *SAE Technical Paper Series*, 2002. <https://doi.org/10.4271/2002-01-0159>
- [15] Trzepieciniski T, Lemu HG. Effect of computational parameters on springback prediction by numerical simulation. *Metals*, 2017; 7: 1-14. <https://doi.org/10.3390/met7090380>
- [16] Firat M, Mete OH, Kocabicak U, Ozsoy M. Stamping process design using FEA in conjunction with orthogonal regression. *Finite Elements in Analysis and Design*, 2010; 46; 992-1000. <https://doi.org/10.1016/j.finel.2010.07.005>
- [17] Esener E, Ercan S, Firat M. (2014) A Sensitivity analysis by using design of experiment and its application in stamping. *An International Conference on Engineering and Applied Sciences Optimization*, Kos Island, Greece, June, 2008.
- [18] Grassel O, Kruger L, Frommeyer G, Meyer LW. High strength Fe-Mn-(Al, Si) TRIP/TWIP steels development-properties-application. *International Journal of Plasticity*, 2000; 16: 1391-1409. [https://doi.org/10.1016/S0749-6419\(00\)00015-2](https://doi.org/10.1016/S0749-6419(00)00015-2)
- [19] Makinouchi A, Nakamachi E, Onate E, Wagoner R. Numerical simulation of 3-D sheet metal forming processes verification of simulation with experiment. *Proceedings of the 2nd International Conference Numisheet'93*, Isehara, Japan, September, 1993.

- [20] Choi J, Lee J, Bong HK, Lee M-G, Barlat F. Advanced constitutive modeling of advanced high strength steel sheets for springback prediction after double stage U-draw bending. *International Journal of Solids and Structures*, 2018; 151: 152-164. <https://doi.org/10.1016/j.ijsolstr.2017.09.030>
- [21] Marc (2018) 2008.1 Volume A: Theory and User Manual.
- [22] Marc (2018) 2008.1 Volume B: Element Library.
- [23] Hill R. A theory of the yielding and plastic flow of anisotropic metals. *Proc. Soc. London A*, 1948; 193A: 291-297. <https://doi.org/10.1098/rspa.1948.0045>
- [24] Nakamachi E. Guide to the benchmark test - simulation and experiment. In: Makinochi A, Nakamachi E, Onate E, Wagoner RH, editors. *Numisheet93*. Tokyo: The Institute of Physical and Chemical Research, 1993; 32-39.

Blank Page



Research Article

Performance of URM structures under earthquake shakings: Validation using a template building structure by the 2019 Albanian earthquakes

Altin Bidaj^{*1,a}, Huseyin Bilgin^{2,b}, Marjo Hysenliu^{1,c}, Irakli Premti^{1,d} Rrapo Ormeni^{3,e}

¹Department of Mechanics of Structures Engineering, Polytechnic University of Tirana, Albania.

²Department of Civil Engineering, Epoka University, Tirana, Albania

³Seismology Department Institute of Geosciences, Energy, Water and Environment (IGEWE), Polytechnic University of Tirana, Albania.

Article Info

Abstract

Article history:

Received 31 May 2022

Revised 13 Jul 2022

Accepted 22 Jul 2022

Keywords:

*Unreinforced masonry;
Macro-modeling;
seismic assessment;
pushover analysis*

A prolonged earthquake series hit the regions of Albania on September 21 and November 26, 2019, causing loss of life and extensive damage to the civilian structures. The main aim of this study is to investigate the structural and earthquake response of a template design, commonly encountered in the region, which was seriously damaged by the 2019 Durrës/Albania earthquake. A 3D mathematical model of the entire structure was prepared, implementing macro-modeling approach to simulate its response under seismic shakings. Inherent material properties of its constituents were determined experimentally and adopted for the analytical model. Initially, an eigenvalue analysis was deployed to identify the dominant vibrations modes of the structure. Then, pushover analyses were performed to assess the earthquake response of the template designed structure, and possible failure mechanisms were examined. Finally, the obtained results from the software were compared with the real-life damage experienced by the building. In the end, it was observed that the analytical model proved to accurately estimate the earthquake behavior exhibited by the structure during the seismic shaking.

© 2022 MIM Research Group. All rights reserved.

1. Introduction

Recent seismic events have shown that URM buildings are prone to damage induced by earthquake shakings. The earthquake performance assessment of these structures becomes a demanding task because of various understandable reasons including the complicated geometry and structural arrangements of connections, flexibility of the diagrams, and its mechanical response [1-4]. In literature, several methods are proposed for the structural evaluation of existing URM buildings having different degrees of complexities [5]. With improvement of computational tools, analytical modeling strategies started to be used frequently for the estimation of the masonry response under different loading cases [6]. On the other hand, several uncertainties arise for the development of a structural model due to the inherent material characteristics, complex geometry arrangements, and the lack of available experimental data. Accordingly, mathematical models need to be validated to confirm their ability to realistically capture structural behavior of URM buildings. One way to accomplish this task is the comparison of calculated modal parameters estimated from the dynamic identification tests following a process of model updating until the mode shapes and frequencies match with the experimental test results. Another way can be used when the structure under consideration experienced

*Corresponding author: altinbidaj@yahoo.com

^a orcid.org/0000-0002-1101-6310; ^b orcid.org/0000-0002-5261-3939; ^c orcid.org/0000-0002-0863-2112;

^d orcid.org/0000-0002-1302-2378; ^e orcid.org/0000-0002-5514-2204;

DOI: <https://dx.doi.org/10.17515/resm2022.440ea0531>

Res. Eng. Struct. Mat. Vol. 8 Iss. 4 (2022) 811-834

considerable damage induced by the seismic shakings, by comparing the mathematical model with the observed damage pattern on the real building.

This study aims at evaluating the earthquake response of a commonly used template designed buildings, an URM structure located in several cities of Albania. This building typology experienced extensive damage due to November 26, 2019 Durres/Albania earthquake sequences and it was decided to demolish afterwards since the upgrading intervention was not found to be economically feasible. Firstly, the authors conducted several site visits to the earthquake-stricken area to monitor and investigate the reasons of the damages. Then, the inspections and several experimental tests performed on the selected buildings provided documentation regarding the construction details of the selected building and used for the characterization of the material properties. The importance of this study lies in the use of such detailed dedicated works by the authors, for the seismic performance of a real building. Based on the post-earthquake survey data integrated with the information about the geometry, structural configurations, and past interventions, authors are enabled to develop an accurate mathematical model of the structure, which was believed that its response was validated according to the obtained results. On the other hand, using the availability of the ground motion data allowed to check the validity of the mathematical model by comparing the real damage and the estimated damage for the seismic input which the building was subjected to.

1.1. Seismic Hazard Assessment of Albania

Albania has a long history of code-adjusted seismic design, as shown in Table 1. The first seismic regulations, accompanied by the first Map of Albania’s Seismic Zone, were adopted in 1952. The 1963 revision increased the requirements of seismic design. The first code of seismic design considered the seismic charge based on static method, regardless of the dynamic properties of the structures. With the introduction of the 1963 standard, the seismic charge is defined considering its dynamic internal effect on structures. In 1978, another amendment was issued with the name of KTP 2-78 that did not bring significant improvements. In 1989, the new seismic design code, KTP-N.2-89 was released and is currently the official code in Albania. It is essential to mention that despite the existence of the seismic design code, many buildings are not in accordance with the code and many buildings have been subjected to illegal interventions in their holding systems.

Table 1. Seismic design codes of Albania and corresponding enforcement period

Seismic Design Code of Albania	Time Period
KTP 52	1952 - 1963
KTP 63	1963 - 1972
KTP 72	1972 - 1980
KTP 2-78	1978 - 1989
KTP -N2-89	1989 - Present

In the Albanian Seismic Zonation Map the hazard is categorized in three areas:

- Areas with main intensity VIII (for low soil conditions, areas with expected intensity IX are expected such as in Vlore, Lushnje, Durres, Korce, Pogradec, Shkoder),
- Areas with main intensity VII,
- Areas with main intensity VI,

The first category comprises the greatest part of Albanian territory 57.8 %. The lowest intensity of VI is mainly in the northern part of Albania 1.3 % only (Fig 1).

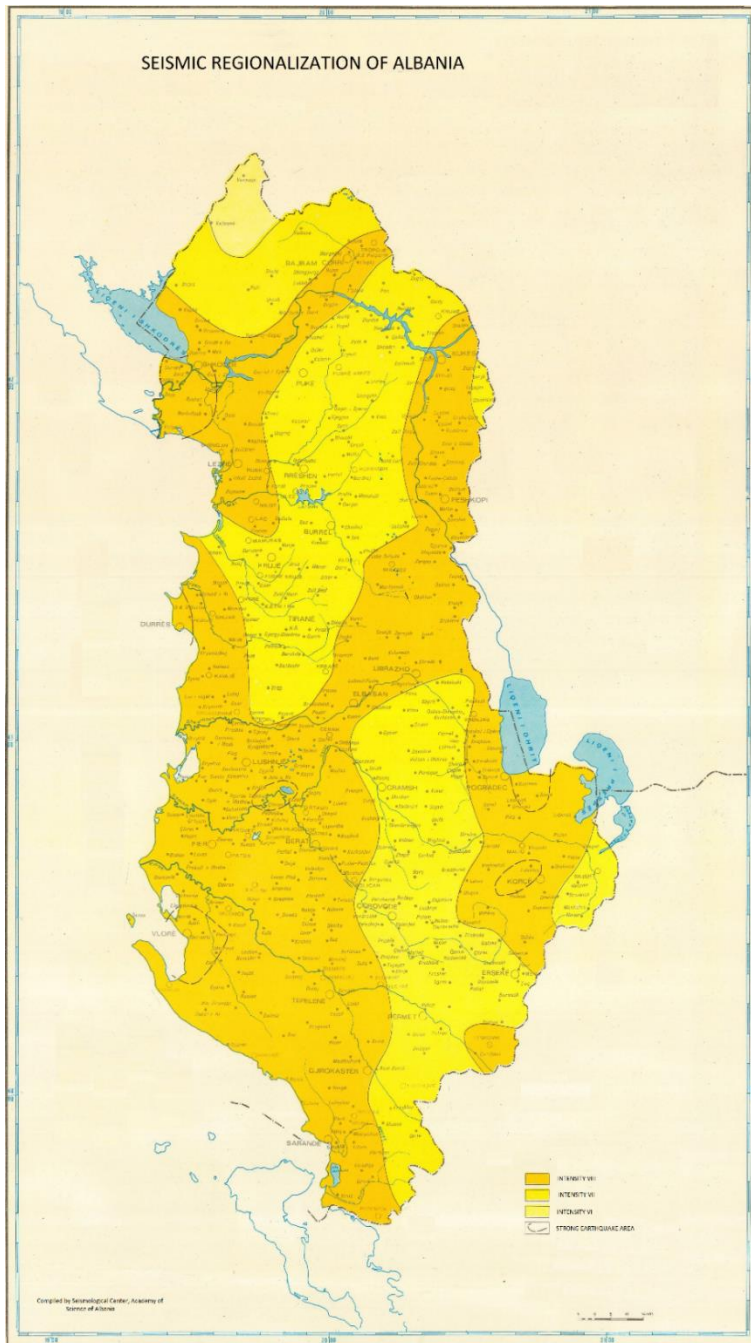


Fig. 1 Albanian Seismic Zonation Map [7]

The November 26, 2019 earthquake Mw6.4 was generated with the activation of reverse faulting of Frakull-Rodon Cape fault zone in western Albania [13]. Due to many complex tectonic fault lines (Fig 2), Albania is currently lying on an active movement with a

potential of producing Mw = 6.5 ground shakings [8]. A complete list of previous important earthquakes is given in Table 2.

Table 2. Earthquakes in Albania After [7]

No.	Year	Place	Magnitude/Intensity
1	1905	Shkodra	M _s = 6.6
2	1911	Pogradec	M _s = 6.7
3	1919	Leskovik	M _s = 6.1
4	1920	Tepelene	M _s = 6.4
5	1920	Elbasan	M _s = 5.6
6	1921	Peshkopia	I ₀ = VIII-IX
7	1926	Durres	M _s = 5.8
8	1930	Llogara	M _s = 5.8
9	1935	Librazhdt	M _s = 5.7
10	1942	Peshkopi	M _s = 6.0
11	1948	Shkoder	M _s = 5.5
12	1959	Lushnje	M _s = 6.2
13	1960	Korce	M _s = 6.4
14	1962	Fier	M _s = 6.0
15	1967	Diber	M _s = 6.6
16	1969	Tepelene,Fier	I ₀ = VII
17	1979	Mali i Zi	M _s = 6.9
18	1982	Fier, Berat	M _s = 5.7
19	2019	Durres	M _s = 6.4

In the first probabilistic spectral hazard maps for Albania ten seismic source zones were used to define the seismicity, and 5% damped spectral acceleration values at 0.2, 0.5, 1.0, and 2 seconds for a 10 % chance of non-exceedence in 50 years [9].

Table 3. Peak ground and spectral accelerations for cities of Albania [7]

City	Lat- N	Lon-W	S _a (0.2)	S _a (0.5)	S _a (1.0)	S _a (2.0)	PGA
Tirana	41.33	19.83	77	58	28	9.6	32
Durres	41.34	19.44	86	66	31	10.3	35
Elbasan	41.12	20.09	90	66	30	10.1	38
Shkodra	42.07	19.52	75	57	28	9.3	30
Vlora	40.47	19.48	88	69	33	11.0	36
Fier	40.73	19.57	86	68	32	10.8	35
Korca	40.62	20.79	99	75	34	11.0	41
Kukes	42.08	20.43	81	58	26	8.6	34
Burrel	41.63	20.02	48	40	20	7.6	18

A new probabilistic seismic hazard assessment of Albania observed that the updated seismic hazard map (Fig 4) yields higher design accelerations than the values introduced in the current regulation [10]. For the 475-year return period, ground motion across Albania represented by PGA is in the range 0.20 – 0.24 g almost over all the territory, up to 0.30 – 0.38 g in NW and SW part of the country [10]. But the reality is that for 33 years it's officially approved the 1989 code. Recently, these probabilistic seismic hazard maps

produced by different authors has gained much consensus among the community of seismologists. But from the limited seismological, geological, and geophysical data, the problems with PSHA, and the increasing exposures, it is necessary to adopt the advanced approaches for seismic hazard assessment, such as a scenario-based neo-deterministic (NDSHA) that utilize seismological, geological, and geophysical data directly and implement them as unified SHA tool at international scale [11]. There are also serious efforts to adopt Eurocode 8 [EN 1998-1, 2005, "Eurocode 8] as Albania's official code of seismic design. Currently significant part our country population is concentrated in two cities, about 34% of the Albanian Population lives in Tirana-Durres area. These cities with hundreds of thousands of buildings and millions of people at stake should receive at a very minimum the same consideration as critical facilities [12]. The last generation of standards (codes) for earthquake resistant design and construction - the common European standard EN1998-1 (Eurocode 8) - has been endorsed in Albania after the earthquake of November 26, 2019. As a conclusion a new seismic hazard maps needs to calculate. The assessment of seismic hazard by the NDSHA method or combined to PSHA, is closer to reality [11].

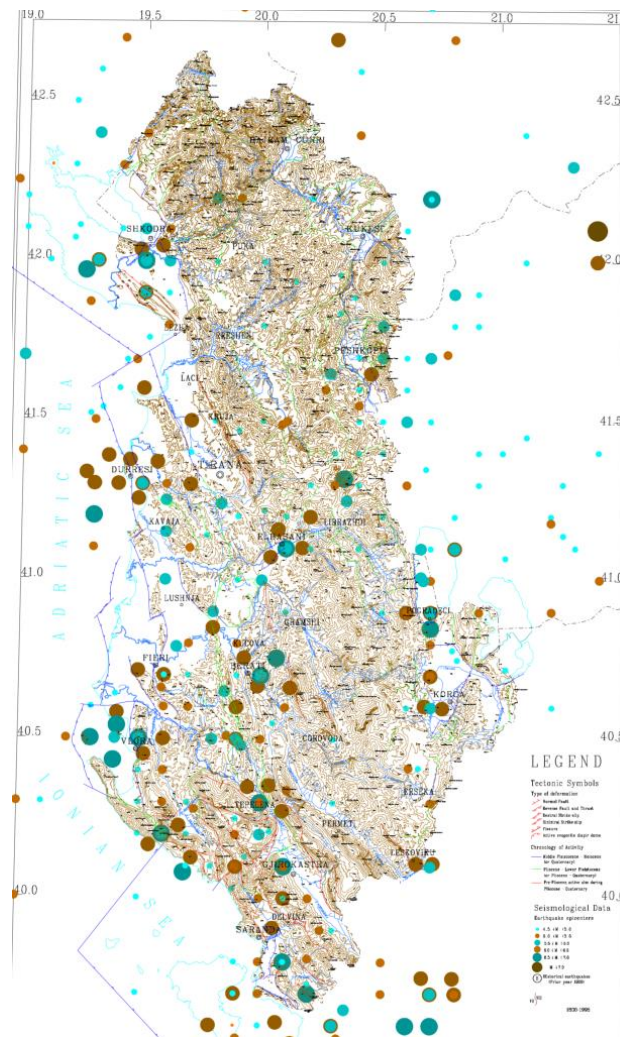


Fig 2 Albanian Seismotectonic map [7]

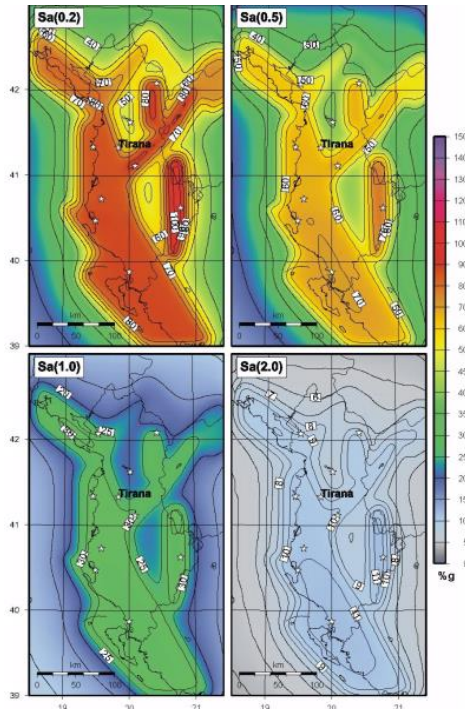


Fig. 3 Seismic hazard on rock for different ground acceleration [7]

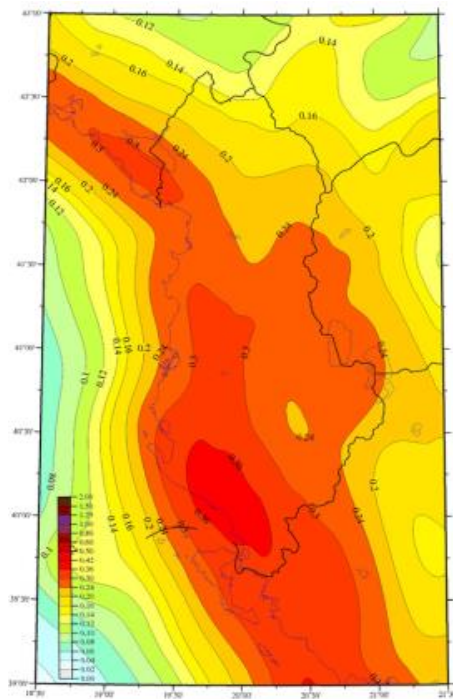


Fig. 4 Probabilistic seismic hazard map for PGA [10]

1.2 The November 26, 2019 Earthquake

The $M_w = 6.4$ magnitude earthquake that occurred on 26 November 2019 at 03:56 local time struck western Albania with a focal depth about 38 km and caused severe damage to many public and residential buildings in Durres, Tirana, Lezha, Shkodër and Berat districts [13]. There are several factors that determined just how destructive this earthquake was: location, magnitude, depth, distance from epicenter, local geological conditions, secondary effects and architecture. The depth of Durres earthquake of 26 November 2019 determined as 38 km is less damaging than an earthquake with 8 km because their energy dissipates before it reaches the surface. The depth generated by earthquakes represents an interest for seismotectonic studies especially in seismic hazard assesment [14]. It was recorded by Albanian Seismological Network, at seven stations [15]. Figures 5a-b show the North-South and East-West components of ground motions measured by the accelerometer station in Tirana, Albania's largest city. This accelerometer station is located at a distance of 34 km from the epicenter. It is located on ground Type C sites according to EC 8 with average shear wave velocities in the upper 30 m $V_{s30} = 312$ m/s [16].

Based on the earthquake time histories, the horizontal PGA recorded in Tirana was around 0.10 g, while in Durres it was around 0.20 g. However, the accelerometer station in Durrës was only able to record the earthquake for the first 15 seconds, due to a power outage caused by the earthquake (Fig 6). To make a clear interpretation of the earthquake impacts, Figures 6 shows the response spectra from recorded ground motions versus elastic response spectrum functions derived as per KTP-N.2-89 (Albanian seismic design code) for soils II and III, represents the ground types at the locations of the stations in Tirana and Durres cities.

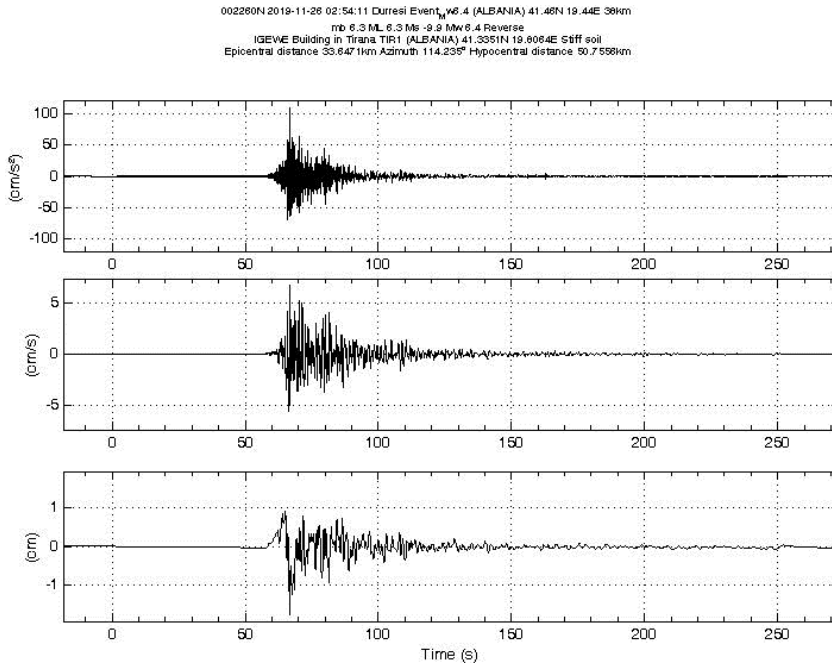
Figure 6 clearly shows that spectral ordinates recorded in Tirana station reaches up to two times more than the spectrum of the seismic code provisions at spectral periods 0.2 to 0.7 s. Buildings having a period in that range are expected to be experienced damages. On the other hand, the recorded spectrum values in Durres were below the code enforcements except around 1 sec. However, this representation might not be realistic due to the missing data after 15 seconds.

2. Description of the Studied Building

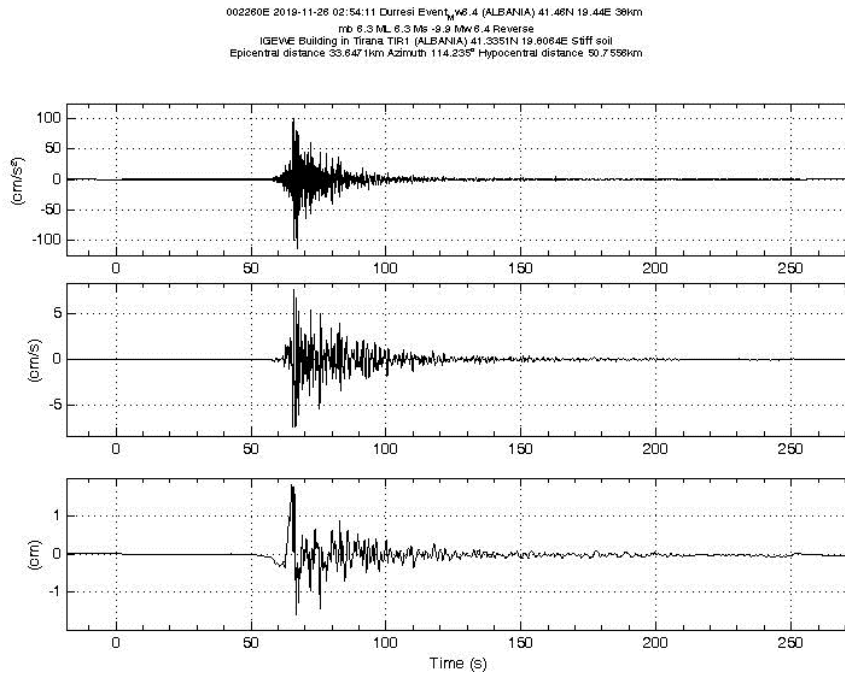
Built in 1970s, this building (Fig 7) is located in Tirana near "Rruga e Kavajes" and was constructed using red clay bricks as one of the most used template design unreinforced masonry (URM) building in Albania [17]. The building had five levels above the ground with the given planimetry (Fig 7-8). It has a regular story height of 2.80 m and an attic floor about 1 m, resulting in a total height above the ground of 15.00 m in corresponding of the main façade. There is no irregularity along the height of the building.

The structure of the studied template design consists of load-bearing walls that were continuous along the height of the building. The prevalent type of masonry is brick masonry, whereas the rare presence of stone masonry is observed in some pillars around staircase. The thickness of the load bearing walls is 38 cm from bottom to top of the building, as shown in Fig 8. Foundations are made of the stone masonry till the planking level of the basement. The floor slabs are lightweight precast slabs with a thickness of 15 cm each. The staircase is made of reinforced concrete and is supported by masonry load-bearing walls on three sides.

This building was lightly damaged by the September 21, 2019 seismic events that struck the regions of Albina. Cracks were mostly on non-load bearing elements and there was no strengthening intervention performed after the event.



November 26, 2019 Earthquake N-S component



November 26, 2019 Earthquake E-W component

Fig. 5 Ground motions recorded in Tirana during the November 26, 2019 earthquake (www.geo.edu.al/newweb/?fq=bota&gj=gj2&kid=20)

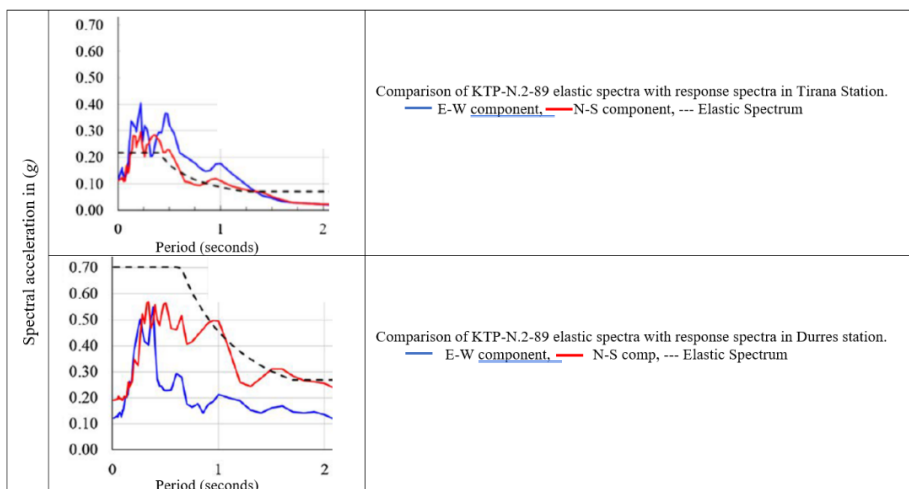


Fig. 6 KTP-N.2-89 response spectra of response spectra

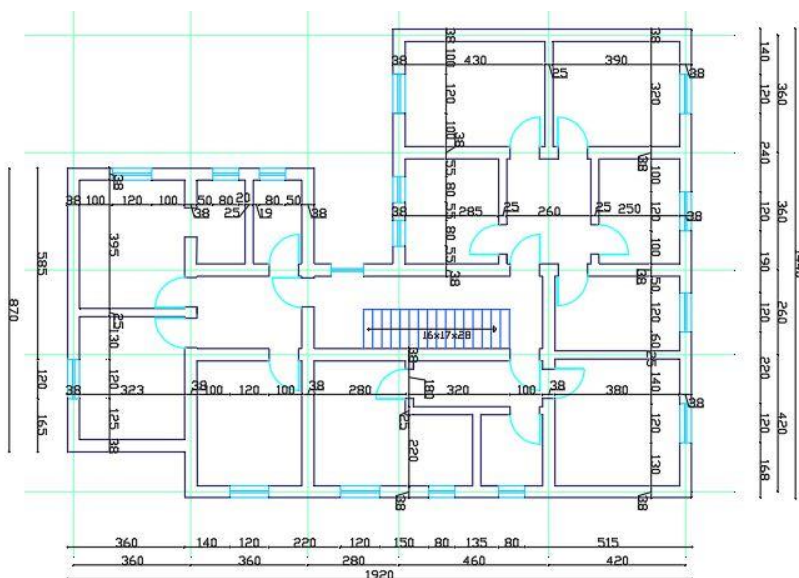


Fig 7. Plan view of the studied building

3. 2019 Earthquakes and Induced Damage

The 2019 Albania seismic sequence started on September 21, 2019, with moderate shakings (Mw 5.6) generated from a shallow focal depth by causing a widespread damage to the built environment at the outskirts of Durres city [14]. This first event had relatively slight effects without causing any casualties. Most of the damage was concentrated on non-structural elements of the RC and URM buildings structures [18-19]. Second severe shaking with Mw 6.4 struck the wider regions of Albania on November 26, 2019 (Fig 9). Its focal depth was about 20 km [20] causing an extensive damage with 51 fatalities and about 3000 injured [16]. The tremor was felt strongly in Tirana where the significant duration of

newly designed and old buildings. Damage patterns commonly encountered in masonry building typologies are shown in Figure 10-12.

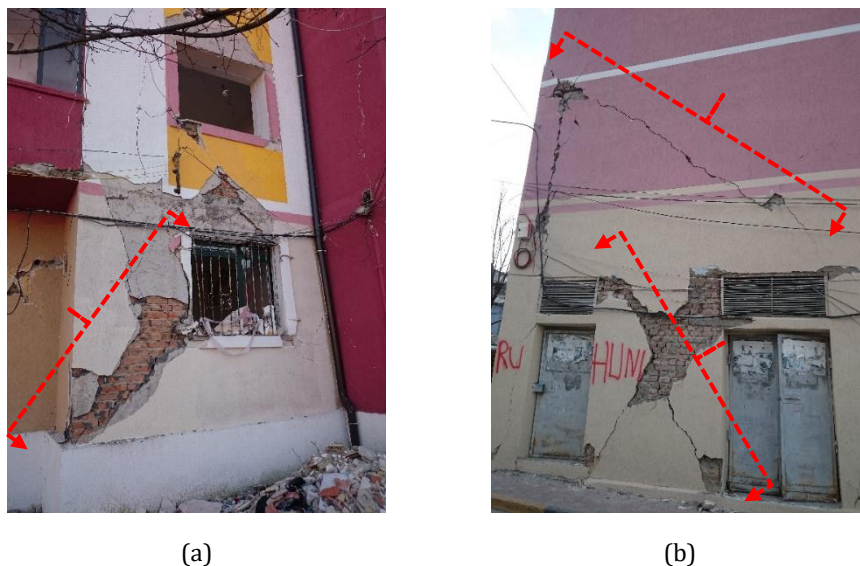


Fig 10. Heavy shear cracks on load bearing walls of the two multi-story masonry buildings

As shown in Figure 10, the load bearing walls were affected by serious cracks at both the raised-up ground and first floors. Most of the damaged buildings presented shear cracks which are diagonal developed along the entire thickness of the walls in both spandrels and piers (Fig 11a-12). Flexural cracks were also observed in several buildings. Moreover, out-of-plane mechanisms were very common both in URM and RC buildings resulting in partial or total collapse of masonry walls (Fig 11b). One of the commonly encountered highlights after the November 26, 2019 earthquake was the out-of-plane collapse of masonry walls (Fig 11b). In some cases, masonry walls collapsed without any vertical load other than their own weight. The most important reason for the out-of-plane collapse of URM walls was the lack of sufficient fastening of the wall with the diaphragm.



Fig. 11 (a) Extensive shear crack on load bearing wall and separation of two orthogonal masonry walls, (b) Heavily damaged partition wall in an URM building

Diagonal shear cracks were observed in several URM walls of residential buildings. Many masonry constructions had diagonal cracks in the infill panels and in the URM piers between the door/window openings (Figure 12). On-site examination of the mortar used on the part of the destroyed URM building has been carried out and the mortar can be easily crushed with naked fingers, indicating that the mortar has relatively low strength [22].

Figure 12 shows a typical diagonal "stair step" cracking of a solid brick wall; this is a sign that the wall has not been able to withstand shear stress from in-plane forces.



Fig. 12 (a) Heavily damaged load bearing wall (built by silicate bricks) and separation of wall and slab edges, (b) Heavily damaged load bearing wall in an URM building built by red clay bricks

4. Material and Mathematical Model

A 3D finite element model (FEM) of the template design was prepared in 3Muri [23]. A macro-modeling approach was adopted to simulated response of masonry. Based on the blueprints and site surveys done on the template design building, numerical model of the building was developed for structural analyses.

There are various analysis procedures to assess the nonlinear response of structures in which the geometric and material nonlinearity are taken into consideration (Fig 13). Analytical modeling of URM structures has always been a demanding task due to the presence of connections as the main source of material weakness, nonlinearity and discontinuity. A suitable model must consider both the response of the mortar and brick units and the interaction between them.

Two types of structural response need be considered in a suitable model: (1) response of masonry units; and (2) the response of the combined material. In recent years, great research has been done on theoretical methods supported by experimental tests.

Analytical techniques can be reviewed at the following three levels of refinement for wall models [24]:

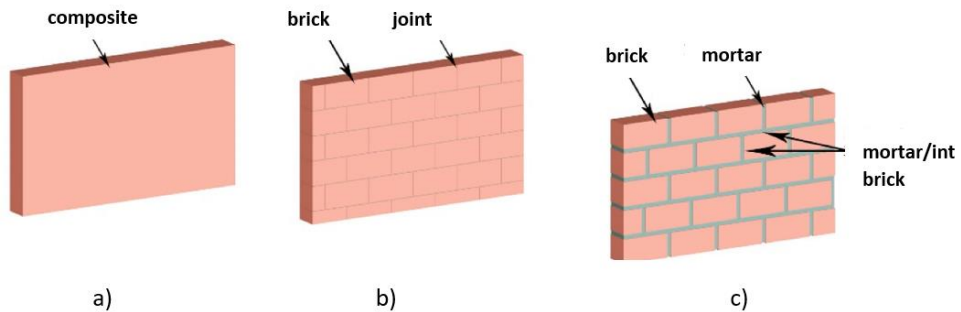


Fig. 13 Modelling techniques of masonry (a) Macro modelling, (b) simplified micro modelling, (c) micro modelling [20].

- **Macro-modeling:** In this approach, bricks, mortar and the brick–mortar interface are spread in a uniform band. Masonry is considered as a homogeneous, isotropic or anisotropic field. The influence of mortar joints as the main cause of weakness and nonlinearity cannot be taken into consideration using this approach. Although this method may be ideal for the analysis of large-scale masonry structures, it is not appropriate for the detailed analysis of small masonry panels, because of the difficulty of capturing all its expected failure modes.
- **Simplified micro-modeling:** In this approach, the structural components are considered as imaginary extended sections by uninterrupted members of the identical size as those of the original bricks merged with the actual joint thickness. The mortar joint is also modeled as a zero-thickness interface. This technique leads to a reduction in computational cost and gives a model applicable to a broader range of structures.
- **Micro-modeling:** In this method, bricks and mortar in the joints are described by continuum elements whereas the unit–mortar edge is characterized by discontinuum elements. While this approach yields more accurate results, the degree of refinement and the consequent analysis is computationally demanding, limiting its use to small-scale structures.

In this study, a simplified geometry of the building was adopted by following the macro-modeling technique since it is mostly used for analyzing large-scale structures and the effect of global factors. Such approach was followed by several researchers [25-26]. 3Muri [23] is utilized to execute the numerical analysis. The nonlinear macro-element method, suggested by Gambarotta and Lagomarsino (1996), allows with a partial number of DOF to describe the two main in-plane failure modes, shear-sliding, and bending-rocking mechanisms on the basis of mechanical characterizations. Deformations are assumed to be lumped on piers and spandrels, and they are connected with rigid nodes.

The macro-element applied for nonlinear static analyses is outlined with the kinematic model shown in Fig. 14. The 3D model of the studied masonry building, where it is apparent that masonry walls are modelled through a mesh of masonry piers and spandrels, is depicted in Fig 15.

In this software, piers are vertical load bearing elements that supports gravity loads and spandrels are straight components positioned between two vertically aligned openings. This a multi-purpose FE program dedicated for the linear and non-linear analysis of masonry buildings (Table 4).

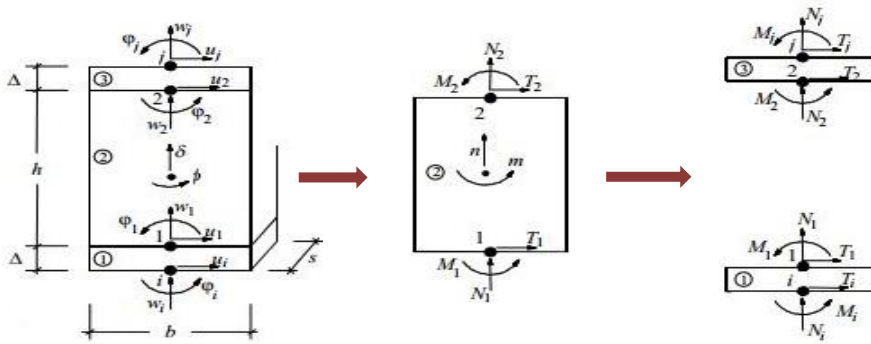


Fig. 14 Macro-element kinematic models in 3Muri

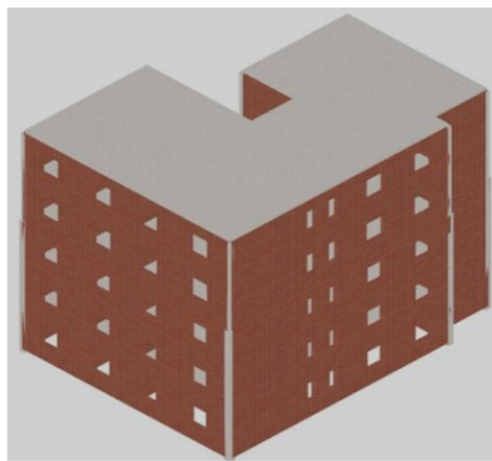


Fig. 15 Three-dimensional model of the building

Table 4. Brief outline of the strength criteria adopted by TREMURI

	Type of mechanism	Ultimate Strength
Spandrel elements	Shear strength	$V_u = f_{v0}ht$
	Rocking/Crushing	$M_u = \left[1 - \frac{H_p}{0.85dtf_{hm}} \right] \frac{dH_p}{2}$
Pier elements	Cracking (diagonal)	$V_{u,s} = lt\check{c} + \acute{\mu}N$ $V_{u,dc,1} = lt \frac{1.5\tau_0}{b} \left(1 + \frac{N}{1.5\tau_0lt} \right)^{1/2}$
	Rocking/Crushing	$M_u = \frac{Nl}{0.425f_m} \left(1 - \frac{N}{lt} \right)$
	Bed joint sliding	$V_{u,bjs} = l't\check{c} + \mu N$

where;

- h : height of the spandrel (transversal section),
- H_p : minimum value between the tensile strength of elements coupled to the spandrel
- criterion with: $\acute{\mu}$ and \check{c} equivalent cohesion and friction parameters,

- τ_0 : masonry shear strength and
- b : reduction factor as a function of slenderness,
- l' : length of section,
- t : thickness
- f_m : masonry compressive strength,
- Mohr-Coulomb criterion with:
- l' : length of compressed section,
- μ : friction coefficient of mortar joint,
- c : cohesion of mortar joint.

Masonry is a conventional composite building material which consists of masonry units and bonding material. Depending on the composition, it is grouped as unreinforced masonry [URM], confined masonry and reinforced masonry. URM consists of masonry blocks connected with mortar. The dominant type in the Albanian building stock is of unreinforced masonry like in many other European countries [27].

To define the strength and structural integrity of the building, fundamental mechanical characteristics of the masonry material are evaluated based on the experimental tests for the studied building. It comprises of compressive tests on brick units and mortar samples, as well as shear tests on small masonry triplets [28-29]. For the determination of the mortar compressive strengths, mortar samples were extracted from the areas where the connection between brick units and mortar has failed. Based on to the several experimental test results, bricks, mortar and masonry wall unit features to be used in mathematical modelling are summarized in Table 5:

Brick tests results: $f_{\text{brick}}=7.48$ MPa, $f_{\text{bt}}=1.71$ MPa

Mortar test results: $f_{\text{mortar}}=4.80$ MPa, $f_{\text{mt}}=1.10$ MPa.

The earthquake performance level of structures can be determined using linear and nonlinear analysis techniques. The response of the structure under seismic loads can be obtained more realistically with nonlinear analysis. This method can be broken in two ways as the nonlinear static (pushover) analysis and nonlinear time-history analysis. In this study, pushover analyses are deployed to estimate the seismic capacity of the structure.

In literature, various methods have been developed for the seismic performance of masonry buildings [30-33]. The earthquake capacity assessment of the studied URM building in this paper is performed through the recommendations provided by Eurocode 8 [34]. Three limit states, namely Limited Damage (LD), Significant Damage (SD), and Near Collapse (NC) are defined as stated in this code.

The modal analysis was performed, and the obtained results were presented for twelve modes of vibrations. The results of the linear modal analyses were synthesized in Table 6 in terms of periods and modal mass participating ratios.

Then, nonlinear static analyses were carried out to assess the seismic performance. The building was pushed by two lateral load patterns (Fig 16) in both orthogonal directions; namely: first mode shape distribution based on the fundamental mode shape of the structure, and a uniform load distribution to all stories. These analyses were done for three more combination: without eccentricity of gravity load and with eccentricity of two different levels. 24 analyses were deployed for all load combinations, along x- and y- global axis of the mathematical model, corresponding to the transverse and longitudinal directions of the building (Fig. 17-18).

Table 5. Material (masonry wall) properties considered in mathematical model

Material Property	Masonry wall properties
Specific weight (kN/m ³)	19.6
Modulus of Elasticity (N/mm ²)	2420
Compressive fracture energy (N/mm ²)	3.87
Shear Modulus (N/mm ²)	605
Poisson's ratio (-)	0.20
Compressive strength (N/mm ²)	2.42
Shear strength (N/mm ²)	0.36
Initial Shear strength (N/mm ²)	0.20
Tensile strength (N/mm ²)	0.12
Shear drift	0.004
Bending drift	0.008
Flexural strength with a plane of failure parallel to the bed joint (N/mm ²)	0.26
Flexural strength with a plane of failure perpendicular to the bed joint (N/mm ²)	0.19

Table 6. Modal analysis parameters

Mode	T [s]	M _x [%]	M _y [%]	M _z [%]
1	0,24719	0,03	76,97	0,00
2	0,21997	77,01	0,10	0,02
3	0,18609	1,93	0,95	0,06
4	0,09254	0,02	14,67	0,00
5	0,08298	13,94	0,04	0,85
6	0,07251	0,03	0,40	6,44
7	0,06949	0,56	0,02	19,71
8	0,06151	0,02	0,00	1,50
9	0,05878	0,02	0,00	35,10
10	0,05489	0,00	0,14	0,55
11	0,05313	0,02	3,25	1,24
12	0,05168	0,07	0,11	3,90

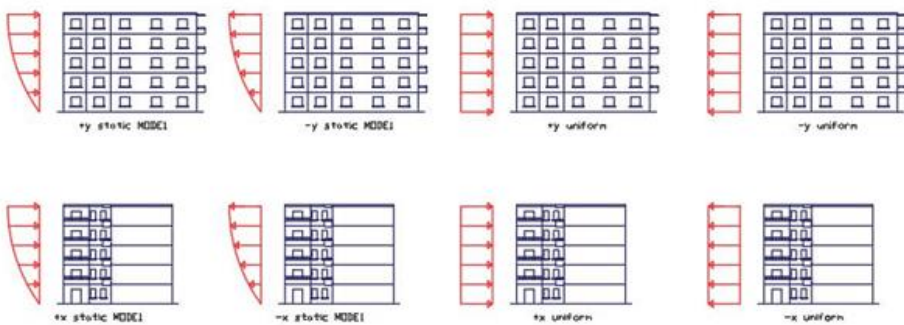


Fig. 16 Load patterns and different cases of pushover analysis

Control points located at the top of the building were adopted as control nodes during the analyses.

The worst cases were chosen as representing the pushover curves for both x- and y-direction of buildings and bi-linearized (Fig. 19). The seismic performance of the building was evaluated considering capacity curves and failure mechanisms.

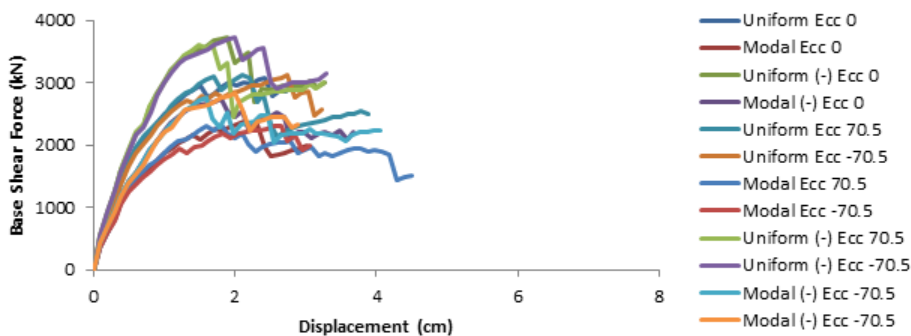


Fig. 17 Pushover analysis in x-direction

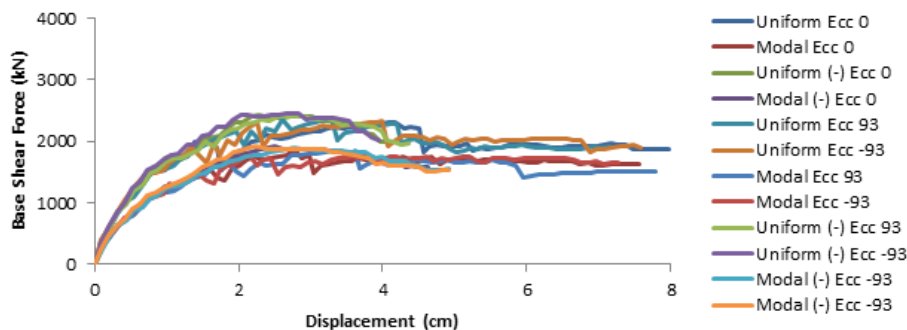


Fig. 18 Pushover analysis in y-direction

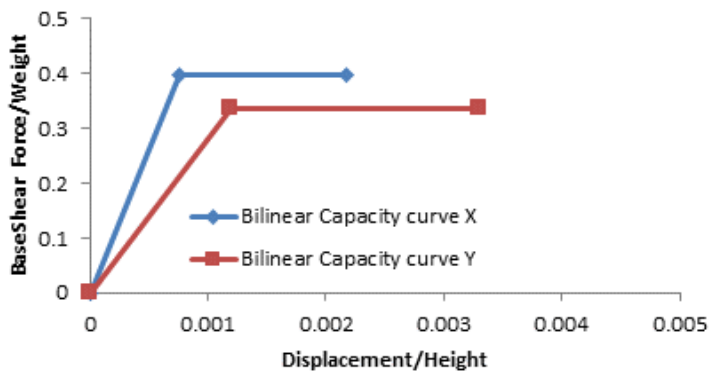


Fig. 19 Normalized bilinear capacity curves

In Figure 19, the maximum displacement attained were marked for both x- and y- directions. The building has a remarkable higher load bearing capacity in x- direction whereas the y- direction exhibits a more ductile response (Table 7).

Table 7. Response parameters for the studied URM building

Direction	Initial stiffness	Yield shear Force/Weight	Yield Disp./Height	Max Disp./Height	Ductility
x-	2386	0.413	0.00079	0.00181	2.30
y-	1334	0.333	0.00105	0.00303	2.89

5. Discussion of Analyses Results

The capacity curves estimated from the nonlinear static analyses in both orthogonal directions are presented in Figs 17-18. The load bearing capacity and the stiffness in x-direction is higher compared to y- direction of the building. These results could be expected since the intensity of the load bearing walls are dominant in this direction. Based on the capacity curves, a max load factor (base shear/seismic weight) of about 41% is observed in x- direction, while a max load bearing load bearing capacity of 0.33 is obtained in other orthogonal direction (Table 7).

With the objective to compare the damage observed induced by 2019 Albania earthquakes and estimated from numerical model, the damage evaluation was performed for the values of applied load comparable to the peak ground acceleration values recorded during the seismic events of September and November 2019. The seismic event of September 21 (Mw 5.6) was not considered since it did not cause a structural damage to the structure. It is essential to highlight that no damage accumulation because of the series of seismic events (Table 8) could be accounted for in the assumed mathematical approach.

Table 8 Recorded PGA values from the strongest shakings of 2019 Albania earthquakes

Date	Moment magnitude	Tirana station (g)	Durrës station (g)
September 21	5.1	0.03	0.10
September 21	5.6	0.18	0.12
November 26	5.4	0.02	0.04
November 26	6.4	0.12	≥0.20*

*: It is important to highlight that the Durrës station only recorded the event for the first 15 seconds due to an electricity cut triggered by the earthquake, thus the 0.20 g could be considered a lower bound value of the actual peak ground acceleration felt at the site.

In Figure 20, the damage state of the building from the last step of the pushover analysis is depicted. Bending damage and tension failure are dominant while a couple of walls and spandrels are damaged in shear.

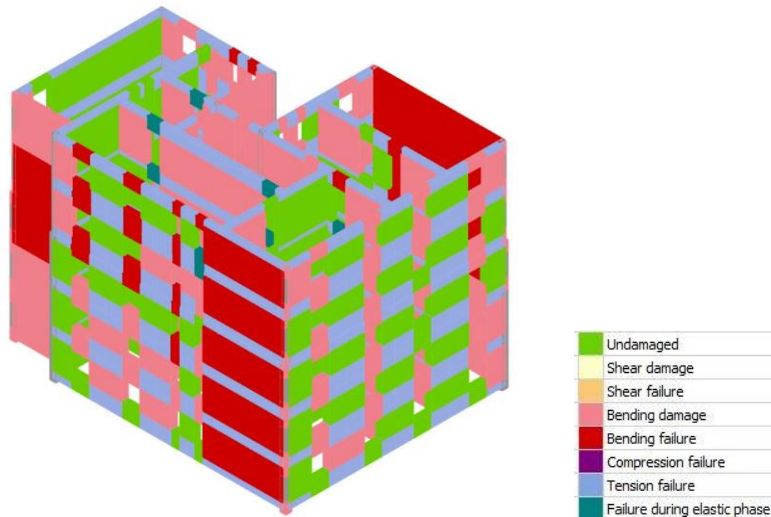


Fig. 20 Damage at maximum deformation capacity in 3D

Detailed damage distribution along the height of the walls of the studied building is shown in Figure 21. Building reached failure when perimeter walls reach their load bearing

capacity in both orthogonal directions. Failure is reached when all the right part of the perimeter wall fails in bending and also in the wall in the back part on upper levels.

In pushover analyses, it is assumed that appropriate connections are achieved between the connected elements and floors to accomplish the building's global in-plane response. However, the 3Muri software does not take into account the out-of-plane loss of stability of the walls.



Fig. 21 Distribution of damage and the failure mechanism of perimeter walls from pushover analysis

For the November 26 earthquake sequences, a global in-plan damage mechanism was observed for the template design building. The findings of the numerical analysis (Fig 20-

21) were compared to the real-life damage (Figs 23-25). The damage observed for the studied building comprise of bending, tensile and shear cracks occurring in both internal and external walls, in agreement with the damage observed on-site. From the comparison of the failure mechanism estimated by the pushover analyses and the modal behavior of the structure, it is observed a good consistency. First three modes of vibration did not include a local mechanism and ensure a global response. On the other hand, estimation of the out-of-plane response induced in a number of walls by the November 26, 2019 earthquake sequences was difficult in the numerical model since the presence of bond beams helps to prevent such behavior. It is believed that such failures occurred due to the fragmentation of materials, that was not considered in the mathematical model.



Fig. 22 The examined building



Fig. 23 Typical damage patterns observed at several locations of the studied template design

As mentioned before, the first event did not cause a visible damage whereas the November 26 produce slight-moderate damage on load and non-load bearing walls. Figure 12 and 13

exhibits a correlation between the mathematical model and real damage occurred in a number of walls induced by November 26, 2019 earthquakes.

Template building, which was damaged during the 26 November 2019 earthquake, has a 5-story unreinforced masonry building constructed by using solid clay bricks (Fig 12.). The construction of the buildings was completed in 1981. Generally, they have regular plans in elevation supported by load bearing unreinforced masonry walls. The load bearing walls were formed by solid clay bricks and the partition walls with hollow bricks. This building underwent changes including some plaster renewals and paintings after the September 12, 2019 earthquake. For that reason, from the outer parts, damages are not clearly observed with visual inspection.

As seen from the photos, the material quality especially the mortar is very weak and could not prevent the segregation of the bricks in several parts. Damage was concentrated on the 1st, 2nd and 3rd floors. Level of the damage on load bearing walls was severe whereas the partition walls were heavily damaged. Typical damage patterns like bending and shear cracks, spalling of mortar, separation of the load bearing wall segments especially over or under the openings are observed all over the first three floors and are shown in the Figs 23-25.



Fig. 24 Diagonal cracks extending over the height of the wall (left), spandrel damage patterns below the openings



Fig. 25 Heavy cracks (more than 3 cm separation) on load bearing walls and extensive damage on non- load bearing wall (left), serious damage observed on outer facade of the building in lower stories (right)

On the upper floors, it was observed that the doors are not closed properly due to the possible drift concentrations on load bearing elements. According to the inspections and damage surveys done on the buildings, the buildings have serious deficiencies which do not meet the conditions stipulated in Eurocode 8. Especially, on the first 3 floors, severe

damage patterns were observed on load bearing walls and very heavy damage was observed on partition walls. Material quality is extremely weak and caused degradation by time.

Using the capacity curves and the following the criteria in Eurocode 8-3, damage limit states of was assessed, and seismic capacity of the template design was predicted. Three limits states levels, i.e, “Damage Limitation (DL)”, “Significant Damage (SD)” and “Near Collapse (NC)” are identified for performance assessment (Table 9).

Table 9. Seismic spectral acceleration capacities for the corresponding performance levels

Estimated Earthquake level [17]	ag DL	ag SD	ag NC
2.0-2.2 m/s ²	1.18 m/s ²	2.02 m/s ²	2.614 m/s ²
	Passed	Passed	Not reached

Based on the detailed inspection on the studies area [17], the level of the PGA acceleration was found to be in the order of 2.0-2.2 m/s². The performance of the studied building is slightly exceeding *Significant Damage* and corresponding to *Near Collapse* level. The inspected damage and performance are in accordance with the results of analysis results from the numerical model.

6. Conclusions

This study presented the seismic evaluation of a commonly used template designed URM masonry building for residential purposes in Tirana, Albania. Template designs were developed during the communist era to save architectures fees and ensures quality control all of the country till 1990s. Selected template design is an interesting one to evaluate the ability of numerical methods to accurately estimate the behavior of existing masonry buildings under horizontal loads.

This URM building was damaged slight-moderate level by the seismic shakings that struck the central Albania during November 2019. The accumulated damage experienced by the template design building because of the serious seismic shakings was investigated in terms of damage patterns and story drifts. Based on the detailed site visits, it was observed that the buildings showed a global failure mechanism associated with the in-plane behavior of load bearing walls. Slight-moderate damage was induced by the November 26, 2019 earthquake sequences, which produced several cracks throughout the structure and triggered out of plane mechanism in some of the non-load bearing walls. The most important in-plane damage occurred on load-bearing walls of the located in y- direction of the building, in line with the PGA values and drift ratios in this orientation compared to the x- direction.

To represent the earthquake behavior of the building, a 3D finite element model was prepared, following a macro-modeling approach. Inherent material characteristics were determined through the experimental tests recommended in in the international guidelines. Then, nonlinear static analyses were deployed in both orthogonal axes of the building. Based on the results of the pushover analyses, weak orientation of the building was identified in y- axis as the vulnerable direction. Relatively lower stiffness and load-bearing capacity were observed in y- direction. The damage was evaluated for values of lateral load considering the PGA values recorded during the November 26, 2019 seismic shakings.

To sum up, observed damage and the estimated failure mechanism in the mathematical model are consistent with each other. As for the out-of-plane mechanism triggered by the November shakings, it is assumed that its occurrence in the mathematical model was

prevented by the presence of bond beams modeled to remain in elastic mode. Moreover, such a response may have occurred from the possible disintegration of the masonry materials, that was not taken into consideration in the numerical model. On the other hand, it should be kept in mind that pushover analysis is an approximate method and findings from such a method may not perfectly simulate the structural performance of the buildings under a particular ground motion. Especially, buildings having irregular floor plans may lead to misleading results due to the influence of torsional mode effects even though this problem might be partially resolved with the use of rigid diaphragms.

References

- [1] Bilgin H, Hysenlliu M. Comparison of near and far-fault ground motion effects on low and mid-rise masonry buildings. *Journal of Building Engineering*. 2020;(30):101248.
- [2] Lourenço PB, Mendes N, Ramos LF, Oliveira DV. Analysis of masonry structures without box behavior, *International Journal of Architectural Heritage*, 2011;(5), pp 51-59.
- [3] Bracchi S, Rota M, Penna A, Magenes G. Consideration of modelling uncertainties in the seismic assessment of masonry buildings by equivalent-frame approach. *Bull Earthquake Eng* 13, 3423-3448 (2015). <https://doi.org/10.1007/s10518-015-9760-z>
- [4] Işık E, Harirchian E, Arkan E, Avcil F, Günay, M. Structural Analysis of Five Historical Minarets in Bitlis (Turkey). *Buildings* 2022, 12, 159.
- [5] Lagomarsino S, Giovinazzi S. Macroseismic and mechanical models for the vulnerability and damage assessment of current buildings. *Bull Earthquake Eng* 4, 415-443 (2006). <https://doi.org/10.1007/s10518-006-9024-z>
- [6] Shkodrani N, Bilgin H. Seismic performance of existing low-rise URM buildings considering the addition of new stories. *Structural Engineering and Mechanics, An International Journal*, 2021; 79(6): 767-777.
- [7] Aliaj S, Kociu S, Muco B, Sulstarova E. Seismicity, Seismotectonics and Evaluation of Seismic Hazard in Albania, Tirana: Academy of Sciences of Albania, 2010.
- [8] Métois M, Benjelloun M, Lasserre C, Grandin R, Barrier L, Dushi E, Koci R. (2019) Subsidence associated with oil extraction, measured from time-series analysis of Sentinel-1 data: case study of the Patos-Marinza oil field, Albania. *Solid Earth Discuss* 11:363-378. <https://doi.org/10.5194/se-11-363-2020>
- [9] Aliaj S, Adams J, Halchuk S, Sulstarova E, Peci V, Muco B. Probabilistic seismic hazard maps for Albania, in 13th World Conference on Earthquake Engineering, Vancouver, B.C., Canada, 2004.
- [10] Duni L, Kuka N, Begu E, Probabilistic seismic hazard assessment of Albania, *ResearchGate*, pp. 465-479, December 2012.
- [11] Marku S, Ormeni R, Panza GF. (2021). "Seismic characterization of Tirana - Durrës - Lezha region (northwestern Albania) and analysis effort through NDSHA method". *Earthquakes and sustainable infrastructure. Neodeterministic (NDSHA) aproch guarantes prevention rather than cure. Elsevier. Elsevier.com/book and journals*, 2021.
- [12] Öztürk S, Ormeni R. (2021). A comprehensive spatiotemporal evaluation of the current earthquake activity in different parts of the Frakull-Durrës fault zone, Albania. *BALTICA Volume 34 Number 1 June 2021: 58-70. Impact Factor (Thomson Reuters, JCR)*.
- [13] Ormeni R, Klodian S, Ismail H, Erald S. (2020). Strong earthquakes in Durres during 2019 and their associated seismogenic zone. *International Conference on Geosciences and Earthquake Engineering, Challenges for Balkan Region (ICGEE) Tirana, November 26-28, 2020*.
- [14] Ormeni R (2020) Assessment of seismoactive layers generated by the 2019 series of earthquakes in Durres. *International Symposium on Durres earthquake and eurocodes, Tirana, September 21-22, 2020*.

- [15] Duni L, Theodoulidis N. (2019) Short Note on the November 26, 2019, Durrës (Albania) M6. 4 Earthquake: Strong Ground Motion with Emphasis in Durrës City. EMSC online report.
- [16] Freddi F, Novelli V, Gentile R, Veliu E, Andreev S, Andonov A, Greco F, Zhuleku E. Observations from the 26th November 2019 Albania earthquake: the earthquake engineering field investigation team (EEFIT) mission. Bull Earthquake Eng 19, 2013-2044 (2021). <https://doi.org/10.1007/s10518-021-01062-8>
- [17] Hysenlliu M. (2021), "Vulnerability Assessment of Current Masonry Building Stock in Albania", Ph.D. thesis, 426 pages, Epoka University, Tirana, Albania.
- [18] Leti M, Bilgin H. Performance of RC and Masonry Structures During 2019 Durrës Earthquake. Civil Engineering Beyond Limits (CEBEL), 2022; 3:1.
- [19] Shkodrani N, Bilgin H, Hysenlliu M. Influence of interventions on the seismic performance of URM buildings designed according to pre-modern codes. Res. Eng. Struct. Mater., 2021; 7(2): 315-330.
- [20] USGS (2020) ANSS Comprehensive Earthquake Catalogue (ComCat). <https://earthquake.usgs.gov/data/comcat/>
- [21] Ormeni R, Hoxha I, Naco P and Gega D, 2019. The strong Earthquake of 26 November 2019 (Mw 6.4) and its associate active tectonic of Durres region IN Albania. Presentations at the EGU General Assembly 2020, https://presentations.copernicus.org/EGU2020/EGU2020-6096_presentation.pdf.
- [22] Bilgin H, Shkodrani N, Hysenlliu M, Ozmen H.B, Işık E and Harirchain E. "Damage and performance evaluation of masonry buildings constructed in 1970s during the 2019 Albania earthquakes", Engineering Failure Analysis, Volume 131, January 2022.
- [23] Lagomarsino S, Penna A, Galasco A, Cattari S (2013). TREMURI program: an equivalent frame model for the nonlinear seismic analysis of masonry buildings. Eng Struct 56: 1787-99.
- [24] Lourenço P.B., P. Roca, C. Modena, S. Agrawal, Structural Analysis of Historical Constructions, New Delhi, 2006.
- [25] P.G. Asteris, M.P. Chronopoulos, C.Z. Chrysostomou, H. Varum, V. Plevris, N. Kyriakides, V. Silva, Seismic vulnerability assessment of historical masonry structural systems, Eng. Struct. 62-63 (15) (2014) 118-134, <https://doi.org/10.1016/j.engstruct.2014.01.031>
<https://doi.org/10.1016/j.engstruct.2014.01.031>
- [26] Valente M, Milani G (2018) Seismic Response Evaluation and Strengthening Intervention of Two Historical Masonry Churches. In: Milani G, Talierno A, Garrity S (eds) 10th International Masonry Conference. Milan.
- [27] Hysenlliu M, Bidaj A, Bilgin H. Influence of material properties on the seismic response of masonry buildings. Res. Eng. Struct. Mater., 2020; 6(4): 425-437.
- [28] American Association State Highway and Transportation Officials Standard, Designation: C67 - 09.: Standard Test Methods for Sampling and Testing Brick and Structural Clay Tile, 2008.
- [29] EN 1996-1. European masonry design code. (2005). "Design of masonry structures. Part 1: General rules for reinforced and unreinforced masonry structures".
- [30] EN 1998-1. European seismic design code. (2004). "Design of structures for earthquake resistance. Part 1: General rules, seismic actions and rules for buildings".
- [31] ATC (1996), "Seismic Evaluation and Retrofit of Concrete Building," Report (ATC-40), Applied Technology Council, California, Vol. 1, USA".
- [32] FEMA-356 (2000), Prestandard and Commentary for the Seismic Rehabilitation of Buildings, Federal Emergency Management Agency".
- [33] FEMA-440 (2005), Improvement of Nonlinear Static Seismic Procedures, ATC-55, Washington.
- [34] EC8-3, Eurocode 8. Design provisions for earthquake resistance of structures. Part 3: Assessment and retrofitting of buildings, European Committee for Standardization, Brussels, Belgium; 2005".



Research Article

Nonlinear behaviour of reinforced concrete moment resisting frame with steel brace

Birendra Kumar Bohara^{1,a*} Prasenjit Saha^{2,b}

¹M. Tech in Structural Engineering Sharda University

²Department of Civil Engineering, Sharda University, India

Article Info

Article history:

Received 04 Apr 2022

Revised 30 May 2022

Accepted 24 Jun 2022

Keywords:

Concentrically braced frames;

Steel braced frames;

overstrength factors;

ductility factors;

yielding limit;

Abstract

In this study, the reinforced concrete moment-resisting concentrically braced frames (RC-MRCBFs) were used with V braced frames in new constructions. The core objective of this study is to understand the earthquake behavior of the RC-MRCBFs in steel V braced frames. The buildings were assumed to be located in Indian city and were designed by using Indian seismic code. The study also investigates the overstrength and ductility reduction factors, failure mapping and collapse mechanism to understand the seismic behavior of the capacity curve, maximum top story displacements and inter-story drift of the buildings. After studying the parametric study of the 4 to 16-story buildings with a nonlinear analysis tool it was observed that to get the effective braced frame with expected failure mechanism, ductility, the columns should be designed such that, it resists at least 50% base shear in a dual system. In conclusion, it was shown that a story yielding $\Delta y = 0.0024$ was the limiting value obtained for RC-MRCBFs when V shape steel bracings were used. It needs some improvements in the Indian seismic codes to develop adequate seismic behaviors of RC-MRCBFs for any steel braced frames.

© 2022 MIM Research Group. All rights reserved.

1. Introduction

Construction of RC structures with a shear wall (SW) and steel structures with steel bracing are common practices in India. Moment resisting frame (MRF), SW and steel braced frames are used to resist the earthquake load and wind load to increase the seismic performance of the structure. It seemed that the earthquake load damaged the buildings and also sometimes collapse. It is because if the buildings do not resist the lateral seismic force, the buildings collapse or fail easily. To improve the lateral load capacity of the buildings, the generally designer used the shear wall in the RC structure. However, after successfully assigning the steel bracing in RC building as a retrofitting technique the result shows good seismic behaviors, the steel bracing is used as new construction as well. In the late 1980 and 1990, most of the research studies were focused on the retrofitting and strengthening of the RC frame with a different type of steel bracing. Both experimental and numerical studies are presented in existing buildings. Steel bracing improves seismic behaviors which are economic to use as compared to others. There are several types of steel bracing systems of which mainly concentrically braced and eccentrically braced frames are the most popular form of bracing. The concentric bracing frame consists of the bracing which is located in the plane of the frame and both the end of the bracing joined at the end of the frames. It provided the stability and stiffness of the building and reduce the lateral displacements effectively. In RC structure the concentric bracing is widely used because it is very easy to use and is also economically sound. Different configurations of bracings are used in a structure such as X bracing, V bracing, inverted V bracings (chevron),

*Corresponding author: bbohara2@gmail.com

^a orcid.org/0000-0002-4654-3428; ^b orcid.org/0000-0002-1238-5636;

DOI: <http://dx.doi.org/10.17515/resm2022.383st0404>

Res. Eng. Struct. Mat. Vol. 8 Iss. 4 (2022) 835-851

diagonal bracing, multi-X bracings and K bracings. Some other concentrically braced frames such as Buckling restrained braced (BRBs) frame, post-tensioning braced, lightweight BRBs, etc. are used in building construction as lateral load resisting systems. Bracings are also classified, based on the connection with beam and columns which is external bracing and internal bracings. When the bracing member is directly inserted into the enclosed space of the columns and beams, this is known as internal bracing and if the members of bracing are connected to the face of the beam and columns externally known as external bracings.

The retrofitting technique is generally used in the existing buildings to improve the strength and stiffness of the member or whole buildings [1]–[3]. It is necessary to retrofit the building. There are several methods of retrofitting such as column jacketing, providing shear wall, and damping. Some researchers found that applying the bracings in the RC structure, improves the seismic performance [4–6], and also is a cheap and effective method for restrengthening the buildings. Providing the steel bracing with a suitable slenderness ratio in RC frames shows the good seismic behaviors [7, 8]. Another researcher Bush TD et al. (1991) [9] implemented the experimental analysis of X braced non-ductile 2/3 scaling two bays frames. The experimentation was performed under the lateral loading and cyclic loadings and the researcher found that when 40-30% of base shear was carried by the columns and the remaining base shear in bracing. And researcher suggested that for best performance and result in the frame, it needed at least 50% base shear capacity in columns. Canales MD and R.B. de la (1992) [10] observed the telephone structure which was retrofitted by the steel bracing in 1992 Mexico. The paper concluded that when the steel bracing was applied in the existing RC buildings, it reduced the inter-story drift and displacement effectively under the earthquake loading. Rahimi, M.R. Maheri (2018), (2020) [11, 12] investigated the positive and negative effects of steel bracing in the RC frame when bracing is used in retrofitting techniques. The paper observed that the bracing improves the shear capacity, and ductility capacity, and also helps in the reduction of drift and top story displacement easily.

Many researchers have done very good research on the RC frame with steel bracing as lateral load resisting members [13–16]. The research gives very useful information about the braced behaviors in RC MRCBFs with different types of steel bracing [17–19]. It was observed that when the X and knee steel bracing was applied in the ductile RC frame, its strength (yielding capacity) and base shear capacity increased and also the maximum displacement of the building was decreased [20]. Godinez. E.A., and Tena-C. A. (2008) [21] performed the four to sixteen-story RC buildings with chevron shape bracing. The researcher considered the ductile RC-MRCBFs and analyzed with pushover analysis. The structures were considered the soft soil profile in Mexican cities with their own code and conduct. The paper observed the overstrength factor, yielding mechanism, drift curves and successfully designed the RC-MRCBFs when columns resist at least 50% of the total base shear strength. In the structures, the researchers also considered the three case studies such as the 25% base shear in bracing, 50% and 75% base shear in bracing, and remained base shear considered in moment resisting frames such as columns. Paper successfully designed the ductile RC-MRCBFs with an inverted V bracing frame when the minimum base shear force was resisted by the columns. The researcher also observed that structure only shows required suitable failure mechanisms such as weaker bracing, weak beam, and strong columns when the columns resist a minimum 50% base shear of the slender structure [22, 23]. For serviceability limits paper gives the acceptable drift limits 0.2% for new construction of the RC-MRCBFs buildings. Alike previous research by the same researchers they found that medium-rise building only gets required failure mechanisms such as the weaker bracing- weak beam and strong columns [23]. Researchers used the hysteretic energy dissipation device (HEDD) attached in inverted V braced configurations.

Researchers observed the structural behaviors when it was attached with steel bracing, HEDD, base shear and seismic weight ratio (V/W) considered as $1/10$ [24]. Godínez, EA and Tena (2016) [25] studied the redundancy factor of the RC-MRCBFs having inverted V braced frames. Eskandari et al. (2017) [26] studied the four-story, eight-story, 12 stories and sixteen-story RC frame with diagonal bracing that was used and analyzed by the time history analysis and Nonlinear pushover analysis (NPA) for seismic analysis. The ground motion was selected so that they were far faults and near faults motions and studied the inter-story drift of the buildings. E. A. Godínez, A. Tena (2019) [27] in this paper, the researcher studied the RC-MRCBFs in a Mexican city and used Mexican codes. The structures have 4 to 20-story RC buildings with X bracings. K. Du, et al (2020) [28] studied the RC frame with the BRBs and observed the effect of forwarding directivity and fling step. The researchers used the diagonal, inverted chevron and chevron types of steel bracing in the RC frames.

In previous research of Godínez and Tena, (2010) and (2016) Godínez et al., 2012, [22], [23], [25], [29] they were focused on pushover and dynamic analysis of RC/MRCBFs using the chevron SB and applied MFDC-04 codes. Eskandari R. et al. (2017) [26] investigated the diagonal steel bracing in concrete frame structure and analysis based on the Iranian Seismic Design Code. K. Du, et al., (2020) [28] investigated the inverted V, diagonal, and V and observed the effect of forwarding directivity (FD) and fling-step (FS) on the RC structure having buckling-restrained braces (BRBs). E. A. Godínez and A. Tena (2019) [27] studied X steel bracing in MRCBFs by using MFDC-04. Except the K. Du, et al (2020) [28] other literature mainly focused on developing the guideline of the new design of RC braced frames. Therefore, the research on the moment-resisting frame with concentrically braced frames using V-shape steel braced with ductility property permits to completion of the research, which is commonly used in bracing arrangements in India and world.

In this paper the nonlinear lateral load behavior of low (4 story) to medium-rise (16 story) moment-resisting RC frames with a concentrically braced structure where steel V bracing (inverted chevron), situated high earthquake zone in India. The study focused on the Indian standard code and some international design codes. The study of key design parameters such as building capacities, strength and overstrength and ductility factors and story displacement corresponding to various states, failure mapping and plastic hinge formation in beams and columns are estimated. The study considers the provision, which is mentioned in IS 1896 (part 1) clauses 7.2.7 dual system, MR frames (columns) are designed to resist at least 25% designed base shear independently and suggested some findings based on the results obtained.

2. Methodology and Analysis

To design the ductile RC-MRCBFs, a capacity design methodology is used to get the expected failure mechanism of a weaker brace-weak beam-strong column. There is a lack of general design guidelines for many international codes and IS codes to design ductile RC moment-resisting concentrically braced frames. The methodology proposed by Godínez and Tena, published in (2010), (2012), and (2019) [22, 23, 25] is known as the 'Conceptual capacity design' methodology which is used in this study. In a previous study, Godínez Domínguez and Tena-Colunga used this methodology in inverted V and X bracing, also R. Eskandari et al. (2017) [26] used the same method to design diagonal bracing in RC buildings. The bracing which is the main earthquake resisting member is designed as the weakest member in the RC-MRCBFs system. Other members Beam and columns are considered the strongest member. It is because of getting an expected failure mechanism for ductile design. There are four elements for earthquake resisting which are designed in such a way, to get the expected failure mechanism. These elements are bracings, beams, columns, and connection design of beam, columns, & bracing.

2.1. Lateral Shear Strength Contribution

According to IS 1896 (part 1) clauses 7.2.7 dual system, MR frames (columns) are designed to resist at least 25% designed base shear independently. In this study, at each building height, three different lateral shear strength values are assigned in the moment-resisting frame and bracing system. In RC-MRCBFs, lateral shear strength percentage resist by the columns are given below:

- In RC-MRCBFs up to 25% of shear force is provided in a MR frame (column). This is the almost minimum shear force balance in columns and which is less than the strength provided in the bracing system. However, this balance is allowed in IS code but some international codes do not allow for ductile design.
- Nearly up to 50% of shear force resist by the MR frame (column).
- Up to 75% of the shear force is provided in the moment-resisting frame (column).

Above three shear strength balances are used to know the seismic behavior of the RC-MRCBFs at the different shear values in their dual system in both structural systems and the height of the building [20, 22]. It also reviews the minimum strength requirement in the dual system, especially in V braced RC-MRCBFs according to the IS code for ductile designing.

2.2. Geometry and Design Parameters of the Buildings

12 RC-MRCBFs of V braced buildings are designed by using the Indian standards code. For seismic design IS 1896 part1 [30], reinforced concrete design IS156, IS800 for steel design, ductile design guideline IS 13920:2016 [31], IS 4923:1997, are used to achieve the required seismic behavior. The regular RC buildings with the concentrically braced frame using V-steel bracings are designed for the soft soil's condition, using response reduction factor $R=4.5$ [30]. Which is corresponding to a 5% damping ratio. The building models are four-story, eight-story, twelve-story, and sixteen-story regular RC-MRCBFs having 7m spans in each X and Y direction and 3.2 m story height. Outer RC frames consist of steel bracing which is used to resist earthquake loads. The plan and elevation view is given in Figure 1. RC-MRCBFs are designed using various lateral force ratios of base shear in columns/base shear in bracings. The H/L (slenderness ratio) mainly affects the seismic behavior of the building so different height ranges of buildings are studied carefully. The live load and dead load are considered as follows:

Live load = 5 kN/m^2 (business and office building)

Live load at roof level= 2 kN/m^2

Finishing dead load = 2.5 kN/m^2

The material property used in the RC and steel members for design are given in Table 1, where E_c and f_{ck} are the modulus of elasticity and compressive strength for concrete respectively, f_y is the yield strength for steel reinforcement bar used in RC structure, f_{ys} and E_s are the yield stress and modulus of elasticity of steel bracing respectively.

The design section of RC-MRCBFs changes along the height to reduce the strength and stiffness irregularities along with the height as much as possible. The sectional of columns and beams change their steel reinforcement or cross-section every four stories for eight, twelve, and sixteen-story buildings. The box cross-sectional of steel V-bracing changes its thickness every four stories for eight, twelve, and sixteen story frames, to get the design optimum as much as possible. The designed section of beam, columns and bracings are taken from the thesis (see Tables 2 to 5) [14].

Table 1. Material Properties

Building height	Concrete member properties			Steel member properties		
	f_{ck} , MPa	E_c , MPa	f_y , MPa	f_{ys} , MPa	E_s , MPa	μ
4 to 16-story models	25	$5000\sqrt{f_{ck}}$	415	250	210000	0.3

To design the RC MRCBFs, the following seismically design procedure was considered.

- Initially all design factors and modeling parts are determined.
- Calculate the design equivalent lateral force.
- Calculate the percentage of shear strength provided separately in the moment frame and steel bracing.
- Design the braces according to their lateral base shear contribution.
- Now design the beams and columns for their base shear contribution in frame structure and also consider the strong column weak beam principle.
- Check ta allowable inter-story drift limit and some of the steps are repeated to get the required design section.

Table 2. Detailing of 4 Story Buildings

Model	Story	Beams	Bracing	Columns
				Section
VF25D4	1-3	350X450	180X180X8	450X450
	4	300X350	180X180X5	350X350
VF50D4	1-3	350X450	113.5X113.5X6	500X500
	4	300X350	113.5X113.5X4.5	400X400
VF75D4	1-3	350X500	72X72X4.8	600X600
	4	300X400	72X72X4	500X500

Table 3. Detailing of 8 Story Buildings

Model	Story	Beams	Bracing	Columns
				Section
VF25D8	1-4	350X450	210X210X16	570X570
	5-8		210X210X12	400X400
VF50D8	1-4	400X500	180X180X6	600X600
	5-8		180X180X5	550X550
VF75D8	1-4	400X500	100X100X5	700X700
	5-8		100X100X4	650X650

To categorize the 12 models, a cryptogram is well-defined as VFpDn, where VF specifies V bracing frame, p known as shear strength percentage provided in columns, D represent the direction (X and Y axis) as shown in (Figure 1), and 'n' defines the number of floors. For example, VF25X4.

Table 4. Detailing of 12 Story Buildings

Model	Story	Beams	Bracing	Columns Section
VF25D12	1-4	400X500	300x300x22	650x650
	5-8	400X450	300x300x20	570x570
	9-12	375X450	300x300x18	500x500
VF50D12	1-4	400X500	200X200X8.5	675X675
	5-8	400X450	200X200X6.5	625X625
	9-12	375X450	200X200X5	550X550
VF75D12	1-4	400X500	113.5X113.5X6	780X780
	5-8	400X450	113.5X113.5X5.4	750X750
	9-12	375X450	113.5X113.5X4.8	725X725

Table 5. Detailing of 16 Story Buildings

Model	Story	Beams	Bracing	Columns Section
VF25D16	1-4	400X550	350X350X30	700X700
	5-8	400X500	350X350X28	650X650
	9-12	400X450	350X350X26	600X600
	13-16	400X450	350X350X24	575X575
VF50D16	1-4	400X550	200X200X14	750X750
	5-8	400X500	200X200X12	700X700
	9-12	400X450	200X200X10	650X650
	13-16	400X450	200X200X8	600X600
VF75D16	1-4	400X550	125X125X8	900X900
	5-8	400X500	125X125X6	875X875
	9-12	400X450	125X125X5	850X850
	13-16	400X450	125X125X4	825X825

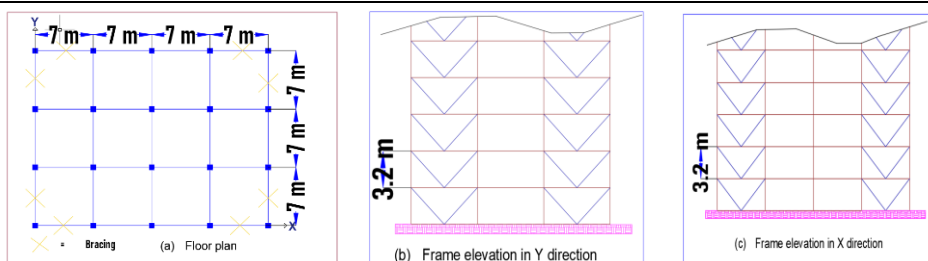


Fig. 1 Floor plan and elevation view in dual systems under study (all units are in meter (m))

3.1. Nonlinear Static Analysis

Mwafy and Elnashai (2001) [32] studied both nonlinear static and time history analysis of the RC building one of the conclusions is suggested that NPA is more appropriate for the low period that is low to medium-rise regular RC frame structure. A similar result also suggested by Goel RK, Chopra AK (2004) [33]; Chopra and Goel RK. (2002) [34]; Godínez & Tena (2010) [22] used NPA to study the behavior of 4 to 24 stories, RC-MRCBFs with chevron steel bracing. Eskandari et al. (2017) [26] conducted nonlinear static analyses for

4- to 16 stories in RC-braced, Eber Alberto Godínez et al. (2019) [27] in 4 to 20 stories RC, X braced frame. Nonlinear static analyses help to obtain the story and global shear, drift curve, yielding mapping, overstrength factor, ductility factor, peak story drift, and global ductility capacity. Uang CM (1991) [35] developed the design of the formula of response reductions factor (R) and displacement factor (Cd). And also studied the structural strength factor and structural ductility factor ($R\mu$).

Table 6. Characteristics of the Investigated Buildings

Model	Slenderness ratio H/L	Shear distribution		Time period (t)s	Model	Slenderness ratio H/L	Shear distribution		Time period (t)s
		Columns %	Bracing %				Columns %	Bracing %	
VF25X4	0.46	25	75	0.425	VF25X12	1.37	25	75	1.12
VF50X4	0.46	50	50	0.512	VF50X12	1.37	50	50	1.34
VF75X4	0.46	75	25	0.547	VF75X12	1.37	75	25	1.54
VF25Y4	0.61	25	75	0.426	VF25Y12	1.83	25	75	1.11
VF50Y4	0.61	50	50	0.514	VF50Y12	1.83	50	50	1.35
VF75Y4	0.61	75	25	0.552	VF75Y12	1.83	75	25	1.55
VF25X8	0.91	25	75	0.754	VF25X16	1.83	25	75	1.61
VF50X8	0.91	50	50	0.908	VF50X16	1.83	50	50	1.74
VF75X8	0.91	75	25	1.035	VF75X16	1.83	75	25	1.99
VF25Y8	1.22	25	75	0.752	VF25Y16	2.44	25	75	1.61
VF50Y8	1.22	50	50	0.914	VF50Y16	2.44	50	50	1.75
VF75Y8	1.22	75	25	1.047	VF75Y16	2.44	75	25	2.01

This paper used the NEHRP and the Uniform building code (1988) recommended provision. One of the conclusions of this paper is ‘the structural overstrength factor which is governed by on structural redundancy, the story displacement or Inter story drift limitations, load combination, strain hardening, and other parameters’. 4- to 16 stories buildings were analyzed in ETABS 2018. To know the seismic behavior of the buildings, NPA is used. In beam and columns, flexural and shear hinges are provided and in bracing axial hinges are provided. Where the maximum lateral load and resultant moments are present, the flexural (M3) plastic hinges are assigned to each end of the beam and in columns, axial biaxial moment (P-M2-M3) plastic hinges are placed on each end. In the ETABS software, the hinge length is defined to obtain the inelastic performance by the integration of the plastic curvature and plastic strain. The hinge properties in the software are defined as a force-displacement or moment rotation way and assigned in the fixed location in the length of beam bracing or columns. The number of hinges and location of hinges is highly affecting the analysis time and behavior of the structure so assigning the hinges needs to be careful. In the ETABS, the hinges are defined the various way. Auto hinges property, user-defined hinges property, and program generated hinges properties are the way to provide the hinges in the ETABS software. Structures show different performance levels according to their structural and non-structural components. The capacity curve help to understand the performance level of the structures, different structural and non-structural members have their performance level under the loading. Figure 2. AB- linear range from the unloading state (A) to the yield state (B). B to C represents inelastic ranges CD indicates the rapid decrease in strength resistance and followed by a reduced resistance from D to E. some key points Immediate Occupancy (IO), Life Safety (LS), and Collapse Prevention (CP) are also considered. These points are generally found when dividing B-C into four parts as shown in Fig. 2, and represent IO, LS, and CP which are states of each hinge. At the Operational level in structure means, in the building, there is no major damage or crack in structural members. The structure has its original strength at this level. At the immediate occupancy level, the structural members and walls have some minor cracks observed. The structure has no any permeant drift and also has original strength. At the life safety level, the structure loses some original strength and stiffness. The structure shows some drift and the nonstructural members are under

failure stages. The structure has large displacement and the failure of members is observed in the collapse prevention level.

The NPA is used to get the strength capacity of the building its limit state up to the failure strength. The lateral load is distributed along with the height with a predefined pattern vertically. The lateral load along with the height looks like an inverted triangular shape. The lateral load pushes the structure and the base shear is recorded for every push that is displacement and the graph is plotted. At the displacement where the buildings behave the in-elastically and known as the target point also known as the performance point. The analysis is completed when two things are observed one target point and another is the capacity curve. The analysis predicts potential weak areas.

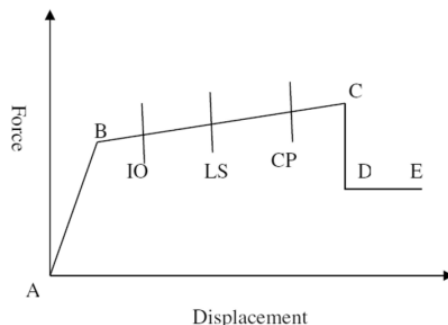


Fig. 2 Performance level for pushover analysis

3.1.1. Capacity Curve

The curve plotted between base shear and displacement known as a capacity curve which is obtained after pushover analysis is performed in each designed model. The curves are obtained from the 4 stories, 8 stories, 12 stories, and 16 story models as shown in Figs. 3 to 6. The curve represents the lateral shear strength in columns and bracing and is plotted to understand the behavior of each structure. Previous literature provided that the sum of each individual strength (columns and bracing) indicate the total lateral shear force for the RC-MRCBFs [20]. It is obtained that the base shear is increased as height and lateral force contribution in columns decrease. For the observation, the three (25%, 50%, 75%) cases of each story (4, 8, 12, 16) are put in the same graph. The x-axis and y-axis are separated and observed nonlinear behaviors.

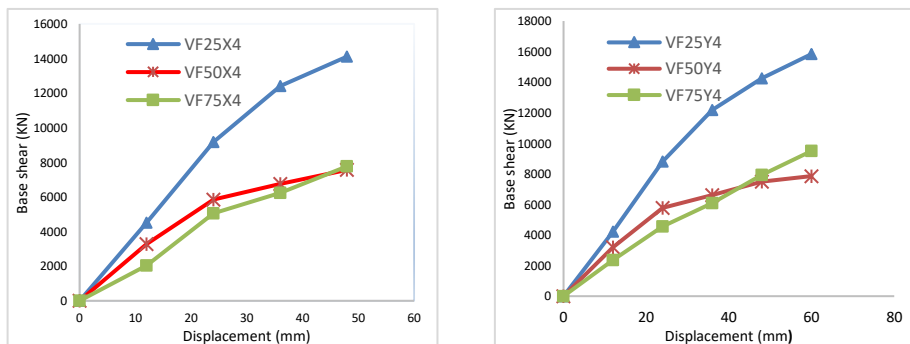


Fig. 3 Base shear vs displacement graphs for 4 story steel braced RC frame along both axes with different base shear in columns

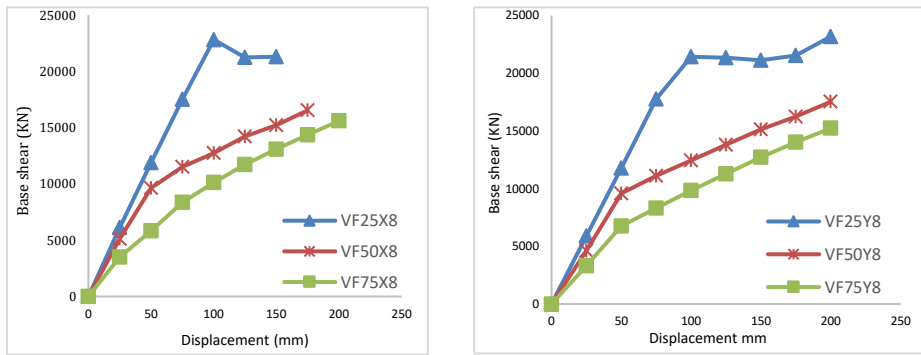


Fig. 4 Base shear vs displacement graphs for 8 story steel braced RC frame along both axes with different base shear in columns

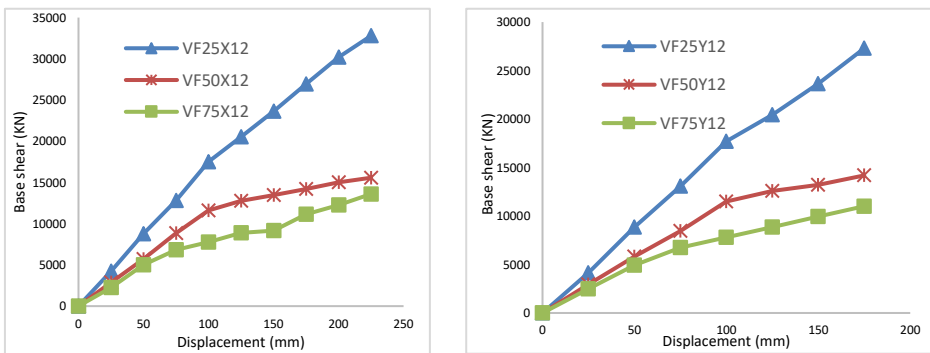


Fig. 5 Base shear vs displacement graphs for 12 story steel braced RC frame along both axes with different base shear in columns

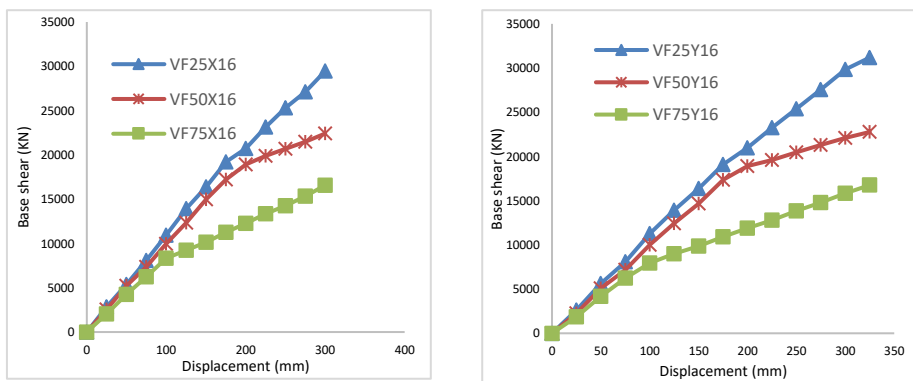


Fig. 6 Base shear vs displacement graphs for 16 story steel braced RC frame along both axes with different base shear in columns

When the base shear contribution in the bracings is increased the structural strength also increased. The 50% base shear contribution configurations have shown the uniform distribution of the energy decapitation capacity. Models VF25X4, VF25X8, VF25X12 and VF25X16 have the main line of defense is steel and these model have high strength. The models VF75X4, VF75X8, VF75X12 and VF75X16 have the main line of defense in the

columns and have low shear strength. The steel bracing increased the strength of the structure and reduced the maximum top story displacement which is shown in Figures 3 to 6. Also observed is that the V bracing in the 4-story building shows irregular behaviors. It is because in the lower story the gravity load plays the main role in the structural response. While the base shear increases up to 25% in columns the seismic response is quite different. The first hinges are formed in the bracing then it may be in columns or beams. Hence it is observed, that higher contribution in the bracing should be avoided as possible in the new construction of the RC-MRCBFs. Also when the columns get a high lateral shear contribution (75% or more than 75%) the bracing loses its contribution importance. The bracing easily comes in fail and it does not resist the more seismic forces. To get the balance seismic behaviors and economic column sections, there should avoid a lower shear contribution in the bracing as well. From an economical point of view, the heavy cross-section of the columns and steel bracing should not be used in new constructions. However for the retrofiting, there is already the column sections are fixed, at that condition, may use the heavy cross-section of the steel. As a sectional area of the bracing increased the lateral shear resisting capacity also increased as shown in Figures 3 to 6.

3.1.2. Collapse Mechanism

The failure mapping shows the hinge formation in the structure at the final stage where the structure shows collapse behavior. The collapse mechanism study shows that the nonlinear behavior of the structures and energy dissipate capacity for input earthquake force. For the observation of the failure mechanisms, it helps to conclude the weaker brace-weak beam and strong-column collapse mechanisms can be obtained or not by the observation of the plastic hinge in the columns, beams, and bracing. It is observed that the percentage of the strength provided in the columns increases, the rotation demands decrease in columns and increased in a brace.

Failure mapping is the development of plastic hinges in the structural members (beam, column, and bracing) in a different stage in NPA. The plastic hinges in the bracing are divided into compression bracing hinges and tension bracing hinges. The yielding in steel bracing due to the compression force is also known as buckling failure. The maximum bracings are failing due to buckling failure.

In the observation of the graph and the development of the plastic hinges pattern, it is found that the models having 25% base shear contribution are the non-ductile models and the model having 50% and 75% base shear contributions in the columns are the ductile models. These models VF25 are the non-ductile failure and other models VF50, and VF75 have ductile failures. However, the Indian standard code allowed the 25% base shear in columns in the dual system structures. In the study of each model, it is found that only ductile models show the expected failure mechanism. In the models VF50 and VF75, only the first failure is seen in the steel bracing than the beam and last in the columns. Which followed the adequate failure pattern such as weaker bracing, weak beam and strong columns. This type of failure pattern not seen in the models when the model (VF25) contributes the 25% base shear in the columns. However, the first plastic hinges are formed in the steel bracing in all the models. It is also noticed that the failure mechanism in the VF25 models the unsuitable and irregular pattern of the development of the plastic hinges. In the models having 50% and 75% base shear contribution, the formation of plastic hinges is formed in a regular pattern.

In previous research in the inverted V bracing [22], diagonal [26] and X bracings [27], the same results are obtained in the V bracing RC frame as well. The result of this section is for getting a suitable failure mechanism, the shear stress contribution in the columns should be a minimum of 50% of the total lateral shear. Also in IS 1893:2016, a dual system for

steel bracing in RC frame should be reviewed and consider the minimum 50% base shear contribution of the moment-resisting frame to get adequate failure and ductile buildings.

3.1.3. Ductility Reduction Factor and Ductility Capacity (μ)

Displacement capacity, ductility, and ductility ratio are the interrelated seismic response parameter. The ductility factor depends upon the story level and system. The ductility reduction factor ($R\mu$) is used for the calculation of the nonlinear seismic response of the buildings which is caused by the hysteretic energy. The term ductility reduction factor depends upon the damping, ductility, and the fundamental time period. Equations give the ductility reduction and ductility capacity respectively.

However, in this study to calculate the response ductility factor, Newmark and Hall (1982) [36] proposed equations are used (Eqs. 1 - 5). Newmark, Hall (1982) [36] proposed the essential study in ductility reduction factor. This method is widely accepted by other researchers for their study.

Periods (T) \leq 0.03 sec:

$$R\mu = 1.0 \tag{1}$$

T: 0.03 < 0.12 sec:

$$R\mu = 1 + \frac{(T - 0.03) \cdot (\sqrt{2 \cdot \mu - 1} - 1)}{0.09} \tag{2}$$

T: 0.12 \leq T \leq 0.5 sec:

$$R\mu = \sqrt{2 \cdot \mu - 1} \tag{3}$$

T: 0.5 < T < 1.0 sec

$$R\mu = \sqrt{2 \cdot \mu - 1} + 2(T - 0.5) \cdot (\mu - \sqrt{2 \cdot \mu - 1}) \tag{4}$$

T \geq 1.0 sec:

$$R\mu = \mu \tag{5}$$

Where T is the natural time of the buildings (also known as the fundamental time period). V_0 and V_d are the maximum base shear and design base shear respectively. Δ_m and Δ_y are the maximum displacements and first yield displacement respectively from the pushover curve. μ , R_μ , R_s , and R are the ductility ratio ($\mu = \Delta_m / \Delta_y$), ductility reduction factors, overstrength factors ($R_s = V_o / V_d$), and response modification factors ($R = R_\mu \cdot R_s$) respectively. In this method, it is assumed that redundant factors are taken 1.

It is observed that the ductility ratio (μ) is greater than 3 or 4 which is generally assumed as a have a high deformation demand. The models VF50 and VF75 have a value greater than 3, which shows the ductile behaviors of the buildings. It is observed in shown in Figure 7 that when the H/L value increased, the ductility ratio decreased. Same results also observed in the paper E.A. Godínez, A. Tena (2010) [22] for inverted V braced RC frame and Godínez Domínguez et al. (2019) [27] for X steel braced RC frame for the relationship between the μ and H/L. For 4 to 16 story buildings, the ductility ratio decreases when the base shear contributions by the columns increase. Thus observation suggested that for suitable ductile and failure mechanisms of the buildings, minimum of 50% lateral base shear contribution by the columns should be used in dual systems. As shown in Figure 8

(a) for the monotonic pushover load, the ductility reduction factors increase as the FTP of the buildings increases. In the other words, for the short time period buildings, the ductility reduction factors are low for V-shaped steel bracing RC frame buildings. It is also noted that greater shear strength contributions in the columns have higher ductility reduction factors. However, in the paper, Godínez and Tena (2010) [22] for inverted V braced RC frame the result is opposite as compared to the V braced RC frame results. In this paper the ductility reduction factors increased as a FTP of the buildings decreased. When the H/L ratio increases the ductility reduction factors also increase as shown in Figure 8 (b).

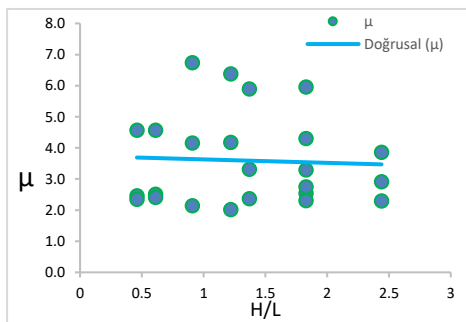
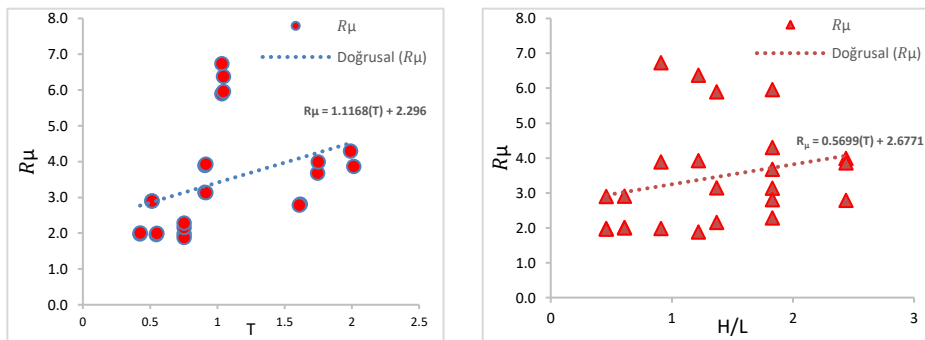


Fig. 7 Relationship between the ductility ratio and slenderness ratio



(a) Relation with natural time period

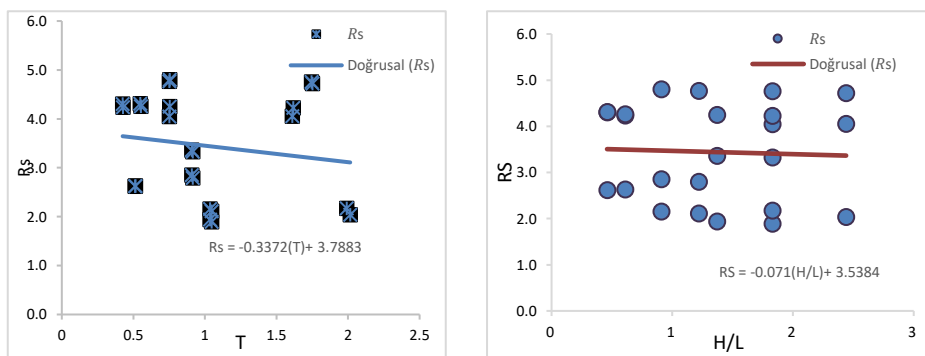
(b) Relation with H/L

Fig. 8 Relationship of the ductility reduction factors with fundamental time and slenderness ratio

3.1.4. Strength Factor and Response Modification Factors

It is the ratio of the maximum base shear and design base shear which are obtained by the NPA. The individual members of the buildings have over reserved strength, it's due to the redundancy of the structural members. Many things affect the strength factors, such as actual and practical construction differences actual strength of the materials, seismic zone, and gravity loads. Generally, the actual strength of the structures is high as compared to the design strength. It's the main reduction factor used in response modification factors (R). It is observed that the strength contribution of the columns increases, the Rs factors decrease ways. The observation is similar to the previous study in paper E.A. Godínez and A. Tena (2010) [22] for inverted V braced RC frame. However, the result is the opposite for the X-bracing RC frame in the paper Godínez et al. (2019) [27]. The buildings with increasing the natural time period (4 stories to 16 stories) have lower the overstrength factors as shown in Figure 9 (a). The result is also similar to the Godínez and Tena (2010)

[22]. Figure 9 (a) is the relationship between the FTP of the structures and overstrength factors which help to understand the behaviors of the R_s factors with time versions. To know the geometrical property related to the R_s factors the second plot Figure 9 (b) used, which shows the relation to the R_s and slenderness ratio. The slenderness ratio of each model lies between 0.46 and 2.44 ($0.46 \leq H/L \leq 2.44$). It is shown in Figure 9 b, the strength factors are decreased as the aspect ratio (H/L) increases. When the H/L ratio has a larger value the R_s factors have a lesser value. The linear relationship is obtained as shown in (plot H/L vs R_s) Figure 9 (b). Response modification factors (R) are the function of the ductility reduction factors, overstrength factors, and redundancy factors. The product of the R_s , R_μ , and redundancy factors ($=1$) gives the R . In the IS 1893:2016 the response modification factor is named as 'response reduction factor'. The response reduction factors in the Indian code seem incomplete such as the code does not tell as R factors for RC frame with concentrically braced steel bracing. It just tells as a concentrically braced frame with R factors 4.5. In the observation, it is noticed that the increases in the response modification factors as increasing the aspect ratio (H/L) as shown in Figure 10. It means increasing the story (4-16 story) also found increases in the R factors. The linear relationship observed between the R factors vs H/L ratio is shown in Figure 10.



(a) Graph between R_s and T

(b) Graph between R_s and H/L

Fig. 9 Overstrength factors having a relationship with natural period and slenderness

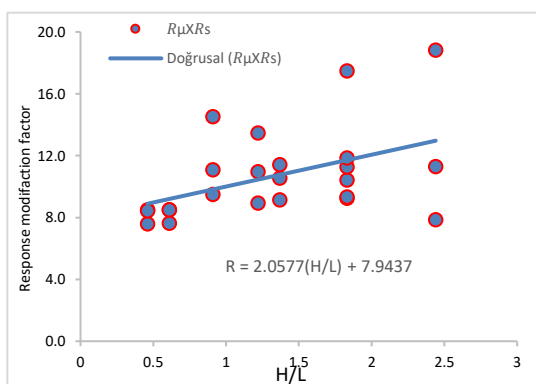


Fig. 10 Relationship between the response modification factors and slenderness ratio

3.1.5. Maximum Drift at a Yield Level

It is observed that the story drift at the yielding level is lesser than the 0.004 which is proposed by the code. The 0.004 drift is generally known as the drift limit at the service level and this value is generally proposed for the simply moment-resisting frame. This is because the maximum drift value for RC-MRCBFs is lesser than the service limit value. Yielding drift is computed by using the pushover curve with a bilinear idealized curve. It is observed that as the height of the building increases the maximum yield drift also increases (Figure 11). Figure 11, which is the relation between the yielding drift and slenderness ratio. The yielding values are only considered for the 50% and 75% of the base shear contribution of the columns. It is because the 25% base shear contribution by the columns is quite unfavorable for design and these models (VF25) show the unexpected failure mechanism. It is also noticed that the maximum yield drift is shown in the middle height of the structures. The average of each maximum drift at the yield level is 0.0024 which is nearly similar to the previously calculated value of 0.002 in [22] for inverted V braced RC-MRCBFs.

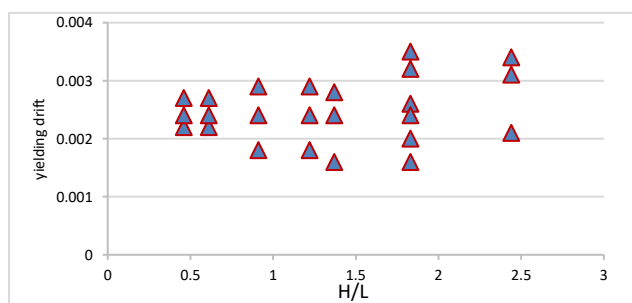


Fig. 11 Relationship between the maximum yielding drift and slenderness ratio for the VF50 & VF75 models

4. Conclusions

The nonlinear analysis was performed in 4 to 16-story buildings with three cases (25%, 50% and 75% base shear contributed by the columns) to study the nonlinear seismic behaviors of the structures. The RC-MRCBFs with steel V bracing structures were assumed to locate in the soft soil in India with high seismic zone factors. In this study the “moment resisting frames are designed to resist independently at least 25 percent of the design base shear” was considered for the design of the RC-MRCBFs. Based on the result obtained the conclusion are made as follows:

- Providing the steel V bracings in RC frames improves the seismic performances such as stiffness, strength and ductility of the structures effectively.
- The results shows that when the columns are designed to resist 25% base shear in dual systems, it is not possible to design columns as a strongest member. Many international codes suggested that columns are designed to resist minimum 50% base shear. So the Indian standard code should be revised. IS 1893:2016, a dual system for steel bracing in RC frame should be reviewed and consider the minimum 50% base shear contribution of the moment-resisting frame to get adequate failure and ductile buildings.
- The study observed that in the RC-MRCBFs for V shape steel bracings system when the moment-resisting system (columns) resists at least 50% base shear, those frames show the strong-column, weak-beam and weaker-bracing system. It

also improves the ductility and capacity of the structures for 4 story to 16 story structures.

- As increasing the strength of columns that is when base shear contributions of the columns increase, the capacity of the structures is decreased. However, when columns resist less than 25% base shear, the steel bracings are the main line of defense, which means, the structures do not show expected failure mechanism and non-ductile behaviors.
- Higher the shear force contributions in columns, the higher the ductility reduction factors, and the lower the ductility ratio obtained.
- When the aspect ratio (H/L) ratio increases, the ductility ratio of the structures decreases. It is also observed that the overstrength factors decrease as the aspect ratio (H/L) decreases. In the observation, it is noticed that the increase in the response modification factors as increasing the aspect ratio (H/L).
- When the base shear capacity increases in the columns, it decreases the overstrength factors and increases the response modification factors.
- The study shows that the story yielding $\Delta y = 0.0024$ which is the limiting value obtained for RC-MRCBFs when V shape steel bracings is used. This value is obtained for the service limit state.
- As increasing the height of the structures (in this study 4 to 16 stories), to get ductile and expected failure mechanism (weaker bracing, weak beam and strongest columns), it is ensured that to avoid the formations of plastic hinges at the lower stories columns end, it is done by the increasing the base shear capacity contributions in the columns to resist the lateral load.

This research is mainly focused on the regular buildings with 4 to 16 story buildings. The study is limited to nonlinear static analysis (pushover analysis) of up to 16 story RC buildings with V braced frame and a future study is needed to study the tall buildings with steel bracing with a suitable design methodology. The future research is needed to insure and to observe the effectiveness the design of RC-MRCBFs by using the nonlinear time history analysis of the models with different acceleration record. Further study is needed in the field of irregular buildings with different steel bracing with different shear contributions in the columns to understand the failure pattern of the structures.

References

- [1] Maheri MR, Sahebi A. Use of steel bracing in reinforced concrete frames. Eng Struct, vol. 19, 1997. [https://doi.org/10.1016/S0141-0296\(97\)00041-2](https://doi.org/10.1016/S0141-0296(97)00041-2)
- [2] Yoo JH, Roeder CW, Lehman DE. Simulated behavior of multi-story X-braced frames. Eng. Struct., vol. 31, 2009. <https://doi.org/10.1016/j.engstruct.2008.07.019>
- [3] Yeom HJ, Yoo J.-. H. Analytical investigation on seismic behavior of inverted V-braced frames. Int. J. Steel Struct., vol. 18, 2018. <https://doi.org/10.1007/s13296-018-0315-4>
- [4] Pincheira JA, Jirsa JO. Seismic Response of RC Frames Retrofitted with Steel Braces or Walls. J. Struct. Eng., vol. 121, pp. 1225-1235, 1995. [https://doi.org/10.1061/\(ASCE\)0733-9445\(1995\)121:8\(1225\)](https://doi.org/10.1061/(ASCE)0733-9445(1995)121:8(1225))
- [5] Pincheira JA. Design strategies for the seismic retrofit of reinforced concrete frames. Earthquake Spectra, vol. 9, no. 4. pp. 817-842, 1993. <https://doi.org/10.1193/1.1585742>
- [6] Badoux BM, Jirsa JO. Steel Bracing of RC Frames for Seismic Retrofitting. J. Struct. Eng., vol. 116, no. 1, pp. 55-74, 1990. [https://doi.org/10.1061/\(ASCE\)0733-9445\(1990\)116:1\(55\)](https://doi.org/10.1061/(ASCE)0733-9445(1990)116:1(55))
- [7] Osman A, Rashed A, El-Kady M. SEISMIC RESPONSE OF R.C. FRAMES WITH CONCENTRIC STEEL BRACING. in Proceedings of the 8th U.S. National Conference on Earthquake Engineering, 2006, pp. 18-22.

- [8] Said A, Nehdi M. Rehabilitation of RC frame joints using local steel bracing. *Struct. Infrastruct. Eng.*, vol. 4, no. 6, pp. 431-447, 2008. <https://doi.org/10.1080/15732470600822033>
- [9] Bush TD, Jones EA, Jirsa JO. Behavior of RC Frame Strengthened Using Structural Steel Bracing. *J. Struct. Eng.*, vol. 117, no. 4, pp. 1115-1126, 1991. [https://doi.org/10.1061/\(ASCE\)0733-9445\(1991\)117:4\(1115\)](https://doi.org/10.1061/(ASCE)0733-9445(1991)117:4(1115))
- [10] Canales M, de la Vega RB. Retrofitting techniques used in telephone buildings in Mexico. in *Earthquake Engineering, Tenth World Conference*, 1992, pp. 5143-5147.
- [11] Rahimi A, Maheri MR. The effects of retrofitting RC frames by X-bracing on the seismic performance of columns. *Eng. Struct.*, vol. 173, no. August 2017, pp. 813-830, 2018. <https://doi.org/10.1016/j.engstruct.2018.07.003>
- [12] Rahimi A, Maheri MR. The effects of steel X-brace retrofitting of RC frames on the seismic performance of frames and their elements. *Eng. Struct.*, vol. 206, no. December 2019, 2020. <https://doi.org/10.1016/j.engstruct.2019.110149>
- [13] Mahmoudi M, Zaree M. Evaluating response modification factors of concentrically braced steel frames. *J. Constr. Steel Res.*, vol. 66, no. 10, pp. 1196-1204, 2010. <https://doi.org/10.1016/j.jcsr.2010.04.004>
- [14] Birendra Kumar Bohara (2021). *Nonlinear Behavior of Moment Resisting Reinforced Concrete with Steel Braced Frame under Lateral Loading*. Mtech in Sharda University, 2021.
- [15] Bohara BK. Ductility, R, and Overstrength Factors for V Braced Reinforced Concrete Buildings. *Int. J. Struct. Constr. Eng.*, vol. 16, no. 3, pp. 101-105, 2022.
- [16] Bohara BK, Ganaie KH, and Saha P. Effect of position of steel bracing in L-shape reinforced concrete buildings under lateral loading. *Res. Eng. Struct. Mater.*, vol. 8, no. 1, pp. 155-177, 2022. <https://doi.org/10.17515/resm2021.295st0519>
- [17] Ganaie KH, Bohara BK, Saha P. EFFECTS OF INVERTED V BRACING IN FOUR-STORY IRREGULAR RC. *Int. Res. J. Mod. Eng. Technol. Sci.*, vol. 03, no. 04, pp. 2346-2351, 2021, [Online]. Available: www.irjmets.com.
- [18] B. K. Bohara. Seismic Response of Hill Side Step-back RC Framed Buildings with Shear Wall and Bracing System. *Int. J. Struct. Constr. Eng.*, vol. 15, no. 4, pp. 204-210, 2021.
- [19] Bohara BK, Ganaie KH, and Saha P. Seismic Analysis of Retrofitting of RC Regular Frame with V-Braced Frame. *J. Eng. Technol. Plan.*, vol. 2, no. 1, pp. 55-63, 2021, doi: 10.3126/joetp.v2i1.39229. <https://doi.org/10.3126/joetp.v2i1.39229>
- [20] Maheri MR, Kousari R, Razazan M. Pushover tests on steel X-braced and knee-braced RC frames. *Eng. Struct.*, vol. 25, no. 13, pp. 1697-1705, 2003. [https://doi.org/10.1016/S0141-0296\(03\)00150-0](https://doi.org/10.1016/S0141-0296(03)00150-0)
- [21] Godínez-Domínguez EA, Tena-Colunga A. Behavior of moment resisting reinforced concrete concentric braced frames (RC-MRCBFS) in seismic zones. 14th World Conf. Earthq. Eng., pp. 12-17, Paper No. 05-03-0059, 2008.
- [22] Godínez-Domínguez EA, Tena-Colunga A. Nonlinear behavior of code-designed reinforced concrete concentric braced frames under lateral loading. *Eng. Struct.*, vol. 32, no. 4, pp. 944-963, 2010. <https://doi.org/10.1016/j.engstruct.2009.12.020>
- [23] Godínez-Domínguez EA, Tena-Colunga A, and Pérez-Rocha LE. Case studies on the seismic behavior of reinforced concrete chevron braced framed buildings. *Eng. Struct.*, vol. 45, pp. 78-103, 2012. <https://doi.org/10.1016/j.engstruct.2012.05.005>
- [24] Tena-Colunga A, Nanguillasmú-Hernández HJ. Assessment of seismic design parameters of moment resisting RC braced frames with metallic fuses. *Eng. Struct.*, vol. 95, pp. 138-153, 2015. <https://doi.org/10.1016/j.engstruct.2015.03.062>
- [25] Godínez-Domínguez EA, Tena-Colunga A. Redundancy factors for the seismic design of ductile reinforced concrete chevron braced frames. *Lat. Am. J. Solids Struct.*, vol. 13, no. 11, pp. 2088-2112, 2016. <https://doi.org/10.1590/1679-78252827>

- [26] Eskandari R, Vafaei D, Vafaei J, and Shemshadian ME. Nonlinear static and dynamic behavior of reinforced concrete steel-braced frames. *Earthq. Struct.*, vol. 12, no. 2, pp. 191-200, 2017. <https://doi.org/10.12989/eas.2017.12.2.191>
- [27] Godínez-Domínguez EA and Tena-Colunga A. Behavior of ductile steel X-braced RC frames in seismic zones. *Earthq. Eng. Eng. Vib.*, vol. 18, no. 4, pp. 845-869, 2019. <https://doi.org/10.1007/s11803-019-0539-0>
- [28] Du K., Cheng F., Bai J., Jin S. Seismic performance quantification of buckling-restrained braced RC frame structures under near-fault ground motions. *Eng. Struct.*, vol. 211, no. December 2019, 2020. <https://doi.org/10.1016/j.engstruct.2020.110447>
- [29] Godínez-Domínguez EA, Tena-Colunga A, Pérez-Rocha LE. Seismic behavior of chevron-braced RC framed buildings. in 15th World Conference on Earthquake Engineering, 2012, p. Paper No. 2813.
- [30] IS 1893. Part 1. Indian Standard Criteria for Earthquake Resistant Design of Structures: General Provisions and Buildings. New Delhi: Bureau of Indian Standards, 2016.
- [31] Bureau of Indian Standards, IS 13920. Ductile detailing of reinforced concrete structure subjected to seismic forces-Code of Practice. (1993).
- [32] Mwafy AM, Elnashai AS. Static pushover versus dynamic collapse analysis of RC buildings. *Eng. Struct.*, vol. 23, no. 5, pp. 407-424, 2001. [https://doi.org/10.1016/S0141-0296\(00\)00068-7](https://doi.org/10.1016/S0141-0296(00)00068-7)
- [33] Goel RK and Chopra A. Evaluation of modal and FEMA pushover analyses: SAC Buildings. *Earthq Spectra*, vol. 20, no. 1, pp. 225-254, 2004. <https://doi.org/10.1193/1.1646390>
- [34] Chopra AK, Goel RK. A modal pushover analysis procedure for estimating seismic demands for buildings. *Earthq. Eng. Struct. Dyn.*, vol. 31, no. 3, pp. 561-582, 2002. <https://doi.org/10.1002/eqe.144>
- [35] CM. U Establishing R (or R_w) and Cd factor for building seismic provision. *J. Struct. Eng.*, vol. 117, no. 1, pp. 19-28, 1991. [https://doi.org/10.1061/\(ASCE\)0733-9445\(1991\)117:1\(19\)](https://doi.org/10.1061/(ASCE)0733-9445(1991)117:1(19))
- [36] Newmark N.M., Hall W.J. Earthquake spectra and design. Oakland: Earthquake Engineering Research Institute (EERI), 1982.

Blank Page



Technical Note

The strength characteristics of concrete using recycled concrete aggregates

Om V. Vaidya^{*1,a}, Kapil Malviya^{1,b}, Yuvaraj L. Bhirud^{2,c}

¹Department of Civil Engineering, RKDFIST, SRK University, Bhopal MP-462026, India

²SNJB's Late Sau. K.B. Jain College of Engineering, Department of Civil Engineering, Chandwad, Nashik - 423101, Maharashtra, India

Article Info

Article history:

Received 19 Mar 2022

Revised 14 Jul 2022

Accepted 26 Jul 2022

Keywords:

D RAC;

NAC;

Recycled aggregate;

Mechanical properties;

Flexural strength test;

Split- tensile test;

Demolition Waste;

Compressive strength

test

Abstract

In today's world, renovation and demolition is very common. This creates an aggregate waste. One can recycle this waste. Most of the waste that is generated from demolition of structures is dumped in landfills to reclaim land. These create a waste which contain concrete, bricks and other construction material which is of no use. By gathering all these waste and recycled it. The recycled concrete aggregate is created. Transport costs is very high that's make it even worse. Therefore, recycling of RCA (Recycled Concrete Aggregate) is eco-friendly, which reduces the harvesting of Natural concrete and that aggregate might be used for the production of concrete for new construction. Recycled Aggregates Concrete uses demolition concrete and burned clay masonry structures as aggregate. In this research work the demolition waste is used in concrete and the properties were discussed using Compressive strength test, Flexural strength test, Split tensile test with 0, 30, 60 and 100 percent RAC.

© 2022 MIM Research Group. All rights reserved.

1. Introduction

All the man-made construction needs to be demolished after certain period, these create a waste which contain concrete, bricks and other construction material which is of no use. By gathering all these wastes and recycled it. The recycled concrete aggregate is created. Recycled concrete aggregate can be of two type coarse or fine depending upon the application. This can mix with natural concrete aggregate in varying proportion for new construction. This paper includes the study of RCA with coarse aggregate. In 20th century, at the time of wars when there was unnecessary demolition of buildings and roads comes a need to get rid of the waste material. From that time, research has been conducted in RCA (Recycled Concrete Aggregate) for instead of NCA (Natural Coarse Aggregate). Two of the main reason to do so is that to dump demolition waste large space is used, which is increasing day by day. The capacity, area to store such waste is limited. Secondly, use of RCA is eco-friendly, which reduces the harvesting of Natural concrete. As stated by Oikonomou (2005) about main problem linked with use the NCA "NCA takes 50 percent of raw materials from nature, takes 40 percent of total energy and created 50% of total waste." It is necessary to know about the strength, durability and different parameters [1]. Therefore, In this research work first the properties of NCA is discussed. The properties discussed are impact value, crushing value, Bulk density, water absorption, specific gravity.

*Corresponding author: vaidya.om7@gmail.com

^a orcid.org/0000-0002-5493-2722; ^b orcid.org/0000-0001-6124-2191; ^c orcid.org/0000-0001-9596-2883;

DOI: <http://dx.doi.org/10.17515/resm2022.423st0319tn>

Res. Eng. Struct. Mat. Vol. 8 Iss. 4 (2022) 853-860

Secondly, different test such as compressive strength test, flexural strength test, split tensile test were determined with different proportions of RCA and NCA such as 0%, 30%, 60% and 100% and their comparison is studied.

Need to reuse recycled aggregates

- Many old buildings and other structures have exceeded their limit of use and have to be demolished.
- Different structures suitable for use are disconnected because there are new requirements and needs.
- Construction and demolished waste material are present in large amount. The estimated C & D (Construction & Demolished) around a globe is shown below.

ESTIMATED CONSTRUCTION AND DEMOLITION WASTE (C & D)

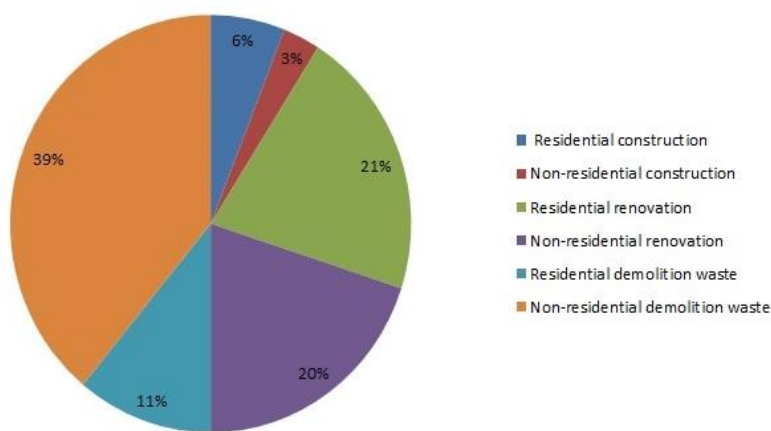


Fig. 1 Shown above it is clear that the use of RCA proves to be effective way to reduce pollution and save space as well Pavan P.S. [1]

Following are the Worldwide Estimated Construction and Demolished waste is as observed from the study in the paper Pavan [1].

- Residential construction: 6%
- Non-residential construction: 3%
- Residential renovation: 21%
- Non-residential renovation: 20%
- Residential demolition waste: 11%
- Non-residential demolition waste: 39%

It means Construction and Demolition (C&D) materials consist of the debris generated during the construction, renovation and demolition of buildings, roads, and bridges. Sustainable Materials Management approach that identifies certain C&D materials as commodities that can be used in new building projects, thus avoiding the need to mine and process virgin materials.

2. Literature Review

Pavan [1] In this research work, the RAC has been used with OPC(Ordinary Portland Cement) and PSC(Portland Slag Cement) with 7 and 28 curing days to study the different mechanical properties such as split tensile and compressive strength test. The concrete is

used is hardened concrete. The recycled concrete is made by using the demolish concrete and natural concrete in 60:40 ratio. The results were compared with naturally available aggregates.

P.C. Yong [2] RCA from site- tested concrete samples was employed in the research. These are 14-day concrete cubes from a local building site after compression testing. These cubes are split into required sizes. Around 200 Kg of recycled concrete aggregate was used in this study. The results shows that RCA has good quality concrete. The compressive strength test of RCA is also higher than Natural recycled aggregate. In terms of split tensile strength, wet density, flexural strength test RA is comparable to regular concrete.

M.C Neil [3] In this research paper, RCA is studied which includes its properties, effects and its production on a major scale. To study the RCA concrete material properties compressive strength test, splitting tensile strength test, crack width and spacing, modulus of rupture and elasticity, structural performance of RCA cubes were discussed. Overall, it is concluded that the RCA properties can vary with different materials admixtures, it can be used to build a structural concrete.

Yehla S. [4] This research paper focuses on the both the properties of RCA that is mechanical and physical of recycled aggregate concrete. The research provided the impact of RCA quality on concrete characteristics. From the time range of around six months sample was collected from an any place, both the aggregate property indicated an acceptable change in properties. All admixtures except three shows the acceptable values in compressive, tensile, flexural, splitting strength test.

M. chakradhara [5] In this paper, the properties of RCA is studied using a various strength test in four grade, M 20, M 25, M 30, M 40 as a NCA concrete and four recycled aggregate RCA 20, RCA 25, RCA 30 AND RCA 40. The study demonstrates that the Mechanical property like compressive strength test of the different M- Grade samples is lower than the RAC grade sample, but the same test conducted with more mixing ratio of M20, M20, M25, with RCA 20, RCA gives acceptable results. RAC absorbs more energy than controlled concrete under flexural test.

3. Objective

There are following objective are to be expected from the present work

- This study demonstrates a method to use Recycled Course Aggregate instead of natural concrete aggregate in ratios 0%, 30%, 60% and 100% and their comparison is studied.
- Secondly, both the concrete properties is discussed and evaluated and their result is compared such as mechanical (compressive, tensile and flexural strength test) and physical property. (water absorption, bulk density, impact value etc).

4. Methodology

The research methodology is divided into three steps:

Step 1: Evaluation of aggregate properties and material use

Step 2: Evaluation of Concrete properties with different grade combination.

Step 3: Mechanical properties test:

- Compressive strength test
- Split tensile strength test
- Flexural strength test

4.1. Material Use

The size of natural and recycled aggregate is around 20 millimeters. The cement used in a research work is grade- 43 PPC cement, sand of 4.75 millimeter passing through IS sieve which retain IS sieve of 150 micron of potable water available in the campus.

Source: The demolition waste of our campus is used in the present work, the waste first smash into pieces with hammer, dried, separation of distinct size takes place the mixed with M25 grade in different proportions such as 0%, 30%, 60% and 100% and their comparison is studied.

4.2. Aggregate Physical Property

The physical property of the recycled and natural concrete aggregate is obtained below as per process discuss in the standard BIS 2386-1963 [14], the various substantial properties of aggregates were tested and BIS 383-1970[11], Specification for coarse and fine aggregates from natural sources for concrete (second revision), Bureau of Indian standards, New Delhi, India.

Table 1. Physical properties of Natural and recycled coarse aggregate

Sr. No.	Particulars	Natural Aggregate	Recycled Aggregate
1	Specific Gravity	2.64	2.73
2	Density (in kg/m ³)	1677.2 Kg/m ³	1470.2 Kg/m ³
3	Water Absorption	0.29 %	0.32 %
4	Crushing Value	18.8 %	35.3 %
5	Impact Value	17.89 %	35.67 %
6	Fineness Modulus	2.86	2.82

Manufacturing process of RAC

- The waste obtained from building demolition sites were taken and tested
- The taken concrete is smashed into smaller fragments using a hammer.
- The fragments are then crushed with an abrasion machine before being removed
- The sample is then dried any amount of wetness has been eliminated.
- Sieve analysis is used to divide aggregates into distinct sizes.
- A 150 mm grade were prepared and used.

4.3. Design of Concrete Mix

As per standard IS: 10262 -2009 the designing is done using M25 grade.

Table 2. Designing of Concrete using M 25 cubes

Weight	W/C	Cement	Fine aggregate	Coarse aggregate
Kg/m ³	186	415	550	1170
Ratio	0.45	1	1.35	2.83

4.4. Property of Hardened Concrete

According to the BIS 516-1959[13], methods of tests for strength of concrete. The mechanical properties of concrete were tested and are given in figure 5.1(Compressive strength), 5.2(Split tensile strength) and 5.3(Flexural strength) respectively.

Cubes of size 15 cm, cylinders of size 7.5 cm radius and 30 cm length and beam of size 50 x 10 x 100 cm were mold, cured and 3 samples were tested at 7 days and 3 samples were tested at 28 days after curing to evaluate the mechanical properties of concrete specimens with and without recycled aggregates using 0%, 30%, 60% and 100% replacement of RCA and NCA respectively.

Following test are conducted to understand the mechanical properties of the RCA:

I. Compressive strength test (CS):

The capacity of a matter to bear failure in the form of cracks gives its compressive strength. The maximum compression that concrete can withstand be without failure is determined using this study by applying a load to both sides of the concrete mold.

II. Split tensile strength test:

To check the tensile strength of a concrete is test is done. It is a ability of a material to resist a force that tends to pull it apart. Universal testing machine is used to evaluate the split tensile strength test. First the cube is cured then the specimen is dried and placed Longitudinally in the machine and aligned. Then load is applied and values are noted down for any cracks the tensile strength is calculated using the formula

$$TS = 2 Q / \pi D L,$$

where Q is the load at which specimen breaks.

III. Flexural strength test:

The compressive and tensile strength of concrete are both developed as it starts to bend, The flexural strength is the strength per unit area. The modulus value is determined by the beam's size as well as the loading configuration. It is also known as modulus of rupture. It is determined by either central point loading or two-point loading machine. In which steel rollers are connected for different specimen. The concrete is prepared after a mold is removed, specimen is cured, dried and specimen is placed longitudinally in a machine and a load is applied of fixed parameters. Note down the reading of load at which the crack appears. Flexural strength is noted using the formula:

$$F_b = P * L / b d^2,$$

Where P is the pressure at which specimen breaks, b is the width of the beam in milli meter mm, d is the failure point in mm.

5. Results

Following results are calculated to evaluate the mechanical property of the RAC, and its comparison is shown with natural aggregate concrete.

From figure 2 it is concluded that the compressive strength test is comparatively high for 60% replacement.

From figure 3 it is concluded that the split tensile strength test is maximum for 60% replacements in both 7- and 28-days curing period.

From the tests of compressive strength, tensile, flexural test quality it is predicted that with 0% and 30% RCA the outcomes are comparatively low, with 60% RCA a results are moderately good. With 100% substitution because it acts as a normal quality. So it is concluded that the RCA and NCA in half proportions gives a acceptable result for any acceptable construction which is essential for demolition waste management as well as environmental friendly.

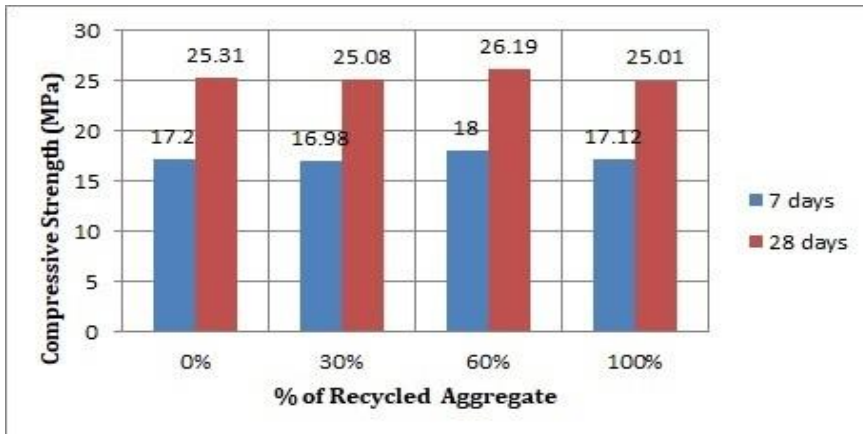


Fig. 2 Compressive strength for 7 days and 28 days

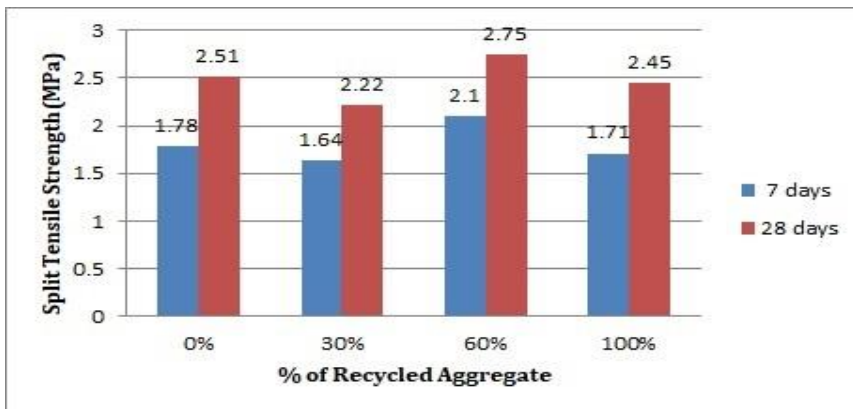


Fig. 3 Split tensile strength for 7 days and 28 days

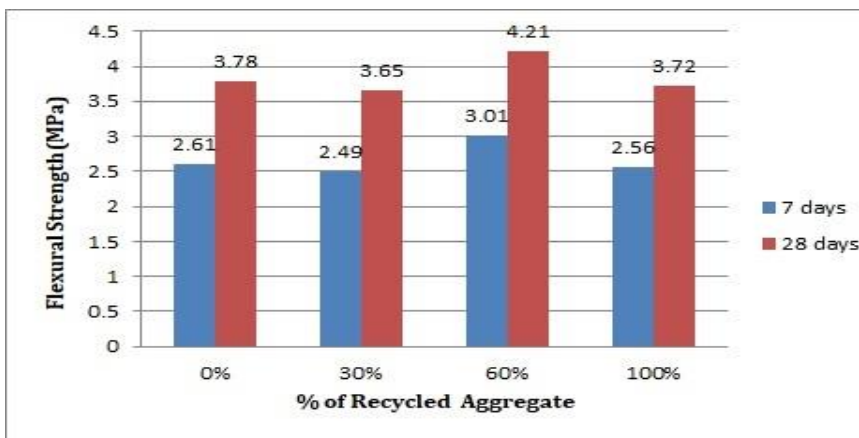


Fig. 4 Flexural strength for 7 days and 28 days

6. Conclusions

The study can lead to following points mentioned below:-

- Presently Recycled concrete aggregate is treated as waste material and is economical than fresh aggregate. Therefore, concrete made up of Recycled aggregate will naturally be economical.
- It is observed that the water absorption of natural aggregate is 0.29% and that of recycled aggregate is 0.32%. This indicates that the workability of concrete mix will reduce at same water cement ratio, as the percentage of recycled aggregate in cement concrete increases.
- The replacement % of RCA and NCA is to be around 60% i.e. 60% use recycled aggregate and 40% use natural aggregate.
- The compressive strength and split tensile strength of concrete is comparatively high.
- Recycled concrete aggregate can be easily used in the low to moderate level constructions.
- Various mechanical tests such as split tensile test, Compressive Strength test, and flexural strength test shows that the partial use of RCA and NCA (in 60:40 ratio) is the finest reasonable, cost-effective way for justifiable and smart technology in future.
- It has been found that the recycled concrete aggregate are more angular and higher specific gravity than Natural coarse aggregate it may result of increase in strength.
- Various tests conducted on recycled aggregates and results compared with natural aggregates are satisfactory as per IS 2386.
- Due to use of recycled aggregate in construction, energy & cost of transportation of natural resources & excavation is significantly saved. This in turn directly reduces the impact of waste material on environment.

References

- [1] Pavan PS. A Study On Recycled Concrete Aggregates, International Journal of Pure and Applied Mathematics Volume 118 No. 18 2018, 3239-3263 ISSN: 1311-8080 (printed version); ISSN: 1314-3395 (on-line version)
- [2] Yong PC, Teo DCL. (2009). Utilisation of Recycled Aggregate as Coarse Aggregate in Concrete. Journal of Civil Engineering, Science and Technology. 1. 1-6. <https://doi.org/10.33736/jcest.60.2009>
- [3] McNeil K, Kang T. Recycled Concrete Aggregates: A Review. International Journal of Concrete Structures and Materials. 2013;7(1):61-69. <https://doi.org/10.1007/s40069-013-0032-5>
- [4] Yehia S, Helal K, Abusharkh A, Zaher A, Istaitiyeh H. Strength and Durability Evaluation of Recycled Aggregate Concrete. International Journal of Concrete Structures and Materials. 2015;9(2):219-239. <https://doi.org/10.1007/s40069-015-0100-0>
- [5] Chakradhara Rao M. Properties of recycled aggregate and recycled aggregate concrete: effect of parent concrete. Asian Journal of Civil Engineering. 2018;19(1):103-110. <https://doi.org/10.1007/s42107-018-0011-x>
- [6] González-Fontebo B, González-Taboada I, Martínez-Abella F, Carro-López D. Study of recycled concrete aggregate quality and its relationship with recycled concrete compressive strength using database analysis. Materiales de Construcción. 2016;66(323):e089. <https://doi.org/10.3989/mc.2016.06415>
- [7] Xiao J, Sun C, Jiang X. Flexural behaviour of recycled aggregate concrete graded slabs. Structural Concrete. 2015;16(2):249-261. <https://doi.org/10.1002/suco.201400008>

- [8] Dosho Y. Use of Low-Quality Recycled Aggregate for Structural Concrete. *Concrete Journal*. 2017;55(8):635-643. https://doi.org/10.3151/coj.55.8_635
- [9] Chakradhara Rao M. Influence of brick dust, stone dust, and recycled fine aggregate on properties of natural and recycled aggregate concrete. *Structural Concrete*. 2020;22(S1). <https://doi.org/10.1002/suco.202000103>
- [10] Yehia S, Helal K, Abusharkh A, Zaher A, Istaitiyeh H. Strength and Durability Evaluation of Recycled Aggregate Concrete. *International Journal of Concrete Structures and Materials*. 2015;9(2):219-239. <https://doi.org/10.1007/s40069-015-0100-0>
- [11] IS 383:1970, Specification for coarse and fine aggregates from natural sources for concrete (second revision), Bureau of Indian standards, New Delhi, India.
- [12] IS: 10262-2009, Guidelines for concrete mix design, Bureau of Indian standards, New Delhi, India.
- [13] IS: 516-1959, Indian standard methods of tests for strength of concrete, Bureau of Indian standards, New Delhi, India.
- [14] BIS 2386-1963. Methods of test for aggregates for concrete, Bureau of Indian standards, New Delhi, India.



Technical Note

Experimental investigation of spalling effect of elevated temperature on concrete containing waste plastic aggregates

Lalit B. Pawar^{*1,a}, Keshav K. Sangale^{1,b}, Yuvaraj L. Bhirud^{2,c}

¹ Department of Structural Engineering, Veermata Jijabai Technological Institute, Mumbai, India.

² Department of Civil Engineering, SNJB's LSKBJ COE, Chandwad, Nashik, India

Article Info

Article history:

Received 18 Mar 2022

Revised 29 May 2022

Accepted 14 Jul 2022

Keywords:

Spalling;
Pore pressure;
High temperature concrete;
Waste plastic aggregates;
Fire resistance;
Concrete beams

Abstract

Fire spalling significantly increases the overall heat deformation of a fire-damaged building, resulting in significantly greater repair costs and, in certain situations, jeopardizing structural stability owing to the loss of reinforcing protection and lowering of bearing cross-sections. Due to intrinsic material characteristics such as unstable fracture behavior and limited permeability, elevated concrete is particularly susceptible to shear. Hence in this paper to improve the thermal stability of structures, aggregate waste plastics are added to the concrete to reduce the pore pressure generated inside the concrete subjected to a thermal environment. Here plastics are added to the concrete mix in various weight proportions as 0%, 10%, 20%, 30% and 40% thereby fabricating three types of specimens as cube, cylinder and beam which are then checked for volumetric degradation stability subjected to various thermal gradients like normal temperature, 600°C and 800°C respectively. Finally, the spalling of concrete at various plastic proportions under varying environments are investigated and the best way to incorporate plastic waste aggregates into concrete is explored.

© 2022 MIM Research Group. All rights reserved.

1. Introduction

Strength endurance of construction materials with increasing temperature exposure is critical for constructions. Reinforced concrete (RC) structures may sustain fire damage during their service life [1]. It is a universal fact that molecular structures are stable only up to a certain temperature. This constancy may be compromised as temperature conditions change as the temperature is the deep-seated characteristic influenced by exposure duration and heating rates to impact the molecular structure; thus, it is responsible for concrete deterioration [2]. Concrete's material properties and stiffness decline drastically as a result of physical and chemical changes, resulting in a loss of strength at extremely high temperatures. [3,4].

Reinforced concrete (RC) structures made of traditional concrete, unlike structures made of other construction materials such as steel, have good fire resistance, which can be attributed to low conductivity, greater temperature capacity, and slower degradation of tensile properties with temperature [5,6]. However, owing to changes in microstructure that occur during fire exposure, the newest concrete types, especially High-Strength Concrete (HSC) and Ultra High-Strength Concrete (UHPC), show quicker strength decline, culminating in concrete spalling [1,7]. Spalling of concrete as a result of fire exposure is a well-known phenomenon with consequences for fire safety, building integrity, and the cost of rehabilitation after a fire. During rapid heating and unsuitable conditions,

*Corresponding author: lalitraj1@gmail.com

^a orcid.org/0000-0002-8337-0626; ^b orcid.org/0000-0003-0618-7526; ^c orcid.org/0000-0001-9596-2883

DOI: <http://dx.doi.org/10.17515/resm2022.422st0318tn>

Res. Eng. Struct. Mat. Vol. 8 Iss. 4 (2022) 861-884

fragments of concrete can explode off the surface, and a whole cross-section heated from two sides can disintegrate completely by spalling [8]. The surface of a concrete structural part will come off when subjected to fast heating conditions, such as during a catastrophic fire. Spalling happens when a fire-exposed concrete section with limited permeability experiences high amounts of pore pressure generated by high temperature gradients [9]. The primary disadvantage of using HSC in reinforced concrete buildings is that it has a higher tendency for heat-induced concrete spalling when exposed to high temperatures, which is due to its thick matrix and refined pore structure [10]. Thermo-hydro-mechanically related heat-induced concrete spalling is affected by thermal dilation and pore pressure gradients [11]. The unlimited water inside the concrete condenses as vapor when exposed to high temperatures, resulting in vapour pressure bubbles and, as a result, tensile stresses that exceed those supported by the concrete. When these concerns are not addressed, the civil structure suffers massive harm [12].

To ensure the safety of reinforced concrete structures designed with HSC, several technological solutions have been implemented, which include limiting the use of HSC to low exposure to fire risk structural components, considering the use of external fire protection systems, and even reducing thermal effects on structural components through design options. [13,14]. Synthetic (polypropylene—PP) and natural (sisal, basalt) fibers distributed in the cement structure, on the other hand, have been effectively employed in concrete to change its microstructure and mitigate the effects on high - temperature cement structural damage [15]. Even though worldwide obligations to the manufacturing process of reusable, recyclable, or biodegradable manufacturing goods originate from greater public concern over inordinate waste production and ineffective disposal practices, waste plastic has also been probed for valuation application fields in concrete buildings, fibres concrete beams, and concrete walkways [16]. Many countries' municipal recycling systems collect but do not recycle plastic waste, resulting in tonnes of plastic being burned, transferred to landfills, or even dumped into the seas. Another source of worry is that dumping plastic waste in landfills pollutes and contaminates soil and water, potentially causing human health concerns due to high levels of lead and cadmium.[17,18]. Despite the fact that the use of High-Strength Concrete (HSC) is increasing dramatically around the world, the use of plastic waste in the manufacture of HSC has not been properly investigated. The paper's main contribution is as follows:

- Improve the stability of concrete in a thermal environment by adding plastic wastes with polycarboxylic-based superplasticizer as aggregates.
- Investigate the spalling behavior of concrete with and without plastic wastes under various environmental conditions and compositions.

Aggregates and plastics increase the thermal stability of concrete to reduce the pore pressure generated inside the concrete when exposed to a heated environment. The structure of the paper has been developed as follows out of which section 1 is the introduction; Section 2 presents the recent works of literature; section 3 depicts the detailed description of the materials and processing methods involved; section 4 deliberates the experimental results and finally, section 5 discusses the conclusion.

2. Literature Survey

Camilo et al [19] in their work, investigated the impacts of high temperature on the residual qualities of concrete, as well as the physical, chemical, and mechanical properties of concrete comprising rejected recyclable plastic waste (RRPW), were explored. After 2 hours of exposure to 200°C, 400°C, and 600°C, concrete compressive and tensile strengths, Young's modulus, crack width, mass loss, water absorption by capillarity, chemical composition, and evidence of heat-induced concrete spalling were measured in

concrete samples made with RRPW particles and compared to those made with commercial polypropylene (PP) fibres. Workability and durability difficulties connected to the use of RRPW in high-strength concrete should be investigated.

Hager et al [20] in their work evaluated the effect of high temperatures (up to 1000 degrees Celsius) on the microstructure and mechanical characteristics of geopolymer mortars With fly ash as the major precursor and four degrees of slag substitution (0, 10, 30, and 50 wt of %), four blends were examined. Ultrasonic pulse velocity, scanning electron microscope, mercury intrusion porosimetry, thermal stresses measurements, differential thermal analysis, and thermogravimetry were used to analyze damage evolution and identification tests. The goal of the study was to create a mortar that is thermally stable at high temperatures. However, further work on green materials is required to advance the technology of building structures in a sustainable manner and to minimize gas emissions.

Mohammad hosseini et al [21] in their work studied the impact of waste metalized plastic (WMP) fibres and palm oil fuel ash (POFA) on concrete performance at high temperatures of 200, 400, 600, and 800 degrees Celsius Four concrete mixes were cast, with 0 and 0.5 percent WMP fibres and 0 and 20% POFA content. The characteristics evaluated include mass loss, compressive strength, and ultrasonic pulse velocity. When compared to ordinary concrete mixes, adding WMP fibre to concrete mixes improves concrete performance at elevated temperatures by reducing the rate of strength loss and eliminating explosive spalling behaviour. Spalling analysis for varied structures, on the other hand, has not been concentrated.

Rohden et al [10] in their research studied the possible use of difficult-to-recycle plastic waste as a polymeric addition in elevated concrete, with a focus on the capacity to reduce thermal concrete spalling and its impact on mechanical properties The garbage correlates to soft and hard plastic, particularly domestic polymers, which are typically disposed of in landfills, while being theoretically recyclable. Mechanical and physical properties, cracking, mass loss, and the incidence of spalling in high strength concrete specimen constructed with either plastic waste or polypropylene fibres were tested after a 2-hour exposure to 600 C. Moreover, the spalling effect of the plastic aggregate induced concrete for beam structures and other structural members has to be analyzed.

Umasabor et al [22] in their work experimentally investigated the PET pulverized mix with the concrete. Crushed PET was used in concrete at weight percentages of 5%, 10%, and 15% of conventional fine aggregate. There were four distinct types of concrete specimens made, including a control. The concrete specimens' flexural and compressive strengths were assessed after 3 days, 7 days, 14 days, and 28 days of curing, respectively. The concrete specimen containing 5% by weight PET had a better compressive strength than the other specimens, according to the findings. However, spalling effect for samples due to increased thermal gradients were not investigated in the work.

Oluwarotimi et al [23] in their study examines the effect of elevated temperature on the strength of concrete containing glass powder (GWP) as Ordinary Portland cement replacement. They partially replaced by 0, 15, 18, 21, 24, 27 and 30 % of cement with GWP. The cube samples are curing in water for 90 days were exposed to 60, 150, 300 and 500°C temperatures increased at a heating rate of 10°C/min. They measured a compressive strength values of unheated samples and after air-cooling period of the heated samples by scanning electron microscope to examine alterations in the matrix and interface. The compressive strength of the concrete matrix should be concentrated for higher temperature.

From the survey, for [19] issues with workability and durability when using RRPW in high-strength concrete, for [20] more development on green materials is required for a sustainable environment and to minimize gas emissions, for [21] analysis of spalling for various structures has not concentrated, for [10] the spalling effect of the plastic aggregate induced concrete for beam structures and other structural members has to be analyzed and for [22] spalling effect of the specimens due to increased thermal gradients. Hence as a result to overcome the issues in spalling effect of reinforced plastic wastes has to be experimentally investigated.

3. Experimental Program

3.1. Materials and Methods

In this investigation, the binder was composed of Portland cement (CEM II 52.5 R) and plastic wastes. The sand-to-binder ratio of 0.4 was employed. Silica sand with a mesh size of 106 to 120 μm (120 to 150 mesh) was included in the mix. A polycarboxylic-based superplasticizer was present in all of the combinations (30 percent solid content). To explore the influence of plastics on the spalling resistance of concrete with appropriate workability of the new mixture and aggregate plastic dispersion, the concrete was prepared with 0 to 40% plastic wastes in the size up to 20 mm to get adequate ductility. The post consumed waste plastic is collected, after grinding and melting it, again cut in to small pieces. The same pieces after cooling are used as coarse aggregate for the concrete.



Fig. 1 Plastic waste aggregate

3.2. Mix Proportions and Batching

To make the specimens five different proportions of plastic wastes are added to the concrete which are 0%, 10%, 20%, 30% and 40% respectively. The 0% indicates the pure concrete specimens without the addition of plastic wastes. The specimens are prepared and tested in such a way to investigate the addition of plastic wastes to the conventional concrete. Three types of specimens are prepared with the above-mentioned proportions which are a cube, cylinder and beam specimen. The cube is prepared with dimensions $150 \times 150 \times 150 \text{ cm}^3$ so that the surface area of the cube is 22500 cm^2 . The cylindrical specimen is made with dimension having diameter as 150 cm and height of 300 cm with a surface area of 176625 cm^2 and the rectangular beam is made with dimensions $150 \times 150 \times 500 \text{ cm}^3$. The numbers of samples prepared for each of variation are 6. Mix design proportions were shown in Table 1.

Table 1. Mix design proportions

Plastic waste		Specimens		
(%)	(size)	Cube	Cylindrical	Rectangular beam
0 to 40%	20 mm	150x150x150 cm ³	150x300 cm ³	150x150x500 cm ³



(a)



(b)



(c)

Fig. 2 Fabricated specimens

3.3. Testing Methods

BS EN 12390-2, 3:2009 was used to create the concrete cube samples. The concrete cubes were dismantled after 24 hours and submerged under water for 90 days. The cubes were then taken from the water tank and left to dry at room temperature, with the mass of the specimens being monitored until they reached a constant weight. Before the heat exposure test, the starting mass of all concrete specimens was recorded, and the

specimens were then examined for a non-destructive UPV test in line with ASTM C597-09 requirements. This test is carried out by sending an ultrasonic pulse into the concrete being tested and measuring the time it takes for the pulse to pass through the construction. Slower velocities suggest concrete with many fractures or voids, whereas higher velocities indicate good quality and continuity of the material. The concrete cubes were then placed inside a furnace that was gradually heated from ambient temperature to 600 and 800 degrees [26]Celsius at a pace of 10 degrees Celsius per minute. The furnaces used for higher temperature have temperature control arrangements, with the help of that temperature inside furnace were kept constant. To establish thermal equilibrium inside the concrete cubes, the peak temperature [26]was kept for 1 hour for each temperature range[25].

The modest temperature increase was intended to avoid substantial temperature gradients in the specimen and, as a result, severe micro cracking, which would have changed the experimental results. The samples were tested to ensure that the pre-heating temperature was reached throughout the specimen. The exposure temperature was kept constant for one hour (1h), and cooling to room temperature was accomplished in the closed and disconnected furnace (about -0.3°C/min). In the oven chamber, the controlled temperature is measured (i.e. not in samples).To investigate the influence of qualities of reinforced plastic wastes, the samples at thermal gradient are compared to the specimen sample at room temperature. Low temperature gradients are used in this procedure and the majority of mortar damage is physicochemical in nature. the samples are prepared in such a way that they represent specimens with and without addition of plastic wastes.

3.4. Effect of Temperature on Conventional Concrete

Even if the temperature is only somewhat raised, the concrete built with portland cement is subjected to heat, which causes a variety of transformations and reactions. Because aggregate materials account for 65 to 75 % of the volume of concrete, the aggregate type has a significant impact on the behavior of the concrete at increased temperatures. Thermal stability of commonly used aggregate materials ranges from 300°C to 350°C. Physical qualities (e.g., thermal conductivity and thermal expansion), chemical properties (e.g., chemical stability at temperature), and thermal stability/integrity are all important aggregate features for concrete behavior at high temperatures. Crystal transitions in aggregate materials result in considerable volume increases [e.g., crystalline transformation of -quartz (trigonal) to -quartz (hexagonal) between 500 and 650 C with a 5.7 percent increase in volume]. With rising temperature, some siliceous or calcareous aggregates with some water of composition display considerable dehydration, which is accompanied by shrinkage (e.g., opal at 373 C shrinks by 13% by volume). Most non-siliceous aggregates may withstand temperatures of up to 600°C. Results show that when the temperature is raised above 600 degrees Celsius, the weight loss of specimens gets increases. Aggregates such as Calcareous aggregates (Calcite - CaCO₃), magnesite (MgCO₃), and dolomite (MgCO₃/CaCO₃) were breakdown into oxides and carbonites CO₂ (CaO + CO₂) at higher temperatures [25]. Calcium carbonate is a white colored powdered compound which on strong heating (calcination) produces calcium oxide along with a release of carbon dioxide. Magnesium carbonate is also a colorless powdered compound which on thermal decomposition produces magnesium oxide and releases carbon dioxide gas.

A mixture of calcium carbonate and magnesium carbonate is heated strongly. The reaction that takes place is as follows:



Evaporable water occupies between 30 and 60 percent of the volume of saturated cement paste and 2 to 10% of the volume of saturated structural concrete at room temperature. Evaporable water is pushed out as the temperature of the cement paste rises, until at a temperature of around 105°C, all evaporable water is lost after a sufficient exposure duration. The firmly absorbed and chemically combined water (i.e., water of hydration) is gradually lost from the cement paste hydrates at temperatures over 105°C, with dehydration virtually complete at 850°C. Calcium hydroxide dehydration is nearly negligible up to around 400°C, accelerates quickly around 535°C, and is complete at about 600°C. Hence at these elevated temperatures, the concrete undergoes complete dehydration and the bond strength decreases, thereby the concrete materials at the face of the structures loses its adhesive property and tends to de-bond thereby creating a failure of the structures which is termed as spalling.

3.5. Effect of Temperature on Plastic Reinforced Concrete

The concrete specimen which is raw without any plastic mix deteriorates much faster at a lower temperature and hence to improve its stability, plastic wastes are added to it. The specimens are made and are tested for its stability in the furnace over a while. The samples are exposed to temperature range of normal temperature, 600 and 800 degrees Celsius in the furnace. The cube specimens have a maximum spalling effect which is denoted by the breakage of the mold specimens under thermal loading. At normal temperature, cube specimen, cylindrical specimen and rectangular beam specimen of concrete samples remains in the same weight. When the weight is increased to 600 to 800 degree Celsius, there is a significant effect on temperature is observed at the specimens with more weight loss. Moreover, the specimens are also observed to undergo a variation of weight due to elevated thermal gradients. the results of the observed investigation are discussed in the following section.

4. Results and Discussion

The section elaborates the results obtained from the fabricated specimens which are subjected to different temperature zones.

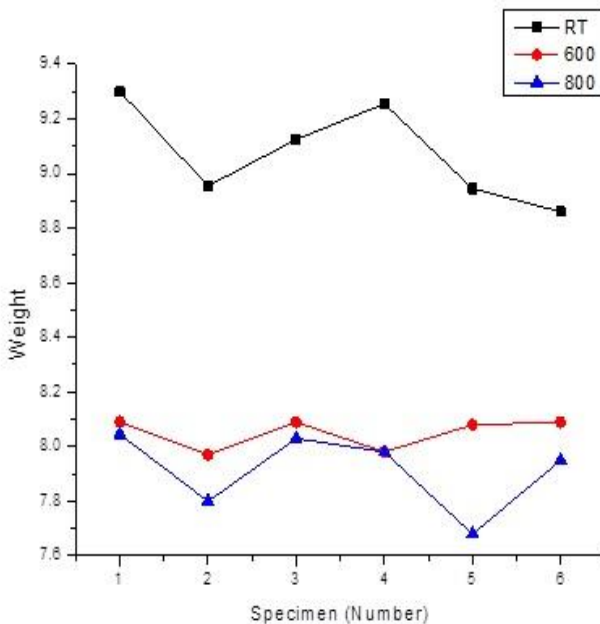
4.1. Weight Loss

In all cases, the spalling process began with a violent event affecting the entire heated region. The spalled layer appeared rather homogeneous after cooling, corroborating the idea that spalling is not strictly related to local mechanisms involving aggregate-to-cement paste interaction under substantially uniform heating and loading conditions, and that a more general explanation based on temperature, pressure, and stress fields can be provided. The evolution of the thermal field was rather constant across genera. This result implies that moisture transport mechanisms play a little impact in concrete thermal behavior. The weight loss at the end of the test for the mortars is nearly identical. The weight loss for the cube specimens are identified and are represented in the graphs. From Fig 3a to 3e, 4a to 4e, 5a to 5e X-axis is showing the specimen's number.

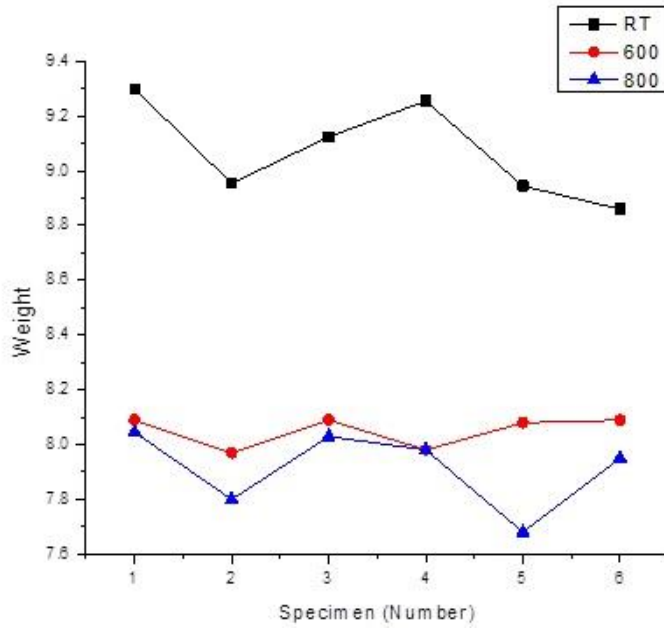
The graphs plotted in fig 3 represents the weight loss of the cube specimens at room temperature, 600 and 800 degrees Celsius for 0%, 10%, 20%, 30% and 40 % plastic addition. From the graph it is clear that the specimens at room temperature has a maximum weight of 9.3 kg at 0% plastic addition. When the specimen is subjected to 600o C the weight loss obtained for the specimen is 8.09 kg which indicates a 13% weight reduction. the minimum weight of specimen obtained is 7.970 kg. When subjected to 800oC the weight reduced for the specimen is 8.045 indicating a 13.5% weight reduction. Moreover, the minimum weight of the specimen is 7.680 kg.

Similarly, for 10 % addition the maximum weight is 8.97 kg for room temperature and when subjected to 600o C the weight for the specimen is reduced to 6.99 kg and for 800o C the weight loss is observed to be 6.60 kg which indicate a weight loss of 22.1% and 26.4 % when increasing temperatures respectively. For 20 % the maximum weight corresponds to 8.32 kg and the weight loss percentage during elevated temperatures corresponds to 17.7% and 28.1% respectively at 600o C and 800o C. The values of maximum weight loss at the corresponding temperatures are 6.95 kg and 6.580 kg.

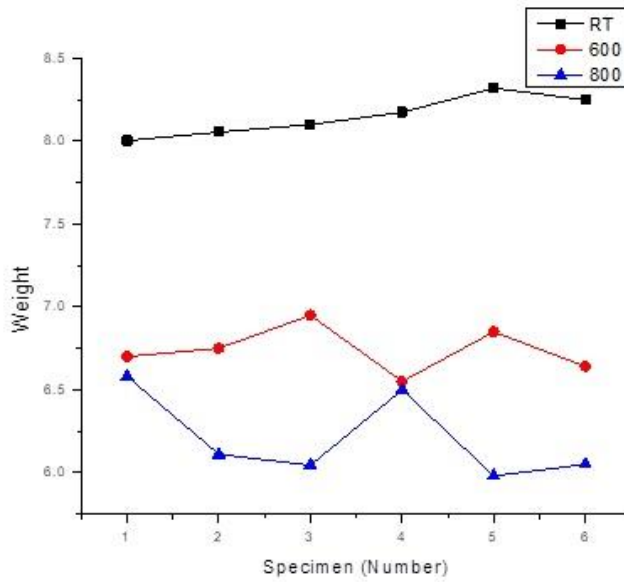
The weight loss percentage for the 30% addition is 17.3 % and 28.2% for 600o C and 800o C respectively as the maximum weight losses denoted the value of 8.05 kg at room temperature to the increased temperature are 6.66 and 5.78 kg respectively. For maximum 40% weight addition the specimen at room temperature is 7.87 kg and weight loss in maximum for 800-degree and 600-degree temperature which is 29.6% and 25.2 % respectively while the maximum weight corresponds to 5.89 and 5.54 kg respectively. From figure 3, it is clear that when temperature raises from 600 to 800, there is a weight loss of concrete samples. Hence, in this research, plastic wastes were added to concrete samples to reduce weight loss by reducing the pore pressure generated inside the concrete subjected. When the addition of plastic waste is increased from 0 % to 40%, the weight loss decreases since plastic waste in concrete reduces the direct effect of high temperature on concrete surface.



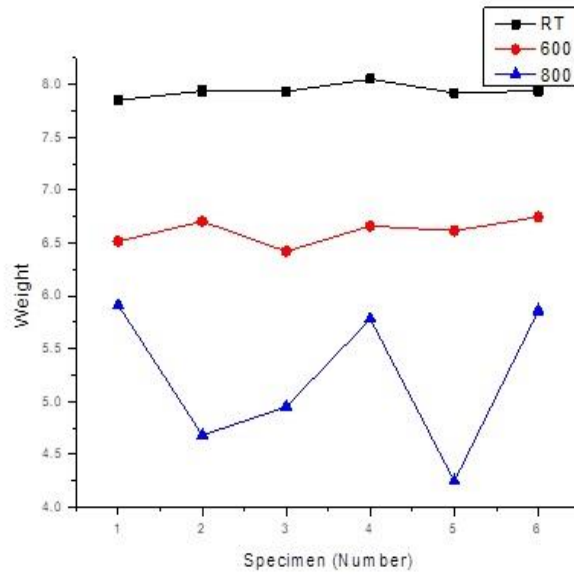
(a) 0% plastic waste



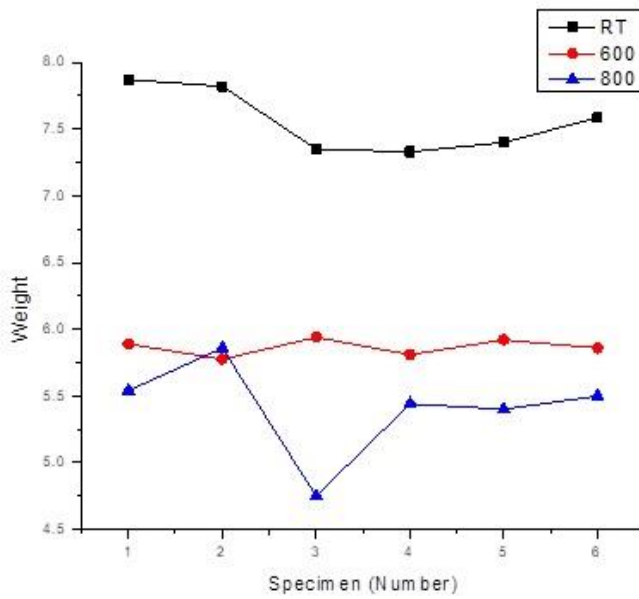
(b) 10% plastic waste



(c) 20% plastic waste

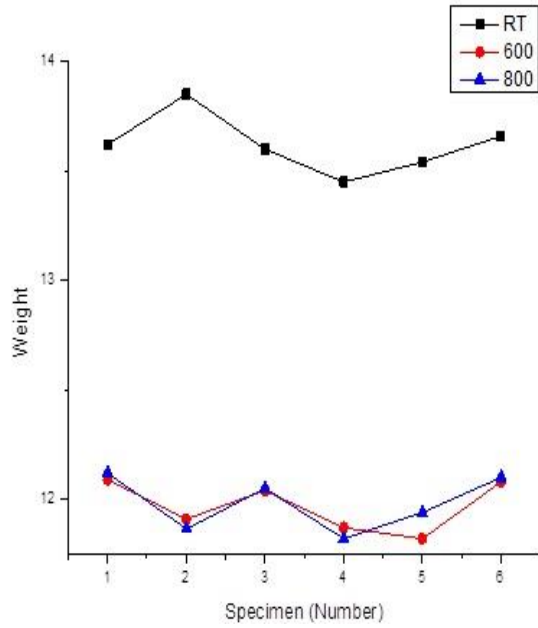


(d) 30% plastic waste

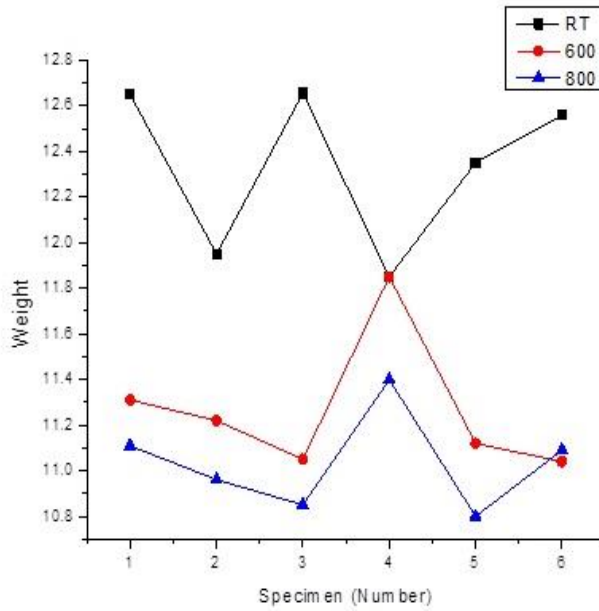


(e) 40% plastic waste

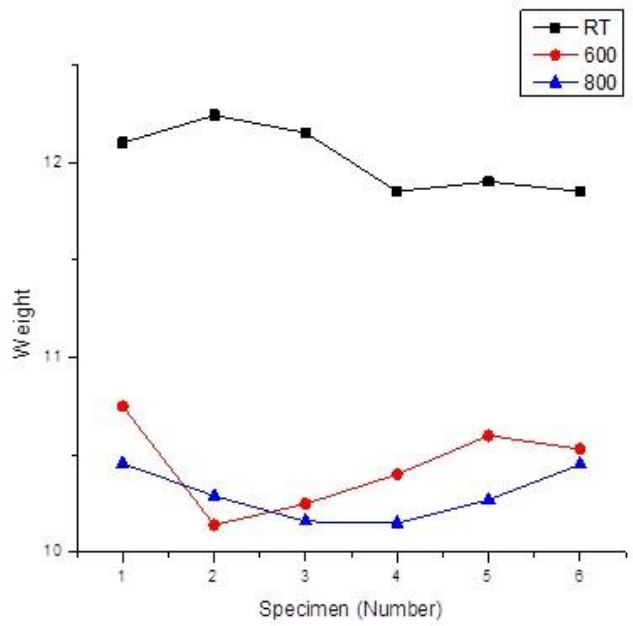
Fig. 3 Weight loss in cube specimens



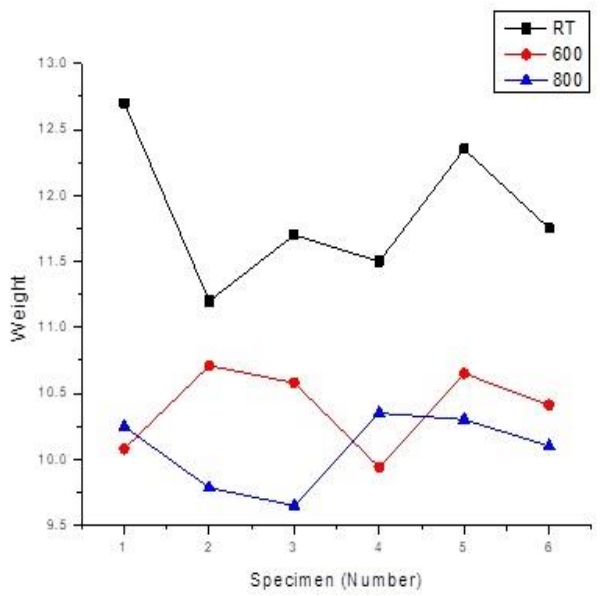
(a) 0% plastic waste



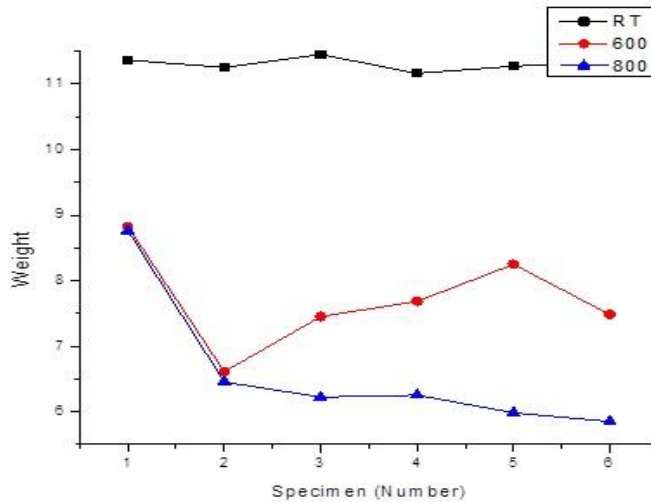
(b) 10% plastic waste



(c) 20% plastic waste



(d) 30% plastic waste



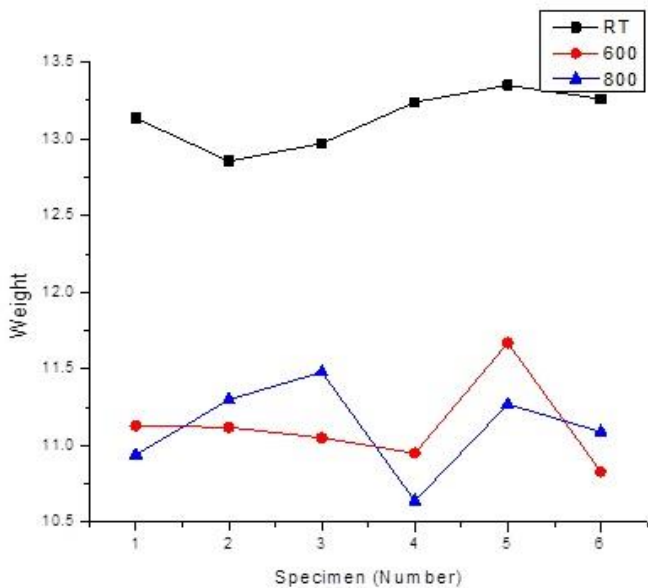
(e) 40% plastic waste

Fig. 4 Weight loss in cylindrical specimens

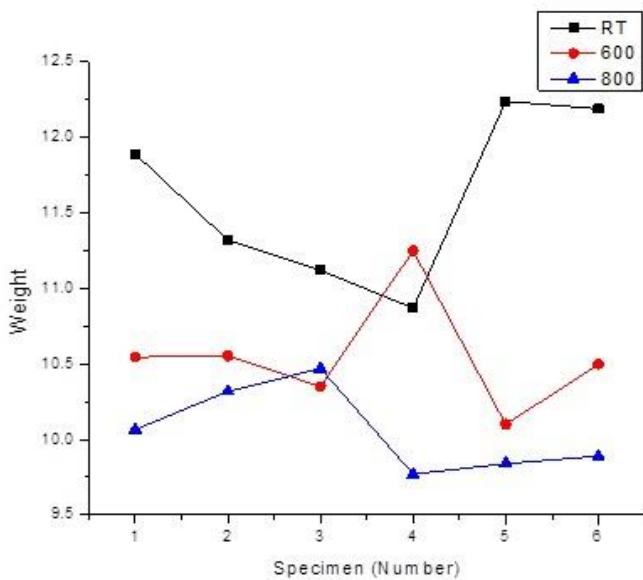
The graphs plotted in fig 4 represents the weight loss of the cube specimens at room temperature, 600 and 800 degrees Celsius for 0%, 10%, 20%, 30% and 40 % plastic addition. From the graph it is clear that the specimens at room temperature has a maximum weight of 13.85 kg at 0% plastic addition. When the specimen is subjected to 600o C the weight loss obtained for the specimen is 12.09 kg which indicates a 11% weight reduction. the minimum weight of specimen obtained is 11.87 kg. When subjected to 800oC the weight reduced for the specimen is 12.12 indicating a 11.12% weight reduction. Moreover, the minimum weight of the specimen is 11.82kg.

Similarly, for 10 % addition the maximum weight is 12.655 kg for room temperature and when subjected to 600o C the weight for the specimen is reduced to 11.31 kg and for 800o C the weight loss is observed to be 11.11 kg which indicate a weight loss of 10% and 12 % when increasing temperatures respectively. For 20 % the maximum weight corresponds to 12.24 kg and the weight loss percentage during elevated temperatures corresponds to 17.2% and 15.9% respectively at 600o C and 800o C. The values of maximum weight loss at the corresponding temperatures are 10.14 kg and 10.29 kg respectively.

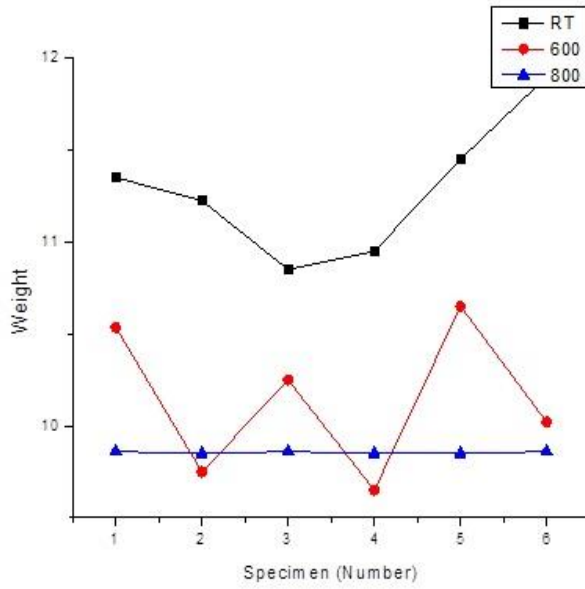
The weight loss percentage for the 30% addition is 20.1 % and 19.3% for 600o C and 800o C respectively as the maximum weight losses denoted the value of 12.700 kg at room temperature to the increased temperature are 10.08 and 10.25 kg respectively. For maximum 40% weight addition the specimen at room temperature is 11.45 kg and weight loss in maximum for 800-degree and 600-degree temperature which is 34.9 % and 45.6 % respectively while the maximum weight corresponds to 7.45 and 6.22 kg respectively. It is observed that the maximum amount of weight loss is observed at the 40% plastic addition which indicates that as the amount of plastics increase, they get converted into ash upon elevated temperature which indicates the maximum weight loss. From figure 4, it is observed that for cylindrical specimen, the weight loss is increased with addition of plastics and increase in temperature. Hence, for this type of specimen, the additions of plastics reduce the effect of high temperature on concrete but conversion of plastic into ash cause maximum weight loss.



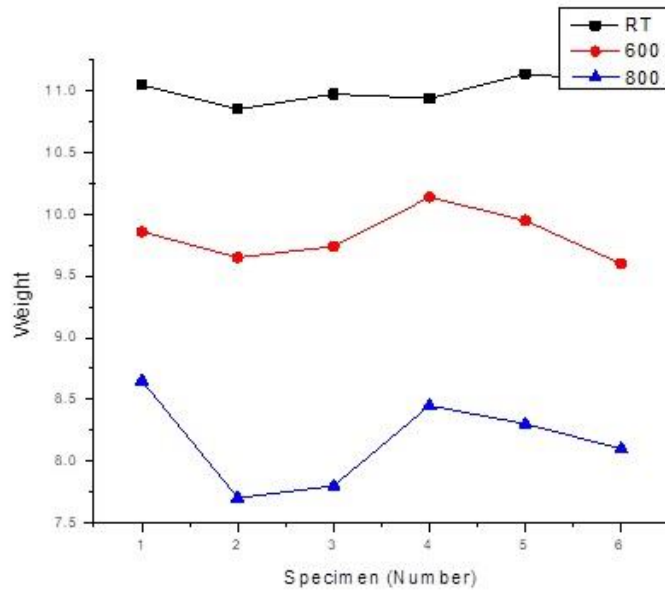
(a) 0% plastic waste



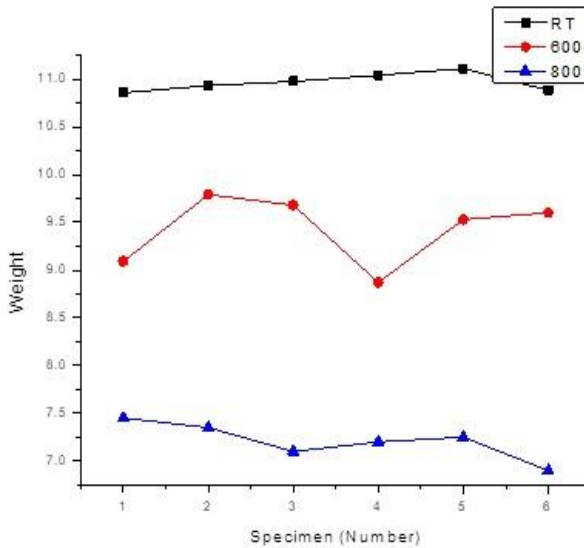
(b) 10% plastic waste



(c) 20% plastic waste



(d) 30% plastic waste



(e) 40% plastic waste

Fig. 5 Weight loss in beam specimens

The plots in fig 5 depict the weight loss of the beam specimens at room temperature, 600 and 800 degrees Celsius for 0 percent, 10%, 20%, 30%, and 40% plastic addition. The graph clearly shows that the specimens at room temperature have a maximum weight of 13.35 kg with 0% plastic addition. When the specimen is exposed to 600°C, the weight loss obtained is 11.67 kg, indicating a 12 percent weight drop. The minimum specimen weight obtained is 10.83 kg. When exposed to 800°C, the weight of the specimen is reduced by 11.27, suggesting a 15% weight reduction.

Similarly, for 10% addition, the maximum weight is 12.24 kg at room temperature, and when subjected to 600°C, the weight for the specimen is reduced to 10.1 kg, and when subjected to 800°C, the weight loss is observed to be 9.8 kg, indicating a weight loss of 17.1% and 19.4% when increasing temperatures, respectively. The maximum weight for 20% amounts to 11.90 kg, and the weight loss percentage with elevated temperatures relates to 15% and an average of 14 percent at 600°C and 800°C, respectively. Maximum weight loss values at the corresponding temperatures are 10.02 kg and 9.850 kg, respectively.

The weight loss percentage for the 30% addition is 10% and 25.5% for 600°C and 800°C respectively as the maximum weight losses denoted the value of 11.14 kg at room temperature to the increased temperature are 9.9 and 8.3 kg respectively. For maximum 40% weight addition the specimen at room temperature is 11.11 kg and weight loss in maximum for 800-degree and 600-degree temperature which is 14.2% and 34.7% respectively while the maximum weight corresponds to 9.5 and 7.25 kg respectively. It is obvious from the preceding results that as the temperature rises, the weight loss of the beam specimen decreases due to the addition of plastic wastes. This is because when plastic waste deteriorates at high temperatures, it turns into ash, which has a lower density than plastic and hence causes low weight loss in concrete specimens.

4.2. Edge Spall

All of the data on spalling are reported below after the edge effects have been neutralized, as seen in Figure. These effects are mostly caused by stress patterns along the edges, which is frequently referred to as the "corner effect." The results in Table[2] indicate the corner effect and the deterioration of the molded sample which provide a valuable assessment of the phenomenon's variability. The depth of the damaged concrete ranges from 4 to 15 cm, with a considerable degree of variability. Spalling frequently reaches or even through the reinforcing mesh. Figures show the quantitative influence of the edge effect on the test results.

From the graph the edge spalling of the cube specimen is described for room temperature, 600 degrees and 800 degrees Celsius for various specimens with 0 %, 10%, 20%, 30% and 40% addition of plastic aggregates. All the edge spalling for room temperatures are zero as it does not show any deviation of specimens. Hence the specimen is considered to be zero at room temperature. At 600 degrees the cube specimen has deteriorated to an edge effect of 11 cm and for 800 degrees it is indicated to be 15 cm for 0% plastic addition. For 10% addition the value is found to be maximum at 12 cm for both temperatures. for 20% addition of plastics the edges of the cubes deteriorated to 15 cm and 11.5 cm respectively for the 600 degrees and 800-degree Celsius elevation of temperature. The edge was found to remove from the mold for a measurement of 11 cm and 12.5 cm in the 30% addition and as the temperature increases the 40percent addition showed an edge effect of 11.6 and 12 cm respectively. From the graphs it is clear that the addition of plastic wastes reduces the edge spalling till 20% and beyond that the spalling increases at elevated temperatures and hence the 20% plastic addition is depicted to the optimum value of spalling.

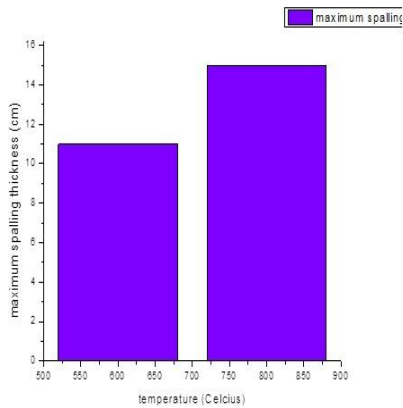
Figure 7 depicts the edge spalling of the cylindrical specimen at room temperature, 600 degrees and 800 degrees Celsius for various specimens with 0 percent, 10%, 20%, 30%, and 40% addition of plastic aggregates. All of the edge spalling for room temperatures is 0 because there is no specimen variance. As a result, the specimen is found to be zero at room temperature. The cube specimen has degraded to an edge effect of 3 cm at 600 degrees and 8 cm at 800 degrees with 0% plastic addition. The value for 10% addition is determined to be greatest at 5.5 and 7 cm for both temperatures. The edges of the cubes degraded to 4 cm and 5 cm for the 600degrees and 800-degree Celsius temperature elevations, respectively, with a 20% increase of plastics. The edge was found to remove from the mold for measurements of 8 cm and 7 cm in the 30% addition, and as the temperature increased, the edge effect was 7 and 8 cm in the 40% addition. From the results the addition of 20% plastic addition depicts the optimal addition of reinforcement in the concrete.

The values for spalling depths in these figures were calculated on a series of six specimens built with five concretes of proportions and values are calculated from the only measured depth within the center zone. When the edge effect is considered, the deviation decreases slightly, the distance between maximum and minimum values decreases slightly, but average spalling increases. This is supported by the observation of the exposed specimens which shows that the edges are less influenced with addition of plastic wastes.

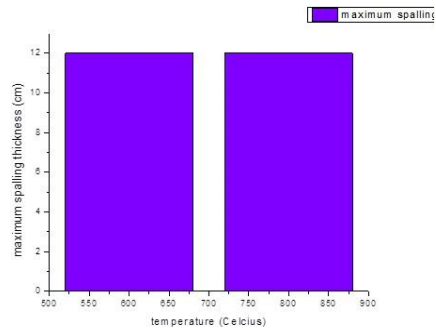
From the results obtained, the addition of plastic waste (0% to 40%) in three specimens, namely cube specimen, cylindrical specimen and rectangular beam specimen of concrete samples, can tolerate the effect of high temperature on concrete surface up to 800 degrees Celsius. However, Calcium carbonate break down when the temperature exceeds 700o C. At higher temperatures that is more than 600 degree celsius, aggregates such as

calcite (CaCO₃), magnesite (MgCO₃), and dolomite (MgCO₃/CaCO₃) were broken down into oxides and carbonites CO₂ (CaO + CO₂) [25].

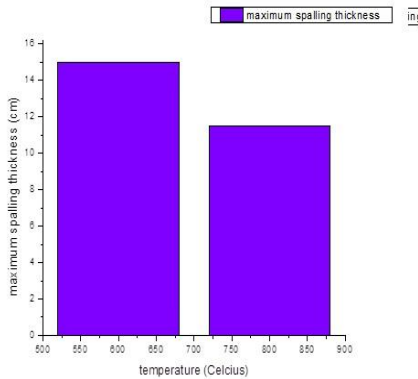
From the graph the edge spalling of the cube specimen is described for room temperature, 600 degrees and 800 degrees Celsius for various specimens with 0 %, 10%, 20%, 30% and 40% addition of plastic aggregates. All the edge spalling for room temperatures are zero as it does not show any deviation of specimens. Hence the specimen is considered to be zero at room temperature. At 600 degrees the cube specimen has deteriorated to an edge effect of 11 cm and for 800 degrees it is indicated to be 15 cm for 0% plastic addition. For 10% addition the value is found to be maximum at 12 cm for both temperatures. for 20% addition of plastics the edges of the cubes deteriorated to 15 cm and 11.5 cm respectively for the 600 degrees and 800-degree Celsius elevation of temperature. The edge was found to remove from the mold for a measurement of 11 cm and 12.5 cm in the 30% addition and as the temperature increases the 40percent addition showed an edge effect of 11.6 and 12 cm respectively. From the graphs it is clear that the addition of plastic wastes reduces the edge spalling till 20% and beyond that the spalling increases at elevated temperatures and hence the 20% plastic addition is depicted to the optimum value of spalling.



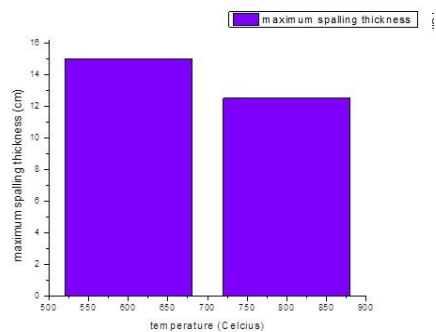
(a) 0% plastic waste



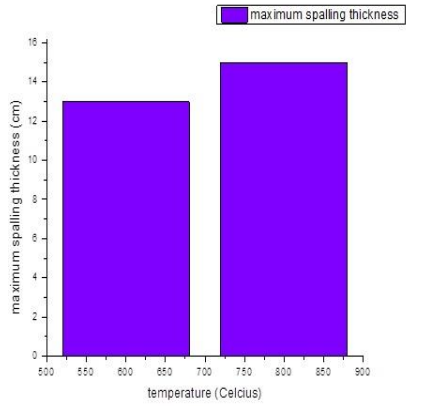
(b) 10% plastic waste



(c) 20% plastic waste

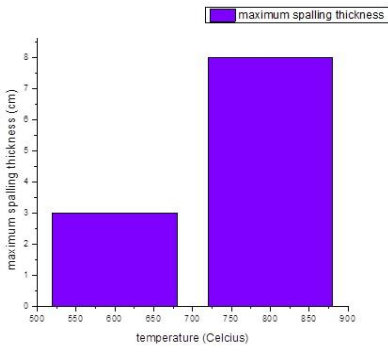


(d) 30% plastic waste

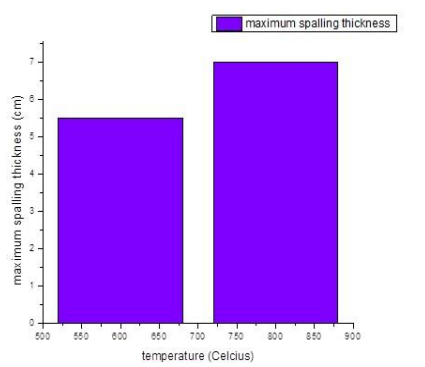


(e) 40% plastic waste

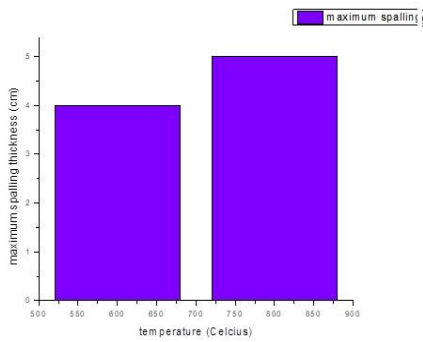
Fig. 6 Edge spalling of cube specimens



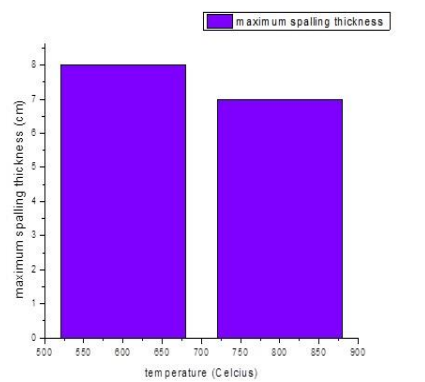
(a) 0% plastic waste



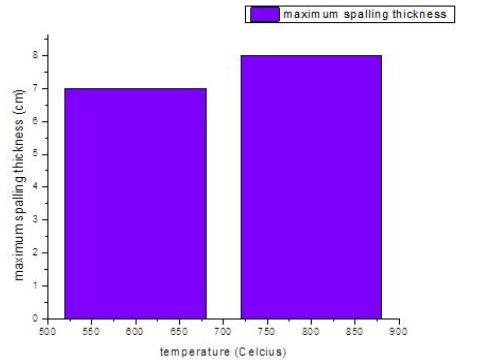
(b) 10% plastic waste



(c) 20% plastic waste



(d) 30% plastic waste



(e)

Fig. 7 Edge spalling of cylindrical specimens

Figure 7 depicts the edge spalling of the cylindrical specimen at room temperature, 600 degrees and 800 degrees Celsius for various specimens with 0 percent, 10%, 20%, 30%, and 40% addition of plastic aggregates. All of the edge spalling for room temperatures is 0 because there is no specimen variance. As a result, the specimen is found to be zero at room temperature. The cube specimen has degraded to an edge effect of 3 cm at 600 degrees and 8 cm at 800 degrees with 0% plastic addition. The value for 10% addition is determined to be greatest at 5.5 and 7 cm for both temperatures. The edges of the cubes degraded to 4 cm and 5 cm for the 600degrees and 800-degree Celsius temperature elevations, respectively, with a 20% increase of plastics. The edge was found to remove from the mold for measurements of 8 cm and 7 cm in the 30% addition, and as the temperature increased, the edge effect was 7 and 8 cm in the 40% addition. From the results the addition of 20% plastic addition depicts the optimal addition of reinforcement in the concrete.

The values for spalling depths in these figures were calculated on a series of six specimens built with five concretes of proportions and values are calculated from the only measured depth within the center zone. When the edge effect is considered, the deviation decreases slightly, the distance between maximum and minimum values decreases slightly, but average spalling increases. This is supported by the observation of the exposed specimens which shows that the edges are less influenced with addition of plastic wastes.

From the results obtained, the addition of plastic waste (0% to 40%) in three specimens, namely cube specimen, cylindrical specimen and rectangular beam specimen of concrete samples, can tolerate the effect of high temperature on concrete surface up to 800 degrees Celsius. However, Calcium carbonate break down when the temperature exceeds 700o C. At higher temperatures that is more than 600 degree celsius, aggregates such as calcite (CaCO_3), magnesite (MgCO_3), and dolomite ($\text{MgCO}_3/\text{CaCO}_3$) were broken down into oxides and carbonites CO_2 ($\text{CaO} + \text{CO}_2$) [25].

4.3. Aggregate Variation Effect

The results enable the examination of the impact of aggregate nature of the added plastic wastes at varying proportions. Part of the variation in recorded spalling depths for the of aggregates is very definitely due to material loss during the cooling phase. It should be noted that, as stated, spalling depths were assessed following the test. Materials may fall off the tested elements during the cooling phase. The thickness reduction measured after

the test includes every phenomenon that resulted in material loss, whether it occurred during the heating or cooling phases. Material loss might be seen during the cooling period. Calcium carbonate breakdown occurs when the temperature exceeds 700° C. This is followed by re-hydration and carbonation during the cooling phase, which causes material separation resulting in spalling. Which identified by a phenolphthalein solution to determine the carbonation depth in concrete as an indicator.

Table 2. Corner effects of cubes

% Plastic addition	Cube (normal temperature)	Cube at 600°C	Cube at 800°C
	Spalling corners brokes	Spalling corners brokes (cm x cm x cm)	Spalling corners brokes (cm x cm x cm)
0	No change	2.5x6.5x9	corner broken
	No change	5.5x7.5x1	3x15x4.5
	No change	2x6x10	3x14x4.6
	No change	5.5x7.5x2	3x12x4.7
	No change	2.5x6.5x11	3x15x5
	No change	5.5x7.5x3	3x13x4
10	No change	2.5x12x1.5	3.5x11x2.5
	No change	9.5x11.5x5.5	8.5x11.5x6.5
	No change	cracks and plastic burns	3.5x11x2.6
	No change	2.5x11x2	8.5x12x6.6
	No change	9x11x5	3.5x11x2.7
	No change	2x10x1	8.5x11.5x6.7
20	No change	7.5x15x10	8.5x11x7.5
	No change	small corner broken	9.5x11.5x7.5
	No change	9x10x6.5	8.5x11x7.6
	No change	9x9x7	9.5x11.5x7.6
	No change	8x8x11	8.5x11x7.7
	No change	7x10x10	9.5x11.5x7.7
30	No change	15x10x11	15x11x11
	No change	4x11x7	6x11x7
	No change	5x6x10	5x10x11.5
	No change	7x6x11	6x11x8
	No change	8x9x11	6x12x10
	No change	10x8x7	10x10x12.5
40	No change	13x10x11.5	15x10x11
	No change	5.5x11x7	4x11x7.5
	No change	5x8x10	5.5x8.5x10
	No change	13x10.5x11.6	15x10x12
	No change	5.5x11.5x8	4x12x7.6
	No change	5x8.5x11	5x8x11

The specimens' sections were identical, but their thickness varied. The position of the plastic in the concrete identified by passing ultrasonic wave through the specimens. Plastic on the surface which is exposed to high temperature melts early as compare to the plastic which in not exposed to high temperature. At room temperature as the slabs are not loaded, thickness may have an effect on stress distribution due to thermal non-linear gradients. On the other hand, it can contribute to water migration. Because the reinforcement is so dispersed, there is no clear trend toward thicker specimens. This

discovery is almost definitely owing to the fact that numerous phenomena, such as mechanical strength and thermal gradients, are fighting for attention.

Table 3. Corner effects of cylindrical specimens

% Plastic addition	Cylinder (normal temperature)	Cylinder (600°C)	Cylinder (600°C)
	Spalling corners brokes	Spalling corners brokes	Spalling corners brokes
0	No change	2x2	6x7
	No change	corners broken	6.5x8
	No change	1.5x2	7x6.5
	No change	2.5x2	7x5
	No change	2x3	6x6.5
	No change	3x1.5	7x7
10	No change	3x5.5	5x3
	No change	cracks	4x5.5
	No change	4x4	5x4
	No change	3.5x4.5	4x6
	No change	5x4	5x5
	No change	5.5x3.5	4x7
20	No change	small croner	5x4.5
	No change	3x4	3.5x4.5
	No change	2x3	5x4.6
	No change	2.5x3.5	3.5x4.6
	No change	3x2	5x4.7
	No change	2.5x2.5	3.5x4.7
30	No change	8x2.5	5.5x6
	No change	4x6.5	6.5x5
	No change	corner broken	5x6
	No change	3x7	4x7
	No change	2x6	6.5x7
	No change	3.5x7.5	5.5x6.5
40	No change	5.5x6.5	6.5x6.5
	No change	6x6.5	7x6.5
	No change	5.8x6.6	6.5x6
	No change	6.5x6	7x6
	No change	6x7	6.5x8
	No change	6x6	6.5x7.5

5. Conclusion

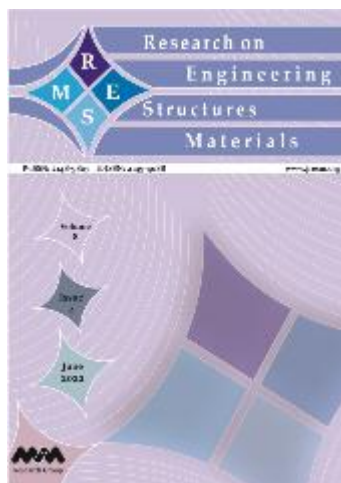
Cracking and spalling can occur as a result of sudden temperature fluctuations, and aggregate expansion can cause friction in the concrete. Concrete's compressive strength is also affected by high temperatures due to inherent material features such as unstable fracture behavior and limited permeability. Hence experimental investigation of spalling effect of elevated temperature on concrete containing waste plastic aggregates utilized the addition of aggregate waste plastics to concrete in order to minimize the pore pressure formed inside the concrete when it is exposed to a thermal environment, thereby boosting building thermal stability. Plastics are added to the concrete mix in

various weight proportions, such as 0%, 10%, 20%, 30%, and 40%, resulting in three types of specimens: cubes, cylinders, and rectangular beams which are then tested for volumetric degradation stability under various thermal gradients including room temperature, 600°C, and 800°C. The spalling of the edges in the specimens were identified and concluded based on the findings. For 600°C and 800°C temperature elevations, the margins of the cubes deteriorated to 15 cm and 11.5 cm respectively with a 20 percent plastic addition, and therefore the 20 percent plastic addition is depicted to the optimal value of spalling for cubes and cylindrical specimens. A 40 percent plastic addition results in the largest weight reduction because as the number of plastics grows, they are turned into ash at high temperatures, resulting in the greatest weight loss. Plastic position in the specimens is also essential; when exposed to higher temperatures, it degrades more quickly than specimens with plastic that has not been exposed to higher temperatures. In the future, researchers should concentrate on different types of aggregates and plastic wastes to be added to the concrete surface in appropriate size and concentration to tolerate high temperatures of more than 800 degrees Celsius thereby analyze the spalling as well as cracking effect on concrete.

References

- [1] Qin D, Gao P, Aslam F, Sufiyan M, Alabduljabbar H. A comprehensive review on fire damage assessment of reinforced concrete structures. *Case Studies in Construction Materials* 16(2022): e00843. <https://doi.org/10.1016/j.cscm.2021.e00843>
- [2] Naser MZ, Hawileh R, Abdalla J. Fiber-reinforced polymer composites in strengthening reinforced concrete structures: A critical review. *Engineering Structures* 198 (2019): 109542. <https://doi.org/10.1016/j.engstruct.2019.109542>
- [3] Luhar S, Nicolaidis D, Luhar I. Fire resistance behaviour of geopolymer concrete: an overview. *Buildings* 11.3 (2021): 82. <https://doi.org/10.3390/buildings11030082>
- [4] Li L, Khan M, Bai C, Shi K. Uniaxial tensile behavior, flexural properties, empirical calculation and microstructure of multi-scale fiber reinforced cement-based material at elevated temperature. *Materials* 14.8 (2021): 1827. <https://doi.org/10.3390/ma14081827>
- [5] Nasser IM, Ibrahim MH, Zuki SS, Algaifi H, Alsharif AF. The effect of nanosilica incorporation on the mechanical properties of concrete exposed to elevated temperature: a review. *Environmental Science and Pollution Research* (2022): 15318-15336. <https://doi.org/10.1007/s11356-021-18310-8>
- [6] Huang J, Xu Y, Haung H, Dai J. Structural behavior of FRP connector enabled precast geopolymer concrete sandwich panels subjected to one-side fire exposure. *Fire Safety Journal* 128 (2022): 103524. <https://doi.org/10.1016/j.firesaf.2022.103524>
- [7] Naser MZ. Heuristic machine cognition to predict fire-induced spalling and fire resistance of concrete structures. *Automation in Construction* 106 (2019): 102916. <https://doi.org/10.1016/j.autcon.2019.102916>
- [8] Zhu Y, Husam H, Kumar A, Chen G. A review: Material and structural properties of UHPC at elevated temperatures or fire conditions. *Cement and Concrete Composites* 123 (2021): 104212. <https://doi.org/10.1016/j.cemconcomp.2021.104212>
- [9] Ye L, Pimienta P, Pinoteau N, Tan K. Effect of aggregate size and inclusion of polypropylene and steel fibers on explosive spalling and pore pressure in ultra-high-performance concrete (UHPC) at elevated temperature. *Cement and Concrete Composites* 99 (2019): 62-71. <https://doi.org/10.1016/j.cemconcomp.2019.02.016>
- [10] Bernardo RA, Camilo JR, Amaral RC, Garcez EO, Garcez MR. Effects of plastic waste on the heat-induced spalling performance and mechanical properties of high strength concrete. *Materials* 13.15 (2020): 3262. <https://doi.org/10.3390/ma13153262>
- [11] Dorjan D, Pont SD, Briffaut M, Weber B. Modeling of 3D moisture distribution in heated concrete: from continuum towards mesoscopic approach. *International*

- Journal of Heat and Mass Transfer 134 (2019): 1137-1152.
<https://doi.org/10.1016/j.ijheatmasstransfer.2019.02.017>
- [12] Meng C, Sun Z, Tu W, Yan X, Zhang M. Behaviour of recycled tyre polymer fibre reinforced concrete at elevated temperatures, Cement and Concrete Composites 124 (2021): 104257. <https://doi.org/10.1016/j.cemconcomp.2021.104257>
- [13] Abdelazim W, Mohammad H, Benmokrane B, Nolan S. Strength of bridge high-strength concrete slender compression members reinforced with GFRP bars and spirals: experiments and second-order analysis, Journal of Bridge Engineering 25.9 (2020): 04020066. [https://doi.org/10.1061/\(ASCE\)BE.1943-5592.0001601](https://doi.org/10.1061/(ASCE)BE.1943-5592.0001601)
- [14] Junaid MF, Rehman Z, Cekon M, Curpek J, Farooq R, Cui H, Khan I. Inorganic phase change materials in thermal energy storage: A review on perspectives and technological advances in building applications. Energy and Buildings 252 (2021): 111443. <https://doi.org/10.1016/j.enbuild.2021.111443>
- [15] Luhar S, Luhar I, Shaikh F. A Review on the Performance Evaluation of Autonomous Self-Healing Bacterial Concrete: Mechanisms, Strength, Durability, and Microstructural Properties. Journal of Composites Science 6.1 (2022): 23. <https://doi.org/10.3390/jcs6010023>
- [16] Awoyera PO, Adesina A. Plastic wastes to construction products: Status, limitations and future perspective. Case Studies in Construction Materials 12 (2020): e00330. <https://doi.org/10.1016/j.cscm.2020.e00330>
- [17] Li X, Ling T, Mo K. Functions and impacts of plastic/rubber wastes as eco-friendly aggregate in concrete-A review. Construction and Building Materials 240 (2020): 117869. <https://doi.org/10.1016/j.conbuildmat.2019.117869>
- [18] Faraj RH, Ali H, Sherwani A, Hassan B, Karim H, Use of recycled plastic in self-compacting concrete: A comprehensive review on fresh and mechanical properties. Journal of Building Engineering 30 (2020): 101283. <https://doi.org/10.1016/j.jobe.2020.101283>
- [19] Camilo JR, Rohden AB, Garcez MR. Concrete with rejected recyclable plastic waste at high temperatures. Magazine of Concrete Research 73.19 (2021): 973-987. <https://doi.org/10.1680/jmacr.19.00485>
- [20] Hager I, Sitarz M, Mróz K. Fly-ash based geopolymers for high-temperature application-Effect of slag addition. Journal of Cleaner Production 316 (2021): 128168. <https://doi.org/10.1016/j.jclepro.2021.128168>
- [21] Mohammadhosseini H, Tahir M, Alyousef R, Alabduljabbar H, Samadi M. Effect of elevated temperatures on properties of sustainable concrete composites incorporating waste metalized plastic fibres. SN Applied Sciences 1.11 (2019): 1-12. <https://doi.org/10.1007/s42452-019-1587-9>
- [22] Umasabor RI, Daniel SC. The effect of using polyethylene terephthalate as an additive on the flexural and compressive strength of concrete. Heliyon 6.8 (2020): e04700. <https://doi.org/10.1016/j.heliyon.2020.e04700>
- [23] Olofinnade OM, Ede AN, Ndambuki JM. Experimental investigation on the effect of elevated temperature on compressive strength of concrete containing waste glass powder, International Journal of Engineering and Technology Innovation 7.4 (2017): 280-291.
- [24] Novak J, Kohoutkova A. Fire response of hybrid fiber reinforced concrete to high temperature. Procedia Engineering 172 (2017): 784-790. <https://doi.org/10.1016/j.proeng.2017.02.123>
- [25] Memon SA, Shah SFA, Khushnood RA, Baloch WL. Durability of sustainable concrete subjected to elevated temperature-A review, Construction and Building Materials 199 (2019): 435-455. <https://doi.org/10.1016/j.conbuildmat.2018.12.040>
- [26] Kodur V. Properties of Concrete at Elevated Temperatures, International Scholarly Research Notices, vol. 2014, Article ID 468510, 15 pages, 2014. <https://doi.org/10.1155/2014/468510>



Leverage of high-volume fly ash along with glass fiber for sustainable concrete

Mahesh V. Raut

Online Publication Date: 15 May 2022

URL: <http://www.jresm.org/archive/resm2022.349st1005.html>

DOI: <http://dx.doi.org/10.17515/resm2022.349st1005>

Journal Abbreviation: *Res. Eng. Struct. Mater.*

To cite this article

Raut M. Leverage of high-volume fly ash along with glass fiber for sustainable concrete. *Res. Eng. Struct. Mater.*, 2022; 8(4): 885-904.

Disclaimer

All the opinions and statements expressed in the papers are on the responsibility of author(s) and are not to be regarded as those of the journal of Research on Engineering Structures and Materials (RESM) organization or related parties. The publishers make no warranty, explicit or implied, or make any representation with respect to the contents of any article will be complete or accurate or up to date. The accuracy of any instructions, equations, or other information should be independently verified. The publisher and related parties shall not be liable for any loss, actions, claims, proceedings, demand or costs or damages whatsoever or howsoever caused arising directly or indirectly in connection with use of the information given in the journal or related means.



Published articles are freely available to users under the terms of Creative Commons Attribution - NonCommercial 4.0 International Public License, as currently displayed at [here](#) (the "CC BY - NC").



Research Article

Leverage of high-volume fly ash along with glass fiber for sustainable concrete

Mahesh V. Raut*

Department of Civil Engineering, G.H. Rasoni Institute of Engineering & Technology, Maharashtra, India

Article Info

Article history:

Received 5 Oct 2021

Revised 13 Apr 2022

Accepted 12 May 2022

Keywords:

Sustainable;

Fine-grain fly ash;

Glass fiber;

Durability;

Ultrasonic pulse

velocity;

Electrical resistivity

Abstract

The production of fly ash is mounting steadily every year all over the globe, but the rate of recovery is insufficient compared to its production. The disposal of fly ash is becoming more and more difficult in India. Reusing fly ash for some valuable uses is one of the most convenient solutions to this problem. As a result, the present study has focused on the use of high volume fine grain fly ash as a partial alternative material for cement and sand with a low volume fraction of glass fiber. Glass fiber reinforced concrete mixtures consisting of up to 40% replacement of cement and sand by fly ash were produced for making sustainable concrete. The experimental work was carried out by preparing diverse mixes with a 0.40 water-cement ratio and analyzing the fresh as well as hardened properties of mixes. The experimental results reveal that the separate and combined replacement of cement and sand by fly ash together with glass fiber, enhance the durability and strength of concrete. When combining 20% of cement and 40% of sand replaced by fly ash together with glass fiber, better result was observed than all other mixes. The compressive strength, electrical resistivity (ER), and ultrasonic pulse velocity (UPV) increased by 36.33%, 65.82%, and 7.25% over control mix (C0-0). This discovery is very useful for making dense, durable and sustainable concrete by using proposed mixes.

© 2022 MIM Research Group. All rights reserved.

1. Introduction

Concrete is the utmost versatile and widespread construction material throughout the world, in which cement and sand (fine aggregate) are, basic components. The main role of cement in concrete is as a binding material while sand is used as a filler material. The sources of lime curtail due to the huge production of cement as the demand for infrastructure increases gradually. But during the production of cement, CO₂ is released into the atmosphere which creates environmental issues. Besides cement, the demand for natural sand also increases day by day due to the huge developmental work. The growth of society demands the generation of a wide range of waste items and industrial by-products. These materials end up in the environment, producing major issues. [1]. Today's need is to utilize these industrial-by-products for reducing the adverse effects on the environment. Researchers have thoroughly investigated the use of industrial by-products as supplementary cementitious materials in concrete, as well as their influence on strength and durability criteria. But the combined replacement for cement and fine aggregate by fly ash and their influence on strength and durability characteristics are lacking in the literatures. The recent efforts of researchers, concrete technologists and construction industries are to produce high strength, high performance and sustainable concrete at the lowest possible cost. Hence the present research was taken up to study the feasibility of and for purpose of comparison of locally available industrial by-products like fly ash as a partial alternative material for cement and fine aggregate along with glass fiber for making durable and sustainable concrete.

*Corresponding author: mahesh_raut777@rediffmail.com

^a orcid.org/0000-0002-5334-3061

DOI: <http://dx.doi.org/10.17515/resm2022.349st1005>

Res. Eng. Struct. Mat. Vol. 8 Iss. 4 (2022) 885-904

For generating one ton of cement, almost one ton of CO₂ is released [2], which is harmful to our society. Therefore, to reduce cement utilization, cement producers should use supplementary cementitious materials such as fly ash up to 25% to 35% in Portland Pozzolana Cement (PPC). On the other hand, due to government restriction on sand mining from a river bed, projects are delayed which increase the total cost of construction, thus the contractor always requires partial or full replacement material for sand. Presently, India is having about 167 major coal-based thermal power stations with an installed capacity of 177,070 Mega Watt (MW) which produced over 196.44 million tons (MT) of fly ash, out of which 131.86 MT is utilized [3]. According to the notification after 3rd November 2009 by the Ministry of Environment and Forest (MoEF), the utilization of fly ash should be 100% after four years from the date of commission i.e. at 2013, but at present consumption of fly ash is 67%, that means still 33% fly ash is unused creating environmental problems. The Indian government's Ministry of Energy estimates that around 600 million tons of fly ash will be produced annually between 2031 and 2032 [4]. Management of fly ash will pose a serious issue in the upcoming year if not handled properly, and it will require a huge land area for dumping. To fulfil this requirement, present paper discusses the use of high-volume fine grain fly ash as a partial alternative material for cement as well as fine aggregate with the addition of a low quantity of glass fiber for making durable and sustainable concrete.

Numerous researchers disclosed that fly ash is used as a supplementary cementitious material due to its major advantages. One of the most important results of fly ash in a concrete is to improve its workability, as the fly ash particles are comparatively spherical than cement particles. Researcher's concluded that, Fly ash has a ball bearing effect due to its spherical shape hence, the flowability of fly ash concrete increases [5]. By substituting 30% of the cement with fly ash, 7% less water was required than the control mix of an equal slump [6]. By using 50% ultra-fine fly ash the rheological properties such as yield stress and plastic viscosity were increased by 76% and 169% respectively [7]. An improvement in rheological parameters and workability is due to increase in fly ash amount in the mix [8]. Researchers found that with increasing fly ash percentage in concrete as cement replacement (50% to 60%) the strength decreases [9-14]. The reduction in strength with the addition of high-volume fly ash could be largely associated with the slow pozzolanic reaction of fly ash. However, author also reported that in concrete with 50% fly ash as cement replacement including 0.5%, 0.75% and 1% steel fibres, the 28 days compressive strength increased by 7.3%, 7.46% and 9.2% respectively [15]. The laboratory experiment using 35%, 45% and 55% of class F fly ash as a replacement of fine aggregate, conclude that depending upon the fly ash content the compressive strength, splitting tensile strength, flexural strength and modulus of elasticity increased by 25 to 41%, 12 to 21%, 14 to 17% and 18 to 23% correspondingly at 28 days. Also, the enhancement in strength was continuous at 91 and 365 days [16]. By using fly ash as a partial alternative for fine aggregate (20% -30%) it is possible to preserve the supposed technological properties of cementitious composites and to greatly limit the costs of these undesirable residues for the environment [17]. By adding fly ash to the desalinated ocean sand mortar, the performance and mechanical properties of modified cement were extensively improved [18]. The researchers mention that, the inclusion of different fibers gives an excellent concrete performance, whereas fly ash in the mix can make up for the loss of workability owing to the incorporation of fibers and boost the strength [19-20].

Also, the investigators find that, the addition of finest particles such as the fly ash in mixture improves the durability of concrete. With the addition of 50% fly ash through cement replacement, the ER value of concrete samples increased after 28 and 365 days of curing period [21]. When 50% of cement was substituted with fly ash the ER of concrete samples increased by about 4.8 times over plain concrete [22]. Replacing 20% of cement with a

varying fineness of class C fly ash reduced the alkali-silica reaction by more than 50% at 14 days [23]. To know the outcomes of fly ash on carbonation depth (CD), the author concluded that, with the increasing replacement of cement with fly ash up to 50%, the carbonation depth also increases [24]. The heterogeneities in the microstructure of the hydrated portland cement paste, particularly the existence of large crystalline products and large pores in the transition zone were highly decreased by the inclusion of fine particles of fly ash [25]. As per Neville, the replacement of cement up to 20% by fly ash improves strength and workability [26]. According to IS 10262: 2019, the dosages of fly ash by mass of entire cementitious materials is recommended in between 15-30% [27]. For reducing the production of cement and due to scarcity of sand, present research focused on using up to 40% fly ash as a cement replacement and up to 40% fly ash as a sand replacement separately and in combined along with glass fiber. This innovation is also very useful for reducing the CO₂ emission which is produced during cement production as well as reducing the use of natural sand in concrete whose resources are depleting day by day.

2. Experimental Program

The present paper discusses the study of physical properties of procured materials by conducting various tests on OPC, fly ash, fine aggregate and crushed stone aggregate (20 mm & 10 mm). Also, the authentic outcome of individual and combined percentage replacement of cement and fine aggregate by fly ash along with glass fiber on fresh and hardened concrete properties such as workability, rheology, ultrasonic pulse velocity (UPV), bulk electrical resistivity (ER), carbonation depth and compressive strength tested at the ages of 7, 28, 56 and 119 days. The rate of gain of compressive strength of normal concrete is faster over the first 28 days of casting and then gradually decreases. However, in fly ash concrete mixes, large pozzolanic activation activities occur among the first 56-90 days [28]. Researchers also stated that, the concrete strength increased up to 6.2 to 16% over a period that varies between 28 and 56 days when fine aggregates are replaced by fly ash [29]. In order to determine the effect of high-volume fly ash on proposed mixes over a long term curing period, the samples were tested up to 119 days in the current study.

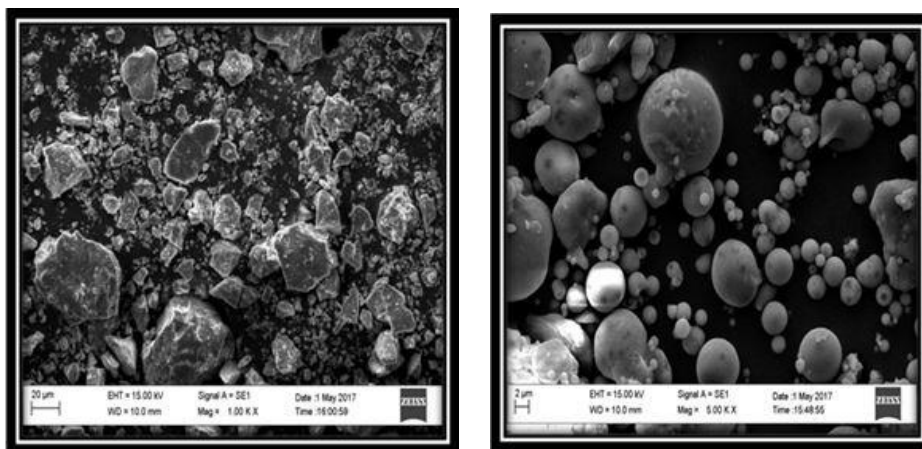
2.1. Materials used

2.1.1 Cement

The 53 grade Birla A-1 gold Ordinary Portland Cement (OPC) was purchased from locally available cement supplier was used in the present study. The initial and final setting time was found to be 118 minute and 220 minutes respectively. The specific gravity and soundness was observed as 3.15 and 2 mm respectively, while 3, 7 and 28 days compressive strength was observed as 31.5 N/mm², 38.5 N/mm² and 55 N/mm² respectively. All the results on cement were used as per the results of OPC conforming to the IS 12269-1987 [30]. The scanning electron microscope (SEM) test was performed on cement and revealed that the cement particles exhibit an irregular shape as shown in Figure 1 (a). The energy dispersion X-ray test (EDX) carried out on cement particles and its results are also organized in Table 1.

2.1.2 Fly Ash

According to IS 1727:1967 [31], the substantial properties of fly ash such as specific gravity and fineness were found as 2.15 and 12% (retained on 45-micron sieve) respectively. The SEM and EDX tests were conducted circular shape of the fly ash particles is observed as shown in Figure 1 (b) and their elemental content is shown in Table 1. The circular particle shape of fly ash helps for upgrading the workability of fresh concrete mix. The particle size distribution curve of fly ash and cement is shown in Figure 2.



(a) SEM image of cement particles

(b) SEM image of fly ash particles

Fig. 1 SEM image of cement and fly ash particles

Table 1. Elemental content of ordinary portland cement (OPC) and fly ash (%)

Chemical's elemental contents (%)	Si	Ca	Al	Fe	Mg	K	Na
OPC	16.68	67.82	4.74	3.67	1.88	2.42	0.39
Fly Ash	62.84	1.21	24.53	5.14	0.37	2.37	0.22

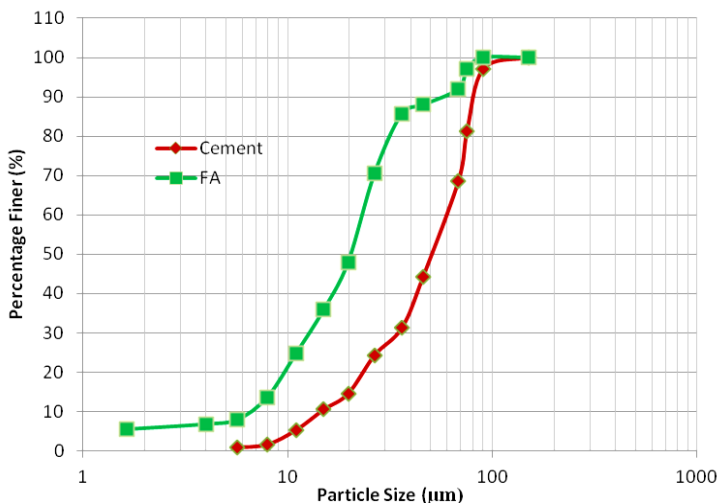


Fig. 2 Particle size distribution curves of fly ash and cement

2.1.3 Crushed Stone Aggregate

The crushed stone aggregates (20 mm and 10 mm) are collected separately from the local supplier. While collecting, it was ensured that the crushed stone aggregates were free from impurities, dust and clay particle etc. According to BIS 2386-1963 [32], the various substantial properties of aggregates were tested and are given in Table 2. As per BIS 383-1970 [33], to achieve the final grading of crushed stone aggregates, the aggregates of 20 mm and 10 mm are combined to 60% and 40% respectively. The mixing proportions were decided for achieving a crushed stone aggregate grading closer to the average of the desired grading guidelines.

2.1.4 Fine Aggregate

Nearby accessible Kharun river sand was procured from a local supplier and to protect it from dust it was stored in clean cement bags. According to IS 2386-1963, the various substantial properties of fine aggregate were tested and the results are arranged in Table 2 as an average of three samples.

2.1.5 Glass Fiber

In the present investigation, the discrete; alkali resistance (AR) glass fiber was used. The physical properties of the glass fiber, such as length were 12 millimeters, diameter 14 micrometers, tensile strength 1700 megapascals and elastic modulus 72 gigapascals, according to the available datasheet from the dealer. The nominal doses of glass fiber i.e. 0.6 kg/m³ were decided based on trials to maintain the strength and workability at lower cost criteria. The investigator stated that as the volume fraction of the glass fiber increases, the compressive strength reduces caused by the difficulty of fully dispersing the fiber, and inability of good compact of mixes [34]. They also mention that additions of a minute quantity of fiber in the mix improve the compressive and splitting tensile strength than higher dose of fiber. In present study, while mixing the glass fiber in cement, care was taken that glass fiber should be mixed uniformly without the formation of balls.

2.1.6 Plasticizer

To improve the durability of concrete, polycarboxylic ether-based water-reducing solutions were used, the dosage was kept constant at 1% of the cementitious material.

Table 2. Physical properties of crushed stone aggregates and fine aggregate

Properties	Test Result		
	20 mm crushed stone aggregate	10 mm crushed stone aggregate	Fine aggregate
Specific gravity	2.68	2.65	2.56
Water absorption (%)	0.4	0.60	0.60
Bulk density (Loose in kg/m ³)	1480.34	1520.36	1648.7
Bulk density (Rodded in kg/ m ³)	1710	1730.14	1779
Bulk density (Vibrated in kg/ m ³)	1780.52	1811	1880
Percentage void (Loose)	45	43	35.50
Percentage void (Rodded)	36	35	30.50
Percentage void (Vibrated)	33.50	32	26.50
Impact Value (%)	9.71	6.57	---
Crushing Value (%)	22.57	17	---

2.2. Concrete Mix Proportions and Sample Preparation

To understand the effect of fly ash as a partial replacement material for cement and fine aggregate together with glass fiber, the mix design was prepared using 0.40 W/C ratios and mix percentages are specified in Table 3. In the present study, 20% and 40% cement was replaced by fly ash on a weight basis while 20% and 40% fine aggregate was replaced by fly ash on a volume basis.

Total 10 mixes were designed for 0.40 W/C including control mix, mix with glass fiber and mixes with a fly ash as a partial substitute material for cement and fine aggregate together with glass fiber. The control concrete mix is represented as Cx-y and concrete with glass fiber is represent as Fx-y. Here 'x' represents a percentage replacement for cement and 'y' represents a percentage replacement for fine aggregate. The specific gravity of cement was higher than the specific gravity of fly ash. The volume of fly ash was more than the volume of replaced cement. Hence, to counterbalance the total volume, the quantity of fine aggregate was reduced keeping the crushed stone aggregate same. The glass fiber content remained constant for all mixtures. According to IS 10262: 2019, when the cement was replaced by fly ash, the cementitious material increased by 10%. The crushed stone and fine aggregate used in this study were in a saturated surface dry condition.

Table 3. Concrete mix proportions for a 1m³ concrete (0.40 W/C)

MIX	Cement (kg)	Fly ash (kg)	Crushed stone aggregate (kg)	Fine aggregate (kg)	Water (kg)	Glass Fiber (kg)	Admixture (kg)
C ₀₋₀	418.5	0	1102	732	167.40	0.0	4.18
F ₀₋₀	418.5	0	1102	732	167.40	0.6	4.18
F ₂₀₋₀	368.4	92	1102	685	167.40	0.6	4.18
F ₄₀₋₀	276.5	184	1102	671	167.40	0.6	4.18
F ₀₋₂₀	418.5	150	1102	557	167.40	0.6	4.18
F ₀₋₄₀	418.5	293	1102	383	167.40	0.6	4.18
F ₂₀₋₂₀	368.4	230	1102	522	167.40	0.6	4.18
F ₄₀₋₂₀	276.5	319	1102	510	167.40	0.6	4.18
F ₂₀₋₄₀	368.4	366	1102	360	167.40	0.6	4.18
F ₄₀₋₄₀	276.5	453	1102	351	167.40	0.6	4.18

All the ingredients of concrete for different mixes were uniformly mixed in a laboratory mixer. Weigh batching was conducted for the required quantities of all the materials. For proper mixing of glass fibers, the filaments of fibers were separated by hand and mixed with cement only. While mixing the fibers, proper care was taken that no balling of fibers should be created inside the mix. For proper mixing of the materials, firstly crushed stone and fine aggregates were mixed in a mixer for about two to three minutes. Water and superplasticizer were weighed and properly mixed in one container. A measured amount of cement was then poured into the mixer along with 50% of water, for proper mixing of materials the mixer was rotated for another two to three minutes. The 25% of water with superplasticizer was again poured inside the mix and rotated for two to four minutes in the mixer to get a homogeneous mix. The concrete mixed materials inside the mixer were taken out in a mixing tray. The remaining 25% of water was added to the rotating mixer for removing the cement and other concrete ingredients sticking to the inside of the mixer. At last, all the concrete materials in the mixing tray were properly mixed. Within 10

minutes of final mixing, the workability of mixture was measured via slump cone test followed by rheology test. The cube moulds of size 100 mm X 100 mm X 100 mm were filled in three different layers and slightly vibrated on the vibration table to eliminate the air bubbles and voids inside the concrete. All the samples were finished with a steel trowel after casting. Using wet gunny bags all the filled moulds were properly covered and de-moulded after 24 hours. After de-moulding of concrete cubes, they were submerged in a water curing tank for a period of 7, 28, 56 and 119 days.

2.3. Test on Fresh Concrete

To check the outcome of proposed mixes on the fresh properties of concrete, rheology and slump cone tests were performed. Especially attention was given to the behavior of workability and rheology of fresh concrete mixes. By using a rheometer as shown in Figure 3, yield stress and viscosity were measured for all 10 mixes and the results are tabulated in Table 4. Under stress conditions, to study the flow of material or deformation is termed as rheology, which generally consists of yield stress and viscosity. To begin the flow of a material, the minimum stress required is known as yield stress while viscosity is the resistance to the flow of the material. Rheological parameters help to illustrate the workability, placeability, compactability, finishability, flowability and pumpability of freshly mixed cementitious materials. The rheometer consists of two probes with 90 mm length on both sides of the centre of the shaft. Firstly, the freshly mixed concrete was poured into a container as shown in Figure 3 (a) and then inside the shaft of the container, the rheometer was placed as shown in Figure 3 (b). Then an input profile was chosen and stored in the smartphone which is supplied with a rheometer. By turning on the blue-tooth of the smartphone (used as a remote control) all the input commands of the rheometer are provided. With corresponding time, the rheometer recorded the torque at different locations, and for further analysis; the graphical measurements in the smartphone were transferred to the computer. The rheology is mainly used for such materials whose flow properties are difficult. Rheology expresses the workability in terms of numeric value which is more accurate and reliable than the slump cone test.

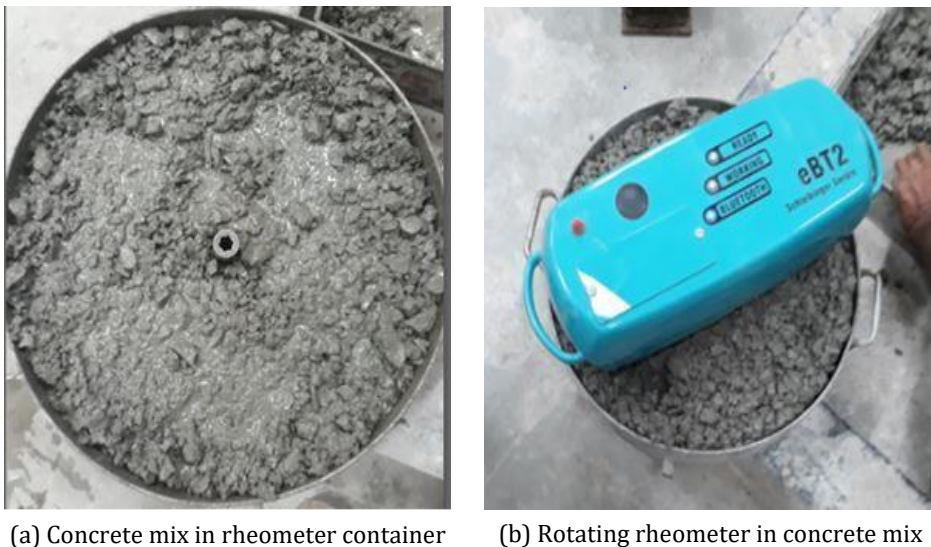


Fig. 3 Working of rheometer test apparatus

2.4. Test on Harden Concrete

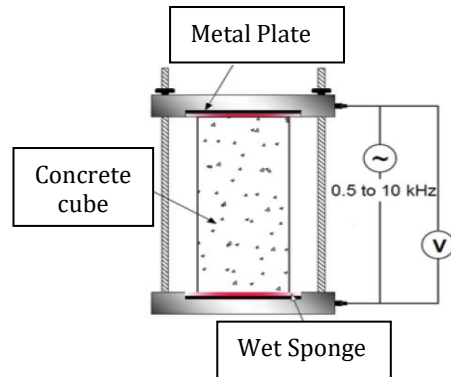
For all 10 concrete mixes, the 100 mm x 100 mm x 100 mm cubes were tested for the required tests. The 160 cubes were tested for bulk electrical resistivity (ER) test and ultrasonic pulse velocity test (UPV) and same 160 cubes were tested for compressive strength by using a compressive testing machine at the age of 7, 28, 56 and 119 days. For the carbonation test, separate 40 cubes were tested at 28 days of curing period only. For each mix on each curing period, 4 cubes were tested for each test. Total 200 cubes were cast and tested for all 10 concrete mixes at different curing periods for different tests. To measure the ER of concrete cubes, a two-probe laboratory method was used. In this method, the soaked cubes were shifted between two similar metal plates of ER meter with a damp sponge placed on the bottom and the top face of the cube to provide contact between the concrete surface and electrode plates as shown in Figure 4 (a). By applying a small, irregular current at the proposed frequency, the voltage between the two ends of the concrete sample was measured. The electrical resistivity monitor displayed the impedance value (Z), through this impedance value, the resistivity of concrete was determined according to Eq. (1). The Simplified illustration of ER is shown in Figure 4 (b). This method gives a better suggestion of concrete electrical resistance as current is flown through the bulk of concrete.

$$\rho = \frac{A}{L}Z \quad (1)$$

Wherein, " ρ " is the resistivity of a concrete mix (Ωcm), " A " is the cross-sectional area of the specimen (cm^2), " L " is the length of the sample (cm) and " Z " is the impedance (Ω). By using Eq. (1) the result of ER are calculated and shown in Figure 8.



(a) ER equipment with concrete cube



(b) Illustration of ER (Component)

Fig. 4 Arrangement of Electrical Resistivity Meter.

UPV test gives an idea about the strength, density and porosity of concrete. The UPV consists of computing the time travel of the pulse of longitudinal ultrasonic wave transient throughout the concrete sample. As per IS 13311 (Part-1) 1992 the results of UPV are calculated and shown in Figure 8. The UPV tester consists of two transducers and a monitor screen. To level and smoothen the rough surface area of the concrete cube, grease or petroleum jelly was applied on two opposite faces of the cubes. After that, the transmitting

and receiving transducers were touched on both the sides of cubes to measure the time travel. In the transmitting transducer (T_x) the ultra-pulses of natural frequency within the range 20 kHz to 150 kHz were produced, which travel through concrete and then detected by receiving transducer (R_x) as shown in Figure 5 (a). The travel time period among the beginning of a pulse created at the passing transducer and the beginning of its arrival at the collecting transducer was measured and displayed on a monitor as shown in Figure 5 (b). With the help of the displayed value of travel time (T), the pulse velocity was determined by using Eq. (2).

$$V = \frac{L}{T} \quad (2)$$

To determine the carbonation resistance of the proposed concrete, 4 sample cubes measuring 100 mm x 100 mm x 100 mm were formed from each mix, a total of 40 cubes were formed for 10 different mixes and cured for 28 days. After curing, all cubes were taken out from the curing tank and allowed to dry at normal temperature. The air-dried cubes were placed in a carbonation chamber for 28 days. The “one week-time exposure of concrete specimen inside the carbonation chamber is to some extent equal to 12 months exposition beneath natural environment” [35]. According to this, in the present study, 28 days of cubes in the carbonation chamber gives an equivalent result after 4 years of concrete. The dose of temperature was kept at 35°C, carbon dioxide (CO_2) at a rate of 5% and humidity at 70% as shown in Figure 6 (a). After 28 days of accelerated carbonation, the cubes were removed from the carbonation chamber and broken into two parts. To measure the depth of carbonation, a phenolphthalein indicator was applied on the broken surface of concrete cubes. On application of phenolphthalein indicator, pink colour was observed in an uncarbonated portion and in the carbonated portion, no change was seen as shown in Figure 6 (b). By using a measuring scale, the depth of carbonation was measured as shown in Figure 6 (c) and the results are shown in Figure 10. From the carbonation test, it can be concluded that fly ash as a partial sand replacement is very effective to reduce the carbonation depth of concrete. Wherein, “ V ” represents the ultra-pulse velocity, “ L ” represents the sample length and “ T ” represents the time travel.

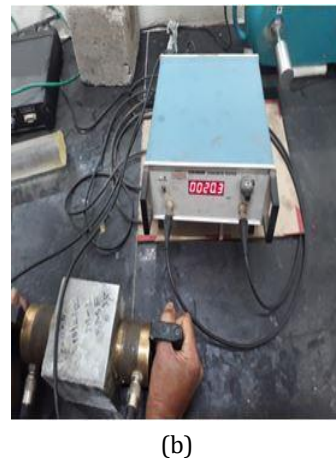
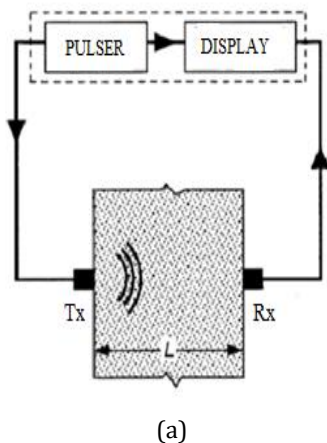


Fig. 5 Arrangement of Ultrasonic Pulse Velocity Test

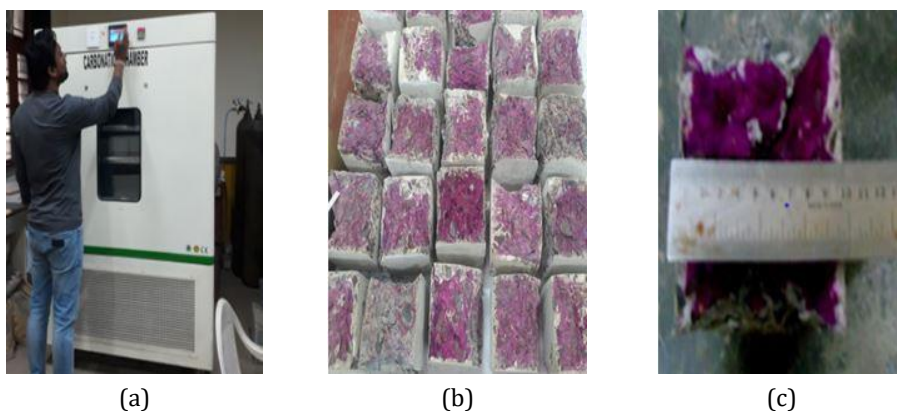


Fig. 6 Working of rheometer test apparatus

3. Result and Discussions

3.1. Workability and Rheology

By using a 0.40 water-cement ratio, all the mixes were prepared and the influence of fly ash together with the glass fibers on the workability and rheology parameters of the concrete was measured concerning the slump, yield stress and viscosity as shown in Table 4. According to the current investigation, it is seen that, glass fiber in the mix decreased the workability of concrete in contrast to the control mix. Also, the inclusion of glass fiber without any replacement in the mix signified that the yield stress and viscosity increased by 14.62% and 12.40% respectively than control concrete. The decrease in workability and increase in the yield stress and viscosity is due to the presence of glass fiber in mix which hinders the flow-ability of freshly mixed concrete [36]. It is also observed that as an alternative of cement increases by fly ash together with glass fiber, the workability of concrete also increases and is found to be 18.36% for higher replacement (40%) than control concrete. Similarly, the rheological parameters like yield stress and viscosity decreased 36.98% and 29.85% respectively than control concrete. The increase in workability and drop in yield stress and viscosity accounts due to the addition of fine grain fly ash which is spherical in shape and acts as a ball bearing effect which reduced internal friction and increases the flowability of fresh concrete [37]. In combined replacement, when 40% cement and 20% sand were replaced by fly ash together with glass fiber the slump was observed up to 14.28% more and yield stress and viscosity was observed as 31.69% and 29.43% respectively lower than all control mix.

Table 4 Result of slump and rheology test

Mix	Slump (mm)	Yield Stress (τ_0)	Viscosity (μ)
C0-0	49	356.54	19.16
F0-0	46	408.67	21.50
F20-0	53	281.65	16.18
F40-0	58	224.67	13.44
F0-20	49	373.28	19.44
F0-40	42	426.34	21.96
F20-20	51	310.62	16.87
F40-20	56	243.54	13.52
F20-40	43	446.32	22.36
F40-40	37	591.54	26.53

3.2. Compressive Strength

The compressive strength was calculated for 10 concrete mixes over 40 cubes for a 0.40 W/C ratio. Figure 7 shows the result of the compressive strength of various mixtures with diverse curing periods. The result shows that by adding 600 g/m³ glass fiber to the mix, the compressive strength at 7, 28, 56 and 119 days of curing period increased by 4.88%, 5.08%, 5.53% and 5.63% respectively over normal concrete. Plain concrete possesses low tensile strength and low tensile strain capacities i.e. brittle materials due to which cracks are inherently present in concrete even before loading. On the other hand, glass fiber has high tensile strength and high modulus of elasticity which are discontinuous and most commonly arbitrarily dispersed throughout the mix. Glass fiber in the cementitious matrix provides a bridge for stress to transfer across the cracks, which results in a decrease in the propagation of cracks in the fresh mix and increased the strength of concrete [38].

From the present analysis, it is examined that when 20% of cement was substituted by fly ash, slight strength reduced at 7 days but after 7 days the strength developed at an elevated rate than control concrete (C₀₋₀) and concrete with glass fiber (F₀₋₀). The 28 days strength improved by 11.65% while 119 days strength increased by 17.50% over control concrete. As the curing period increases, strength also increases due to slow and continuous pozzolonic reaction of fly ash mixes. The strength of concrete continuously increases, which could be attributed to the late gain of strength from the fly ash in the system [39-40]. The key finding of the present investigation is that even at 40% cement replacement by fly ash together with glass fiber, 56 days strength of mix (F₄₀₋₀) is almost equal to 28 days strength of control mix (C₀₋₀). From the test result, it may be concluded that it is possible to achieve 28 days strength of control mix at 56 days for the same W/C ratios even at 40% cement replacement by fly ash together with low doses of glass fiber, which reduced nearly 153 kg/m³ of cement and consume a higher amount of fly ash and makes the concrete more sustainable by using the proposed method. The reduction in strength observed for 20% cement replacement at an early age (7 days) is because of slow pozzolanic reaction of a fly ash compared to that of cement at the initial stage. At a later age, the increase in strength of concrete is due to the reaction in between hydrated calcium hydroxide in concrete and silica present in fly ash resulting in improved pore allocation in the mix. Finer fly ash offered a better particle packing effect, the unhydrated fine fly ash act as micro filler in the concrete which also improves the compressive strength of concrete [41].

The test results reveal that with an increasing percentage of fine aggregate replacement by fly ash, the compressive strength increased even at 7 days of curing period. When 40% of fine aggregate was replaced by fly ash (F₀₋₄₀) the compressive strength increased by 29% over the control mix at curing period of 28 days. The significant finding is that the compressive strength for 20% sand replacement by fly ash was nearly 2% higher than the compressive strength for 20% cement replacement by fly ash at 28 days. The increment in strength for fine aggregate replacement is due to the formation of extra CSH gel which reduced the pores inside the mixture [42]. The increase in strength due to fine particles is dominant which offered a better particle packing effect than sand particles hence, in sand replacement mixes better compressive strength observed over control and cement replacement mixes. For combined replacement, when 20% of cement and 40% of sand are replaced by fly ash together with glass fiber (F₂₀₋₄₀) best result is obtained than all other mixes. The increase in strength was observed as 36.33% more at the age of 28 days when compared to control concrete (C₀₋₀) as shown in Figure 7. The strength improvement in combined replacement (F₂₀₋₄₀) is because of the formation of extra calcium silicate hydrates (C-S-H) gel in fly ash based concrete and better particle packing arrangement, as it increases the microstructure by reducing the voids inside the concrete.

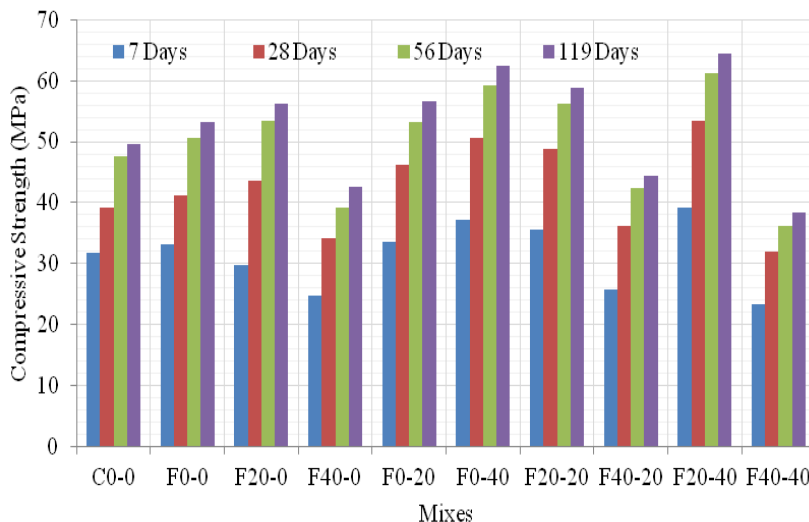


Fig. 7 Effect of separate and combine replacement of cement and sand by fly ash along with glass fiber on compressive strength over control concrete at different curing period

3.3. Bulk Electrical Resistivity

Electrical resistivity (ER) is generally dependent on the concrete microstructure like pore size and interconnection shape. It is observed that when 0.6 kg/m^3 of glass fiber is added to the mix the ER value increased nearly 11.75% than the control mix when the sample tested at 28 days. The discrete and randomly distributed glass fibres in the mix act as a crack arrester and hence reduce the permeability of concrete, resulting in increased electrical resistivity. The ER values for 7, 28, 59 and 119 days of curing periods are shown in Figure 8. From the test result it is seen that when separate 20% and 40% cement is replaced by fly ash together with glass fiber, the ER values increased by 28.50% and 49.20% respectively for a 0.40 water-cement ratio at 28 days of curing period. Fly ash as cement replacement material improved the particle packing which improve the microstructure of concrete, hence the ER values increased as cement replacement by fly ash increased.

In sand replacement mixes the ER values are more improved than cement replacement mixes. For 20% and 40% sand replacement, the ER values increased by 28.57% and 49.20% respectively at 28 days. The enhancement in ER result is due to extra finer contents which improve the packing density. When combine 20% cement and 20% sand (F₂₀₋₂₀) were replaced by fly ash, ER values increased up to 52.78% than the control mix (C₀₋₀). While for 40% cement and 40% sand replacement (F₄₀₋₄₀) the ER increased by 54% than control mix. In combine replacement, ER increased due to high amount of fly ash in concrete producing additional C-S-H gel which fills the voids inside the concrete. As well as finer fly ash fill the capillary pores which will be filled by water in control concrete. Hence combined replacement of cement and fine aggregate by fly ash together with glass fiber shows better results than other mixes.

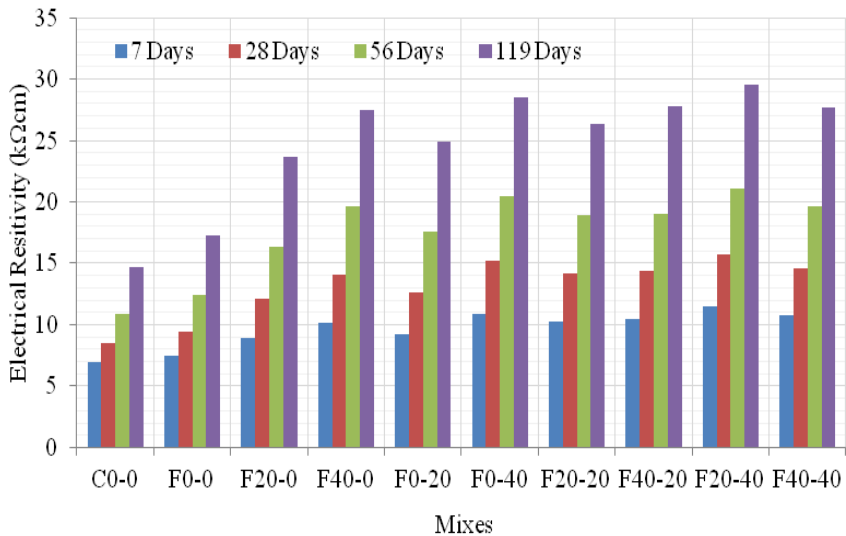


Fig. 8 Effect of separate and combine replacement of cement and sand by fly ash along with glass fiber on electrical resistivity over control concrete at different curing period

3.4. Ultrasonic Pulse Velocity

From a durability point of view, ultrasonic pulse velocity (UPV) is a very useful method that gives the idea about particle packing, homogeneity and quality of a structure. In the present investigation, the UPV values of various mixes reflect minor changes but higher changes in electrical resistivity (ER) were observed for the same mixes. The inclusion of 0.6 kg/m^3 of glass fiber in concrete improve the UPV values by 0.98% and 1.35% at 28 and 119 days respectively over the control mix. From the experimental investigation it is seen that as the percentage of cement replacement by fly ash increases, the UPV values also increased over the control mix. For 40% cement replacement along with glass fiber (F_{40-0}), the UPV increased up to 3.86% at the curing period of 119 days. The UPV values for different curing periods are shown in Figure 9. Fly ash produced more CSH gel which fills the voids inside the concrete. Also, finer fly ash improves the particle packing than cement particles due to which UPV increases as cement replacement by fly ash increases. While 40% sand was replaced by fly ash together with glass fiber the UPV values increased 3.35% to 6.94% at the curing period of 7 to 119 days respectively over the control mix.

Meanwhile, sand is replaced by fly ash together with glass fiber, the UPV values increased, which maybe because of the availability of additional finer fly ash in the mix which form additional CSH gel and reduce the voids inside the mix [43]. Also, coarser material (Sand) was replaced with finer material which improved the microstructure of concrete by increasing packing density. In view of the finer fly ash in concrete, the mix becomes denser than control concrete hence, UPV values increase as the proportion of sand replacement by fly ash increases. In combined mixes when cement and fine aggregate was replaced by fly ash together with glass fiber, the UPV values improved than control concrete (C_{0-0}) and concrete with glass fiber (F_{0-0}) as shown in Figure 9. For mix F_{20-20} and F_{40-40} , the UPV values increased by 5.57% and 8.68% respectively at the age of 119 days than the control mix.

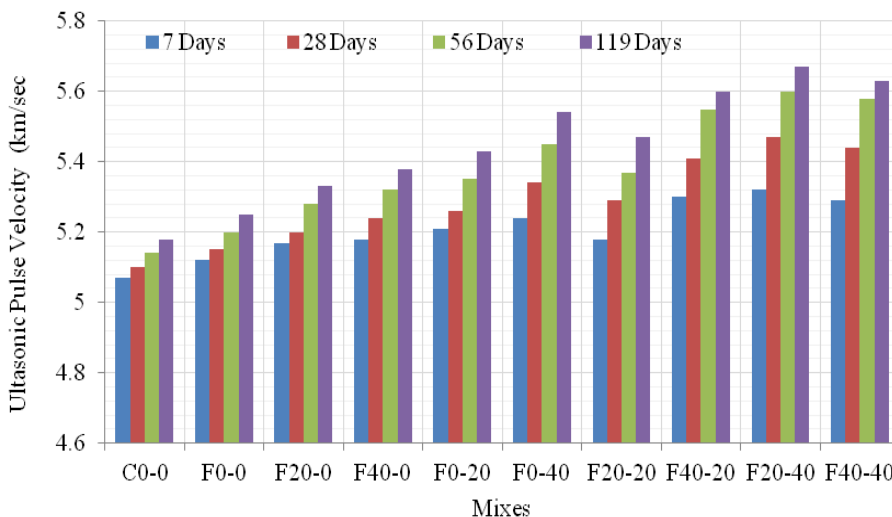


Fig. 9 Effect of separate and combine replacement of cement and sand by fly ash together with glass fiber on U.P.V. over control concrete at different curing period.

3.5. Carbonation Test

From carbonation test, it is seen that the addition of glass fiber in the mix reduced the carbonation depth by 12% over control concrete when samples were placed in a carbonation chamber for 28 days. The anti-cracking effect of glass fiber reduced the large number of microcracks in concrete which prevent the entry of CO_2 inside the concrete. Therefore, the addition of glass fiber in concrete reduced the depth of carbonation. From the experimental result it is also observed that as the cement replacement by fly ash increased, the carbonation depth also increased over control mix (C_{0-0}) and glass fiber mix (F_{0-0}). When 20% and 40% cement is replaced by fly ash together with glass fiber (F_{20-0} and F_{40-0}) the carbonation depth increased 2 times and 4.5 times more than the control mix. The expansion in carbonation depth is owing to the reduction of calcium hydroxide which reduced pH value and increased the depth of carbonation [44-45].

For sand replacement mixes, a positive result is observed on carbonation. The test result shows that as the percentage of fine aggregate replacement by fly ash increases, the depth of carbonation decreases than control mixes as shown in Figure 10. The reduction in carbonation depth was observed as 0.75 to 1.25 times more when 20% sand was replaced by fly ash together with glass fiber, while for 40% of sand replacement the reduction was up to 2 times more over control concrete (C_{0-0}). The carbonation depth reduced due to the total amount of carbonatable constituents remains almost the same and the porosity decreases in sand replacement mix resulting in a reduction in carbonation depth observed than cement replacement mixes.

When combined cement and sand were replaced by fly ash together with glass fiber, the carbonation depth was slightly increased over control concrete (C_{0-0}) as shown in Figure 10. In combined replacement, the rate of increasing carbonation depth observed is lower than when only cement is replaced by fly ash mixes. For mix F_{20-20} the carbonation depth increased by 1.5 to 2 times more when compared to control concrete. For mix F_{20-40} the carbonation depth slightly increased over control mix.

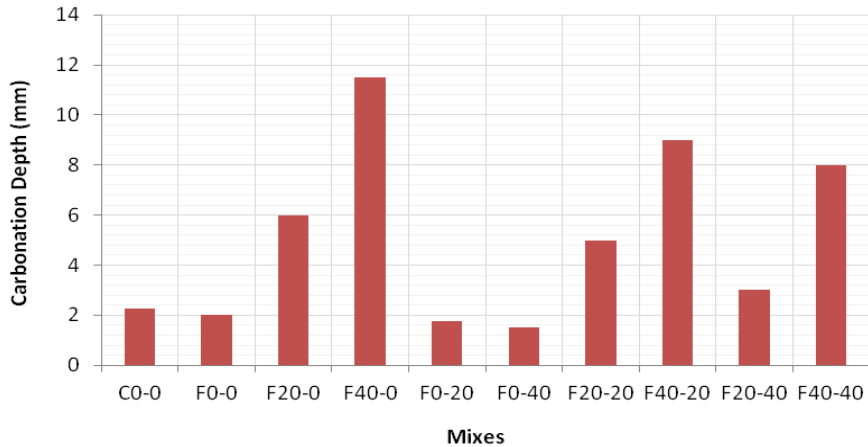


Fig. 10 Effect of separate and combine replacement of cement and sand by fly ash together with glass fiber on carbonation depth over control concrete at different curing period.

4. Conclusion

The prime purpose of the present research is an attempt to produce sustainable concrete by using available industrial by-products. The present research was taken up with the view to encourage the higher consumption of fly ash and minimize the use of cement and sand in concrete. Contractors are concerned about low early age strength because of the addition of fly ash as partial replacement materials for cement as well as a scarcity of sand in concrete. To address these concerns of contractors, glass fiber is used to compensate for the loss of early age strength in concrete when partial cement is replaced by fly ash. While partial replacements of sand by fly ash fulfil the requirements of sand for the construction industry, it also achieves higher strength and durability. The study was also taken up to curtail the use of cement and conserve locally available natural sand by utilizing the maximum quantity of fly ash available in the local region so that landfill area requirement for dumping the fly ash will be reduced. Supporting the test results, the subsequent conclusions were drawn to know the performance of proposed mixes by conducting different tests on fresh and hardened properties of concrete.

- Based on the present investigation it is observed that adding 0.6 kg/m^3 of glass fiber of whole volume of concrete, the slump height reduced by 6.12% and the yield stress and viscosity increased by 14.62% and 12.21% respectively than control mix. But loss of slump height due to inclusion of glass fiber is compensated by addition of fly ash in concrete. The carbonation depth reduced by 11.11%, while compressive strength, ER values and UPV values increased by 5.13%, 11.70% and 0.98% respectively at the age of 28 days than control mix.

- From the test result it is observed that when 20% of cement is substituted by fly ash in conjunction with fiber, the 28 days compressive strength, ER value and UPV improved by 11.65%, 38.90% and 2.40% respectively over control concrete. As the proportion of cement replacement by fly ash increased along with glass fiber, the workability and durability parameters increased while compressive strength decreased for higher replacement. For 40% cement replacement (F₄₀₋₀) the workability, ER, UPV and carbonation depth increased by 18.36%, 49.20% and 2.74% and 4.5 times respectively than control mix at 28 days of curing period.
- The important finding from the proposed mixes is that, even at 40% cement replacement by fly ash together with glass fiber, the 56 days strength of mix (F₄₀₋₀) is almost equal to 28 days strength of control mix (C₀₋₀). Based on the test results, it could be concluded that, it is feasible to attain 28-day compressive strength of control concrete at 56 days for the same W/C ratios even at 40% cement replacement by fly ash together with low doses of glass fiber and save nearly 153 kg/m³ of cement for preparing 1m³ of concrete.
- As the percentage replacement of sand by fly ash increased in conjunction with low volume of glass fiber, the carbonation depth reduces, on the other hand the compressive strength, ER and UPV values increased than control mixes and cement replacement mixes. For mix F₀₋₄₀ the carbonation depth reduced by 2 times more than control mix. The Compressive strength, ER and UPV values increased by 25.61%, 65.31% and 6.94% respectively up to the age of 119 days over control mix.
- In combine replacement of cement as well as fine aggregate by fly ash along with glass fiber, the mixes F₂₀₋₂₀ and F₂₀₋₄₀ shows better result of compressive strength and durability parameters than all other mixes. For mix F₂₀₋₄₀ the compressive strength increased by 36.33%, ER values increased by 65.82%, UPV values increased by 7.25% and nearly equal result obtained on carbonation depth when compared to control mix at 28 days of curing period. Using proposed method, it is possible to consume higher amount of fly ash and make the concrete more sustainable and durable.
- From the current research, it could be concluded that the addition of fly ash as cement replacement together with a small dose of glass fiber improves the durability of concrete in terms of ER and UPV. Also, sand replacement by fly ash together with glass fiber further improves the durability of concrete in terms of ER, UPV and CD. Fly ash in concrete improved the microstructure and proper bonding of fiber with a matrix which increased the durability of concrete. Hence partial replacement of cement and fine aggregate by fly ash together with glass fiber results in durable concrete.
- For combine replacement, up to 20% cement and 40% sand by fly ash along with 0.6 kg/m³ of glass fiber is strongly suggested in general practice use. Without hampering strength, durability and cost of concrete, it will consume a high volume of fly ash and minimize the amount of cement and natural sand and make the concrete more durable and sustainable.
- By using high-volume fly ash in concrete as a partial substitute material for cement and sand, we tend to rescue natural resources to maintain the green environment and increase the durability of the structure at the bottom potential cost.

5. Future Scope of Present Investigation

Considering the surplus amounts of fly ash and use of limited amount of cement and availability of natural sand, the partial alternative of cement and natural sand by fly ash has economic and environmental benefits. The present investigations pertain to study on workability, durability and strength of concrete with separate and combine replacement of cement and natural sand by available fly ash in local region of India together with low doses of glass fiber for making durable and sustainable concrete. In context of the future scope of the present work could be as given below.

- Glass fiber has high tensile strength and arrests the cracks in the specific area and cracks propagation of concrete, hence self-healing capacity may be checked for different mixes.
- For comparison of the results among proposed mixes single constant dose of admixture for all W/C ratios is intentionally used in present investigation. Different doses of admixture with different W/C ratios suggested on case-to-case basis.
- Fly ash as sand replacement up to 40% increases the concrete durability and strength. More than 40% sand replacement by fly ash is suggested to reduce the use of natural sand and increased the strength and durability of concrete.
- Partial replacement of cement and sand by available fly ash together with hybrid fiber is suggested to enhance the concrete strength and durability.

Acknowledgement

I would like to thank, Civil Engineering Department NIT Raipur, for providing the facilities in the Concrete Technology Lab. I am very thankful to Dr. Sourabh Rungta, Director, Rungta College of Engineering & Technology Raipur, Chhattisgarh, India. I would like to also thank all the faculty and staff in the Department of Civil Engineering, NIT, Raipur for their help, inspiration and moral support, which have greatly contributed to the success of my work.

References

- [1] Afrazi M, Yazdani M. Experimental study of sand-rubber mixture. 7th International conference on civil engineering, architecture and urban economic development, Iran 2009; 1-8. https://www.researchgate.net/publication/341495064_Experimental_study_of_sand-rubber_mixtures
- [2] Benhelal E, Zahedi G, Shamsaei E, Bahodori. Global strategies and potentials to curb CO₂ emission in cement industry. Journal of cleaner production. 2013; 51: 142-161. <https://www.sciencedirect.com/science/article/abs/pii/S0959652612006129>
- [3] Report on fly-ash generation at coal/lignite based thermal power station and its utilization in the country for the year 2019-2020. Central electricity authority, India, 2020. https://cea.nic.in/wp-content/uploads/tcd/2021/01/flyash_2019-20.pdf
- [4] Singh Y. Report on fly ash utilization in India. The wealth waste. 2017. <http://www.wealthywaste.com/fly-ash-utilization-in-india>
- [5] Kwan, A, Li Y. Effects of fly ash microsphere on rheology, adhesiveness and Strength of mortar. Construction and building materials, 2013; 42: 137-145. <https://www.sciencedirect.com/science/article/abs/pii/S0950061813000780>
- [6] Mehta P, Monteiro P. High performance high volume fly ash concrete. Concrete: microstructure, properties, and material. 4th edition, New York, 2014:462-446, ISBN

780071797870

<https://www.accessengineeringlibrary.com/content/book/9780071797870>

- [7] Zheng D, Tang W, Li D, Ren C, Tang W. Study of high volume circulating fluidized bed fly ash on rheological properties of the resulting cement paste. *Journal of construction and building materials*, 2017; 135: 86-93. <https://www.sciencedirect.com/science/article/abs/pii/S0950061816320487>
- [8] Jalal M, Fathi M, Farzad M. Effects of fly ash and TiO₂ nano particles on rheological, mechanical, micro Structural and thermal properties of high strength self compacting concrete. *Journal of mechanics of materials*. 2013; 61: 11-27. <https://www.sciencedirect.com/science/article/abs/pii/S0167663613000173>
- [9] Yoo DY, Kang ST, Yoon YS. Effect of fiber length and placement method on flexural behavior, tension-softening curve, and fiber distribution characteristics of UHPFRC, *Journal of construction and building materials*. 2014; 64: 67-81. <https://daneshyari.com/article/preview/257580.pdf>
- [10] Balakrishnan B, Awal A. Durability properties of concrete containing high volume malaysian fly ash. *International journal of research in engineering and technology*. 2014; 3(4): 529-533. <http://eprints.utm.my/id/eprint/59700/>
- [11] Shaikh FUA, Supit SWM, Sarker PK. A study on the effect of nano silica on compressive strength of high volume fly ash mortars and concretes. *Materials and Design*. 2014; 60: 433-442. <https://www.sciencedirect.com/science/article/abs/pii/S0261306914002933>
- [12] Saravanakumar P, Dhinakaran G. Strength characteristics of high-volume fly ash-based recycled aggregate concrete, *Journal of material in civil engineering*. 2013; 25(8): 1127-1133. <https://ascelibrary.org/doi/abs/10.1061/%28ASCE%29MT.1943-5533.0000645>
- [13] Aghabaglou AM, Ramyar K. Mechanical properties of high-volume fly ash roller compacted concrete designed by maximum density method. *Construction and building materials*. 2013; 38: 356-364. <https://www.sciencedirect.com/science/article/abs/pii/S0950061812006216>
- [14] Latha KS, Rao MV, Reddy SV. Estimation of GGBS and HVFA strength efficiencies in concrete with age. *International Journal of Engineering & Advanced Technology* 2012; 2(2): 221-225. <https://www.ijeat.org/wp-content/uploads/papers/v2i2/B0904112212.pdf>
- [15] Sounthararajan VM, Sivakumar A. Performance evaluation of metallic fibers on the low and high volume class F fly ash based cement concrete. *International journal of engineering & technology*. 2013; 5(2): 606-619. <https://www.researchgate.net/publication/285706228>
- [16] Siddique R. Properties of fine aggregate-replaced high volume class F fly ash concrete. *Leonardo journal of sciences*. 2013; 22: 79-90. http://ijs.academicdirect.org/A22/079_090
- [17] Harasymiuk J, Rudzinski A. Old dumped fly ash as a sand replacement in cement composites. *Journal of buildings*. 2020; 10: 1-18. <https://doi.org/10.3390/buildings10040067>
- [18] Feng B, Liu J, Wei J, Zhang Y, Chen Y, Wang L, Chen Y, and Sun Z. Research on properties and durability of desalinated sea sand cement modified with fly ash. *Case studies in construction materials*. 2021; 15: 1-11. <https://www.sciencedirect.com/science/article/pii/S221450952100190X>
- [19] Topcu IB, Canbaz M. Effect of different fibers on the mechanical properties of concrete containing fly ash. *Construction and Building Materials*, 2007; 21: 1486-1491. <https://www.sciencedirect.com/science/article/abs/pii/S095006180600153X>
- [20] Raut MV, Deo SV. A parametric study on effect of fly ash together with fiber for sustainable concrete. *International journal of civil engineering and technology*. 2017; 8: 100-110. https://iaeme.com/Home/article_id/IJCET_08_03_010

- [21] Liu Y, Presuel M. Effect of elevated temperature curing on compressive strength and electrical resistivity of concrete with fly ash and ground-granulated blast-furnace slag. *ACI material journal*, 2014; 111: 531-538. <https://www.researchgate.net/publication/293176716>
- [22] Filho J, Medeiros M, Pereira E, Helene P, Isaia G. High volume fly ash concrete with and without hydrated lime: chloride diffusion coefficient from accelerated test. *Journal of materials in civil engineering*, 2013; 25: 411-418. <https://ascelibrary.org/doi/10.1061/%28ASCE%29MT.1943-5533.0000596>
- [23] Ramjan S, Tangchirapat W, Jaturapitakkul C, Ban CC, Jitsangiam P, Suwan T. Influence of cement replacement with fly ash and ground sand with different fineness on alkali-silica reaction of mortar. *Journal of materials*, 2021; 14: 1-13. <https://doi.org/10.3390/ma14061528>
- [24] Younsi A, Turcry P, Roziere E, Mokhtar A, Loukili A. Performance-Based Design and carbonation of concrete with high fly ash content. *Cement concrete composites*, 2011; 33: 993-1000. <https://www.sciencedirect.com/science/article/abs/pii/S0958946511001259>
- [25] Malhotra VM, Mehta PK. High-performance, high-volume fly ash concrete: Materials, mixture proportioning, properties, construction practice and case histories. High strength concrete. 2nd edition, Ottawa, Canada, 2002. ISBN 0973150726 9780973150728. <https://www.worldcat.org/oclc/60744031>
- [26] Neville AM. Properties of concrete. 4th edition, Longman, England. 2009. ISBN 9780582230705 0582230705. <https://www.worldcat.org/title/properties-of-concrete-standards-updated-to-2002/oclc/750701275>
- [27] IS 10262-2009, Concrete mix proportioning-Guidelines. 2nd revision, 2019. <https://civiconcepts.com/wp-content/uploads/2020/11/4.IS-10262-2019-New-Mix-design.pdf>
- [28] Ojha PN, Singh B, Kaura P, Singh A. Lightweight geopolymer fly ash sand: an alternative to fine aggregate for concrete production, *Research on engineering structures and materials*, 2021; 7(3): 375-391. <http://www.jresm.org/archive/resm2021.257ma0205.html>
- [29] Zeggar ML, Azline N, Safiee NA. Fly ash as supplementary material in concrete: A review. *IOP Conference Series: Earth and Environmental Science*, 2019, 357: 1-10. <https://iopscience.iop.org/article/10.1088/1755-1315/357/1/012025>
- [30] BIS 12269-1987, Ordinary Portland cement 53 grade specifications. First revision 2013. <https://law.resource.org/pub/in/bis/S03/is.12269.1987.pdf>
- [31] BIS 1727-1967. Methods of test for polzonic materials, 2004 <https://law.resource.org/pub/in/bis/S03/is.1727.1967.pdf>
- [32] BIS 2386-1963. Methods of test for aggregates for concrete, Part 1 to 7, 2002. https://www.services.bis.gov.in:8071/php/BIS/bisconnect/pow/is_details?IDS=MTg4MjY%3D
- [33] BIS 383-1970, Specification for crushed stone and fine aggregates from natural sources for concrete. 2nd revision, 2002. <https://www.iitk.ac.in/ce/test/IScodes/is.383.1970.pdf>
- [34] Chen B, Liu J. Effect of fibers on expansion of concrete with a large amount of high f-CaO fly ash. *Cement and concrete research*. 2003; 33: 1549-1552. <https://www.sciencedirect.com/science/article/abs/pii/S000888460300098X>
- [35] Limbachiya M, Meddah MS, Ouchagor Y. Use of recycled concrete aggregate in fly ash concrete. *Construction and building materials*. 2012; 27: 439-449. <https://www.sciencedirect.com/science/article/abs/pii/S0950061811003771>
- [36] Barhum R, Mechtcherine V. Effect of short, dispersed glass and carbon fibres on the behaviour of textile-reinforced concrete under tensile loading, *Engineering fracture mechanics*, 2012; 92: 56-71. <https://www.sciencedirect.com/science/article/abs/pii/S0013794412002342>

- [37] Jiao W, Shi C, Yuan Q, Yn X, Liu Y, Li H. Effect of constituents on rheological properties of fresh concrete-A review. *Cement and concrete composite*, 2017; 83: 146-159. <https://www.sciencedirect.com/science/article/abs/pii/S0958946516303328>
- [38] Barluenga G. and Olivares H. Cracking Control of Concretes Modified with Short AR-Glass Fibers at Early Age, Experimental Results on Standard Concrete and SCC, *Cement and Concrete Research*, 2017: 37: 1624–1638. <https://www.sciencedirect.com/science/article/abs/pii/S0008884607002025>
- [39] Agrawal US, Wanjari SP, Naresh DN, Characteristic study of geopolymers fly ash sand as a replacement to natural river sand, *Construction and Building Materials*. 2019; 150: 681 -688. <https://doi.org/10.1016/j.conbuildmat.2017.06.029>
- [40] Rao SM, Acharya IP, Synthesis and characterization of fly ash geopolymer sand, *Journal of Materials in Civil Engineering*. 2014; 26:2, 186 - 190. [https://doi.org/10.1061/\(ASCE\)MT.1943-5533.0000880](https://doi.org/10.1061/(ASCE)MT.1943-5533.0000880)
- [41] Chen H. and Choi J. Analysis of shrinkage and thermal stresses in concrete slabs reinforced with GFRP rebars, *Journal of materials in civil engineering*. 2011; 23; 612 627. <https://ascelibrary.org/doi/abs/10.1061/%28ASCE%29MT.1943-5533.0000216>
- [42] Hwang K, Noguchi T, Tomosawa F, Prediction Model of Compressive Strength Development of F fly Ash concrete, *Cement and Concrete research*, 2004; 34, 2269-2276. <https://www.sciencedirect.com/science/article/abs/pii/S0008884604001644>
- [43] Deo SV, Pofale AD, Parametric study for replacement of sand by fly ash for better packing and internal curing. *Open Journal of Civil Engineering*, 2015; 5: 118-130. <https://www.scirp.org/journal/paperinformation.aspx?paperid=54586>
- [44] Holland RB, Kurtis KE, Kahn LF, Effect of different concrete materials on the corrosion of the embedded reinforcing steel, *Corrosion of Steel in Concrete Structures*, 2016; 131-147. <https://www.sciencedirect.com/science/article/pii/B9781782423812000079>
- [45] J. Khunthongkeaw J, Tangtermsirikul S, Leelawat T, A study on carbonation depth prediction for fly ash concrete, *Construction and Building Materials*, 2006; 20: 744-753. <https://www.sciencedirect.com/science/article/abs/pii/S0950061805000978?via%3Dihub>



Content

- Research Article
643 Lemiye Atabek Savaş
Synthesis of β -strontium hydrogen phosphate nanosheets and its effect on thermal and tribo-mechanical properties of polypropylene composites
- Research Article
659 Özgür Demircan, Fatma Burcu Uzunoglu, Naser Rezaei Ansaroudi
Influence of multi-walled carbon nanotubes on tensile and flexural properties of polyamide 66/short glass fiber composites
- Technical Note
675 Nasir Mohammed Tahir, Adamu Umar Alhaji, Ibrahim Abdullahi
Performance evaluation of unmanned aerial vehicle wing made from sterculiasetigeradelile fiber and pterocarpuserinaceus wood dust epoxy composite using finite element method Abaqus and structural testing
- Research Article
695 Nikolay Dolgov, Maris Hauka, Leonids Vinogradovs
Adhesion strength evaluation for plasma-sprayed coatings based on intensity of singular stress
- Research Article
707 Prem Kumar V., Vasugi V.
Experimental investigation on bamboo fibre reinforced mortar using artificial neural network – a comparative study
- Research Article
721 Mehmet Topuz
Effect of ZrO₂ on morphological and adhesion properties of hydroxyapatite reinforced poly- (lactic) acid matrix hybrid coatings on Mg substrates
- Research Article
735 Olatunji Oladimeji Ojo, Gbadebo Samuel John
Weldability of interlocked-end friction stir welding of aluminum alloy: single and double-sided welding
- Research Article
751 Mehmet Hakan Demir
Numerical investigation of the combined effects of coating layer properties and specific heat capacities of materials on the heat transfer mechanism in solidification of pure metals
- Research Article
773 Tanvi Saxena, V.K. Chawla
Evaluation of mechanical properties for banana-carbon fiber reinforced nano-clay epoxy composite using analytical modeling and simulation
- Research Article
799 Bora Şener, Toros Arda Akşen, Emre Esener, Mehmet Fırat
On the effect of numerical parameters in finite element through thickness modeling for springback prediction
- Research Article
811 Altin Bidaj, Huseyin Bilgin, Marjo Hysenlliu, Irakli Premti, Rrapo Ormeni
Performance of URM structures under earthquake shakings: Validation using a template building structure by the 2019 Albanian earthquakes
- Research Article
835 Birendra Kumar Bohara, Prasenjit Saha
Nonlinear behaviour of reinforced concrete moment resisting frame with steel brace
- Technical Note
853 Om V. Vaidya, Kapil Malviya, Yuvaraj L. Bhirud
The strength characteristics of concrete using recycled concrete aggregates
- Technical Note
861 Lalit B. Pawar, Keshav K. Sangle, Yuvaraj L. Bhirud
Experimental investigation of spalling effect of elevated temperature on concrete containing waste plastic aggregates
- Research Article
885 Mahesh V. Raut
Leverage of high-volume fly ash along with glass fiber for sustainable concrete

